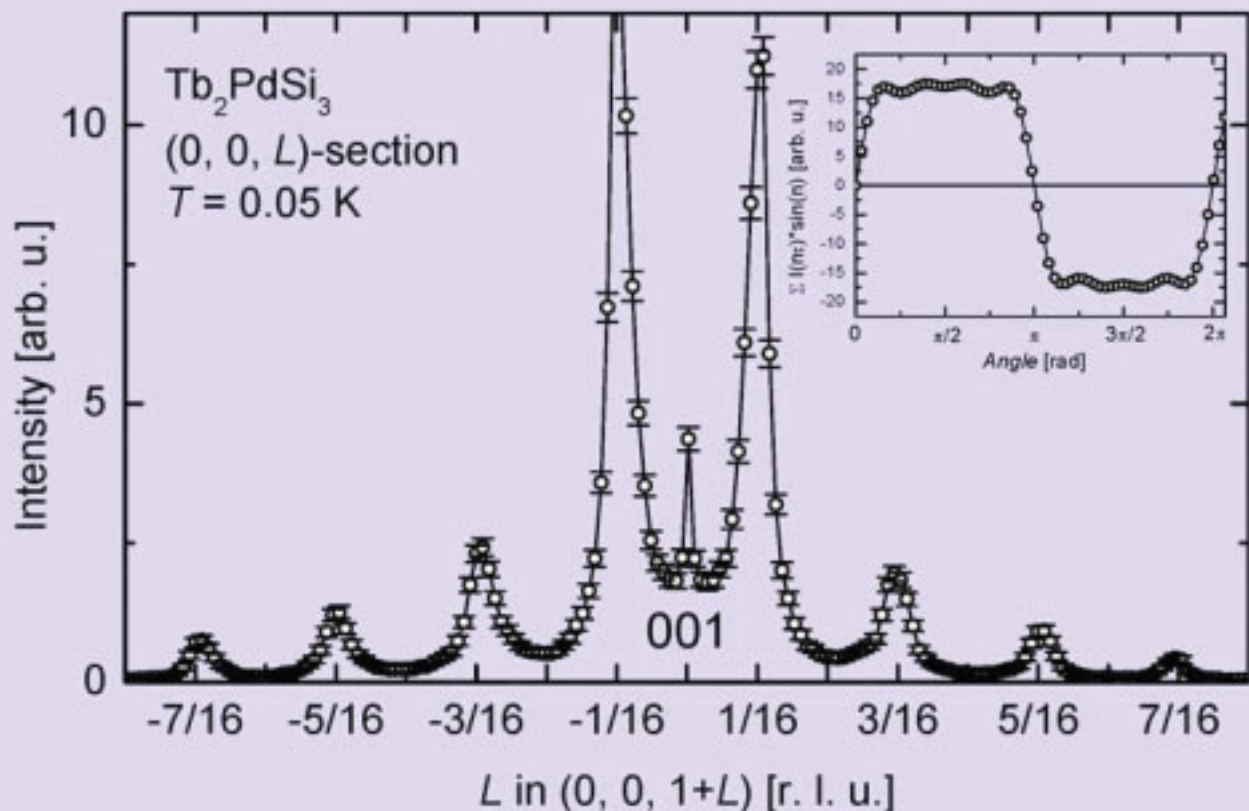


Matthias Dietrich Frontzek

Magnetic properties of $R_2\text{PdSi}_3$ (R = heavy rare earth) compounds



Institut für Festkörperphysik
Fachrichtung Physik
Fakultät Mathematik und Naturwissenschaften
Technische Universität Dresden

Magnetic properties of
 R_2PdSi_3
(R = heavy rare earth) compounds

Dissertation
zur Erlangung des akademischen Grades
Doctor rerum naturalium

vorgelegt von
Matthias Dietrich Frontzek
geboren am 19.09.1977 in Limburg a. d. Lahn

Dresden 2009



Bibliografische Information der Deutschen Nationalbibliothek

Die Deutsche Nationalbibliothek verzeichnet diese Publikation in der Deutschen Nationalbibliografie; detaillierte bibliografische Daten sind im Internet über <http://dnb.ddb.de> abrufbar.

1. Aufl. - Göttingen : Cuvillier, 2009
Zugl.: TU Dresden, Univ., Diss., 2009
978-3-86955-102-9

1. Gutachter: Prof. Dr. Michael Loewenhaupt
2. Gutachter: Prof. Dr. Markus Braden

Eingereicht am 05.06.2009
Verteidigt am 31.08.2009

© CUVILLIER VERLAG, Göttingen 2009
Nonnenstieg 8, 37075 Göttingen
Telefon: 0551-54724-0
Telefax: 0551-54724-21
www.cuvillier.de

Alle Rechte vorbehalten. Ohne ausdrückliche Genehmigung des Verlages ist es nicht gestattet, das Buch oder Teile daraus auf fotomechanischem Weg (Fotokopie, Mikrokopie) zu vervielfältigen.

1. Auflage, 2009
Gedruckt auf säurefreiem Papier

978-3-86955-102-9

Abstract

The $R_2\text{PdSi}_3$ (R = heavy rare earth) have been synthesized first in 1990 in the search for materials with unusual electronic properties. The availability of single crystals was the starting point for several investigations of the magneto-crystalline anisotropy, also in applied magnetic fields. The results of the observed properties in resistivity, magnetization and susceptibility lead to the summary that these compounds range from interesting to exotic and that their magnetic properties are low dimensional, spin-glass like and altogether “novel”.

The focus of this thesis is the careful analysis of the magnetic properties and magnetic structures of single crystalline $R_2\text{PdSi}_3$ (R = Gd, Tb, Dy, Ho, Er, Tm). The investigation of macroscopic properties uses magnetization and ac-susceptibility measurements. Resulting from these investigations are magnetic phase diagrams. Neutron and resonant X-ray diffraction measurements elucidate the magnetic structure for the investigated compounds. The phase diagram of Tb_2PdSi_3 is the starting point of a detailed neutron diffraction study in applied magnetic fields up to 6.5 T and in the temperature range from 0.05 K to 100 K on this compound. Key to the understanding of the $R_2\text{PdSi}_3$ is the strong coupling of crystallographic structure to the magnetic properties. Thus the established framework of exchange interaction and magneto-crystalline anisotropy allows a collective description instead of a “novel” behavior.

Zusammenfassung

Die $R_2\text{PdSi}_3$ (R = schwere seltene Erde) sind erstmals 1990, im Rahmen der Suche nach Materialien mit ungewöhnlichen elektronischen Eigenschaften, synthetisiert worden. Die Verfügbarkeit von Einkristallen war der Startpunkt für eine Vielzahl von Untersuchungen, auch in angelegten Magnetfeldern, der magneto-kristallinen Anisotropie. Das Ergebnis der untersuchten Eigenschaften Widerstand, Magnetisierung und Suszeptibilität führte zu dem Schluss, dass diese Verbindungen interessant bis exotisch und dass ihre magnetischen Eigenschaften niedrig dimensional, Spin-glas ähnlich und insgesamt „neuartig“ sind.

Der Schwerpunkt dieser Dissertation ist die genaue Analyse der magnetischen Eigenschaften und Magnetischen Strukturen von einkristallinen $R_2\text{PdSi}_3$ (R = Gd, Tb, Dy, Ho, Er, Tm). Magnetisierungs- und Suszeptibilitäts-Messungen werden zur Untersuchung der makroskopischen Eigenschaften benutzt. Resultat dieser Untersuchungen sind magnetische Phasendiagramme. Neutronen und resonante Röntgendiffraktometrie klären die magnetische Struktur der untersuchten Verbindungen auf. Das Phasendiagramm von Tb_2PdSi_3 ist der Startpunkt einer detaillierten Neutronendiffraktionsuntersuchung dieser Verbindung in Magnetfeldern bis 6.5 T und im Temperaturbereich von 0.05 K und 100 K. Der Schlüssel zum Verständnis der $R_2\text{PdSi}_3$ ist die starke Kopplung der kristallografischen Struktur und der magnetischen Eigenschaften. Dadurch erlaubt das etablierte System aus Austauschwechselwirkung und magneto-kristalliner Anisotropie eine gemeinsame Beschreibung anstatt „neuartigem“ Verhalten.

Table of contents

Abstract	3
Zusammenfassung	3
Table of contents	4
Abbreviations	6
1. Serving as an introduction – or why R_2PdSi_3 ?	7
1.1 Crystal electric fields in rare earth compounds	7
1.2 Exchange interaction	8
1.2.1 RKKY exchange interaction	8
1.2.2 Dipole-dipole exchange interaction	9
1.2.3 Other types of exchange interaction	9
1.2.4 Dzyaloshinski–Moriya	9
1.3 From the rare earth metals to R_2PdSi_3	9
1.3.1 R_2PdSi_3	11
1.3.2 Growth and preparation of single crystals	12
1.4 Introduction to the employed methods	13
1.4.1 Definition of directions and the use of real and reciprocal space	13
1.4.2 Macroscopic methods - overview	14
1.4.3 Macroscopic methods – experimental setup	17
1.4.4 Systematic errors for magnetisation and ac-susceptibility measurements	20
1.5 Neutron diffraction	20
1.5.1 Single crystal neutron diffraction at the 6T2 diffractometer	22
1.5.2 Single crystal neutron diffraction at the E2 diffractometer	23
1.5.3 Single crystal neutron diffraction at the PANDA spectrometer	24
1.5.4 Special sample holder	24
1.5.5 Extinction correction for Ho_2PdSi_3	25
2. Comparison of the macroscopic properties of R_2PdSi_3 ($R = Gd, Tb, Dy, Ho, Er, Tm$)	26
2.1 Inverse ac-susceptibilities	26
2.2 Magnetization in the magnetically ordered state	36
3. Gd_2PdSi_3	42
3.1 Ac-susceptibility	43
3.2 Phase diagram for Gd_2PdSi_3	45
3.3 Diffraction	47
3.4 Summary	48
3.5 Additional room temperature results of the diffraction experiment	49
4. Crystallographic structure of R_2PdSi_3	51
4.1 Reported indications for a crystallographic superstructure in R_2PdSi_3	51
4.2 Neutron diffraction experiments	52
4.3 Heuristic approach and crystallographic structure model	54
4.4 The modulated structure	58
4.5 Comments on the structural models: triclinic and modulated hexagonal	59
5. Long- and short range magnetic order in Tb_2PdSi_3	62
5.1 Results of ac-susceptibility	62
5.1.1 Ac-susceptibility: Zero field transitions	63
5.1.2 Real part of ac-susceptibility in small external fields	64
5.1.3 Ac-susceptibility in magnetic fields above 0.75 T	66
5.1.4 Field dependency of the ac-susceptibility measured at selected temperatures	68
5.1.5 Confidence intervals in (T, H) space of the anomalies in the ac-susceptibility	70
5.2 Supporting macroscopic measurements	70
5.3 Feature map for Tb_2PdSi_3 derived from the macroscopic measurements	73

5.4 Neutron diffraction in zero magnetic field	75
5.4.1 Long- and short- range order in Tb_2PdSi_3	75
5.4.2 Additional observations leading to a magnetic structure proposal	80
5.4.3 Comment on the published magnetic structure	81
5.4.4 Heuristic magnetic structure model fro Tb_2PdSi_3 - ansatz	81
5.4.5 Heuristic magnetic structure model for Tb_2PdSi_3 - result	83
5.5 Neutron diffraction in magnetic fields – multiple magnetic phase transitions	85
5.5.1 LRO coexistence of two phases in applied magnetic fields	86
5.5.3 Short- to long-range order transition in applied field for $T < T_2$	88
5.5.4 Magnetic phases found for $T_2 < T < T_N$ in applied fields	90
5.6 The high field LRO phase of Tb_2PdSi_3 : FiM	92
5.7 Phase diagram of Tb_2PdSi_3 : interpretations and conclusions	95
6. Ho_2PdSi_3	98
6.1 Ac-susceptibility and a phase diagram for Ho_2PdSi_3	98
6.2 Neutron diffraction on Ho_2PdSi_3	101
6.2.1 Zero and low field ($\mu_0 H < 0.8$ T) magnetic structure	101
6.2.2 High field magnetic structure ($\mu_0 H > 0.8$ T)	103
6.3 Possible scenarios	105
6.3.1 Zero field magnetic structure	105
6.3.2 High field magnetic structure	106
6.4 Conclusion	110
7. Er_2PdSi_3 , Tm_2PdSi_3 and Dy_2PdSi_3	112
7.1 Zero field magnetic structure and the meaning of T_2 in Er_2PdSi_3	112
7.2 Magnetic neutron diffraction of Tm_2PdSi_3	116
7.3 Magnetic neutron diffraction of Dy_2PdSi_3	118
8. Discussion and Conclusions	120
8.1 The role of the CEF effect in $R_2\text{PdSi}_3$	120
8.2 Zero field magnetic structures	123
8.3 Generic phase diagram	124
8.4 Estimation of magnetic exchange coupling	129
8.5 Conclusion	130
Appendix A – Magnetic moment direction of Er_2PdSi_3 and Ho_2PdSi_3	133
Appendix B – CEF transitions	135
Appendix C – Lattice constants of $R_2\text{PdSi}_3$	138
List of figures	139
List of tables	141
Bibliography	142
Danksagung	152
Versicherung	154

Abbreviations

μ_0	permeability of the free space ($4\pi \cdot 10^{-7}$ Vs/Am)
μ_B	Bohr magneton ($9.274 \cdot 10^{-24}$ J/T)
$\mu_0 \mathbf{H}$	(external) magnetic field (in Tesla)
\mathbf{M}	magnetisation (in Tesla)
\mathbf{B}	magnetic inductance (in Tesla)
$\boldsymbol{\mu}$	magnetic moment [μ_B / ion]
χ	susceptibility (Volume susceptibility, unit free in SI)
χ_{ac}	ac-susceptibility
\mathbf{a}	vector
a	norm of vector or in general a scalar
n, m	integer values 0, 1, 2, ...
$[u, v, w]$	vector in real space
(H, K, L)	vector in reciprocal space
h, k, l	reflection with the Miller-indices hkl
$\{h, k, l\}$	cohort of symmetrical equivalent reflections
$(H0L)$	reciprocal plane spanned by the vectors $(H, 0, 0)$ and $(0, 0, L)$
V_{EZ}	volume of the unit cell
r. l. u.	relative lattice units
RKKY	Rudermann-Kittel-Kasuya-Yosida
CEF	Crystal-Electric-Field
DM	Dzyaloshinski–Moriya
PM	paramagnetic
FM	ferromagnetic
AFM	antiferromagnetic
CEF	crystal electric field
LRO	long-range order
SRC	short-range correlation(s)
iS-LRO	incommensurate short-to-long-range order
cS-LRO	commensurate short-to-long-range order
T_N	Néel temperature
T_2	second ordering temperature
T_F	ordering temperature of the field-induced FiM phase
k_B	Boltzmann constant ($1.32 \cdot 10^{-23}$ J/K)
H_D	magnetic field associated to equilibrium condition (in Tesla ($H_D = \mu_0 H$))
H_S	magnetic field associated to a short-to-long range ordered transition (in Tesla)
H_c	critical magnetic field of the magnetic ground state (in Tesla)
H_{c2}	magnetic field for parallel alignment of the magnetic moments (in Tesla)
ILL	Institut Laue-Langevin
LLB	Laboratoire Leon Brillouin
HZB	Helmholtz-Zentrum für Materialien und Energie Berlin
FRM-II	Forschungsneutronenquelle Heinz Maier-Leibnitz
APS	Advanced Photon Source
ESRF	European Synchrotron Radiation Facility

1. Serving as an introduction – or why R_2PdSi_3 ?

Magnetism and magnetic materials play a vital role in our everyday life ranging from more trivial aspects like sticking some notes on the refrigerator to more sophisticated uses like data storage. The latter is in a process of continuously enhancement and the data storage of tomorrow will be based on magnetic materials, too [Kryder1993, Mansuripur1997]. The research field of biomagnetics investigates the compatibility of organic tissue and magnets to find, for instance, magnetic materials which are suitable as dental implants [Tsutsui1979]. In industrial processes, magnets are used for material separation and in permanent-magnet electrical motors [Rahman1985, Soong2001]. A modern car has built in more than a hundred permanent magnets. Their respective field is used as sensor, actuator or again in electric motors [Strnat1990, Chan2007, Harris2002]. The global market volume of magnetic materials was 30 billion \$ in 1999 [Coey2001], a figure which suggests the interest of the industry in new magnetic materials. Applications demand as large as possible magnetic fields with the least amount of material. The increase of the remanent field in hard magnetic materials is determined by the energy needed for domain wall movement. This can be achieved to some extent with pinning centers, e. g. deliberate defects in the magnetic material. However, the material may be difficult to process. It would be more convenient if the material would have anisotropy (leaving aside the macroscopic crystal anisotropy e. g. the shape). And at this part the rare earth elements have to be introduced which are already anisotropic on a microscopic scale.

1.1 Crystal electric fields in rare earth compounds

The crystal electric field (CEF) has a large influence on the magnetic behaviour of rare earth compounds compared to other magnetic materials. The reason is to be found in the distribution of the $4f$ -electrons which are localized. In a metallic compound the state of rare earth ions is normally R^{3+} . As the ground state of the rare earths is $[Xe] 4f^x 6s^2$ where x is ranging from one (La) to 14 (Yb) the trivalent state is realized as $[Xe] 4f^{x-1}$. Exceptions are europium and ytterbium which are found in metallic compounds often in a divalent state R^{2+} which equals a half-filled or filled $4f$ shell, respectively. The $6s$ and $5d$ -electrons form the conduction bands in metallic compounds [Jensen1991]. Their expectation value of radial distribution is larger than the $4f$ electrons. This effectively shields the $4f$ electrons from the conduction band. The $4f$ electrons are considered localized when their energy is much lower than the Fermi energy [Fulde1986].

The splitting of degenerated wave functions by an electric field is known as Stark effect. The electric charges of surrounding ions build an electric field on the position of one ion and split the degenerated wave functions (of the $4f$ electrons). This is known as CEF effect. The CEF is described in terms of the total angular momentum operator \mathbf{J} in the Stevens operator-equivalents [Stevens1952], which transform like the real tesseral harmonics [Hutchings1964]. The eigen-functions are $|JM_J\rangle$. The J_z -axis is the quantization axis and is anti-parallel to the vector of the magnetic moment $\boldsymbol{\mu}$. As a consequence the ground state of the $4f$ electrons (Hunds rules [Hund1925]) yields an anisotropic charge distribution which in return interacts with the CEF resulting in a preferred orientation of the J_z -axis. One experimental consequence of this behaviour is the possibility to determine the main CEF parameter from the magnetic anisotropy. This is true in the lower temperature region of the paramagnetic state and will be exercised in chapter 8 of this thesis. To higher temperatures, where the energy between the split states is comparable to the thermal energy, the various levels become populated. In the high temperature limit all CEF levels are equally populated with the consequence of an effectively isotropic charge distribution. However, to be of interest as a magnetic material the magnetic moments should be permanently ordered. The CEF is a single-ion property and therefore an ion-ion exchange interaction is needed to mediate order.

1.2 Exchange interaction

1.2.1 RKKY exchange interaction

In metallic magnetic materials the RKKY (Rudermann-Kittel-Kasuya-Yosida) exchange interaction [Yosida1965] is the dominant interaction leading to magnetic order. In short, a magnetic ion polarizes the surrounding conduction electrons and the neighbouring magnetic ions order accordingly to the surrounding polarisation. The magnitude of the isotropic RKKY exchange depends on the electron density $\sim n_e^{4/3}$ and the distance $\sim 1/R^3$ [Nolting1997]. The RKKY exchange interaction depends on the shape of the Fermi surface [Buschow1979]. The associated RKKY function is oscillatory. A positive contribution means ferromagnetic exchange and negative contribution means antiferromagnetic exchange. The oscillatory nature of the RKKY interaction often gives rise to incommensurate magnetic structures as observed in the pure rare earth elements [Jensen1991] since the maximum of the Fourier transform of the RKKY interaction $J(\mathbf{Q})$ does in general not coincide with a reciprocal lattice point [Gignoux1991].

1.2.2 Dipole-dipole exchange interaction

Beside RKKY a second exchange interaction is present in metallic systems. However, the classic dipole-dipole exchange is much smaller in magnitude compared to the RKKY interaction but due to the distance dependence of $\sim 1/R^3$ the influence of the dipole-dipole exchange might become relevant for large distances [Nolting1997]. The dipole-dipole interaction is anisotropic and can add a small contribution to the magneto-crystalline anisotropy. In the absence of CEF contributions the anisotropy for instance in Gd-compounds is caused by the dipole-dipole interaction [Rotter2003, Colarieti2004]. Effects due to multipole ordering as quadrupolar ordering in DyB_4 [Watanuki2006] might also play a role if the exchange interactions are very weak, e. g. in the case of frustrated nearest neighbour exchange.

1.2.3 Other types of exchange interaction

RKKY and dipole-dipole interaction are examples for indirect exchange since the wave functions of the different ions (in a metallic compound) do not overlap. Two other possibilities for indirect exchange are double exchange as in Fe_3O_4 or super exchange as in MnO [Blundell2001]. Here the magnetic ions couple through the wave function of their neighboring oxygen ion.

For overlapping wave functions as normally found in materials with ionic or covalent bonds the exchange interaction is directly mediated through the overlap of the wave functions via Pauli principle.

1.2.4 Dzyaloshinski–Moriya

Normally, exchange interactions are symmetric: e. g. the Heisenberg type exchange with $\mathbf{J} = \mathbf{S}_1 \cdot \mathbf{S}_2$. In the presence of strong spin-orbit coupling and sufficient low symmetry, the Dzyaloshinski–Moriya (DM) type interactions [Moriya1960] can occur. The DM interactions are the antisymmetrical part of a general bilinear spin-spin interaction [Moriya1960]. The DM exchange $\mathbf{J} = \mathbf{D} \cdot [\mathbf{S}_1 \times \mathbf{S}_2]$ is found often in magnetic insulators and semiconductors with frustrated next-nearest neighbor exchange interaction and leads to weak ferromagnetism or chiral ordering. The conditions for DM interaction (Moriya’s rules [Moriya1960]) are often not fulfilled in metallic systems although exceptions are known [Sato1990, Gondek2007].

1.3 From the rare earth metals to R_2PdSi_3

The understanding of the magnetic properties and the underlying magnetic structures of the pure rare earth metals is sometimes cited as the “standard model of rare earth magnetism” [Jensen1991]. The magnetic behaviour and the resulting magnetic structures are explained

successfully via the CEF effects and the RKKY exchange interaction. On the other hand, magnetic materials used in significant amount in the industry (e. g. SmCo based and NdFeB based materials) [Thompson2000, Coey2001] are intermetallic rare earth compounds and their magnetic structures and properties are not easily explained in the “standard model”. The difference is obviously to be found in the changes accompanied with the additional elements.

In most cases, as for SmCo and NdFeB based magnetic compounds, the rare earth ions are responsible for the large anisotropy while the high ordering temperature and the large magnetization are associated with magnetic $3d$ atoms (Co or Fe). In the following, a brief outline is given of the magnetic properties of the elemental heavy rare earths (meaning the rare earth elements from gadolinium onwards) passing the rare earth silicides towards the R_2PdSi_3 compounds.

The heavy rare earth metals (Gd to Yb) crystallize in hexagonal closed packed (hcp) structures with the exception of ytterbium which has a face centred cubic structure. The symmetry of the rare earth ions sites in the hcp-structures is hexagonal [Jensen1991]. The structures are formed by stacking planes of the rare earths in an ABAB sequence. The lattice constants are close to $a = 3.6 \text{ \AA}$ and $c = 5.6 \text{ \AA}$. The magnetic ordering temperatures are relatively high with Gadolinium ordering ferromagnetically at 293 K. The heavy rare earth metals obey the DeGennes scaling [DeGennes1962]. This strongly indicates the RKKY exchange interaction to be the relevant interaction for magnetic ordering. Consequently, the antiferromagnetic structures are long-range-incommensurate modulated at high temperatures. However, the CEF effect tends to commensurate structures at lower temperatures. For instance, Holmium orders at the Néel temperature ($T_N = 132 \text{ K}$) with a helical structure and is then driven via a lock-in transition to a commensurate structure at 20 K [Jensen1991].

The interest in rare earth disilicides (RSi_2) compounds has been revived after the discovery of epitaxial growth on silicon substrate material [Pierre1990]. However, these metallic compounds are known already for some time and their structures investigated already 25 years ago [Chevalier1984]. The RSi_2 always form Si-deficient structures with silicon content ranging from 1.6 to 1.8. The observed crystallographic structures are orthorhombic, tetragonal, or hexagonal depending delicately on the preparation process and therewith on the silicon content. The hexagonal structure (e. g. $TbSi_{1.67}$) is derived from the AlB_2 structure ($P6/mmm$) where the rare earth ions occupy the Al sites while the silicon and the deficiencies are to be found on the B sites. This structure can be obtained from the hcp structure of the rare earth metals by replacing one layer by silicon. This is noteworthy as the R_2PdSi_3 compounds have a similar layered structure but without deficiencies (see chapter 4). Furthermore, the

lattice constants of R_2PdSi_3 are of comparable magnitude ($a \approx c \approx 4 \text{ \AA}$; the detailed list of lattice constants is in the appendix) with a ratio of c/a close to 1 (the ideal hcp ratio is 1.6667). This structure gives a Si-Si distance of 2.33 \AA which is smaller than the bond length found in elemental silicon of 2.35 \AA [Chevalier1984]. The role of the distance between neighbouring ions in the Si-layer in the structure will be discussed again in chapter 4 for the R_2PdSi_3 compounds. The magnetic structures of the rare earth “disilicides” are antiferromagnetic. For instance, the magnetic propagation in $TbSi_{1.67}$ is $\tau = (0, 0, 1/2)$ with the magnetic moments perpendicular to τ . The ordering temperature T_N is 39 K for $TbSi_{1.67}$ [Schobinger1989]. DeGennes scaling is not observed. Interestingly, T_N is lower in the tetragonal compounds, which is discussed in the literature as effect of frustration [Pierre1992]. The more obvious potential of frustration due to the triangular arrangement of the rare earths in the hexagonal compound is only considered when the magnetic moments are aligned parallel to the propagation vector.

Based on the “disilicides”, ternary rare earth silicides like R_2RhSi_3 had been synthesized in the search for novel magnetic or superconducting materials. Their structure as well as their magnetic properties had been investigated [Chevalier1984]. The R_2RhSi_3 crystallize also in the AlB_2 derived hexagonal structure. Similar to the deficiency ordering in the rare earth “disilicides”, a superstructure is observed [Chevalier1984]. Here, the rhodium ions and the silicon ions order on the B sites such that one Rh ion is surrounded by three Si ions. The AlB_2 structure is accordingly modified by a doubling of the lattice constants (in the vicinity of 8 \AA with a ratio of c/a close to 1). A small orthorhombic distortion was proposed by Chevalier et al. discussing the formation of the superstructure. This superstructure also gives a Si-Si distance smaller than 2.35 \AA [Chevalier1984]. Additionally, the rhodium atoms have a Rh-Si distance much smaller than the expected value from the sum of their ionic radius [Slater1964] of 2.45 \AA . R_2RhSi_3 have Néel temperatures in the same range as the RSi_2 in the hexagonal structure modification but systematically lower ($T_N = 11 \text{ K}$ for Tb_2RhSi_3). The magnetic structures of some of the R_2RhSi_3 compounds ($R = Ce, Nd, Tb$) are published [Szytula1993]. The magnetic structures are commensurate. In the case of Tb_2RhSi_3 the magnetic moments are within the basal plane and are ordered antiferromagnetically in the plane and obey a stacking sequence of “+ + – –” along the c -direction [Szytula1993].

1.3.1 R_2PdSi_3

The investigation of R_2PdSi_3 ($R = \text{rare earth}$) was motivated firstly due to their similar structure compared to R_2RhSi_3 [Kotsanidis1990] and to the hexagonal rare earth “disilicides”.

The rare earth “disilicides” show a deficiency ordering on the B sites and the $R_2\text{RhSi}_3$ compounds exhibit a crystallographic superstructure with defined rhodium sites. The series $R_2\text{PdSi}_3$ (R = rare earth) crystallizes in the high symmetrical AlB_2 derived hexagonal structure (space group $P6/mmm$) [Szytula1999]. The distribution of the Pd and Si on the B-positions had been thought to be either statistically distributed [Szytula1999] or similar to the $R_2\text{RhSi}_3$ [Chaika2001]. The ordering and the arrangement of the Pd/Si layers are addressed in chapter 4 of this work. The magnetic rare-earth ions occupy the Al positions of the AlB_2 structure forming layers. The rare earth ions form thereby a triangular lattice with the inherent possibility of geometric frustration. Geometric frustration is known to strongly affect the magnetic properties [Ballou1998]. The rare earth layers are intersected by Pd/Si layers. Most of the $R_2\text{PdSi}_3$ (R = Ce, Gd, Tb, Dy, Ho, Er, Tm) compounds order antiferromagnetically at Néel temperatures between 1.8 K (Tm) and 23.6 K (Tb) with exception of the Nd compound which orders ferromagnetically at $T_C = 17$ K [Szytula1999, Frontzek2006]. The magnetic structures proposed from neutron diffraction on polycrystalline samples are very complex, with very large magnetic unit cells [Szytula1999]. However, most of the proposed magnetic structures from powder diffraction are not entirely correct, as will be shown in this thesis. The dc-susceptibility measurements exhibit differences between field cooled / zero field cooled states. Investigations on the $R_2\text{PdSi}_3$ (R = Nd, Tb, Dy) samples revealed a time dependence of the magnetization within the ordered state [Li2003]. In addition, ac-susceptibility measurements show a strong frequency dependence of the temperature of additional phase transitions below T_N in Tb_2PdSi_3 and Er_2PdSi_3 [Paulose2003, Iyer2005]. The underlying mechanism of these phase transitions will be discussed in chapter 5.3 for the case of Tb_2PdSi_3 and in chapter 7.1 for the case of Er_2PdSi_3 [Frontzek2007].

The availability of high-quality single crystals of $R_2\text{PdSi}_3$ compounds (R = Ce, Gd, Tb, Dy, Ho, Er, Tm) [Graw2000, Bitterlich2001, Mazilu2005] made it possible to investigate the magnetic properties in more detail. Investigations on these single crystals yielded anisotropic magnetic behaviour in all substances, surprisingly even for Gd_2PdSi_3 [Saha1999] which is a S -state ion.

1.3.2 Growth and preparation of single crystals

The single crystals were grown by floating zone melting with optical heating at melting temperatures $>1500^\circ\text{C}$ from polycrystalline rods of 6 mm diameter and 55 mm length [Bitterlich2001, Mazilu2005]. The resulting crystals were characterised by scanning electron microscopy and oriented using the X-ray Laue method. In some samples epitaxial $R\text{Si}$ segregation had been observed. These crystals had been annealed and subsequently quenched

which removed the segregation [Bitterlich2001]. For macroscopic measurements, oriented cuboid shaped samples with the sizes ranging from $1.5 \times 2 \times 2.5 \text{ mm}^3$ (Tb_2PdSi_3) to $2.5 \times 2.5 \times 11 \text{ mm}^3$ (Er_2PdSi_3) were cut from the single crystals. The samples for neutron diffraction are shaped more irregular, attributed to the need of scattering volume.

1.4 Introduction to the employed methods

The aim of the present chapter is to give an overview of the methods employed in this thesis. This overview can only be incomplete and further reading is cited for the interested. The depth to which the methods are explained is in line with the knowledge needed in the discussion of the experiments. Additional, definitions and abbreviations which are uncommon are introduced.

1.4.1 Definition of directions and the use of real and reciprocal space

In a crystallographic system where the real space directions are orthogonal the corresponding reciprocal lattice vectors are parallel to the real space directions i. e. the $[1, 0, 0]$ direction is perpendicular on the $(1, 0, 0)$ crystal face as is the respective scattering vector $(1, 0, 0)$. In this case, a mixing of real space and reciprocal directions is without consequence and is often not even recognized. The reciprocal vector \mathbf{a} is always given by

$$\mathbf{a} = \frac{\mathbf{b}' \times \mathbf{c}'}{V_{EZ}} \quad (1)$$

where \mathbf{b}' and \mathbf{c}' denote the unit vectors of the real space lattice and V_{EZ} the volume of the unit cell which is defined as triple product

$$V_{EZ} = \mathbf{a}' \circ (\mathbf{b}' \times \mathbf{c}') \quad (2)$$

of the unit vectors. Cyclic permutation yields the other reciprocal vectors. In non-orthogonal systems the reciprocal vector \mathbf{a} is generally not parallel to the real space vector \mathbf{a}' . The compounds of the $R_2\text{PdSi}_3$ type are described within a hexagonal lattice and directions in the basal plane are different whether real space or reciprocal space vectors are used. Directions in this thesis are always given in the presentation of a reciprocal lattice vector. This is simply a matter of convenience. The orientation of a single crystal is determined in reciprocal space via the x-ray Laue method. Spectroscopic measurements are performed in reciprocal space. The only case where structures in real space are discussed is in the visualization of generated models for crystallographic (chapter 4) and magnetic structures. All presented measurements (macroscopic and microscopic) use the reciprocal lattice notation. In a slight abbreviation from the crystallographic tables [IntTablesCrystA1989] round brackets denote both a

direction parallel to a reciprocal vector and the reciprocal vector itself, curly brackets the cohort of symmetrically equivalent reciprocal vectors and no brackets index a reflection, e. g. a point in reciprocal space. The real space directions are given in squared brackets. The indices are always separated by commas for lucidity, especially needed in the case of fraction numbers.

Thus for example the $(1, 0, 0)$ -direction denotes the direction parallel to the reciprocal lattice vector defined by the reflection $1, 0, 0$. Since this definition is valid for all reflections $H, 0, 0$ the direction is often also noted as $(H, 0, 0)$. For the sake of simplicity this direction is also named \mathbf{a} -axis. This corresponds to the real space direction $[2, 1, 0]$. The real space \mathbf{a}' -direction $[1, 0, 0]$ is consequently $(2, -1, 0)$ in the here used notation. The reflection cohort $\{1, 0, 0\}$ consists of six crystallographic equivalent reflections. Each reflection again defines a direction which in turn is equivalent to each other.

Within the basal plane two directions are to be distinguished in the hexagonal system: the $(H, 0, 0)$ -direction and the $(H, H, 0)$ -direction. These two directions are treated as perpendicular to each other in respect to the six-fold symmetry. In strict definition the direction perpendicular to the $(H, 0, 0)$ direction is the $(-H, 2H, 0)$ direction (which is equivalent to the $(H, H, 0)$ -direction under a symmetry operation viz. a 60° rotation). A sketch of the different directions in the basal plane is in the appendix.

In diffraction experiments the scattering plane has to be named. The scattering plane is defined by the two reciprocal vectors lying in the plane. To distinguish the scattering plane from the direction the indices are not separated. For instance, the scattering plane defined by the $(H, H, 0)$ - and the $(0, 0, L)$ direction is denominated (HHL) . The $(H, -H, 0)$ direction is perpendicular to the (HHL) -plane

1.4.2 Macroscopic methods - overview

According to Landau [Landau1980], a phase transition is in general characterised by the change of an order parameter. The order parameter itself is a derivative of the free Gibb's energy $G(T, H)$ with respect to its associated thermodynamic potentials. In the case of a magnetic system the first derivatives of the free Gibb's energy are:

$$\left(\frac{\partial G(T, H)}{\partial H} \right)_T = M(T, H) \quad (3)$$

and

$$\left(\frac{\partial G(T, H)}{\partial T} \right)_H = -S(T, H) \quad (4)$$

with the magnetisation M and the entropy S . The derivatives at the ordering point can be discontinuous or continuous. If both derivatives are discontinuous the phase transition is also discontinuous. According to the Ehrenfest definition the phase transition is then named a first order phase transition. If one derivative is continuous and a higher derivative is discontinuous then the phase transition is continuous (it is of n -th order if the n -th derivative is discontinuous according to Ehrenfest) [Ehrenfest1933].

The magnetic phase diagrams in this work have been determined by ac-susceptibility (χ_{ac}) measurements. The magnetic susceptibility is the derivative of the magnetisation with respect to the external magnetic field. Two methods of macroscopic susceptibility measurements have to be distinguished: dc- and ac-susceptibility. The first one is simply $\Delta M/\Delta(\mu_0 H_{ext})$ whereas the latter is really the derivative at a specific external field $\mu_0 H_{ext}$ and therefore the second derivative of the free Gibb's energy. A small ac-field (H_{ac}) is used to measure the response of the magnetization at a specific point in the (T, H_{ext}) space

In principle χ_{ac} is independent of the absolute magnitude of the ac-field for small excitation fields. The excitation fields are in the order of 0.001 T, while the smallest applied external field is one magnitude larger. χ_{ac} can be measured either at a constant external field while

$$\chi_{ac}(T, H_{ext}) = \frac{\partial M(T, H_{ext})}{\partial \mu_0 H_{ac}} \quad (5)$$

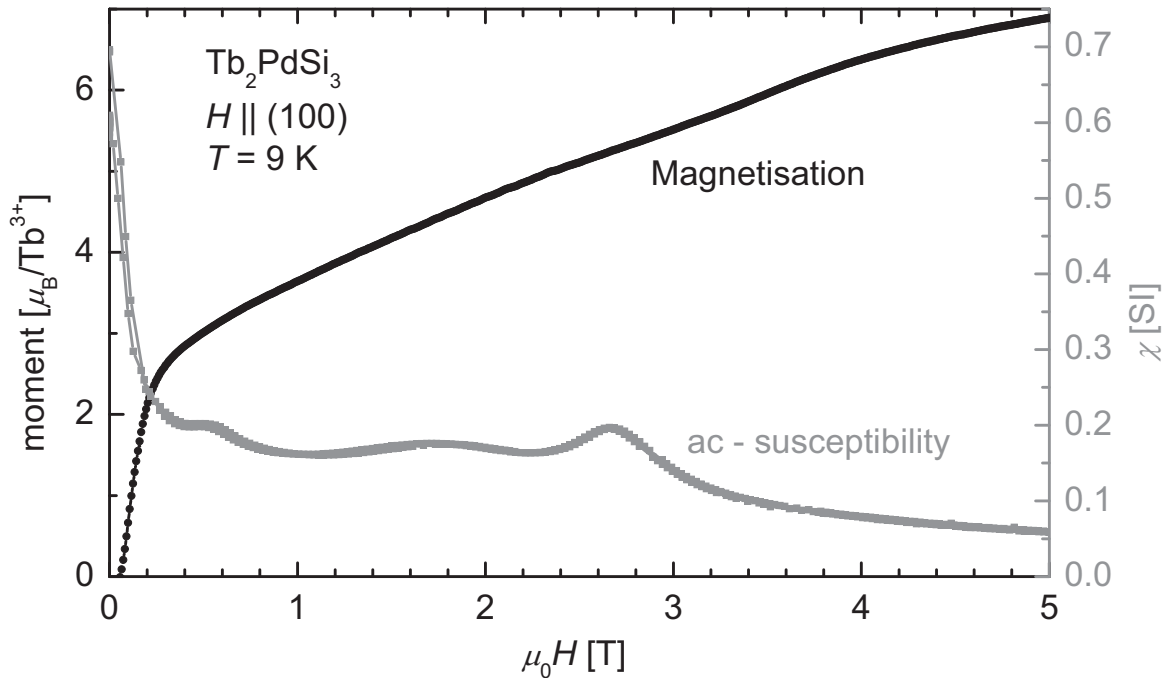


Figure 1.1: Comparison of magnetisation (black) and the real part of the ac-susceptibility of Tb_2PdSi_3 (grey). The identical sample is used in both experiments. and the temperature stability in both experiments shows variations < 0.5 K.

sweeping the temperature or at a constant temperature while sweeping the external field. This allows a scanning of the (T, H_{ext}) space. Measurements in external fields can also be compared with magnetization measurements. The advantage of the ac-susceptibility is the enhanced sensitivity to phase transitions. The anomalies connected to a phase transition that are visible in ac-susceptibility (as maximum) either are invisible or can only be labelled with the knowledge of the ac-susceptibility measurements. This is illustrated in figure 1.1 where a plot of both magnetization and ac-susceptibility vs. magnetic field at $T = 9$ K is shown for Tb_2PdSi_3 . In the magnetisation, the large ferromagnetic contribution overlays the small changes due to spin-reorientation processes. These processes appear as maxima in the ac-susceptibility. The differentiation of the magnetization with respect to the external field generates noise which then overlays the small maxima.

The second order parameter of a magnetic phase transition is the entropy which is also not directly accessible from macroscopic bulk measurements. Similar as the susceptibility is the derivative of the magnetization, the derivative of the entropy is the magnetic contribution to the specific heat

$$C_B = T \left(\frac{\partial S(T, B)}{\partial T} \right)_B \quad (6)$$

which is an experimentally accessible quantity. Additional measurements on a non-magnetic reference compound are often necessary to separate the magnetic contribution from electronic and lattice contributions.

For the sake of completeness a third quantity, often used to characterise magnetic phase transitions, should be mentioned: the magnetostriction coefficient. The magnetostriction coefficient α_M is not a derivative of the Gibb's energy but is connected to the magnetic part of the free energy (F_M) via

$$\alpha_M(T, B) \approx \left(\frac{\partial F_M(T, B)}{\partial \varepsilon^\zeta} \right)_{T, B} \quad (7)$$

where ε^ζ is the strain tensor for the different directions ζ . Macroscopic measurements of the magnetostriction have also been done in the course of this thesis but only one exemplary measurement will be shown. The difficulty with this method is sometimes the clear classification of features in the measurement which makes it in general necessary to compare to other experimental methods. In addition, the formation of magnetic domains can partly cancel their respective contributions to the magnetostriction coefficient.

1.4.3 Macroscopic methods – experimental setup

Normally, macroscopic quantities are measurable with more than one experimental method. Here, only the macroscopic methods used for the measurements presented in this thesis are described. All devices for the different experimental methods are fitted in Variable Temperature Inserts (VTI) of cryomagnets. The employed cryomagnets differ only in the maximal reachable magnetic field. The standard VTI is a ^4He -discharge flow-through cryostat which allows for a temperature range of 1.8 K to 300 K. A gas flow of ^4He is heated and directed to flow around the sample. The gas flow is normally generated with a vacuum pump with pressures in the order of 5 mbar. The stability of temperature control is always an issue to some degree in a flow-through cryostat. The flow-through VTI is also unsuitable for specific heat measurements. Here, the sample is connected with a heat link to a so-called 1 K pot. In the 1 K pot the liquid helium is evaporated in a low pressure atmosphere to reach 1.5 K. If ^3He is used as working gas the base temperature can be as low as ~ 300 mK. An additional heater at the 1 K pot allows to reach temperatures up to 300 K. However, the heat link produces an additional signal to the magnetic measurements, especially the ac-susceptibility. This is one of the main reasons to use flow-through VTI for ac-susceptibility and magnetisation measurements.

The magnetization has been measured with a Vibrating Sample Magnetometer (VSM). The VSM consists basically of two identical antiparallel connected coils and a motor used to shift the sample periodically between the coils. The magnetization of the sample induces a voltage in the coil, the second coil “removes” the effect of the coils. The induced voltage is proportional to the magnetic moment. To measure the voltage a lock-in amplifier SR-830 is used [SR830Man2006]. The fixed parameters for the magnetization measurements are an oscillation amplitude of 0.1 mm with a frequency of 55 Hz. For calibration, the induced voltage of a sample with a known moment is measured and the measured moment of an unknown sample is scaled accordingly. Normally, this calibration sample is polycrystalline Ni with a saturation magnetisation of 0.614 T at 296 K. Ni saturates at 0.7 T (spherical sample) and the field dependence of the saturation can be neglected for small fields. However, the saturation has a temperature dependence which is approximated with a polynomial [Jahn2001]. For calibration a cylindrical Ni sample with a height to radius ratio around one and a mass of 167 mg was used. At an external field of 1 T and at a temperature of 292 K the induction voltage was 49.37 mV which equals a magnetic moment of 9.159 emu (emu = electro-magnetical unit used by VSM software). The measured voltage [mV] multiplied with 0.18551 emu/mV thus gives the measured moment in emu of an unknown sample. The more descriptive unit $\mu_B / \text{magnetic ion}$ is obtained with the formula

$$m^* [R\text{-ion}] = \frac{m^* [\text{emu}] \cdot 10^{-3} \cdot M_{R_2\text{PdSi}_3}}{m \cdot N_A \cdot \mu_B} \quad (8)$$

where m is the sample mass, $M_{R_2\text{PdSi}_3}$ is the molar mass of the respective compound (listed in the appendix) and N_A is the Avogadro constant.

The ac-susceptibility measurement setup consists of two identical antiparallel connected coils called pick-up coils. Around these coils another coil is wired, the excitation coil. Through it an ac-field is generated, which induces a voltage in each of the pick-up coils. Ideally, if the coils are empty, both contributions cancel each other, resulting in total zero voltage. If a magnetic sample is placed in one of these coils the change in inductivity results in a total non-zero induction voltage. The total voltage is then proportional to the susceptibility of the sample. The ac-susceptibility can be expressed as a complex number:

$$\chi_{ac}(T, H_{\text{ext}}) = \chi'_{ac} + i\chi''_{ac} \quad (9)$$

The voltage is measured with a lock-in amplifier SR-830 [SR830Man2006]. The use of lock-in technique allows separating the in-phase ($\pm\pi/2$ phase shift to the ac-excitation) signal and out-of-phase signal. The real part of the susceptibility in (9) is proportional to the in-phase signal and the imaginary part to the out of phase signal. The real part is consistent with the definition (5). The imaginary signal is often referred to as loss signal since it reduces the measured real part signal (magnetization and external field are real variables). The imaginary part of the susceptibility is not easy to interpret and often a phase transition generates a signal in both real and imaginary part and consequently only the real part of the susceptibility is used. However, in some cases the imaginary part of the susceptibility gives a more pronounced signal compared to the real part. In order to understand the imaginary contribution to the ac-susceptibility, when crossing a phase boundary, a qualitative and simplified explanation will be given in the following (1-dimensional case):

The susceptibility is the response function of the magnetic moments to an applied external field. In a paramagnetic state each magnetic moment reacts independently of its neighbor to the external field. The coupling of the magnetic moments to each other by magnetic exchange interaction is destroyed by thermal excitation. In the region where thermal fluctuations are in the same order of magnitude as the magnetic exchange interaction (i. e. at the transition temperature) the magnetic moments are no longer independent. Assume a chain of magnetic moments at the phase transition from the paramagnetic to the magnetic ordered state. An applied external field (z -direction; perpendicular to the chain) will try to align the magnetic

moments parallel to each other. As a consequence, the magnetic moments will precess around the z -direction. Due to exchange interaction the precession of one magnetic moment will be coupled to its neighbor. The magnetic moment will transmit energy to its neighbor. This energy can be dispersed in the fluctuations at the transition point. The response function of the magnetic moment (i. e. the susceptibility) will be dampened and consequently becomes complex and in some cases also time dependent. The imaginary part of the response function can be measured as imaginary part of the ac-susceptibility. In the ordered state (where thermal excitations can be neglected) the transfer energy is conserved and the imaginary part of the ac-susceptibility is zero again.

The absolute values are defined through comparison with a sample of known ac-susceptibility. Here, a superconducting sphere of pure niobium had been used. It has the values $\chi' = 1.5$ and $i\chi'' = 0$.

The standard experimental parameters for the ac-susceptibility measurements comprise an excitation field of 0.5 mT with a frequency of 962 Hz. It will be specifically mentioned if other excitation fields were used. An additional static magnetic field of 70 mT was applied for the measurements from 2 to 300 K in “zero field” in order to suppress weak parasitic signals. The field has insignificant effect on the paramagnetic properties but did increase the quality of the measurements.

Aside the two magnetic methods, measurements of specific heat and magnetostriction have been performed. These methods have been tried in order to provide additional information to the ac-susceptibility measurements but the latter proved superior in terms of phase boundary identification to the former. Therefore, for the characterisation of the magnetic phase diagram only anomalies from ac-susceptibility measurements have been used. Consequently, only a short description is given.

The specific heat is measured on a thermally good insulated sample holder which additionally holds a heater and a thermometer. The specific heat of holder, heater and thermometer should be small compared to the sample and is subtracted later as “addenda” from the raw data. A measurement consists of a short heat pulse whereby the total energy of the heat pulse is transferred to sample and its addenda [diNovi1968]. The cooling of the sample (and addenda) follows an exponential decay ($\sim \exp(-t/\nu)$) and the heat capacity can be calculated from the cooling curve. The characteristic time ν is the ratio of heat link conductivity (which has to be determined separately) and the heat capacity. A compact but comprehensive overview is given in the paper of Bachmann et al. [Bachmann1972].

The magnetostriction effect and along with it the thermal expansion is based on the change of the lattice constant. If measured on single crystals the tiny changes in the lattice constant add up to a macroscopic measurable length change. The sample is mounted between the plates of a capacitor. If the sample length (direction perpendicular to the plates) changes so does the capacitance. The relative change in capacitance is proportional to the relative change of the length. The raw data has to be corrected for the self contribution of the mounting case. The publication of Rotter et al. [Rotter1998] describes the design and construction of the magnetostriction device which was used for the measurements in this thesis.

1.4.4 Systematic errors for magnetisation and ac-susceptibility measurements

The positions (T, H) of anomalies in magnetization and ac-susceptibility measurements will be the basis for phase diagrams. Here, the systematic error in the (T, H) position of the observed anomalies is addressed briefly. The errors for the measurements originating from the magnetization and ac-susceptibility measurement devices are small: the error for the magnetic field value is assumed to be zero; the variance of the temperature is smaller than 0.5 K during the measurements with constant temperature. The temperature dependent measurements have shown a very good reproducibility (less than 0.1 K difference between measurements with identical parameters). To estimate the temperature error higher than in the constant temperature scans is not justified.

1.5 Neutron diffraction

Neutron diffraction has been the first method to reveal ordered (antiferro-)magnetic structures [Shull1949] on the microscopic level. Nearly 60 years later neutron diffraction is still the method of choice for magnetic structure determination. This is mainly due to the nature of the neutron with its large penetration depth for many materials making the realization of complex sample environments (i. e. high magnetic fields up to 15 T and low temperatures down to 50 mK) possible. The theory of magnetic neutron scattering is given in many excellent publications; e. g. [HERCULES1993, Lovesey84] should be consulted for a complete insight into the scattering process. Neutron scattering has a vast area of uses for biology, chemistry and material science. An overview is given in [JülichLectures2005]. In this thesis principles of neutron scattering with special focus on the investigation of $R_2\text{PdSi}_3$ will be discussed. The used diffractometers will be introduced and special features will be outlined.

For neutrons the differential cross section is given by

$$\frac{d\sigma}{d\Omega} = |A(\mathbf{Q})|^2 = \left(\frac{4\pi\hbar^2}{2m_n} \right)^2 \int V(\mathbf{r}) e^{i\mathbf{Q}\cdot\mathbf{r}} d^3r \int V^*(\mathbf{r}') e^{-i\mathbf{Q}\cdot\mathbf{r}'} d^3r' \quad (10)$$

where $A(\mathbf{Q})$ is the structure factor which is the Fourier transform of the interaction potential $V(\mathbf{r})$ [JülichLectures2005]. The interaction potential of the scattering process is different for nuclear and magnetic scattering. The nuclear interaction potential is approximated by the Fermi pseudo potential and the only parameter is the \mathbf{Q} -independent scattering length b . For magnetic scattering the interaction potential is proportional to the Fourier transform $M(\boldsymbol{\tau})$ of the magnetization $M(\mathbf{r})$ perpendicular to the scattering vector \mathbf{Q} . The details of the interaction are unimportant for the understanding of the presented measurements. However, the condition for a reflection is very important in this thesis. A reflection due to the nuclear structure will occur when the scattering vector \mathbf{Q} equals a reciprocal lattice vector \mathbf{G} , the so-called Laue condition. The Bragg condition connects the lattice plane distance with the scattering angle θ . Laue and Bragg condition are equivalent under a transformation. Symmetry consideration lead to so-called extinction conditions which imposes special conditions on \mathbf{G} .

The magnetic unit cell is equal or greater than the chemical unit cell. In the reciprocal space the condition for a magnetic reflection is $\mathbf{Q} = \mathbf{G} \pm \boldsymbol{\tau}$ where $\boldsymbol{\tau}$ is the propagation vector of the magnetic structure.

Measured intensity (the experimental accessible quantity) depends further on several factors according to

$$I_{hkl} = \left(\frac{\lambda^3 V}{V_{uc}^2} \right) \cdot \left(\frac{1}{\varpi} \right) \cdot L \cdot A \cdot T \cdot E \cdot |A(\mathbf{Q})|^2 \quad (11)$$

The factor L stands for the Lorentz-factor which is correlated to the used step distance [HERCULES1993]. The Lorentz-factor is the only one corrected for in the measurements using $L^{-1} = \sin 2\theta$ [ICPWMan]. The further factors A (= Absorption), T (= Thermal) and E (= Extinction) have in general not been corrected since these factors are hard to obtain for a non-regular shaped sample. However, it may be argued if and to which degree these factors influence the experimental results. In most cases the changes are small and, therefore, not important for relative measurements. V is the crystal volume and V_{uc} is the volume of the unit cell. The factor ϖ is the angular scanning velocity.

Figure 1.2 shows the basic setup for a neutron diffraction experiment. The white beam from the neutron source is monochromated normally by the means of a crystal monochromator (using a Bragg-reflection). The monochromatic beam (incident beam) is scattered at the

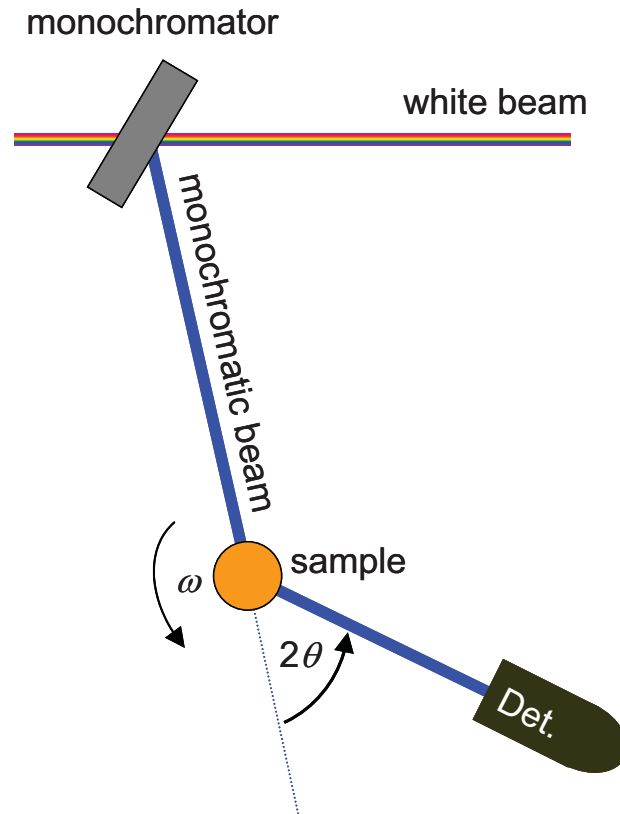


Figure 1.2: Schematic sketch of a neutron diffractometer. The monochromatic beam is scattered on the sample according to the Bragg condition. The sample is rotated around the angle ω .

sample which is rotated around its axis with the angle ω . The detector (Det.) collects the intensity against the scattering angle 2θ . The sample is in the here presented measurements always an oriented single crystal (a powder sample would be fixed and only 2θ would be measured). The orientation is chosen and named after the two directions which are in the plane. A typical example for the $R_2\text{PdSi}_3$ is the (HHL) scattering plane which has the reciprocal lattice vectors $(H, H, 0)$ and $(0, 0, L)$ in plane while the direction $(-H, H, 0)$ is perpendicular.

1.5.1 Single crystal neutron diffraction at the 6T2 diffractometer

The 6T2 at the Laboratoire Léon Brillouin in Saclay, France is close to the setup shown in figure 2.2. It has the additional possibility to lift the detector out of the scattering plane in order to access reflections with a component perpendicular to the chosen scattering plane. The scattering vector is the combination of the in-plane component and the normal beam component. The 6T2 was used in only one experiment to investigate a Ho_2PdSi_3 single crystal. The used wavelength was 2.345 \AA with additional graphite filters suppressing $(\lambda/2)$

contamination of the incident beam. The 6T2 experiment employed a ^3He - ^4He -dilution fridge (base temperature < 200 mK) within a vertical magnet. The highest applied field in this experiment was 5 T.

1.5.2 Single crystal neutron diffraction at the E2 diffractometer

The E2 diffractometer at the Helmholtz-Zentrum für Materialien und Energie (formerly Hahn-Meitner Institut) in Berlin had become the work-horse for single crystal diffraction of the $R_2\text{PdSi}_3$. All with neutron methods accessible $R_2\text{PdSi}_3$ ($R = \text{Tb}, \text{Dy}, \text{Ho}, \text{Er}, \text{Tm}$) samples had been first investigated on the E2. It also has the classical setup of a diffractometer with monochromator – sample – detector. However, two features are uncommon which especially made the E2 suitable for the investigation of unknown magnetic structures. Both features concern the detector. The detector consists of 400 wires in a diboron tetrafluoride gas atmosphere making the detection of a neutron possible in 400 channels over an angle area of 80° (0.2° resolution in 2θ). The measurement consists of taking a 2θ spectrum at fixed sample angle then the (oriented) sample is rotated around the angle ω and the next spectrum is taken. In principle a whole reciprocal plane is measured when the sample had been rotated for 360° . (In the here presented measurements the sample was rotated around 180° and the spectrum had been mirrored). The resulting $\omega / 2\theta$ spectra can be transformed with the lattice constants of the investigated compound to a reciprocal plane with perpendicular axes. The measured data are here presented as a contour map of intensity (color coded) vs. reciprocal space position. The program to process the data is named TvTueb (authors: J.-U. Hoffmann and R. Schneider). On a classical diffractometer intensity is obtained in a so called “rocking scan” moving only the sample angle ω . The same principle holds for the described multidetector of the E2. However, the data treatment is easier after the transformation of the data from ω - 2θ to the reciprocal HKL -space. This transformation uses the lattice constants determined from the selection of certain reflections and an offset angle. Additionally, this transformation normalizes the intensity according to the Lorentz correction ($1/\sin 2\theta$). Intensity is then measured by the integration in the reciprocal HKL -space with always the same width of 0.1 lattice constants in units of the specific direction.

As a second feature the detector can be lifted out of the scattering plane. If also the sample is tilted with the same angle it allows the measurement of a 2-dimensional reciprocal plane consisting of the in-plane values with an additional third dimensional component. This technique is called “flat-cone” and allows to access a large portion of the reciprocal HKL -space. The used sample environment at the E2 spectrometer comprised a field range from 0 to

6.5 T with a temperature range from 50 mK to 300 K. The used wavelength was 2.39 Å with a graphite monochromator. The graphite monochromator (yielding highest available neutron flux at the sample position) allowed the use of additional filters which suppressed the smaller wavelengths ($\lambda/2$). The d_{hkl} -space was limited to a range down to 1.5 Å (105° in 2θ).

1.5.3 Single crystal neutron diffraction at the PANDA spectrometer

The PANDA spectrometer is a “classical” three axis spectrometer with an incident beam of low energy neutrons (“cold” neutrons). The three axis spectrometer features an additional analyzer between sample and detector. The analyzer is used to select the neutrons of a certain energy after the scattering process. The PANDA spectrometer is ideally suited for inelastic neutron diffraction with high energy resolution. An inelastic measurement where this strong point can be seen is shown in the appendix (figure A.4). The neutron (diffraction) data measured at the PANDA spectrometer presented in chapter 5 consist only of elastic neutron scattering where a section in a reciprocal plane is measured only (due to the single detector). This fact requires the information where the magnetic intensity is found in the reciprocal space. Thus the measurements on the PANDA spectrometer have been complementary to the ones at the E2 diffractometer. The used wavelength for the elastic measurements was 4.188 Å with a beryllium filter.

1.5.4 Special sample holder

Normally, the sample is mounted on an aluminium pin which is coated or shielded by a neutron absorbing material. If the space inside the cryostat is sufficiently large the pin can be mounted on a goniometer for exact alignment of the sample. The samples are prepared with grinded surfaces corresponding to crystal faces. The crystal is glued on this face yielding a normally perfect orientation (misalignment often results from a bended sample stick). Two exceptions can occur which require a different sample holder: The first occurs for temperatures lower than 1.2 K. Below this temperature aluminium is superconducting and the heat transfer drops literally to zero. This can be avoided by the use of a copper holder, although copper produces a stronger background signal and is higher activated after the experiment. The second exception occurs when high magnetic fields are required. If the sample is anisotropic and a field is applied not parallel to the easy axis the sample tends to rotate to align its easy axis with the magnetic field. The resulting forces can be quite strong, even deforming 1 mm aluminium wire. For the 6T2 experiment an idea was tried to obviate

the movement of the sample completely. The single crystalline sample was mounted inside a specially constructed sample holder filled with an 1:3 mixture of deuterated (for coherent scattering only) methanol/ethanol to avoid movements of the sample due to the application of the magnetic field. This mixture freezes in an amorphous phase. As result we observed no significant background signal from the methanol/ethanol in the investigated limited range. However, we did not perform a full 2θ scan to fully characterize this special sample holder technique. In principle one would expect a broad peak from the mean molecular distance in the amorphous material. In a second experiment on a smaller sample with the same sample holder the absorption of the mixture was found to be too large. As a consequence, the sample holder has to be constructed individually for each sample to minimize the amount of mixture in the beam path.

1.5.5 Extinction correction for Ho_2PdSi_3

The used large, irregular shaped single crystals are susceptible for extinction effects, especially when the intensity of a reflection is large. In the beginning of this chapter it had been emphasized that an extinction correction normally is only possible for selected sample shapes. Extinction is given by the approximation equation [Zachariasen1967] $y = (1+2x)^{-1/2}$. In general, x depends on a multitude of parameters (wavelength, sample thickness, etc.). In the case of Ho_2PdSi_3 the interest is on the change of intensity on the 1, 0, 0 reflection in dependence of a magnetic field. The only parameter changing in x is the intensity itself. The intensity is proportional to the square of the ordered magnetic moment. Therefore, the chosen correction is $y = (1+(0.31 + 2.26*\mu/\mu_s)^2)^{-1/2}$ with μ the macroscopic measured magnetic moment [see chapter 2] and μ_s the theoretical saturation magnetisation of $10 \mu_B$. The scaling factor is chosen to replicate the intensity at 5 T where the ferromagnetic component is around $7.5 \mu_B$

2. Comparison of the macroscopic properties of $R_2\text{PdSi}_3$ ($R = \text{Gd, Tb, Dy, Ho, Er, Tm}$)

In the introduction some properties of the $R_2\text{PdSi}_3$ ($R = \text{heavy rare earth}$) for which the series caused some interest have been named. The series of $R_2\text{PdSi}_3$ ($R = \text{heavy rare earth}$) has been found to be isostructural with the crystallographic structure described in the introduction (in the $P6/mmm$ space group) [Szytula1999].

Measurements of macroscopic magnetic properties on single crystals had been made for Gd_2PdSi_3 [Mallik1999, Saha1999, Saha2000_2], Tb_2PdSi_3 [Majumdar2000, Paulose2003], Dy_2PdSi_3 [Majumdar2001], Ho_2PdSi_3 [Sampathkumaran2002] and Er_2PdSi_3 [Iyer2005]. Summarizing, the anisotropy in the magnetic properties and the occurrence of multiple metamagnetic transitions had generated interest. Especially, the spin-glass like phase transitions found in Tb_2PdSi_3 and Er_2PdSi_3 [Paulose2003, Iyer2005] have been remarked as unusual. Citing the conclusion of Paulose et al.: “These results clearly reveal that this compound is an exotic magnetic material” [Paulose2003].

The systematic, if present, of the observed effects through the series, had not been investigated. For instance, the role of the crystal-electric field and the exchange interaction had not been separated. This chapter compares macroscopic magnetic properties of different $R_2\text{PdSi}_3$ in the paramagnetic and the ordered state. The role of the different rare earth ions is evaluated. The here presented data have partially been published [Frontzek2006].

2.1 Inverse ac-susceptibilities

Figures 2.1 to 2.6 show the real part of the zero field ac-susceptibility measurements for $R_2\text{PdSi}_3$ with $R = \text{Gd, Tb, Dy, Ho, Er}$ and Tm in the low temperature region. Both directions in-plane ($H, 0, 0$) and perpendicular to the basal plane ($0, 0, L$) (in the following addressed as crystallographic \mathbf{a} - and \mathbf{c} -direction) are shown. The \mathbf{a} -direction is depicted with a grey color while the \mathbf{c} -direction is shown in black. In figure 2.1, the left and right y-axis of the graph has the identical scale. In the other graphs the scale is adjusted to ideally display the zero field ac-susceptibility of both the \mathbf{a} - and \mathbf{c} -direction. The scale differs up to two orders of magnitude (in the case of Tb_2PdSi_3). Tm_2PdSi_3 has been measured in an inhomogeneous ac-field in a complete different ac-susceptibility setup since the normally employed ac-susceptometer allows temperatures only down to 2 K. Due to this neither a comparison of the value nor the magnitude of both curves is possible.

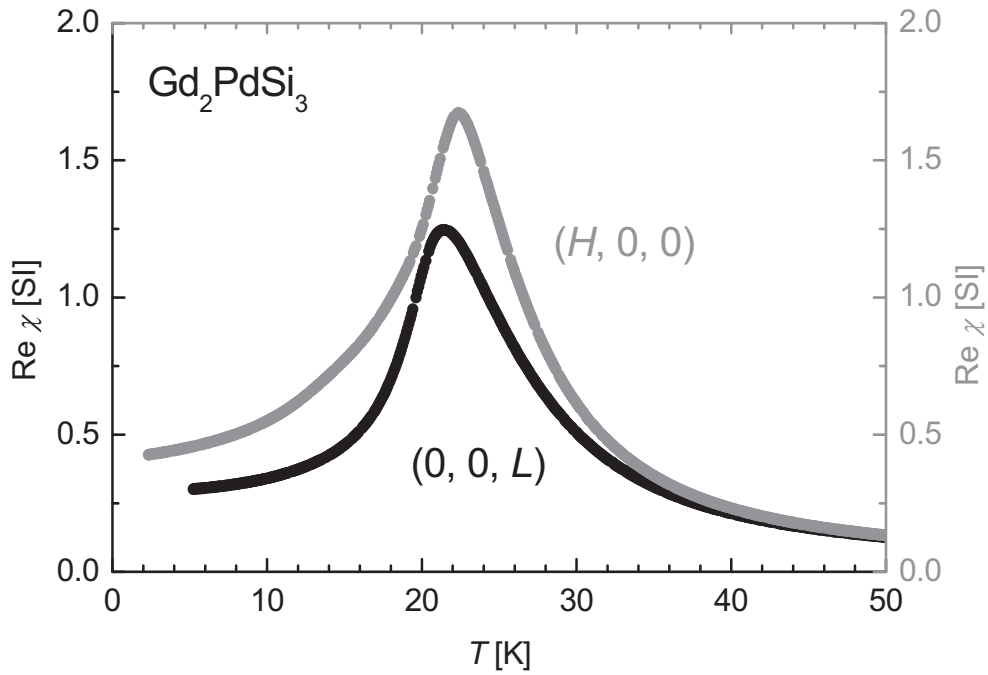


Figure 2.1: Real part of the zero field ac-susceptibility of single crystalline Gd_2PdSi_3 . The measurement with the ac-field along $(0, 0, L)$ and $(H, 0, 0)$ are shown in black and grey, respectively.

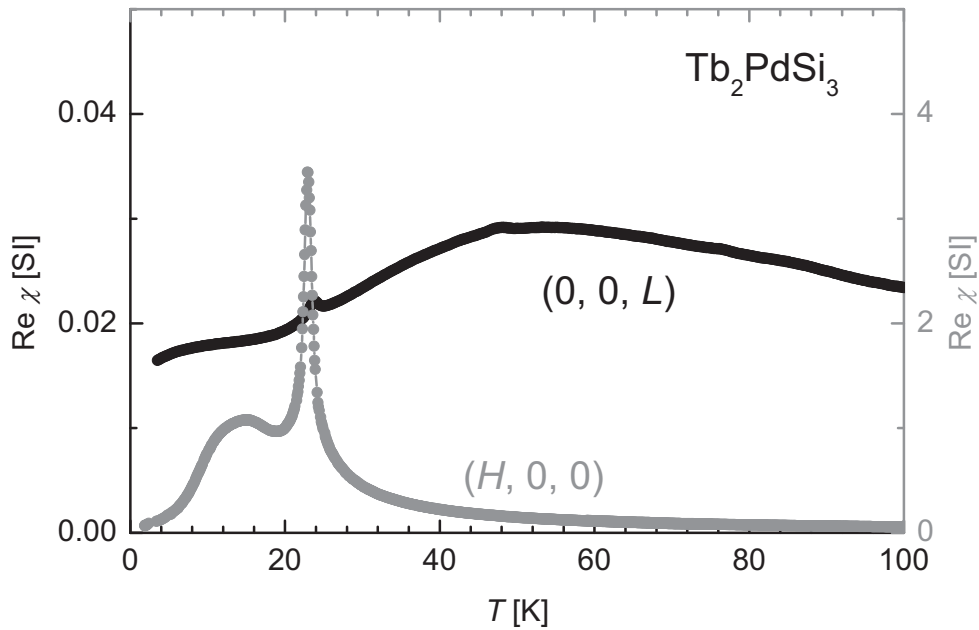


Figure 2.2: Real part of the zero field ac-susceptibility of single crystalline Tb_2PdSi_3 . The measurement with the ac-field along $(0, 0, L)$ and $(H, 0, 0)$ are shown in black and grey, respectively. Mind the different values of the susceptibility (left and right y-axis).

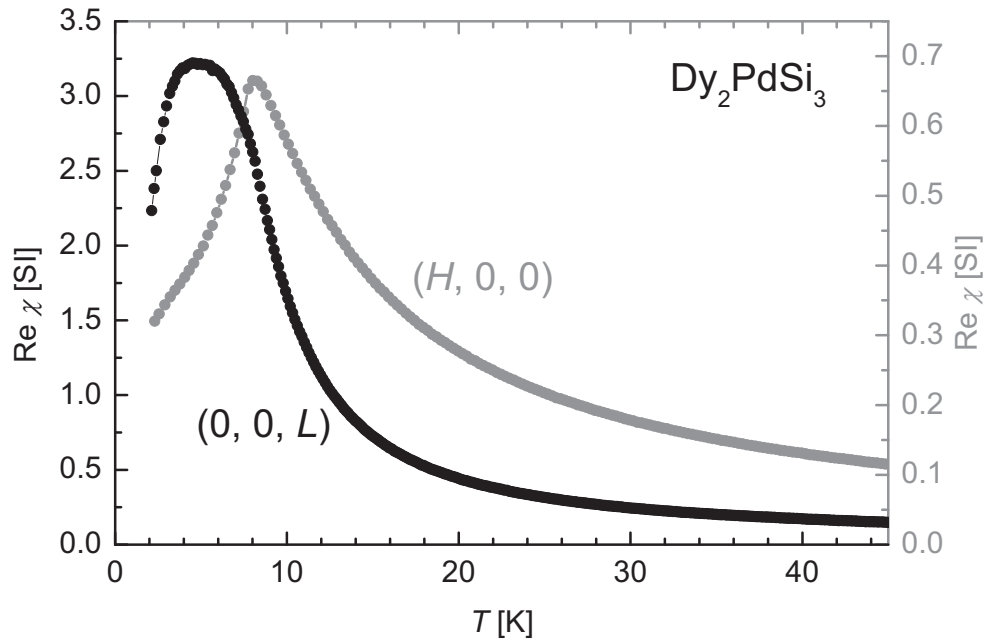


Figure 2.3: Real part of the zero field ac-susceptibility of single crystalline Dy_2PdSi_3 . The measurement with the ac-field along $(0, 0, L)$ and $(H, 0, 0)$ are shown in black and grey, respectively. Mind the different values of the susceptibility (left and right y -axis).

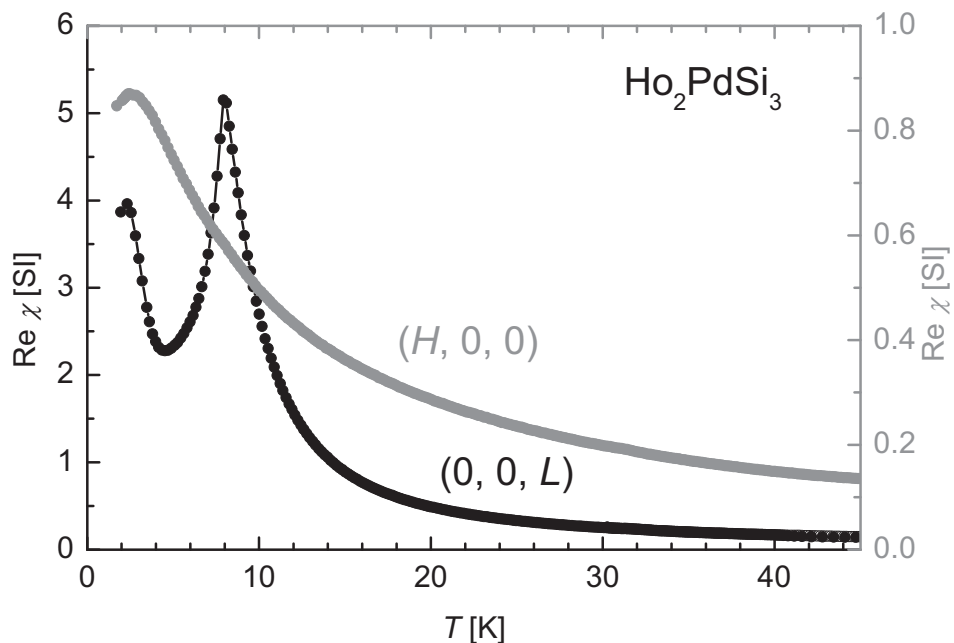


Figure 2.4: Real part of the zero field ac-susceptibility of single crystalline Ho_2PdSi_3 . The measurement with the ac-field along $(0, 0, L)$ and $(H, 0, 0)$ are shown in black and grey, respectively. Mind the different values of the susceptibility (left and right y -axis).

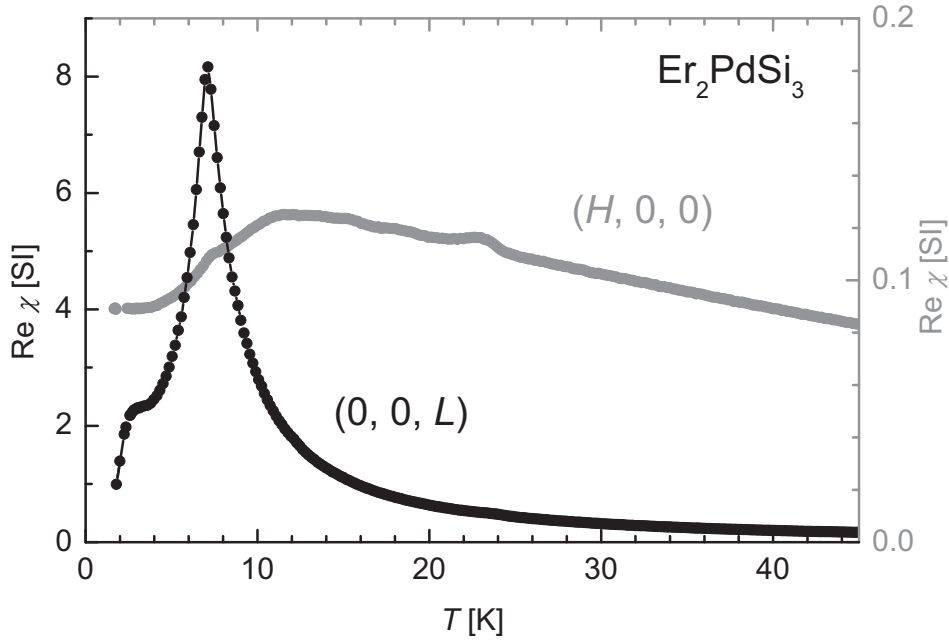


Figure 2.5: Real part of the zero field ac-susceptibility of single crystalline Er_2PdSi_3 . The measurement with the ac-field along $(0, 0, L)$ and $(H, 0, 0)$ are shown in black and grey, respectively. Mind the different values of the susceptibility (left and right y -axis).

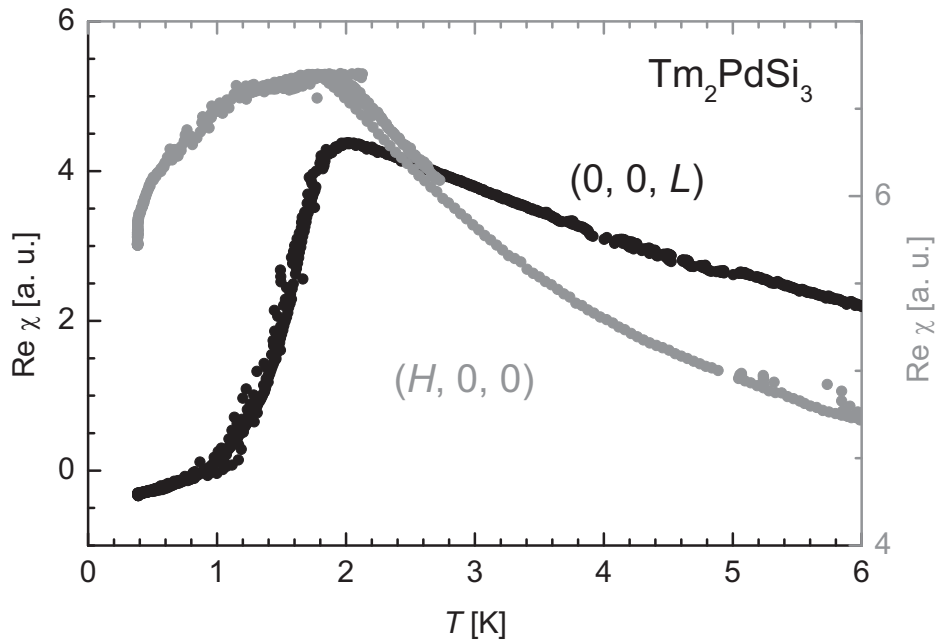


Figure 2.6: Real part of the zero field ac-susceptibility of single crystalline Tm_2PdSi_3 . The measurement with the ac-field along $(0, 0, L)$ and $(H, 0, 0)$ are shown in black and grey, respectively. The values of the susceptibility are arbitrary (also relative to each axis) due to the special measurement setup.

2. Comparison of the macroscopic properties of $R_2\text{PdSi}_3$ ($R = \text{Gd, Tb, Dy, Ho, Er, Tm}$)

The comparison of the value of the ac-susceptibility for both measured directions defines the easy (hard) magnetic axis of the compound. In the following the magnetic hard (easy) direction is defined by the low (high) values of the susceptibility in the paramagnetic state.

From the positions of the absolute maxima of the respective easy magnetic axis the ordering temperatures T_N have been determined and are listed in Table 1.

R	T_N [K]	$\frac{(g_J-1)^2}{J(J+1)}$	$\mu_{\text{eff}} [\mu_B]$	$\mu_{\text{th}} [\mu_B]$	θ_c [K]	θ_a [K]	$\alpha \cdot 10^2$
Gd	22.3	15.75	8.0±0.2	7.937	30.3±0.7	30.7±1.2	-
Tb	23.6	10.5	9.6±0.3	9.72	-32.5±1.4	24.0±1.4	-1.0101
Dy	8.2	7.083	10.3±0.3	10.65	-1.4±1.4	11.5±1.4	-0.6349
Ho	7.7	4.5	10.2±0.3*	10.61	-	4.3±1.4*	-0.2222
Er	7.0	2.55	9.4±0.2	9.58	15.2±1.1	-7.5±1.1	0.2540
Tm	1.8	1.2	7.5±0.2	7.56	19.1±0.6	-15.6±0.6	0.10101

Table 1: Compilation of results of the Curie-Weiss analysis for $R_2\text{PdSi}_3$ and theoretical values for R^{3+} ions:

- T_N Néel temperature determined from experiments;

- $(g_J-1)^2 J(J+1)$ DeGennes factor;

- μ_{eff} effective paramagnetic moment from the Curie-Weiss analysis.

- μ_{th} theoretical value according to Hund's rule;

- θ_c and θ_a asymptotic paramagnetic Curie temperatures from the Curie-Weiss analysis for the measurements parallel c and a , respectively;

- α Stevens parameter from reference [Hutchings1964]

* For Ho_2PdSi_3 only the values for the a -axis are considered (see text);

Below T_N the c -axis is the easy magnetic axis for the compounds with $R = \text{Dy, Ho}$ and Er while it is the magnetic hard axis for $R = \text{Gd}$ and Tb . The magnetic easy axis of Tm_2PdSi_3 cannot be determined from the special ac-susceptibility setup. The compounds with $R = \text{Dy, Ho}$ and Er order at $T_N = 8.2$ K, 7.7 K and 7.0 K, respectively, while the Tb compound has the highest ordering temperature of the whole series with $T_N = 23.6$ K. These temperatures are in agreement with the previously reported values from powder measurements [Szytula1999, Kotsanidis1990]. Interestingly, the ordering temperatures of the series do not obey a DeGennes scaling law [DeGennes1962]. Figure 2.7 shows the comparison of the ordering temperatures and the DeGennes factor for the different $R_2\text{PdSi}_3$ compounds. Four compounds show an additional anomaly below T_N in the investigated temperature range which probably corresponds to a second phase transition. These four compounds are Tb_2PdSi_3 , Ho_2PdSi_3 , Dy_2PdSi_3 and Er_2PdSi_3 . In Tb_2PdSi_3 the broad maximum at about 10 K has been connected to a spin-glass like transition [Paulose2003]. The additional anomaly in Ho_2PdSi_3 , a maximum observed for both easy and hard axis, is found around 2 K. In Dy_2PdSi_3 a kink is observed in

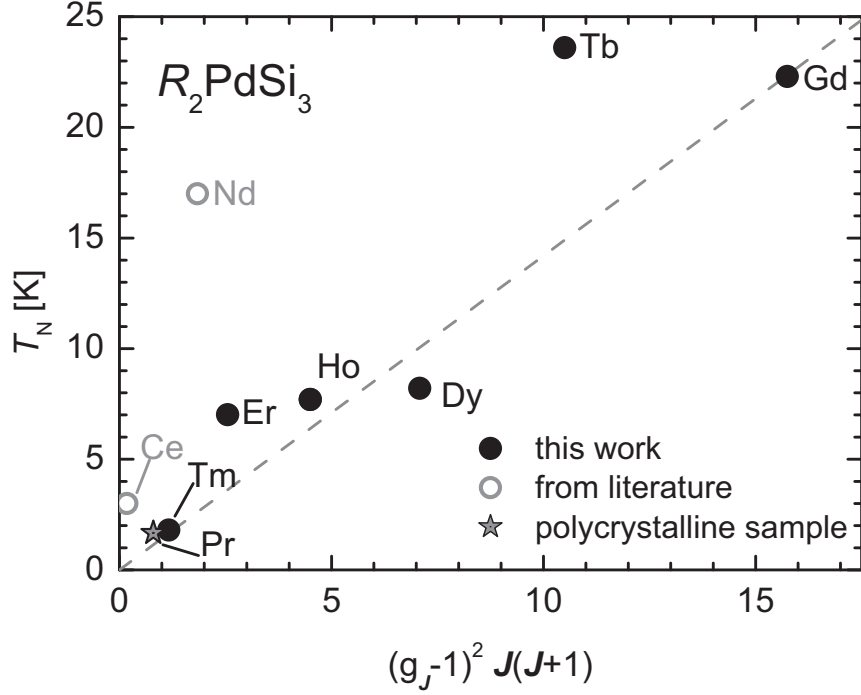


Figure 2.7: Ordering temperatures of $R_2\text{PdSi}_3$ (T_C in the case of Nd) compounds vs. the DeGennes factor. The literature values are from reference [Szytula1999].

the easy direction while in the hard direction a strong reduction of the signal is found around 2 K. For Er_2PdSi_3 the anomaly has been attributed to a spin-glass like transition at $T = 2$ K [Iyer2005].

Figures 2.8 to 2.13 show the inverse ac susceptibility vs. temperature for $R_2\text{PdSi}_3$ ($R = \text{Gd, Tb, Dy, Ho, Er, Tm}$). At high temperatures the susceptibility is described by a Curie-Weiss law:

$$\chi = \frac{C}{T - \theta_p} \quad (12)$$

The light grey lines represent a Curie-Weiss fit used to yield the asymptotic paramagnetic Curie temperatures θ_p for each crystallographic direction (in the following labeled θ_a and θ_c for the asymptotic-paramagnetic Curie temperature in the crystallographic a - and c -direction, respectively). The antiferromagnetic transition temperatures determined from the maximum of the ac-susceptibility curves (see figure 2.1 to 2.6) are marked by an arrow in Figs. 2.8 to 2.13.

The inverse zero-field ac-susceptibilities up to 300 K for the crystallographic a - and c -direction on Gd_2PdSi_3 are shown in figure 2.8. The paramagnetic properties of Gd_2PdSi_3 above the ordering temperature of 22 K are isotropic within the experimental variance. This is expected since Gd^{3+} is an S -state ion and is not susceptible to the crystal electric field effect.

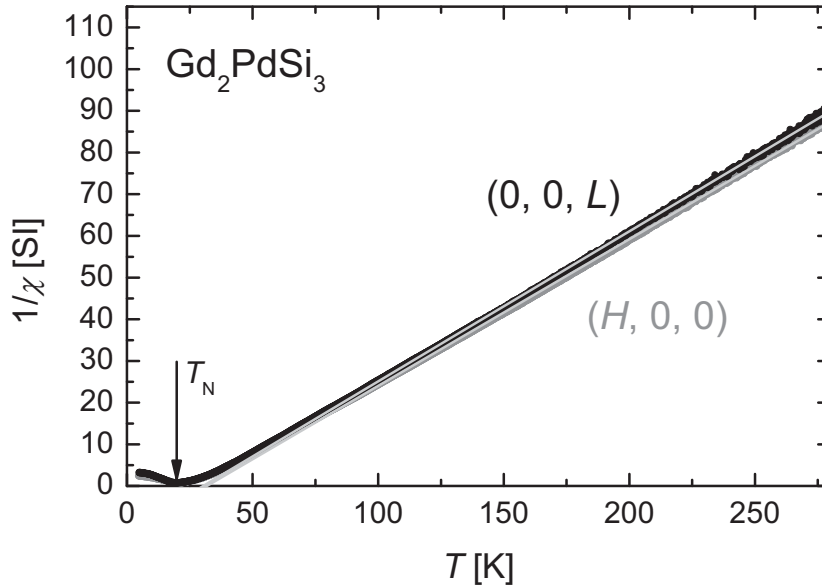


Figure 2.8: Inverse Gd_2PdSi_3 single crystal ac-susceptibility data along the $(0, 0, L)$ and $(H, 0, 0)$ direction. The Néel temperature is marked. The light grey lines are the Curie Weiss fit (see text).

Roughly above 55 K the course of the inverse susceptibility can be effectively described by a Curie-Weiss behavior. The effective paramagnetic moment is $\mu_{\text{eff}} = 8.0 \mu_{\text{B}}$ in excellent agreement with the expected value of $\mu_{\text{th}} = 7.937 \mu_{\text{B}}$ [Hund1925]. The asymptotic paramagnetic Curie temperature is around +30 K. The surprisingly large positive value of θ_{p} indicates ferromagnetic correlations of the antiferromagnetically ordering compound. The values of the effective paramagnetic moment and the asymptotic paramagnetic Curie temperatures are summarized in table 1.

In the case of Er_2PdSi_3 (Fig. 2.9) the magnetic hard axis is the \mathbf{a} -axis and the magnetic easy axis is the hexagonal \mathbf{c} axis. This behavior is associated with a prolate shape of the $4f$ -charge distribution of the trivalent Er^{3+} ion with a positive Stevens factor $\alpha > 0$ (see table 1). Above 50 K (corresponding to seven times T_{N}) paramagnetic behavior according to the Curie-Weiss law is found for both axes (fit from 50 K to 250 K). The anisotropy between magnetic hard and easy axis is well pronounced, yielding a small negative θ_{a} and a larger positive θ_{c} (see table 1). The slopes of both inverse susceptibility curves are equal resulting in an experimental paramagnetic moment of $\mu_{\text{eff}} = 9.4 \mu_{\text{B}}$ in good agreement with the theoretical free-ion value for Er^{3+} ($\mu_{\text{th}} = 9.58 \mu_{\text{B}}$).

In contrast to Er_2PdSi_3 one observes for the Tb_2PdSi_3 compound (Fig. 2.10) that the magnetic easy axis is the in-plane \mathbf{a} -axis and the magnetic hard axis is the hexagonal \mathbf{c} -axis. The interchange of magnetic easy and hard axis corresponds to the opposite sign of the Stevens factor α of Tb^{3+} ($\alpha < 0$) in comparison to Er^{3+} . The anisotropy found for the Tb_2PdSi_3

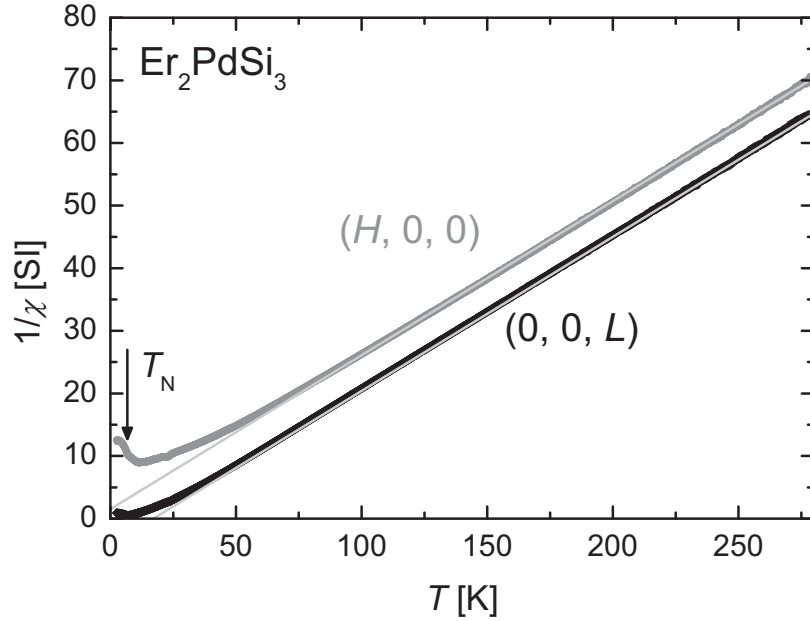


Figure 2.9: Inverse Er_2PdSi_3 single crystal ac-susceptibility data along the $(0, 0, L)$ and $(H, 0, 0)$ direction. The Néel temperature is marked.

compound is even more pronounced than for the Er_2PdSi_3 compound. One observes for the magnetic easy axis paramagnetic Curie-Weiss behavior right above the ordering temperature of 23.6 K while a deviation from the Curie-Weiss law is observed in the magnetic hard direction up to 100 K (4 times T_N). For temperatures above 100 K the slopes of the inverse susceptibility curves for both directions are equal. The paramagnetic moment from the Curie-

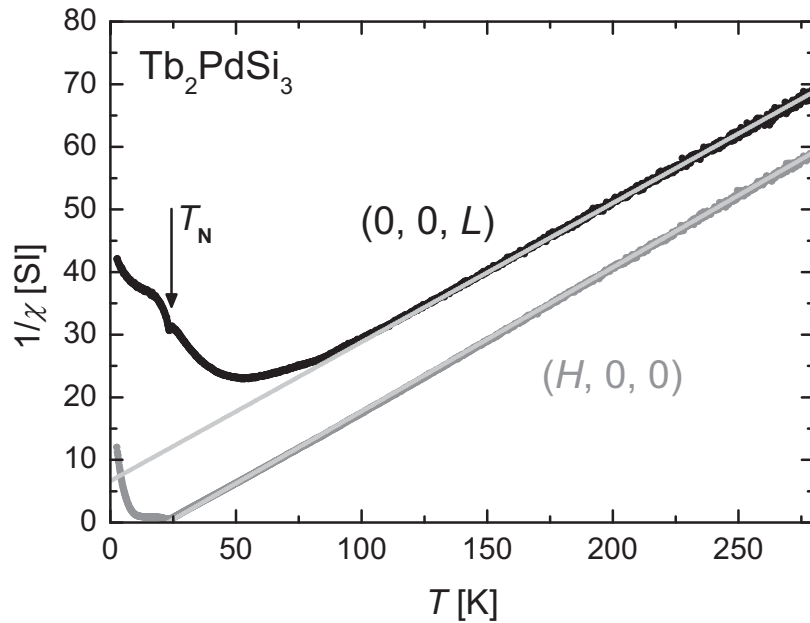


Figure 2.10: Inverse Tb_2PdSi_3 single crystal ac-susceptibility data along the $(0, 0, L)$ and $(H, 0, 0)$ direction. The Néel temperature is marked.

Weiss fit is $\mu_{\text{eff}} = 9.68 \mu_{\text{B}}$ in good agreement with the free-ion value of Tb^{3+} ($\mu_{\text{th}} = 9.72 \mu_{\text{B}}$). The asymptotic paramagnetic Curie temperature is positive for the a -direction and negative for the c -direction.

The anisotropic $4f$ -charge distribution of the rare earth ions Dy^{3+} and Ho^{3+} (both having $\alpha < 0$) is expected to produce the same anisotropy as for the Tb_2PdSi_3 compound although less pronounced because of the smaller values for α . In the case of Dy_2PdSi_3 (figure 2.11) the expected anisotropy as well as the Curie-Weiss behavior is found for temperatures above 70 K (9 times T_{N}). The observed anisotropy for Dy_2PdSi_3 is smaller than for Er_2PdSi_3 though the magnitude of α is larger. The analysis of the linear behavior yields an effective magnetic moment of $\mu_{\text{eff}} = 10.3 \mu_{\text{B}}$ which is insignificantly smaller than the free-ion value for Dy^{3+} ($\mu_{\text{th}} = 10.64 \mu_{\text{B}}$). The behavior is characterized by a positive asymptotic paramagnetic Curie

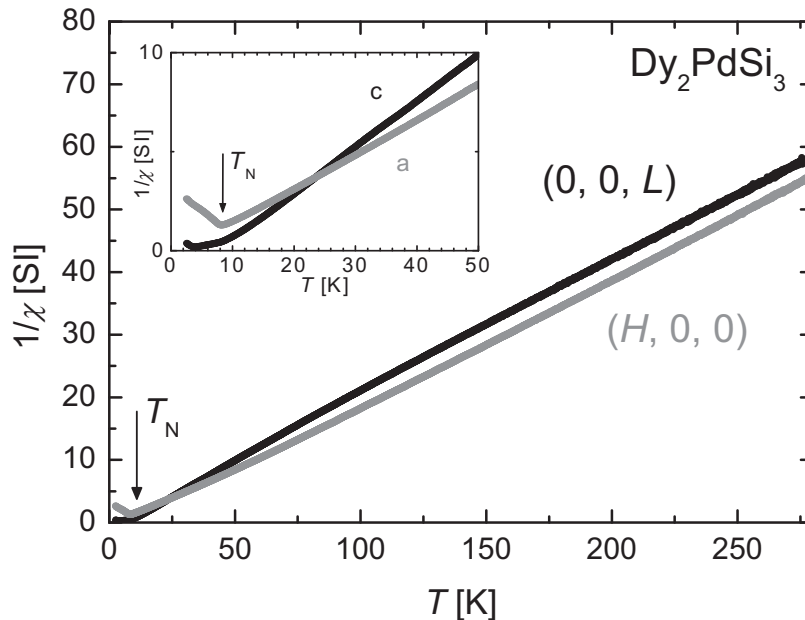


Figure 2.11: Inverse Dy_2PdSi_3 single crystal ac-susceptibility data along the $(0, 0, L)$ and $(H, 0, 0)$ direction. The Néel temperature is marked.

temperature for the a -direction while the Curie temperature for the c -direction is negative but close to zero. Below 70 K a deviation from the Curie-Weiss behavior is observed leading to a crossing point at around 25 K, well above the ordering temperature of $T_{\text{N}} = 8.2$ K. Below 25 K the a -axis is the magnetic hard axis while the c axis has become the magnetic easy axis.

From the magnitude of α , Ho_2PdSi_3 (fig. 2.12) is expected to show a small anisotropy. In figure 2.12 the inverse susceptibility curves have different slopes for the two crystallographic directions. This unusual behavior yields $\mu_{\text{eff}} = 10.2 \mu_{\text{B}}$ and $9.6 \mu_{\text{B}}$ for the a - and c -direction, respectively. The value for the c -direction is significantly lower than the free ion value for

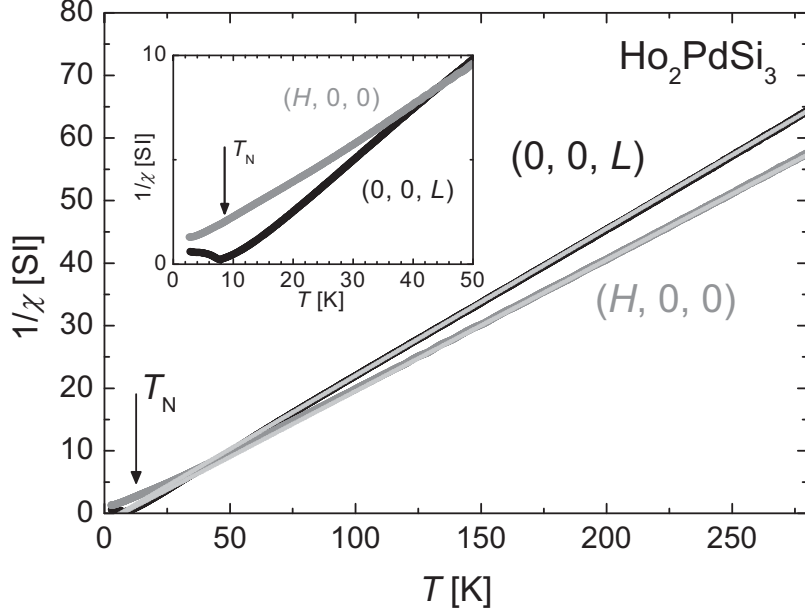


Figure 2.12: Inverse Ho_2PdSi_3 single crystal ac-susceptibility data along the $(0, 0, L)$ and $(H, 0, 0)$ direction. The Néel temperature is marked.

Ho^{3+} ($\mu_{\text{th}} = 10.61 \mu_{\text{B}}$) while the value for the \mathbf{a} -direction is only slightly below that value. Therefore, for μ_{eff} of Ho_2PdSi_3 we have only used the latter value (see table 1). In addition, no value for θ_{c} is listed in Table 1. In the high temperature regime the \mathbf{a} -axis is the magnetic easy axis as one would expect from the negative sign of the Stevens factor. At a temperature of about 40 K one observes a crossing of the inverse susceptibilities. Below 40 K the \mathbf{a} -axis becomes the magnetic hard axis while the \mathbf{c} axis becomes the magnetic easy axis.

Tm_2PdSi_3 (fig. 2.13 on the next page) undergoes a magnetic transition around 1.8 K. This transition was confirmed by an additional specific heat measurement (see inset of fig. 2.13). The magnitude of the Stevens factor α for the Tm^{3+} ion is the same as for the Tb^{3+} ion but with opposite sign. Therefore, the anisotropy is similarly pronounced as in the case of the Tb_2PdSi_3 compound. Because of the opposite sign of the Stevens factor the \mathbf{a} -axis is the magnetic hard axis and the \mathbf{c} axis is the magnetic easy direction as in the Er_2PdSi_3 compound. Above a temperature of 80 K for the easy \mathbf{c} axis and above 25 K for the hard \mathbf{a} -axis the susceptibility is in accordance to a Curie-Weiss law. Interestingly, in the other investigated compounds the temperatures for which deviation from a Curie-Weiss behavior is observed are lower for the easy and higher for the hard direction in contrast to Tm_2PdSi_3 . The Curie-Weiss fit yields an effective moment of $\mu_{\text{eff}} = 7.5 \mu_{\text{B}}$ which agrees well with the expected value for Tm^{3+} ($\mu_{\text{th}} = 7.58 \mu_{\text{B}}$).

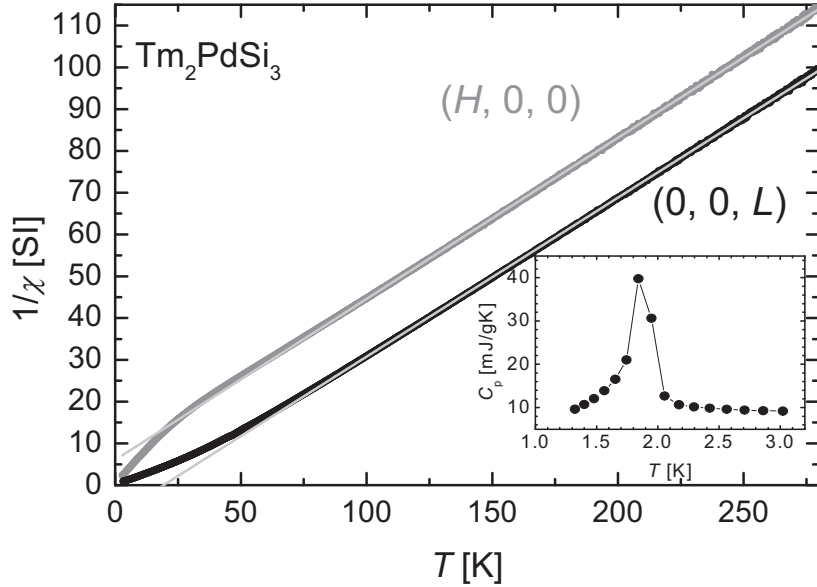


Figure 2.13: Inverse Tm_2PdSi_3 single crystal ac-susceptibility data along the $(0, 0, L)$ and $(H, 0, 0)$ direction. The inset shows a specific heat measurement used to determine the Néel temperature.

2.2 Magnetization in the magnetically ordered state

In many magnetic rare earth compounds, the parameters deduced from the paramagnetic ac-susceptibility measurements are sufficient to describe the general magnetic behavior even through the ordering temperature down to lowest temperatures. However, the presented ac-susceptibility measurements indicate already that this is not valid for the $R_2\text{PdSi}_3$ compounds. For further examination of the magnetic behavior we performed full magnetization loop measurements in the well ordered state at $T \approx 2$ K for the $R_2\text{PdSi}_3$ compounds ($R = \text{Gd, Tb, Dy, Ho, Er}$) in external magnetic fields along the main crystallographic directions \mathbf{a} and \mathbf{c} .

The magnetization curve of Gd_2PdSi_3 (Fig. 2.14) had been previously published and the anisotropy within the ordered state has been remarked. Also the two step-like transitions seen in the measurement along \mathbf{c} around 0.5 and 1.16 T had been identified as metamagnetic transitions and had been labeled H_1 and H_2 [Saha1999, Saha2000]. A third yet undiscussed point in the magnetization measured along the \mathbf{c} -direction is a change of slope at 3.3 T. Furthermore, the magnetization shows an upper critical field for the transition to a saturated state at around 9 T. The saturation value is about $8.5 \mu_B$, far too large for Gd^{3+} ($gJ_S = 7 \mu_B$). The reason for this large saturation value is unclear. The published magnetization measurements on Gd_2PdSi_3 are only up to 5 T [Saha1999].

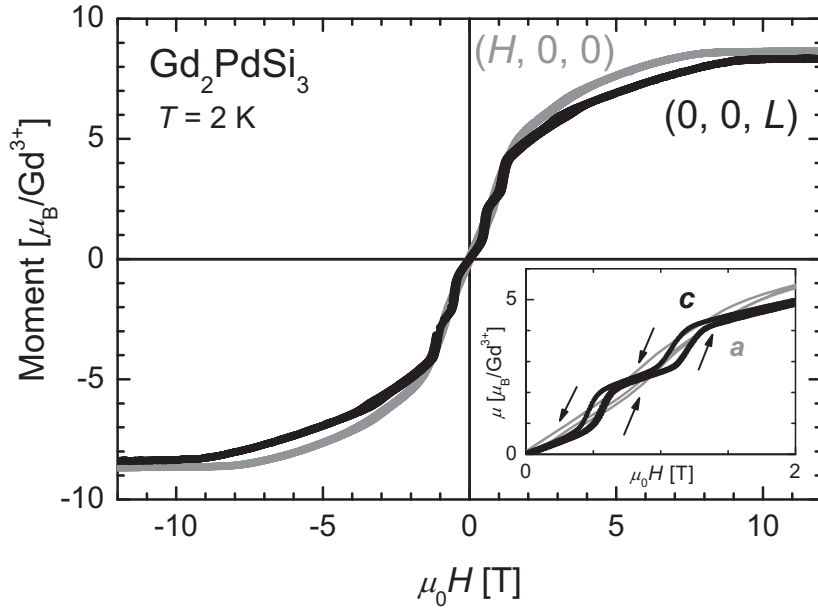


Figure 2.14: Gd_2PdSi_3 single crystal magnetization data at $T = 2 \text{ K}$ well below the ordering temperature ($T_N = 22 \text{ K}$). The inset shows the low-field part of the magnetisation curve with the two step-like transitions observed along the $(0, 0, L)$ direction.

Experimentally, an error has been tried to exclude by repeated measurements and control measurements on the calibration standard. Elemental gadolinium also has a slightly enhanced saturation value of $7.55 \mu_B$ [Köbler2006]. This enhancement is contributed to the polarization of conduction electrons [Maeda1999]. The magnetization curve of Gd_2PdSi_3 along the \mathbf{a} -direction does not show step-like transitions. The slope of the curve is slightly steeper than in \mathbf{c} -direction in agreement with the anisotropy found in the zero field susceptibility at low temperatures. The saturation value in \mathbf{a} -direction is nearly the same as found for the \mathbf{c} -direction. The difference can be used as estimation for the experimental error.

The magnetization curves of Er_2PdSi_3 (Fig. 2.15 on the next page) show that the strength of the antiferromagnetic exchange interaction along the hexagonal \mathbf{c} -axis is rather weak. Saturation is already reached at an applied external field of 1.4 T with a saturation moment of $\mu_S = 9.4 \mu_B$ (theoretical value $g\mathbf{J}_S = 9 \mu_B$). The magnetization curve shows two changes of slope at external fields of 0.15 T and 0.9 T that probably correspond to transitions to antiferromagnetic intermediate phases with an induced ferromagnetic component since no spin-flip transitions can be seen. The observed hysteretic behavior between 0.15 T and 0.9 T also indicates the existence of an induced ferromagnetic component. In the magnetic hard direction within the basal plane two changes of slope are observed (at external fields of 4.5 T and 10.5 T) probably corresponding to transitions to similar antiferromagnetic phases. At 13.5 T the magnetization in \mathbf{a} -direction reaches only half the value of the saturation moment.

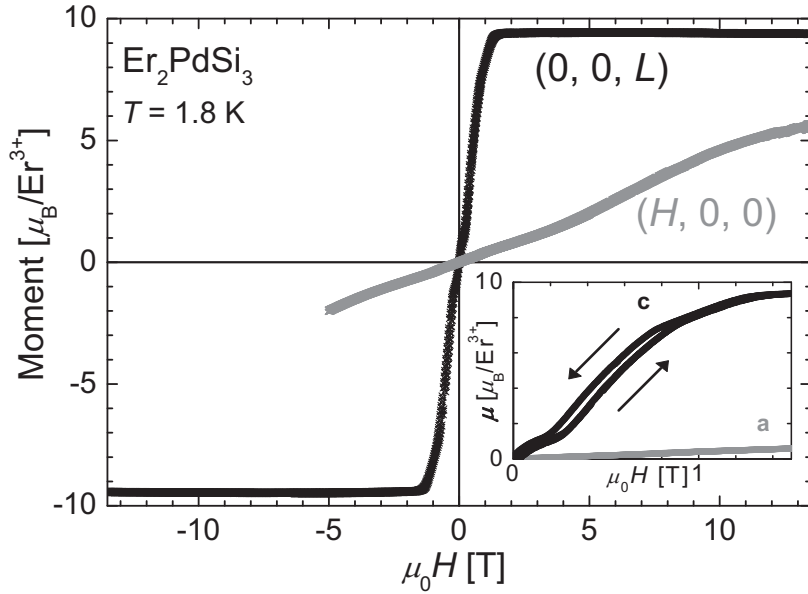


Figure 2.15: Er_2PdSi_3 single crystal magnetization data at $T = 1.8$ K well below the ordering temperature ($T_N = 7$ K). The inset shows the low-field part of the magnetisation curve with the small hysteresis observed between 0.15 T and 0.8 T.

The magnetization measurements for the a -direction in comparison to the c -direction of Tb_2PdSi_3 are shown in figure 2.16. Hysteresis in both directions indicates the existence of ferromagnetic correlations in an applied external field. Interestingly, the hysteresis also shows that the zero field state is not recovered when the field is switched off. This is in agreement

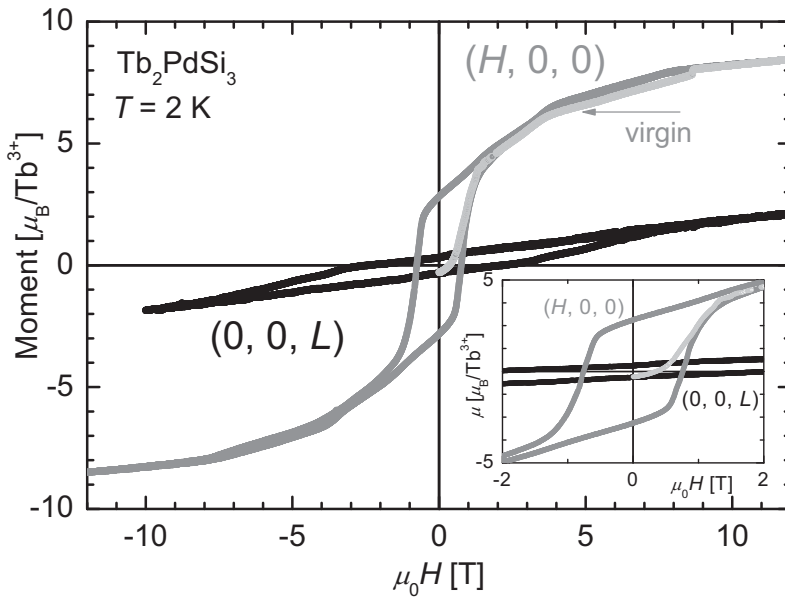


Figure 2.16: Tb_2PdSi_3 single crystal magnetization data at $T = 2$ K well below the ordering temperature ($T_N = 23.6$ K). The inset shows the low-field part of the magnetisation curve with the detailed hysteresis observed for both directions. For $(H, 0, 0)$ the virgin curve is accentuated.

with published experimental data, e.g. the time dependent decay of the remanent magnetization [Li2003] and the observed difference between zero field cooled / field cooled measurements [Szytula1999]. The slope of the magnetization in the a -direction changes at fields of 0.8 T and 4.1 T in the vicinity of the identified magnetic fields H_s and H_c . The value of the magnetization for the easy direction ($8.5 \mu_B$) at 12 T is slightly below the theoretical value of $gJ_S = 9 \mu_B$. The magnetization measured along the magnetic hard axis also shows hysteretic behavior. The magnetization is linear (if the change of the slope at the coercive field is neglected). No field induced phase transition is observed in contrast to the magnetization measured along the magnetic easy axis.

The magnetization measurement within the ordered state for Dy_2PdSi_3 (Fig. 2.17) is different to the in a previous publication [Frontzek2006]. The here presented measurement does agree better with the data published by others groups [Majumdar2001] and with the susceptibility measurement (see figure 2.3). Recalling figure 2.11, the Dy_2PdSi_3 compound undergoes an exchange of its respective magnetic easy axis at around 25 K. The application of

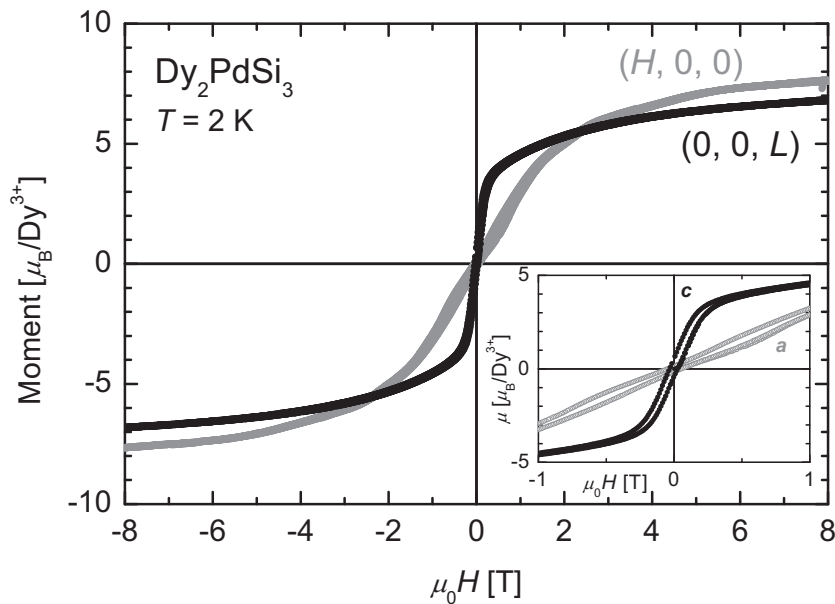


Figure 2.17: Dy_2PdSi_3 single crystal magnetization data at $T = 2$ K well below the ordering temperature ($T_N = 8$ K). The inset shows the low-field part of the magnetisation curve with the small hysteresis observed up to 0.5 T in the $(0, 0, L)$ -direction.

a magnetic field of about 2.4 T reverses the magnetic easy axis once more as can be seen in figure 2.17. For magnetic fields higher than 2.4 T the a -direction is the magnetic easy axis as it already was in the high temperature regime.

In small fields the magnetization in the c -direction is increasing rapidly. After a kink at 0.2 T the slope decreases steadily with increasing external field in the c -direction. A small

hysteresis is observed between -0.2 T and 0.2 T. At a field of 13.5 T the measured magnetization $\mu = 7.8 \mu_B$ is still below the theoretical saturation value of $gJ_S = 10 \mu_B$ for a trivalent Dy^{3+} ion. The magnetization measured within the basal plane along the \mathbf{a} -axis increases nearly linear up to an external field of 2.4 T where a distinctive change of slope occurs. Between -2.4 T and 2.4 T hysteretic behavior is observed. A second change of the slope seems to be around 5 T.

The magnetization of Ho_2PdSi_3 (Fig. 2.18) measured along the \mathbf{c} -direction initially rises slowly with an applied external field. Above 0.18 T the magnetization increases strongly. At 0.32 T one observes a sharp kink. Similar to Er_2PdSi_3 the behavior between these two fields is hysteretic. For higher fields the magnetization seems to saturate. However, the magnetic

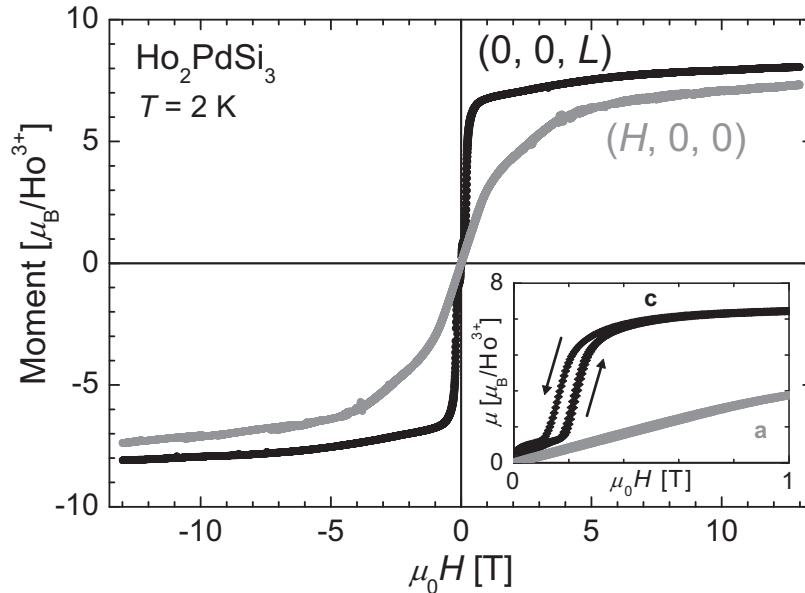


Figure 2.18: Ho_2PdSi_3 single crystal magnetization data at $T = 1.8$ K well below the ordering temperature ($T_N = 7$ K). The inset shows the low-field part of the magnetisation curve with the small hysteresis observed between 0.15 T and 0.8 T.

moment of $\mu = 8.1 \mu_B$ at 13 T is still below the expected saturation value of $gJ_S = 10 \mu_B$ for Ho^{3+} . The magnetization measured along the \mathbf{a} -direction exhibits a behavior comparable to the \mathbf{c} -direction except for the lack of a hysteresis. One observes a kink at around 1.2 T followed by a decrease of the slope with increasing field. At 13 T the magnetic moment is $\mu = 7.3 \mu_B$.

The magnetization of Tm_2PdSi_3 has been measured in the same VSM-setup used for the other $R_2\text{PdSi}_3$ compounds. The base temperature of the VSM (chapter 1.4.3) is 2 K, which is near but still above the Néel temperature of Tm_2PdSi_3 . The behavior of the magnetization might be modified in the ordered state. Two details can be seen in figure 2.19. First, the easy

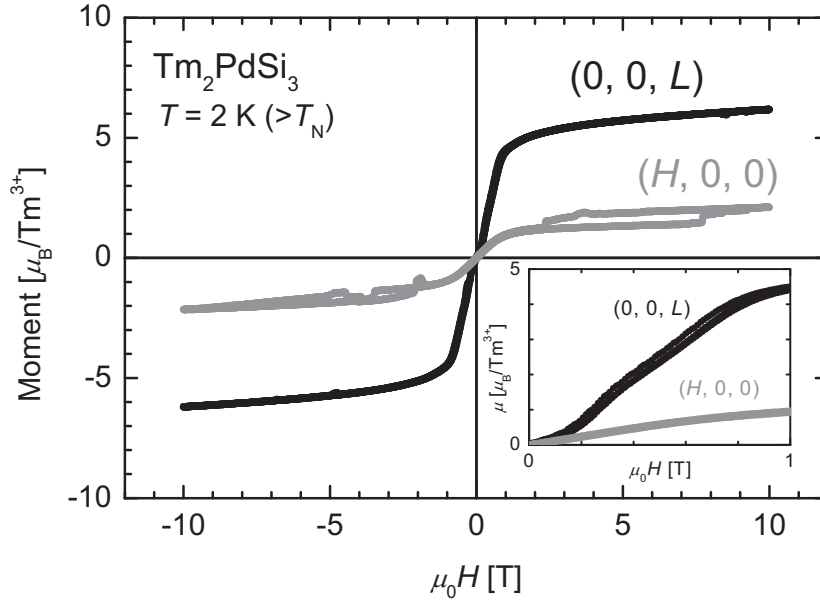


Figure 2.19: Tm_2PdSi_3 single crystal magnetization data at $T = 2 \text{ K}$ in the vicinity the ordering temperature ($T_N = 1.8 \text{ K}$). The inset shows the low-field part of the magnetisation curve. The magnetisation curve measured in the $(H, 0, 0)$ direction shows irregular jumps which are attributed to movement of the sample in higher fields.

magnetic axis in Tm_2PdSi_3 in the ordered state is the c -axis. In low field values ($< 0.2 \text{ T}$) the anisotropy seems to be small. The second detail is the occurrence of two kinks at 0.5 T and 0.8 T in the magnetization along the c -axis (see inset of figure 2.19). In the field range in-between the magnetization shows the hint of hysteretic behavior. The magnetic moment in an external field of 10 T is $\mu = 6.25 \mu_B$ which is $1.25 \mu_B$ below the theoretical saturation value ($gJ_S = 7.5 \mu_B$).

The macroscopic magnetic properties of the $R_2\text{PdSi}_3$ seem to arise from ferromagnetic and antiferromagnetic exchange interaction as well as crystal-electric field effects. In the high temperature regime the magneto-crystalline anisotropy seems to be dominated by the CEF. The detailed analysis of the CEF parameters from the ac-susceptibility is made in chapter 8.1. At lower temperatures, the CEF scheme is modified and the susceptibility cannot longer be described with a Curie-Weiss behavior as is illustrated by the exchange of the magnetic easy and magnetic hard directions in Dy_2PdSi_3 and Ho_2PdSi_3 .

The observation of anisotropy in Gd_2PdSi_3 indicates that the exchange interaction itself must be anisotropic. To evaluate the influence of exchange without CEF effects the Gd_2PdSi_3 compound will be examined in the next chapter in more detail.

3. Gd₂PdSi₃

In order to understand the magnetic behavior of the $R_2\text{PdSi}_3$ it is important to understand the role of the crystal electric field and the exchange interaction in the isostructural series. Chapter 2 (and 8) featured the description of the anisotropy due to the CEF using the second order parameter only. This description is only valid in the high temperature region (100 to 300 K) and even there the Ho_2PdSi_3 compound is an exception. Additionally, the anisotropy in the ordered state is due to both CEF and exchange interaction.

Gd^{3+} is an S -state ion and thus not susceptible to the CEF effect. Therefore, the magnetic properties of Gd_2PdSi_3 are ideally suited to evaluate the exchange interaction in these compounds. In chapter 2 ac-susceptibility and magnetization data of Gd_2PdSi_3 have been introduced. The anisotropy in the ordered state has already been a subject of exaggerated interest [Mallik1999, Saha1999, Saha2000_2]. The magnetic and electronic properties of Gd_2PdSi_3 have been already investigated with various methods on polycrystalline and single crystalline samples (without claiming completeness: magnetization, susceptibility [Kotsanidis1990], resistivity [Mallik1999, Saha1999, Saha2000_2], electron spin resonance [Deisenhofer2003], Mössbauer spectroscopy [Mallik1998_2] and photoemission [Chaika2001]).

Gd_2PdSi_3 orders antiferromagnetically at $T_N = 22$ K. The magnetic properties in the ordered state are anisotropic. Measurements of the resistivity in applied fields in the ordered state showed anisotropy also in the magneto-resistance which is attributed to an anisotropic Fermi surface [Saha2000_2]. The plot of resistivity vs. temperature shows a minimum at 45 K ($2 \cdot T_N$) [Mallik1998_2, Saha2000_2]. The resistivity vs. temperature behavior is interesting since the Kondo effect does not apply in this case [Saha2000_2, Chaika2001]. To understand the increase of the resistivity a complex magnetic structure that forms magnetic super-zone gaps at the Fermi surface was predicted. Above T_N , short-range correlations were assumed to produce equivalent super-zone gaps [Mallik1998_2]. It had been shown that a field of 5 T suppresses the upturn in resistivity around 45 K, restoring metallic behavior [Saha1999].

The zero field susceptibility (figure 2.1), does support this assumption insofar that around 40 K the susceptibility becomes anisotropic. Since only the exchange interaction can be the cause for the anisotropic behavior it is safe to assume significant short-range correlations to occur below this temperature and T_N . In the following the detailed magnetic phase diagram is derived from ac-susceptibility measurements. With the means of neutron scattering on powder at the ILL and resonant magnetic X-ray scattering at the APS the zero field magnetic structure is elucidated.

3.1 Ac-susceptibility

The magnetic phase diagrams (measured along both $(H, 0, 0)$ and $(0, 0, L)$) for Gd₂PdSi₃ is derived by means of ac-susceptibility. The phase diagrams are nearly identical for both directions and therefore the phase diagram for $(H, 0, 0)$ is shown without the detailed derivation from the ac-susceptibility. Most of the phase transitions in Gd₂PdSi₃ result in a signal in the real part of the susceptibility. Accordingly, only the real parts of the measurements are shown in the following. In this chapter the detailed derivation of the phase diagrams from the measurements along the $(0, 0, L)$ -direction will be presented.

Figure 3.1 shows the real part of the ac-susceptibility measured at constant field with varying temperature for the $(0, 0, L)$ direction. The black curve is measured in zero field with the maximum at T_N of 22 K and has been shown already in chapter 2. In addition, the grey curve is measured at zero field after the sample was field cooled in an external field of 2 T. The curves are identical. As expected for an antiferromagnet the application of a magnetic field shifts the maximum (connected to T_N) towards lower temperatures. Interestingly, after an

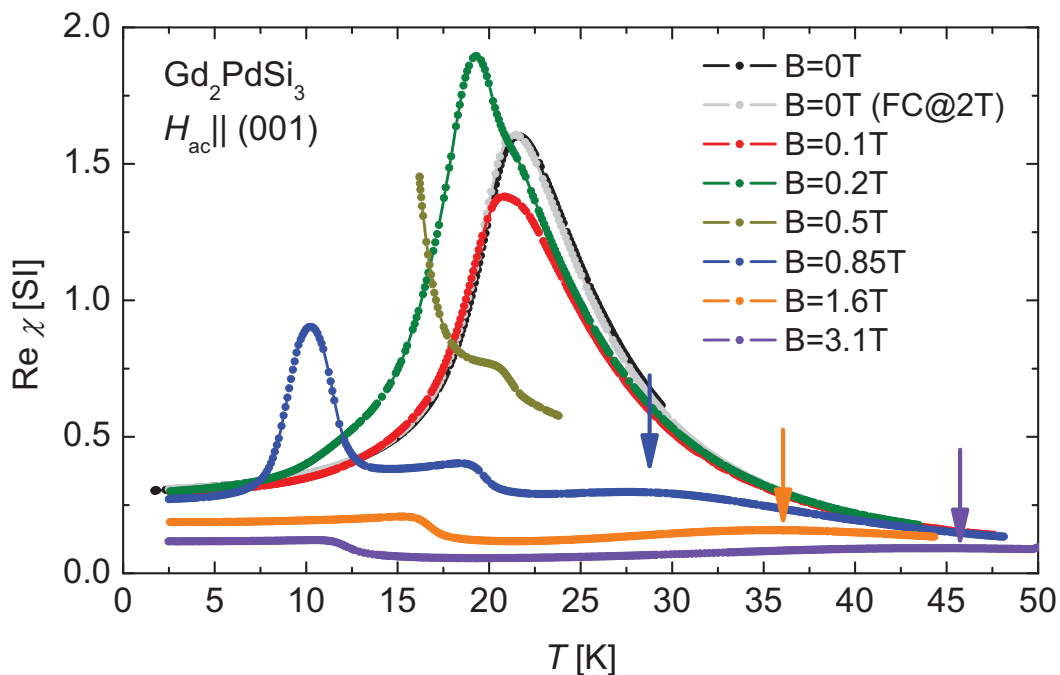


Figure 3.1: Real part of the ac-susceptibility of Gd₂PdSi₃. The ac-field is along the crystallographic $(0, 0, L)$ direction. The magnetic field is constant while the temperature is varied. The curves are not shifted. Arrows indicate a broad maximum which is difficult to see in the chosen scale.

initial decrease in magnitude, the signal of the ac-susceptibility apparently gains in magnitude for small fields around 0.2 T. Apparently a second phase transition occurs in applied fields. The signal magnitude decreases again for increasing fields as the measurement at 0.85 T

(blue) demonstrates. This curve shows altogether three features: a maximum at 10.2 K, a step-like decrease at $T = 19.8$ K and a broad maximum at 28 K (indicated with an arrow). The step-like decrease and its progress with increasing field has the typical course of the phase boundary of an antiferromagnet. The temperature and the critical magnetic field connected to this transition are denoted T_N' and H_{c1} .

The maximum at 10.2 K for an applied field of 0.85 T shifts in the further measurements with higher fields also to lower temperatures, but more quickly than the T_N' transition. This feature vanishes in the 1.6 T measurement (orange).

The broad maximum found at 28 K for 0.85 T is found at higher temperatures with increasing magnetic field. The assigned temperature to this transition is T_F . All features in the imaginary part have corresponding features in the real part and no additional anomalies were derived.

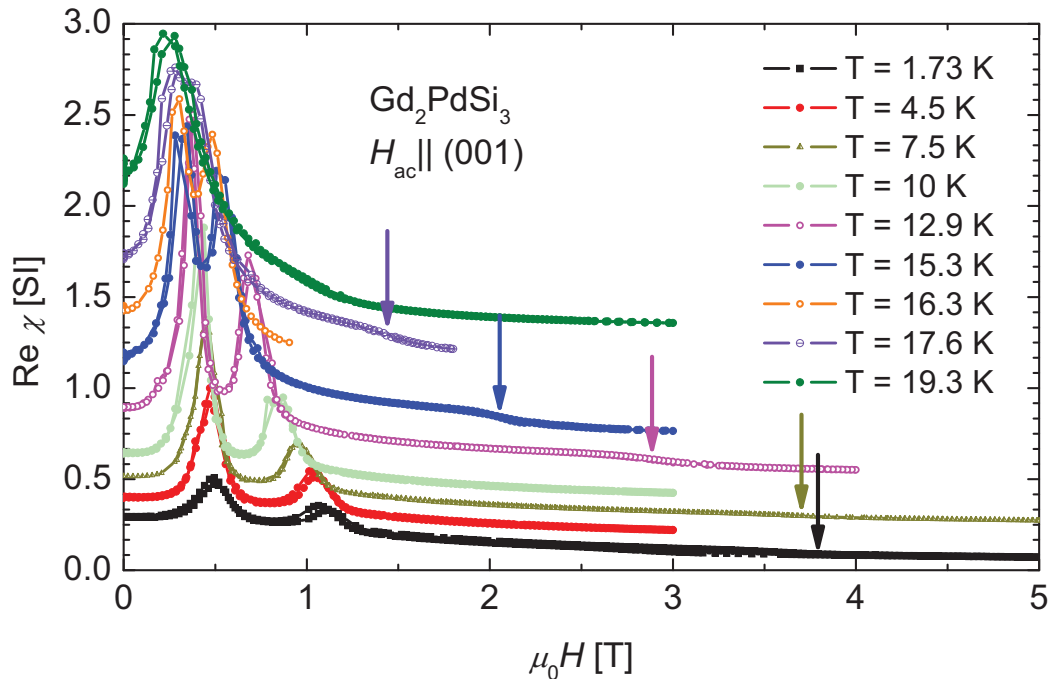


Figure 3.2: Real part of the ac-susceptibility of Gd₂PdSi₃. The ac-field is along the crystallographic $(0, 0, L)$ direction. The temperature is constant while the magnetic field is varied. The curves are shifted by 0.1 up to the 10 K measurement and then by 0.2. Arrows indicate a small step barely visible in the chosen scale.

The field dependent measurements at constant temperature are shown in figure 3.2. At lowest temperature (1.73 K, black curve) the curves show two maxima and a small step indicated by an arrow in the figure. The distance between the two maxima decreases with increasing field. At the highest measured temperature of 19.3 K this distance is practically zero and only one maximum appears in the measurement. The maxima are easy to identify

and correspond to the two step-like transitions also seen in the magnetization data (figure 2.14). The fields corresponding to this feature are labeled H_1 and H_2 as used in chapter 2. The additional feature marked with arrows at higher field values is harder to identify. It is a small step stretched over a field range of approximately 0.2 T. The step is barely visible in the chosen scale and the correct assignment of a specific field value is difficult. The chosen field value for the phase diagram is in the middle of this step since this point is most easy to assign. The field corresponds to H_{c1} .

3.2 Phase diagram for Gd₂PdSi₃

Combining the above discussed anomalies, figure 3.3 shows resulting the phase diagram for Gd₂PdSi₃ for a field applied along $(0, 0, L)$. The error bars are both related to measurement (see chapter 1.4.4) and confidence of the assignment of a specific value. The latter contribution is the larger one. For instance the field H_{c1} determined by a constant temperature scan is assigned an error corresponding to the dilation of the step by which it is identified.

The derived points can be connected with four lines discussed in detail in the following. The shown phase diagram only covers a field range up to 5 T. In chapter 2 the saturation field H_{c2} (at which the sample is ferromagnetic) for Gd₂PdSi₃ has been determined to be around 9 T. Above T_N Gd₂PdSi₃ is paramagnetic in zero field although the presence of magnetic

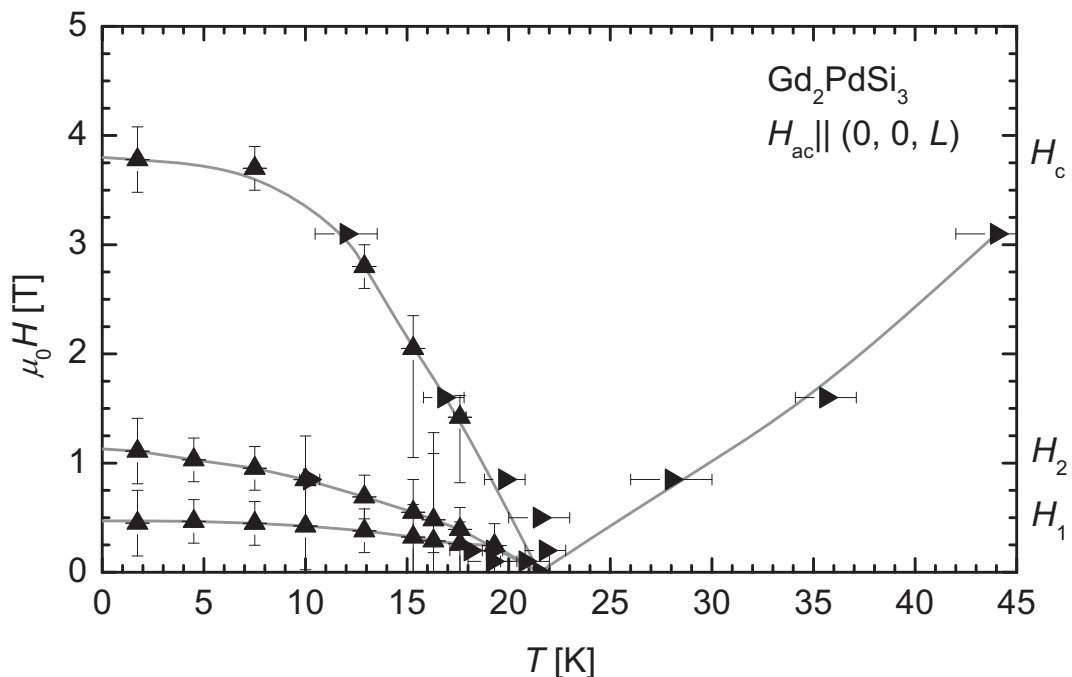


Figure 3.3: Magnetic phase diagram of Gd₂PdSi₃ determined by the means of ac-susceptibility with an ac-field along $(0, 0, L)$. The triangles indicate whether the measurement was performed with field or temperature variation. The fields H_1 , H_2 and H_c are indicated on the right y-axis. The grey lines are guide to the eye.

correlations is indicated in the susceptibility and the resistivity below 45 K.

It seems that at T_N all phase lines meet. Below T_N and in applied magnetic fields lower than H_{c2} an antiferromagnetic component might be present. The phase line from T_N to $T \rightarrow 0$ at approx. 4 T ($= H_{c1}$) seems to engulf the zero field structure. This assumption is also based on the compatibility of the field value and the ordering temperature. However, the nature of the two metamagnetic transitions at H_1 and H_2 in Gd₂PdSi₃ remains unknown so far.

The phase diagram derived from measurements with the field applied along $(H, 0, 0)$ is shown in figure 3.4. The phase diagrams show similarities i. e., the same qualitative behavior. The points can be connected with four lines, where the one from T_N to H_{c1} is the same for both diagrams. Two differences are observed:

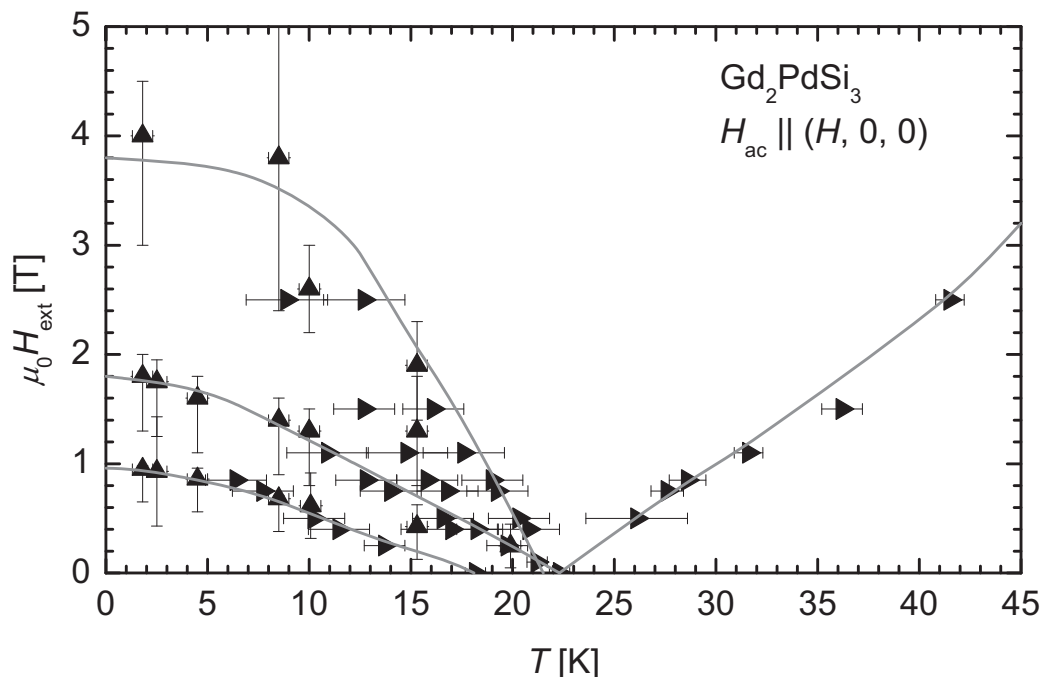


Figure 3.4: Magnetic phase diagram of Gd₂PdSi₃ determined by the means of ac-susceptibility with an ac-field along $(H, 0, 0)$. The triangles indicate whether the measurement was performed with field or temperature variation. The grey lines are guide to the eye.

First, some points on the line from T_N to H_{c1} have a neighbor point at lower temperature values. The gap between these two points is 3.8 K and seems independent of the applied field. This can be attributed to the different behavior magnetic domains exhibit when a field is applied in the plane. The field in the plane distinguishes one (e. g., $(H, 0, 0)$) direction from the other two symmetrical equivalent ($((H, -H, 0))$ and $(0, H, 0)$). It is impossible to conclude from the macroscopic observation which point belongs to which domain.

Second, the apparent higher values of H_1 and H_2 with the field applied along $(H, 0, 0)$. This can be attributed partly to the determination of the point of the transition. The according

anomaly in the ac-susceptibility is one broad peak (in contrast to the well separated two peaks in the case $\mathbf{H} \parallel (0, 0, L)$). The points drawn in the phase diagram correspond to the maximum and to a kink at the right tail of this peak. These anomalies show slightly different behavior in the temperature / field dependence and can be therefore interpreted as connected to the two transitions observed in the case $\mathbf{H} \parallel (0, 0, L)$.

3.3 Diffraction

Naturally, the next step was to investigate the magnetic structure. Since gadolinium has a very large absorption cross-section for thermal neutrons the method of resonant magnetic X-ray scattering (see [Hercules2003]) was chosen. The magnetic X-ray investigation was performed at the Mu-Cat instrument in sector 6 at the Advanced Photon Source (APS) at Argonne. The incident energy was tuned to the Gd-L3-absorption edge. To reach temperatures down to 8 K a displax cryostat was used. The main result was the observation of reflections due to magnetic order. Figure 3.5 shows a scan along the $(H, -H, 3)$ -direction (equivalent to $(H, 0, 3)$). Dwarfed by the crystallographic reflections 0, 0, 3 and 1, -1, 3 satellite magnetic reflections are found on positions describable with the commensurate propagation vector $\boldsymbol{\tau} = (1/7, 0, 0)$. With the measured data it is impossible to determine the magnetic moment direction and therefore the magnetic structure. An additional neutron

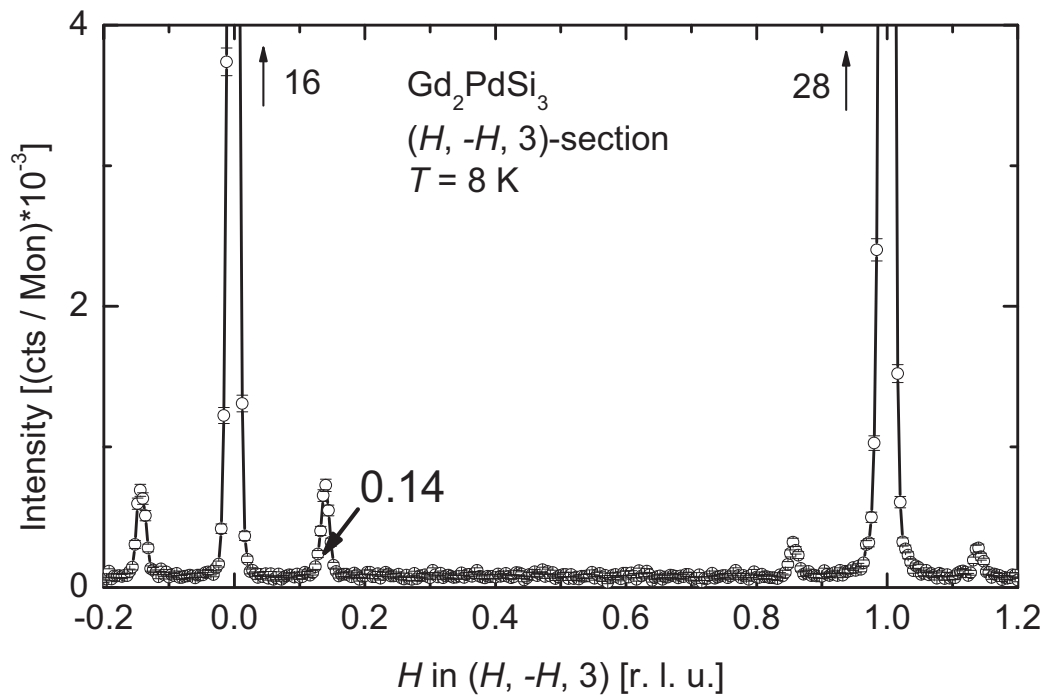


Fig. 3.5: $(H, -H, 0)$ section of resonant magnetic x-ray scattering measured at the APS. The direction is symmetrical equivalent to $(H, 0, 3)$. Magnetic satellites are observed on commensurate positions of $\pm 1/7$ from the crystallographic reflections. The peak maximum of the latter is written aside.

scattering experiment on powder has been performed on D4, situated at the hot source of the ILL [ILL-Report2006]. The difference spectrum (the paramagnetic spectrum is subtracted from the one measured in the ordered state) is shown in Fig 3.6. The propagation vector found at the APS experiment could be confirmed insofar that the magnetic reflections could be indexed with $\tau = (1/7, 0, 0)$. This is illustrated in the figure by a model calculation for an in-plane spiral shown as red curve. The assumption of a spiral agrees better with the observed data than a sine modulation, although both assumptions do not fully agree with the data. A further magnetic structure refinement was not successful due to relaxed resolution and a low

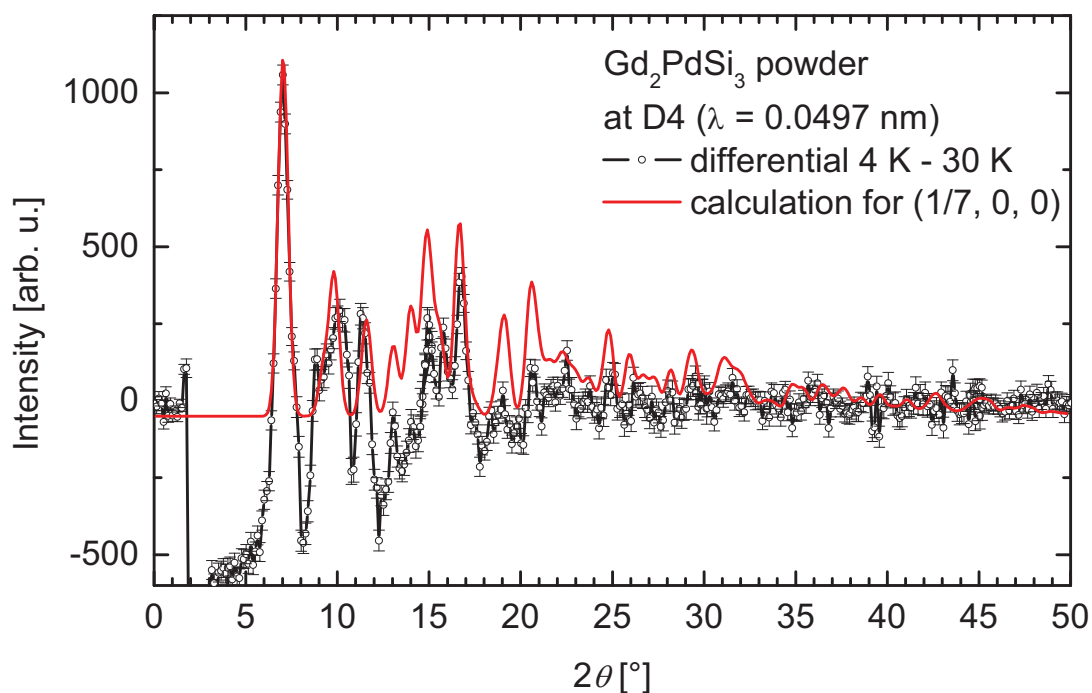


Figure 3.6: Differential neutron spectra of polycrystalline Gd₂PdSi₃ measured at the hot neutron diffractometer D4 at the ILL. The position of the magnetic reflections can be described with the propagation vector of $(1/7, 0, 0)$ as is emphasized by a model calculation. The model is an in-plane spiral (the spiral axis is parallel $(0, 0, L)$) with a moment magnitude of $7.0 \mu_B$.

signal to noise ratio [Devishvili2008]. The difference spectrum does not indicate the presence of a ferromagnetic component.

3.4 Summary

The Gd₂PdSi₃ compound shows a complicated magnetic behavior. The magnetic phase diagram indicates two magnetic ordered phases in intermediate field below H_{c1} and a high-field magnetic ordered phase below H_{c2} . The second critical field H_{c2} (to induced ferromagnetism) is around 9.4 T, deduced from the magnetization measurement (see figure

2.14). If a magnetic field is applied along the $(0, 0, L)$ -direction a phase covering a large area in the (T, H) -space is found between H_c (3.8 T for $T \rightarrow 0$) and H_{c2} . This phase is possible a ferrimagnetic state which is stabilized by an applied field. The existence of this phase might also be responsible for the reported suppression of the resistivity upturn [Saha1999] in applied fields.

Resonant magnetic X-ray scattering and neutron powder diffraction yielded a long-range ordered antiferromagnetic zero field magnetic structure with $\tau = (1/7, 0, 0)$. The direction of the magnetic moment is ambiguous. The analysis of azimuth-scans excluded a moment direction either strictly parallel to $(H, 0, 0)$ or $(0, 0, L)$. The best fit of the powder data was achieved with an in-plane spiral. The large magnetic unit cell indicates a frustration of the next nearest neighbor exchange interaction. Single crystal neutron scattering experiments at a hot source are planned to study more details of the magnetic order in applied fields.

3.5 Additional room temperature results of the diffraction experiment

The diffraction experiment on the Gd₂PdSi₃ single crystal was also used to characterize the crystal. The strong reflections due to the crystallographic structure could be described with the reported AlB₂ structure model [Szytula1999]. However, additional weak reflections have been observed which could not be indexed with the known structure model. An exemplary section along $(1/2, 1/2, L)$ measured at room temperature is shown in figure 3.7 (see next page). The reflections are found for values of $L = 2/8, 3/8, 5/8$ and $6/8$. An additional contribution appears as a sharp peak on the shoulder of the $3/8$ and $5/8$ reflection. This peak on the shoulder probably originates from epitaxial GdSi segregation (see 1.3.2) which has been observed in this sample. Surface texture due to grinding could be another possibility for the sharp peak. Both arguments could also be valid in the case of the $n/8$ reflections, especially since no superstructure reflections had been observed in previous powder measurements. The occurrence of the superstructure reflections called for a more detailed investigation on the crystallographic structure of the other R_2 PdSi₃ compounds. These investigations used neutrons (to exclude surface effects) on single crystals without R Si segregation and are presented in the next chapter.

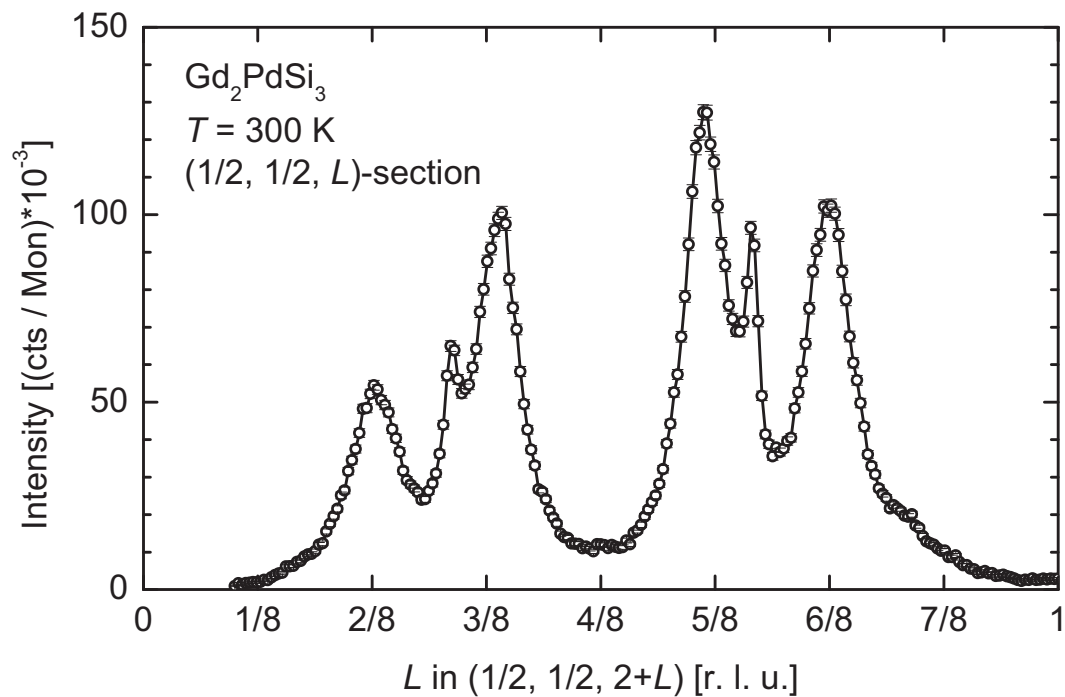


Figure 3.7: $(1/2, 1/2, L)$ -section of resonant magnetic X-ray scattering measured at the APS. At room temperatures crystallographic superstructure reflections are observed on commensurate position for $L = 2/8$ and $3/8$. The sharp peak on the shoulder of the $3/8$ reflection probably originates from epitaxial GdSi segregation.

4. Crystallographic structure of $R_2\text{PdSi}_3$

The observation of superstructure reflections in single crystalline Gd_2PdSi_3 made it necessary to investigate the occurrence of superstructure reflections also in other available $R_2\text{PdSi}_3$ single crystals. The chapter starts with the detailed listing of previously reported structures for the $R_2\text{PdSi}_3$ based on X-ray and neutron diffraction on powder samples. Consequently the results of neutron diffraction on $R_2\text{PdSi}_3$ ($R = \text{Tb}, \text{Ho}, \text{Er}, \text{and Tm}$) single crystals at room temperature is presented and ideas how to interpret the observed structures are discussed.

4.1 Reported indications for a crystallographic superstructure in $R_2\text{PdSi}_3$

The existence of a crystallographic superstructure in the series $R_2\text{PdSi}_3$ was already suspected. The rare earth “disilicides” compounds and the rhodium compounds $R_2\text{RhSi}_3$ from which the $R_2\text{PdSi}_3$ have been derived show superstructures. These superstructures have already been described in chapter 1.3.1.

Early X-ray investigations on powder proved the hexagonal symmetry of $R_2\text{PdSi}_3$ [Kotsanidis1990] and the lattice parameters were determined to be around 8 Å, twice the later published values [Szytula1999] (note: the quality of these lattice constants are unclear since no spectra are shown in [Kotsanidis1990]). The lattice parameters are in agreement with the $R_2\text{RhSi}_3$ compound series [Chevalier1984], but Kotsanidis et al. did not observe the formation of a superstructure. Later neutron scattering experiments [Szytula1999] (also on powder samples) and their refinements had yielded ($P6/mmm$) [IntTablesCrystA1989] as the most likely space group with both lattice constants (a and c) in the order of 4 Å. All investigated members of the series ($R = \text{Ce}, \text{Nd}, \text{Tb}, \text{Ho}, \text{Dy}, \text{Er}$) had been found to be isostructural [Szytula1999]. The atomic positions according to space group ($P6/mmm$) 191 [IntTablesCrystA1989] are the $1a$ Wyckoff position for the rare earth atoms and the Pd and Si atoms distributed statistically on the $2d$ position. For Ce_2PdSi_3 , a superstructure with a ($2a, 2a, 4c$)-unit cell had been reported earlier [Gordon1997] but could not be confirmed by neutron diffraction [Szytula1999]. The doubled values for the lattice parameters [Kotsanidis1990], the occurrence of non-indexable reflections [Szytula1999], the Ce_2PdSi_3 superstructure [Gordon1997], and attempts to explain measured magnetic properties [Paulose2003, Chaika2001] encouraged the discussion of a possible crystallographic superstructure also in the heavy rare earth compounds $R_2\text{PdSi}_3$.

4.2 Neutron diffraction experiments

Through the availability of large single crystals, neutron diffraction became an interesting opportunity. Investigating the magnetic structure of Tb_2PdSi_3 , the first result was the observation of crystallographic reflections which could not be indexed with the existing structure model [Frontzek2004]. Figure 4.1 shows a similar measurement, the full reciprocal (HHL)-plane of a Ho_2PdSi_3 single crystal as an example. The reflections according to the known structure model are $\{0, 0, 1\}$, $\{0, 0, 2\}$, $\{1, 1, 0\}$ and $\{1, 1, 1\}$ and are marked in the

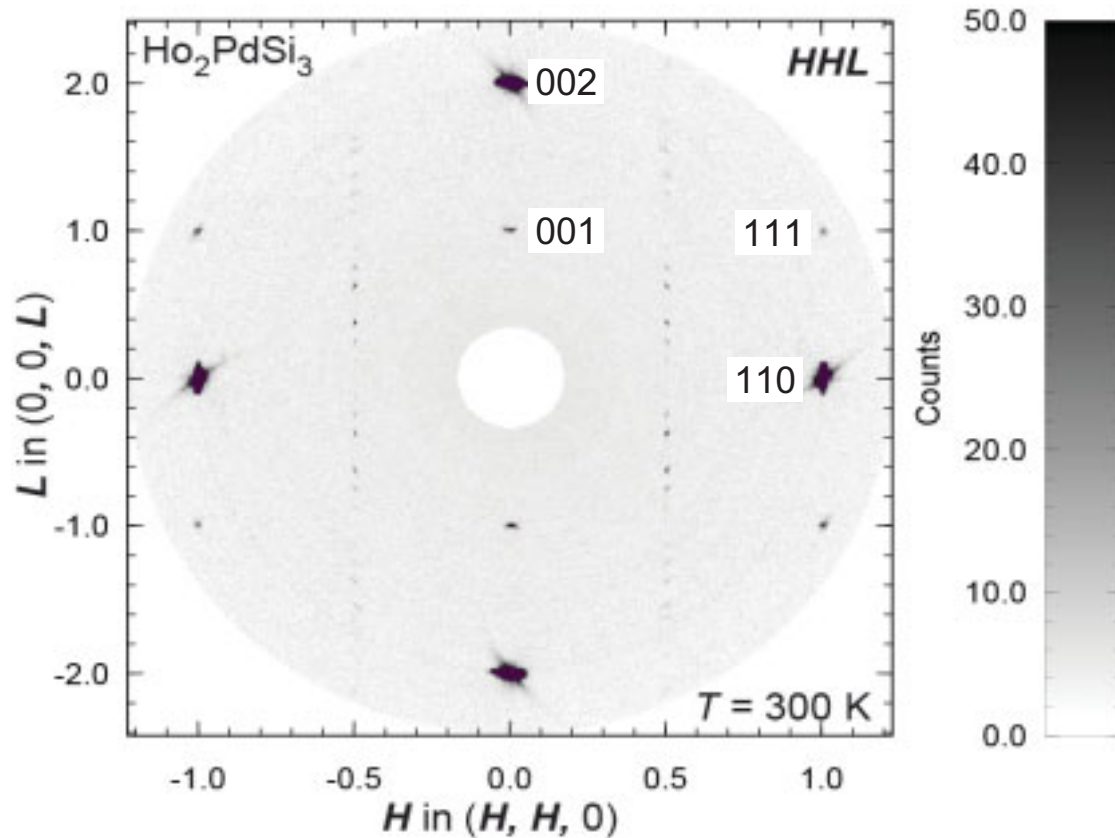


Figure 4.1: Reciprocal (HHL)-plane of single crystalline Ho_2PdSi_3 . The measurement was done at room temperature. The reflections expected from the published crystallographic structure are indexed, the strong $0, 0, 2$ and $1, 1, 0$ exceed the grey scale. The reflections due to the nuclear superstructure are found on $\pm 0.5, \pm 0.5, L$ positions ($L = \pm 1/8, \pm 3/8, \dots$).

figure. Their d_{hkl} values yield the same lattice constants (around 4 \AA for both directions) as the model published by Szytula et al. [Szytula1999]. However, additional reflections were found on $m/2, m/2, n/8$ positions where n and m are integers. No intensity was found on $0, 0, 1/2$; $1/2, 1/2, 0$ and $1/2, 1/2, 1/2$ positions (and analogues), which would be expected from the $R_2\text{RhSi}_3$ superstructure [Chevalier1984] and the lattice parameters published by Kotsanidis et al. [Kotsanidis1990]. Further investigation with the E2 diffractometer at the HZB (see 1.5.2 for further information) showed superstructure reflections on $m/2, 0, n/8$ also. The findings of

the neutron scattering experiments have recently been confirmed by detailed single crystal X-ray measurements on the same Ho_2PdSi_3 single crystal [Dshemuchadse2008].

Additional experiments on $R_2\text{PdSi}_3$ ($R = \text{Gd, Tb, Dy, Ho, Er, Tm}$) single crystals at E2 had shown the existence of the same crystallographic superstructure [HMI-Report2004]. The task is to determine a new structure model describing the superstructure reflections and to answer connected questions like: What is the reason for the observed superstructure? Can the structure still be described in space group ($P6/mmm$)? Is hexagonal symmetry conserved? In the following, the discussion is not confined to a specific member of the series, but applies to all heavy rare earth $R_2\text{PdSi}_3$ compounds.

However, two problems which have to be faced should be mentioned. Figure 4.2 shows two sections along $(0.5, 0.5, L)$ and $(0.6, 0.6, L)$, taken from figure 4.1. The intensity of the superstructure reflections is very small, and a quantitative analysis is therefore difficult. The next problem is the small d_{hkl} range, accessible with the E2 diffractometer. Only the reflections up to relatively large d_{hkl} (i.e. $3/2, 3/2, 7/8$) were measured. Limiting the used wavelength to 2.39 \AA allowed suppressing the $\lambda/2$ contamination of the incident beam. Both problems have been addressed by X-ray diffraction measurements in the Institute of Structural Physics [Dshemuchadse2008]. The consequences of the above mentioned problems are severe for a structure refinement, making it impossible to achieve directly a structure proposal. Building a structure model requires the knowledge of the applicable symmetry operations

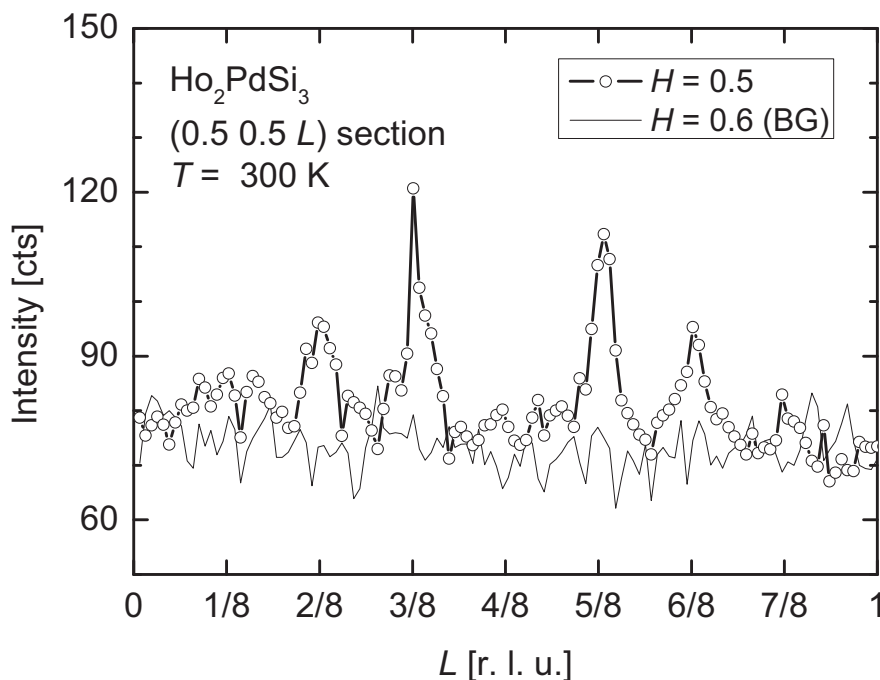


Figure 4.2: Section along $(0.5, 0.5, L)$ for Ho_2PdSi_3 . The reflections due to the crystallographic superstructure are on positions $L = n/8$. The $L = 1/8$ reflection is barely visible. Additionally, a section along $(0.6, 0.6, L)$ is shown to illustrate the signal-to-background ratio.

(e. g. the sixfold rotational symmetry parallel to the c -axis). In addition, if symmetry operations are broken in a quasi-symmetric compound, the possibility of twins arises. From the measured intensity of the superstructure reflections it is impossible to determine the existence of symmetry operations of the superstructure. This leads to a more heuristic approach for the crystallographic structural model. The reflections of the resulting models were calculated with IC-Powls [ICPWMan]. Only the existence of calculated vs. measured reflections were used as selection criteria for validity.

The structure model from the heuristic approach based on neutron data is compared with the model based on the X-ray measurements.

4.3 Heuristic approach and crystallographic structure model

In this chapter a crystallographic structural model based on the available neutron diffraction data with a triclinic symmetry is presented. Triclinic symmetry is the lowest of all and thus no restrictions of occupation have to be made. All symmetry operations are removed and the B sites are treated non-equivalently. The first restriction is imposed to account for the occurrence of crystallographic superstructure reflections: an ordering of the Pd and Si ions on the B sites of the AlB_2 structure is assumed. The primitive unit cell with its lattice parameters (a, a, c) is thus enlarged to $(2a, 2a, 8c)$. The new unit cell contains 96 atoms and the lattice constants are $(8.04 \text{ \AA}, 8.04 \text{ \AA}, 32.68 \text{ \AA})$, with the c' axis perpendicular to a' and b' while the angle between a' and b' still is 120° . The rare earth atoms remain on the Al position of the primitive cell. At this point, it should be mentioned that an ordering of Pd and Si might also result in a modulation of the rare earth atoms' positions along the c -axis. This was neglected since a modulation of the rare earth atoms easily gives rise to reflections on $0, 0, m/8$ which were not observed. Configurations with a modulation of the rare earth z -position that comply with the observed intensity are, however, possible. In addition, the Pd and Si ions are not modulated in the z -position, mainly to restrict the number of free parameters. The remaining possibilities are planes of ordered Pd and Si atoms on the $2d$ Wyckoff position of the AlB_2 -type unit cell. The different models vary in the stacking order of these 8 layers, each containing 8 ions from altogether 16 Pd and 48 Si. A possible model has to comply with the findings from the neutron scattering experiments, i. e. intensity observed for $m/2, m/2, n/8$ and $m/2, 0, n/8$ reflections. No intensity was found for $0, 0, n/8$; $m, m, n/8$ and $m, 0, n/8$ (except for the main reflections arising from the AlB_2 -type basic structure, e. g. for $n = 8$). These findings are referred to as “no-intensity” rule in the following. First calculations quickly yielded exclusions of possible arrangements of the Pd and Si ions which violated the “no-intensity”

rule. Two main exclusions were derived. The first concerns the content of a layer: Any non-stoichiometric Pd-Si distribution (e. g. 8 Si in one layer and 4 Pd and 4 Si in the next) leads to a violation of the “no-intensity”-rule and are therefore excluded. Such a distribution would lead to $0, 0, n/8$ reflections. Therefore, every Pd/Si layer does always consist of two Pd-ions and six Si-ions. The other exclusion applies to arrangements of all layers without a two-fold axis. The two-fold axis yields intensities for $m/2, m/2, n/8$ reflections since the symmetry entails the $(2a, 2a)$ enlargement. An arrangement exclusively of layers without a two-fold axis yields a $(2a, a)$ enlargement with intensities only for $m/2, 0, n/8$ and is therefore excluded. Figure 4.3 shows the remaining four possible arrangements of Pd and Si atoms within a layer. The purple colored balls represent the Pd atoms, while the yellow balls represent the Si atoms. The four possible layers are stoichiometric and have a two-fold axis in c -direction. They are denoted A, B, C, and D. The possibilities are now narrowed down to the search for the eight-times-stacking sequence of these four layers. Calculations of intensity for all possible arrangements were performed using the program IC-Powls. The sorting routine of the results

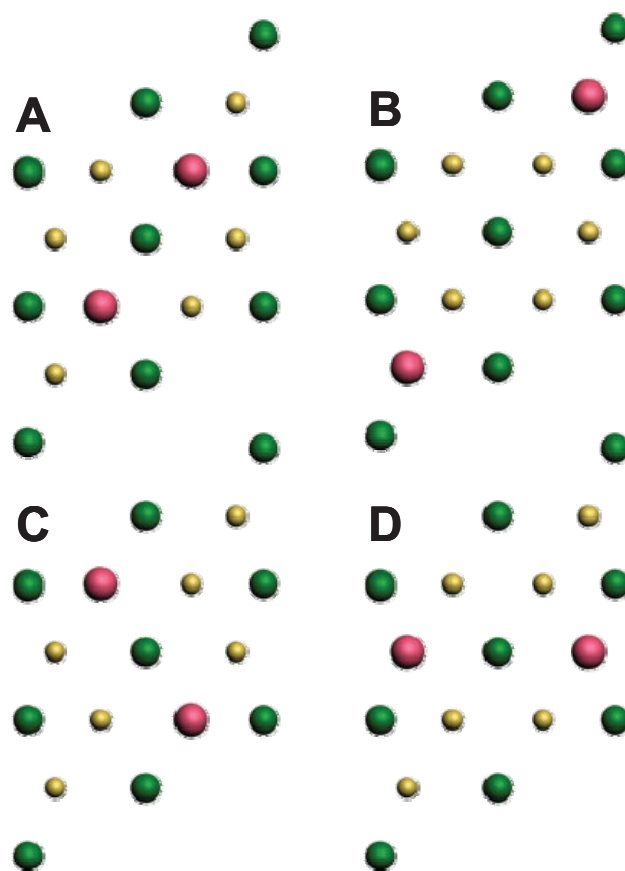


Figure 4.3: Basal plane projection of the four possible layers of the triclinic model named A, B, C, and D. The rare earth atoms are depicted in green. The position of the silicon (yellow) and palladium (purple) atoms is $c/2$ above the basal plane.

used the four constrictions of the “no-intensity” rule, which had been experimentally verified. All results with considerable intensities on one of the reflection positions $0, 0, 3$; $0, 0, 4$; $1, 0, 0$ or $1, 1, 0$ were neglected. Finally, 16 layer arrangements were found to fulfill the selection rules: AABBCDD, AABBDCCD, AABCCBDD, AABCCDDB, AABDCBDC, AACBBCDD, AACBDCBD, ABBACCDD, ABBCCADD, ABBDCADC, ABCABDDC, ABCADDBC, ABDABDCC, ABDACCBD, ABDACDBC, and ACBBDACD.

All listed layer arrangements produce intensities for the crystallographic reflections of the AlB_2 basic compound equal to the primitive case. Intensity is calculated for the $m/2, m/2, n/8$ and $m/2, 0, n/8$ superstructure reflections respecting the “no-intensity” rule. Unfortunately, the experimental precision of the neutron diffraction experiments do not allow the separation of the possible layer arrangements. The results for one of the possible arrangements compared to the experimental values are listed in table 2. The magnitude of the intensity is reproduced but systematically too large. The calculations yield slightly different intensities for the “quasi”-symmetric reflections $m/2, 0, n/8$ and $0, m/2, n/8$. These differences are within the resolution limit.

H	K	L	I_{calc} [int. int.]	I_{obs} [int. int.]
0	0	2	5800	5800
0.5	0	3/8	2.2	0.5
0.5	0.5	1/8	3.0	1.4
0.5	0.5	2/8	4.5	4.7
0.5	0.5	3/8	9.5	4.2
1.5	0	1/8	1.9	0.3
1.5	0	2/8	2.9	0.8
1.5	0	3/8	3.9	3.1
1.5	1.5	2/8	3.0	0.3
1.5	1.5	3/8	4.2	0.3

Table 2: Comparison of measured and calculated nuclear intensity with the model described in the text (layer sequence ACBBDACD). The intensity is scaled to match the $0, 0, 2$ reflection. The error of the intensity fitting is in the order of 10 %. The real observation error is probably twice as large if signal to background ratio is considered. Observation errors are therefore not given.

The main disadvantage of the triclinic model is the lost hexagonal symmetry. Therefore, the real crystal has to be treated in principle as multiple twinned. The intensities from different twins average in the measurement. The fact that the calculated intensity is not in agreement with the experiment is therefore to be put into perspective. It is very likely, that the real crystal does not consist of one arrangement of layers, but of several different stacking. A sequence from A to C seems as likely as a sequence from A to D. Therefore, stacking faults may be expected. Figure 4.4 shows two X-ray diffraction scans (ID20, ESRF) of one superstructure reflection, which were recorded in different scan directions. Obviously the same reflection does have different full widths at half of the maximum value (FWHM), depending on the direction of the scan. The comparative measurement on a reflection of the primitive structure, e. g., 1, 0, 3 yielded for both directions nearly the same FWHM. The observed FWHM_{obs} consists of an intrinsic part $\text{FWHM}_{\text{intr}}$ and an instrument resolution part FWHM_{RS} . With the approximation, that the FWHM of the 1, 0, 3 reflection is mainly due to

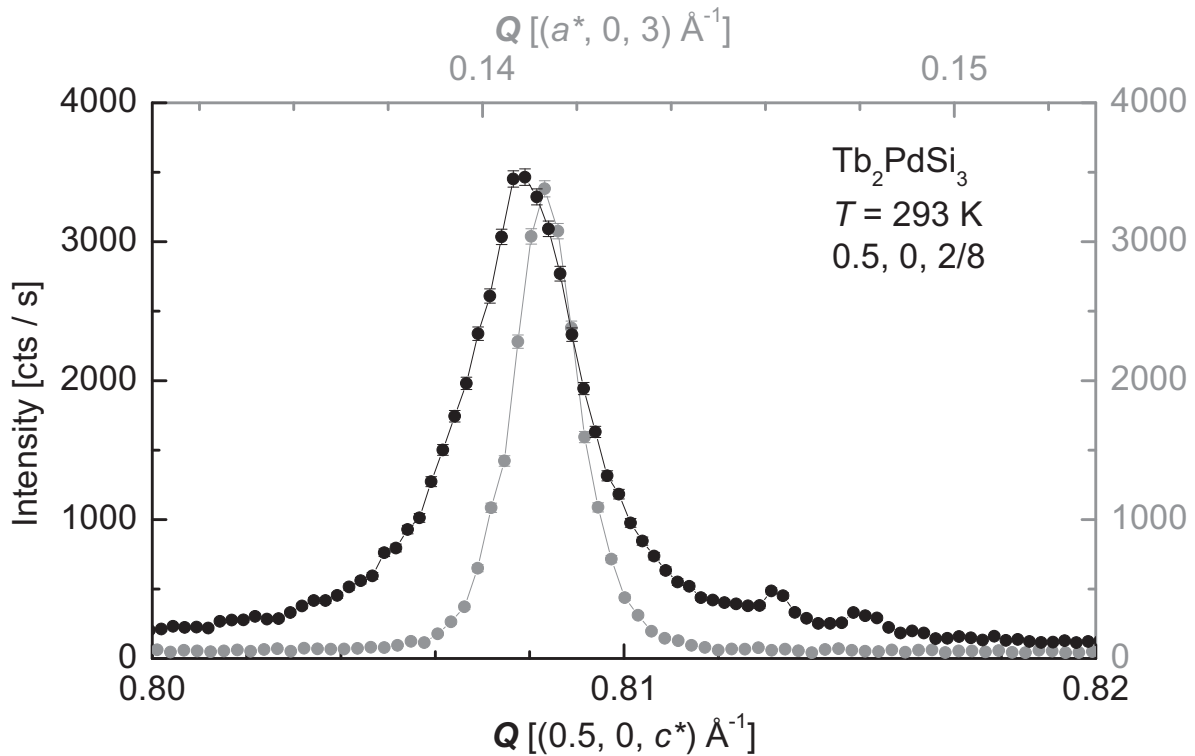


Figure 4.4: The superstructure reflection $0.5, 0, 3+2/8$ measured at the ID 20 beamline at ESRF, Grenoble. The reflection was measured along $(0, 0, L)$ (black curve and axes) and along $(H, 0, 0)$ (grey curve and axes) with the same instrumental parameters. Plotted on the x -axis is the scattering vector \mathbf{Q} . The difference in FWHM is around the factor of two (see text).

the resolution the intrinsic part for the superstructure reflections can then be calculated according to formula (16).

$$\text{FWHM}_{\text{obs}} = \sqrt{(\text{FWHM}_{\text{intr}})^2 + (\text{FWHM}_{\text{RS}})^2} \quad (16)$$

The intrinsic part of the FWHM is proportional to the inverse correlation length l_c . The values calculated for the $\text{FWHM}_{\text{intr}}$ of the different reflections measured in this experiment are shown in table 3. The FWHM_{RS} of the nuclear reflection 1, 0, 3 corresponds to a correlation length of 1000 Å and 700 Å for the (0, 0, L) and (H , 0, 0) direction.

H	K	L	FWHM_{obs} (0, 0, L)	FWHM_{obs} (H , 0, 0)	l_c [Å] (0, 0, L)	l_c [Å] (H , 0, 0)
1	0	3	0.00389	0.00508	-	-
1/2	0	3+1/8	0.0234	0.00758	174	628
1/2	0	3+2/8	0.01552	0.00678	268	786
1/2	0	3+3/8	0.0134	0.00906	314	471

Table 3: Observed FWHM for the different reflections measured both along (0, 0, L) and (H , 0, 0). The correlation length l_c has been calculated as the inverse of the intrinsic FWHM.

In the crystallographic structure, defects like stacking faults decrease the correlation length. Additionally, the correlation length can be used to estimate the average size of a crystallographic domain. Two important results can be derived from table 3. Firstly, the correlation length is larger for the 1, 0, 3 reflection than for the superstructure reflections. The contrast for the X-ray intensity mostly results from the rare earth atoms, which are on the well defined positions of the AlB_2 structure. The intensity of the superstructure reflections only arises from the Pd/Si atoms. The different correlation lengths support the argument of stacking faults in the superstructure, e. g. the occurrence of multiple layer arrangements. Secondly, the correlation length depends on the scan direction. The measurements of the in-plane direction and along the hexagonal axis differ roughly by a factor of two. Either, the order in-plane is better defined or the energy of a stacking fault is larger in-plane than along the hexagonal axis. The in-plane correlation length might be correlated to the twin / domain size.

2.3 The modulated structure

Based on single-crystal X-ray investigations a structure model was developed for Ho_2PdSi_3 . This model is mentioned since it successfully describes the measured intensities. The detailed work on the structure of Ho_2PdSi_3 has been done by Dshemuchadse et al. [Dshemuchadse2008]. The lattice constants in the basal plane are doubled and the modulation

vector is $(0, 0, 3/8)$. The structure is still based on the $P6/mmm$ space group with Ho atoms on the Wyckoff positions $1a$ and $3d$ and Pd/Si atoms on $2d$ and $6f$ ($x_{6f} = 1/6$). The description uses the formalism of super space groups. The chosen super space group is $P6/mmm(0, 0, 3/8)0000$. This structural model was calculated with modulated occupancies of Pd and Si atoms on the shared sites and slight modulations of the atomic positions. The structure model is shown in figure 4.5. With this approach, all measured reflections could be indexed and furthermore intensities of the reflections could be calculated and refined. The main elegance of this structural model is the maintaining of the hexagonal symmetry. The

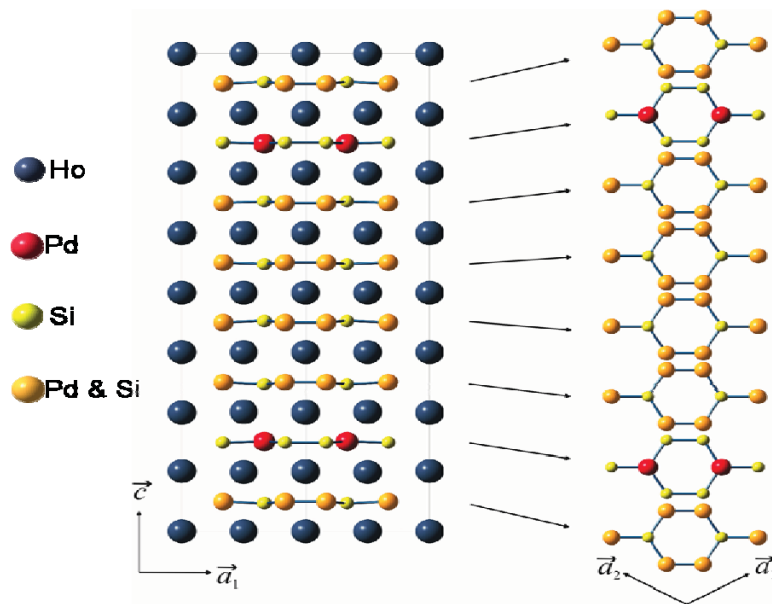


Figure 4.5: Picture of the structure model for Ho_2PdSi_3 according to [Dshemuchadse2008]. The slight modulation of the z-position is visible on the Pd/Si layers. The sites with shared occupancy have the probability of $1/3$ Pd and $2/3$ Si ions.

drawback is, that for only two out of eight layers the $2d$ sites are occupied by the Pd atoms and the $6f$ sites are occupied by Si atoms. The other layers exhibit a statistical distribution on the $6f$ sites, while the $2d$ sites are occupied by Si atoms. The model describes the observed intensities in position and magnitude. Further steps to increase the consistency with the measured data (e. g. symmetry reduction) were not successful [Dshemuchadse2008_2].

2.4 Comments on the structural models: triclinic and modulated hexagonal

The crystallographic superstructure of $R_2\text{PdSi}_3$ can be successfully described either within the triclinic model or the modulated hexagonal structural model. The problem of the existence of multiple twins in the real structure is present in the triclinic model for which twins are conditional. However, the crystallographic superstructure cannot be a product of chance: The

same superstructure reflections had been found in all investigated $R_2\text{PdSi}_3$ ($R = \text{Gd}, \text{Dy}, \text{Tb}, \text{Ho}, \text{Er}, \text{Tm}$) single crystals. The phase $R_2\text{PdSi}_3$ is stable, i. e. a parasitic phase of $R_2\text{Pd}_x\text{Si}_{3+x}$ does not exist. The detailed investigation of neighboring phases had been done for Er_2PdSi_3 [Mazilu2006]. The neighboring stable phases are ErSi and ErPd_2Si_2 [Mazilu2007]. The results of this investigation are generalized for the other $R_2\text{PdSi}_3$ compounds with respect to their similar behavior in the growing process. Also, a chemical analysis and EDX (Energy-dispersive X-ray spectroscopy) measurements had resulted in the stoichiometric formula $R_2\text{Pd}_{1.01(1)}\text{Si}_{2.99(1)}$ [Dshemuchadse2008], meaning that no deficiencies are observed within the experimental error. The driving force leading to the formation of the observed structure is still under discussion. It causes order of Pd and Si in the quasi-hexagonal AlB_2 structure in the process of crystal growth where the influence of the entropy is large (due to high temperature). The observed lattice parameters yield a Pd-Si distance within the layer, which is too small for Pd neighboring a second Pd (Pd ion radius is 1.4 \AA). Within the layers, one can therefore expect the Pd to be surrounded by three Si atoms. This distribution scheme for Pd/Si was found also for the rhodium compound $R_2\text{RhSi}_3$ [Chevalier1984]. The arrangement of layers along the c -axis might be the result of small deviations of the z -position of the rare earth atoms. For instance, the Pd neighbors in the next layer along the c -axis might always be Si atoms (this result is not reproduced by both models). However, deviations from the positions of the rare earth atoms in an AlB_2 -type structure have to be very small (otherwise they would have been visible in the experiment), so the position of the rare earth atoms may still be fully described with the primitive hexagonal cell. The modulated structure model uses displacements of the rare earth ions. The sum of these displacements is zero, resulting in a common position.

The influence of the superstructure on the magnetic structure of the $R_2\text{PdSi}_3$ compounds is not obvious. In zero field the magnetic structure can be described satisfactorily by the primitive unit cell in the case of Gd_2PdSi_3 . In chapter 5 (Long- and short range magnetic order in Tb_2PdSi_3) the magnetic structure in applied fields is presented which mimics the crystallographic superstructure. The addition of the superstructure complicates the discussion of the magnetic properties. When the magnetic structures are determined mainly by RKKY interaction the influence of the superstructure seems to be weak. But in applied fields or when the magnetic structure is influenced by the CEF the superstructure has large influence. The crystallographic superstructure yields different rare earth surroundings in each layer. In the enlarged unit cell, three rare earth atoms have the same lattice site on a triangular lattice with inherent geometric frustration. One of the rare earth atoms is in the origin (Wyckoff site $1a$).

The surrounding of three out of four rare earth atoms sees two Pd atoms from the next neighboring layer. The fourth rare earth atom then has a “hexagonal” surrounding of only Si. In some cases, the Pd/Si layers below and above have the same rare earth atoms in a hexagonal surrounding. For instance, in a CDDA sequence the $1a$ site has hexagonal symmetry. However, the site symmetry changes along the “hexagonal” direction for all layer arrangements. The difference in the correlation lengths for the different superstructure reflections (table 2) might be attributed to stacking faults. The correlation length is largest for the $L = 3/8$ reflection and this reflection is also the most pronounced (the vector of the modulated structure was chosen accordingly). The occurrence of only two defined layers in the modulated structure can be attributed to a stricter rule. This rule sees a specific layer to be repeated every fifth layer in the unit cell (and therefore every third layer, regarding the neighboring unit cell). Except for AABBCDD, at least one layer repeating in the aforementioned fifth and third scheme could be found (e. g. AACBBCDD or ABDABDCC) in the possible arrangements of the heuristic model.

In summary, the crystallographic structure of $R_2\text{PdSi}_3$ ($R = \text{Gd, Tb, Ho, Er, Tm}$) is still unresolved. Within this work, a structural model has been derived. The superstructure has quasi hexagonal symmetry and is derived from the AlB_2 -type structure. The hexagonal symmetry is obtained in the rare earth layers. Depending on the neighboring Pd/Si layers the symmetry is lowered. The layers of Pd and Si are stoichiometric with composition 1:3. Only four possible layer arrangements satisfy the observed extinctions “rules”, although this is not confirmed by the modulated structure model. Out of maximal 65536 (4^8) possibilities of stacking sequences only 16 are in agreement with the observed reflections. The symmetry reduction from the hexagonal structure to the triclinic case opened the possibility of twin domains, further complicating a structure solution. The here proposed superstructure can be used to understand the arrangement of Pd and Si in the $R_2\text{PdSi}_3$ compounds. In the following the description “crystallographic structure” refers to the primitive AlB_2 structure. The term “crystallographic superstructure” relates to the here presented model.

In chapter 3 the zero field magnetic structure of Gd_2PdSi_3 had been presented. An influence of the crystallographic superstructure on the magnetic structure had not been found. This can be understood since the relevant exchange interaction orders the magnetic moments in the Gd-planes in which the hexagonal symmetry is conserved. What happens if the relevant exchange is through the Pd/Si layers? The Tb_2PdSi_3 compound gives an answer.

5. Long- and short range magnetic order in Tb_2PdSi_3

Tb_2PdSi_3 has been named “exotic” in the literature since it shows huge changes in its magnetic properties when parameters as external field and temperature are varied [Paulose2003]. Also, as had been emphasized in chapter 2, among the investigated compounds only Tb_2PdSi_3 has its easy magnetic axis in the basal plane.

5.1 Results of ac-susceptibility

The behavior of Tb_2PdSi_3 in magnetic fields was studied with detailed ac-susceptibility measurements, from which a magnetic phase diagram is derived for a field parallel to $(H, 0, 0)$. In fields smaller than 5 T the ac-susceptibility within the basal plane (for both $(H, 0, 0)$ and $(H, H, 0)$) does not exhibit strong anisotropy. The ac-susceptibility shows no significant changes when the magnetic field is applied parallel to $(0, 0, L)$. This is in

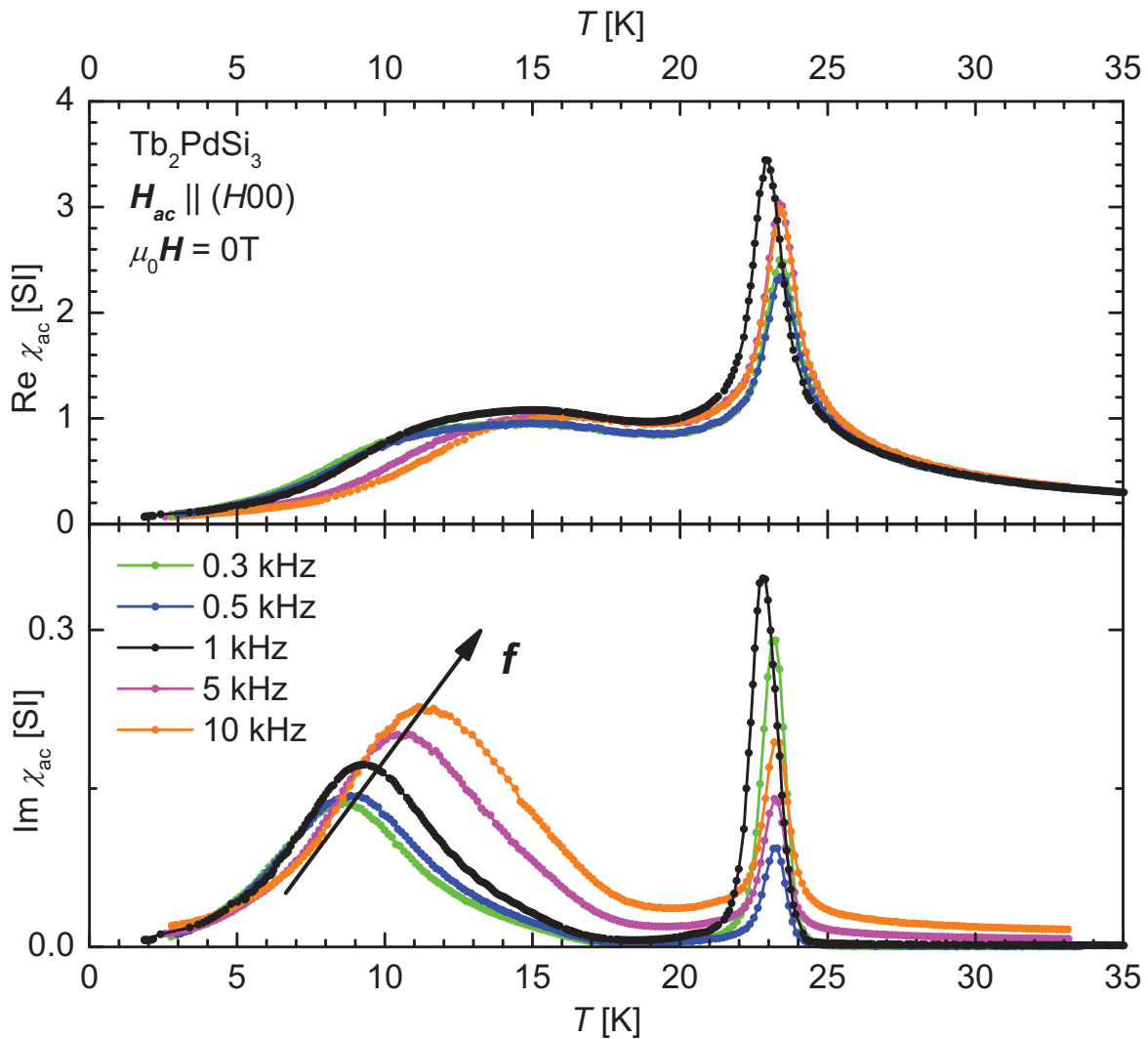


Figure 5.1: Real and imaginary part of the ac-susceptibility of Tb_2PdSi_3 measured with different ac-frequencies. The ac-field is along the $(H, 0, 0)$ -direction.

agreement with the apparently linear response of the magnetization.

5.1.1 Ac-susceptibility: Zero field transitions

Figure (5.1) shows the real (upper part) and imaginary (lower part) zero field ac-susceptibility vs. temperature for Tb₂PdSi₃ with the ac-field along the $(H, 0, 0)$ direction. Five similar curves are shown for both real and imaginary part. The susceptibilities are measured with different ac-frequencies. Above the Néel temperature ($T_N = 23.6$ K) the curves follow a Curie-Weiß law (details of the paramagnetic properties have been shown and discussed in chapter 2). Two features are observed for each curve: the sharp maximum at the Néel temperature and the broad shoulder above 10 K in the real part. In the imaginary part this feature is seen as a broad maximum. For different ac-frequencies the sharp maxima at the Néel temperature differ in their peak value but not in (temperature) position and half-width. For a detailed analysis of the frequency dependence of the maximum at T_N (as hypothetically done in a Cole-Cole plot [Cole1941] where the imaginary part is plotted vs. the real part for different frequencies) more frequencies would have to be included.

The broad maxima in the imaginary part shows a distinctive dependency from the ac-frequency comparing the curves. As expected from the real part they show a pronounced shift in temperature from 8.5 K at 300 Hz up to 11.5 K at 10 kHz. In general, a spin-glass of collectively magnetically interacting moments is expected to obey a Vogel-Fulcher law [Cardoso2003]. The Vogel-Fulcher law

$$f = f_0 \cdot \exp\left(\frac{-E_a}{k_B(T - T_0)}\right) \quad (17)$$

correlates the excitation frequency f to the temperature shift. Here, f_0 is a phenomenological parameter which is used for fitting. It can be correlated to the relaxation time t_0 [Saslow1988] which in this case is 1.25 μ s. Also, E_a is adapted and can be interpreted as potential barrier. This equation is normally used to describe the behavior of glasses and the legitimacy to use it here is disputable. Figure 5.2 shows the measured data and a fit with equation (17). The fit yields a potential barrier of 27.8 K. The temperature T_0 from this fit is 5 K. This temperature is expected for $f \rightarrow 0$. Again, five frequencies are not enough for a definite conclusion but this temperature coincides with other measurements presented later. On the other hand, the results for t_0 and E_a are in a reasonable magnitude. The time dependency of the magnetization at low temperatures, the frequency shift in the ac-susceptibility and the differences in field-cooled (FC) / zero-FC dc-susceptibility results have been published before [Li2003, Szytula1999, Paulose2003] and have been interpreted as spin-glass behavior. Interestingly, ac-susceptibility

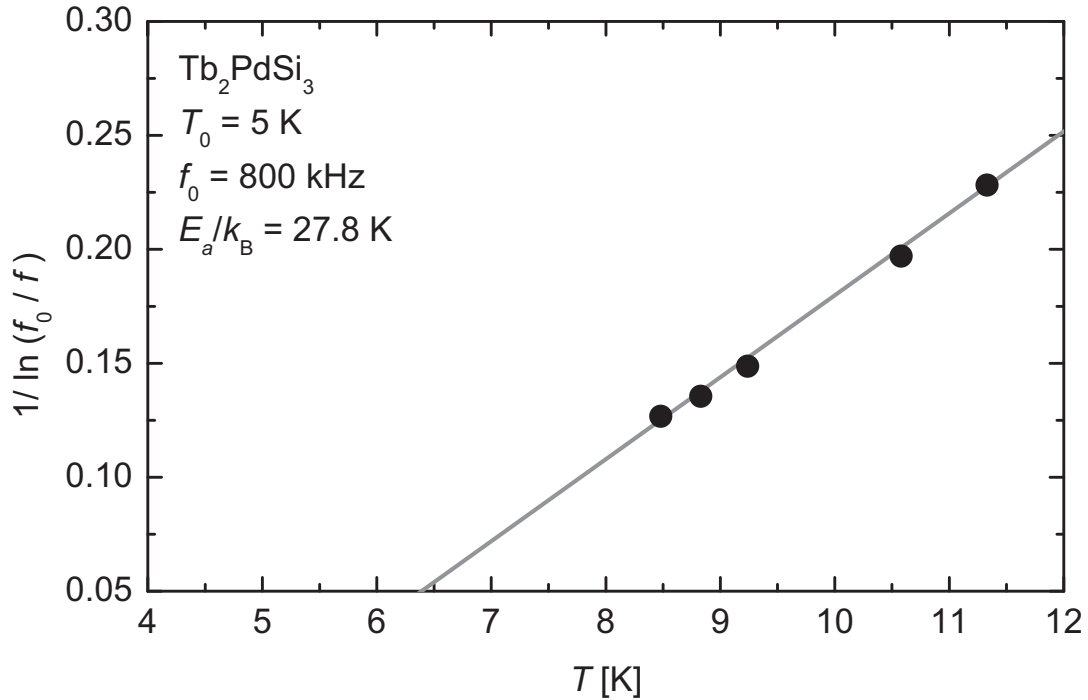


Figure 5.2: Vogel-Fulcher plot for the frequency shift of T_2 found in Tb_2PdSi_3 . The dots are the points from the measurement and the grey line is the fit of the Vogel-Fulcher law with the parameters shown in the figure.

does not show any difference when FC / zero-FC measurements are compared. While true spin-glasses (the term itself is ambiguous, see for instance [Heber1976]) show a comparable behavior the observed temperature shift is in general less pronounced (in the order of 5 % for PtMn alloys or the Perovskites) [Lecomte1982, Motohashi2005]. Furthermore, a spin-glass is characterized by the “randomness” of spin-orientation [Binder1986]. The macroscopic measurements alone cannot decide whether Tb_2PdSi_3 is really a spin-glass or a modified picture has to be applied. A possibility is the occurrence of low-dimensional magnetism as observed in $\text{Ca}_3\text{CoRhO}_6$ [Sampathkumaran2002, Loewenhaupt2003]. This has been proposed also for Tb_2PdSi_3 [Paulose2003]. The origin of the phase transition will be revealed in chapter 5.3 “Neutron diffraction in zero field”. Summarizing the zero field phase transitions of Tb_2PdSi_3 : two phase transitions are found. One is at T_N (23.6 K) and another is around 5 K, in the following referred to as temperature T_2 . The transition at T_2 shows a strong frequency dependence.

5.1.2 Real part of ac-susceptibility in small external fields

Figure 5.3 shows the color coded real and imaginary part of the ac-susceptibility vs. temperature measured in small magnetic fields ranging from 0 to 0.75 T. The black curve is the same zero field curve as already shown in figure 5.1. The application of a magnetic field

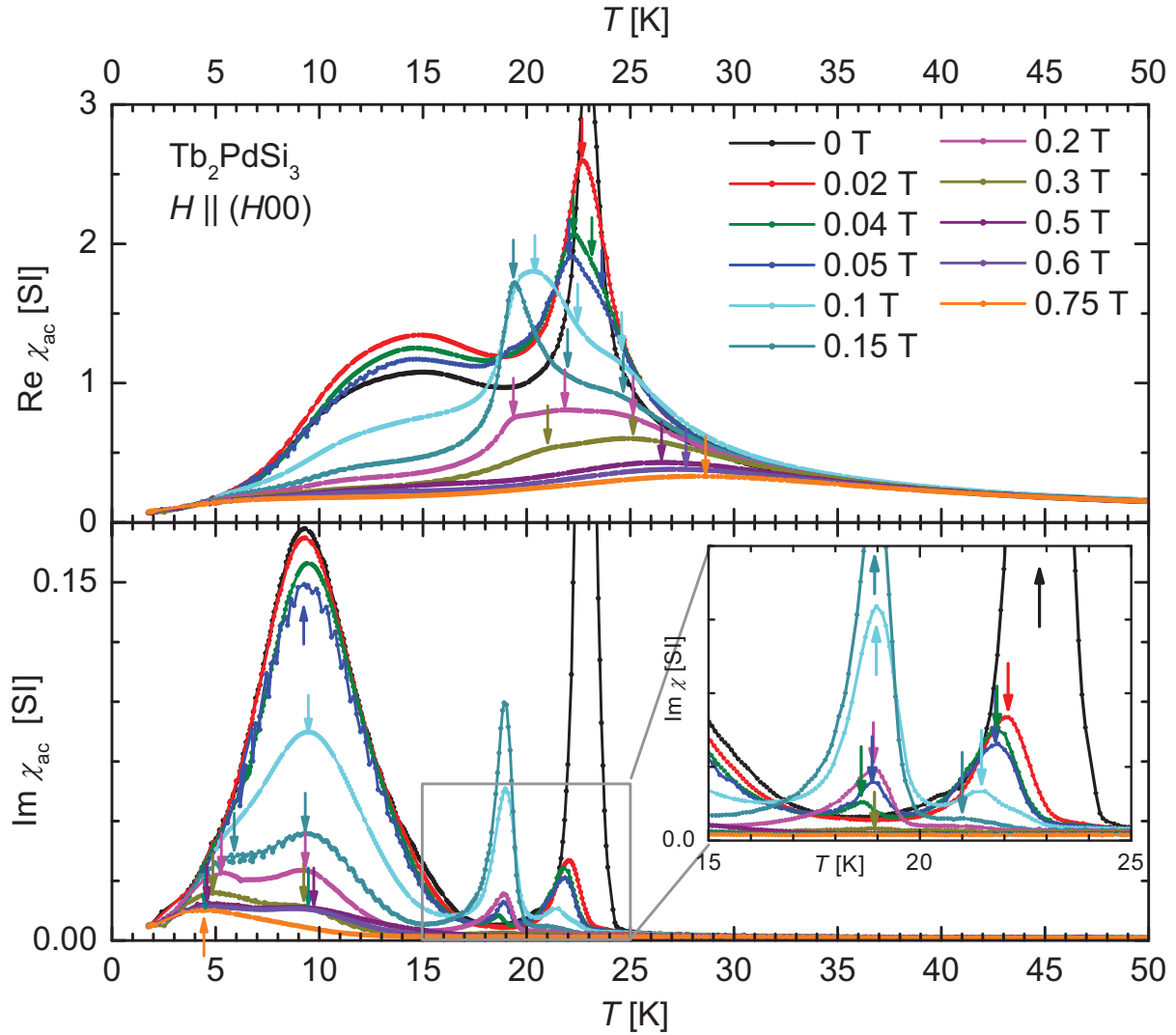


Figure 5.3: Real and imaginary part of the ac-susceptibility of Tb_2PdSi_3 measured at different magnetic fields as indicated in the figure. Arrows indicate points which are discussed in the text. The inset in the imaginary part compares especially the behaviour between zero field measurement and smallest applied field. The ac-frequency is 962 Hz.

of only 0.02 T (red curve) affects the magnitude of the signal. The maximum is now measured at a slightly lower temperature $T_{N'}$. The susceptibility in the vicinity of the phase transition at T_2 behaves similar. This trend holds on until a magnetic field of 0.05 T. The maxima at $T_{N'}$ and T_2 are smaller in magnitude and shifted to lower temperatures. Important to note is that the curve around $T_{N'}$ is broader as the one in zero field. The reason for this broadening becomes clear when the shape of the curve measured at 0.1 T is analyzed. This curve can be best described with altogether four maxima instead of two in zero field: One is found at a temperature near T_2 but now three peaks are found around T_N . One of them appeared at a temperature slightly higher than T_N ($T_F = 24$ K). Moreover, the peak at $T_{N'}$ has split into two maxima around 20 K. Comparing the 0.1 T curve with the measurements at 0.15 T and 0.2 T the interpretation of four maxima can be verified (especially from the measurement at 0.2 T).

The real part of the susceptibility in the field range 0.2 T to 0.75 T is used for the discussion of the trend of the temperature T_F which marks the broad maximum above T_N . This broad maximum has no detectable counterpart in the imaginary susceptibility. Interestingly, T_F increases steadily with increasing applied external field (around 29 K at 0.75 T).

The lower part of figure 5.3 shows the color coded imaginary part correlated to the real part of the susceptibility discussed above. The inset of figure 5.3 shows the enlarged temperature interval from 15 to 25 K. The black curve is again similar to the zero field curve shown in figure 5.1 with two maxima at T_N (exceeding the diagram) and T_2 . In the imaginary part of the ac-susceptibility the magnitude of the signal at T_N' is stronger reduced in small applied fields compared to the real part. The interesting feature of the imaginary part is observed first in the curve of the 0.04 T measurement. Beside the two maxima at T_N' and T_2 another maximum is now found at $T_N'' = 18.5$ K (see arrows in the inset). While increasing the field the maximum at T_N'' changes only slightly in temperature but seems to increase in signal magnitude as the maximum at T_N' decreases. However, at fields higher than 0.15 T the magnitude of the signal at $T_N'' = 18.5$ K also decreases steadily with increasing field. Both maxima are detectable up to a field of 0.6 T around which T_N' is roughly 18.5 K. For higher fields only one maximum around 18.5 K is observed. Above 0.6 T, T_N'' and T_N' merge to one temperature which seems connected to the critical temperature of the zero-field antiferromagnetic structure of Tb₂PdSi₃.

A similar trend is observed (at the position of the maximum) at T_2 . The magnitude of the signal decreases while the magnetic field is increasing. At an external field of 0.15 T the signal at T_2 has decreased considerably while a shoulder at lower temperatures appears. The curve measured at 0.2 T shows that again the single peak at smaller fields in fact consists of two maxima, one at T_2 and one at around $T_2' = 5$ K. With higher magnetic fields the signal of the peak at T_2 decreases further until it is undistinguishable from the background at a magnetic field of 0.75 T. Until then there seems to be no shift in temperature for T_2 . However, the peak at T_2' shifts to lower temperatures with increasing field. This is in contrast to the pair of peaks around T_N where the peak at higher temperature shifts while the one at lower temperature shifts only slightly.

5.1.3 Ac-susceptibility in magnetic fields above 0.75 T

Figure 5.4 shows the real (upper part) and imaginary (lower part) ac-susceptibility in the magnetic field range from 0.75 to 4.5 T. The orange curve measured at 0.75 T is the same as in figure 5.3 drawn here again to link both figures. Again, first the real part of the ac-susceptibility is discussed.

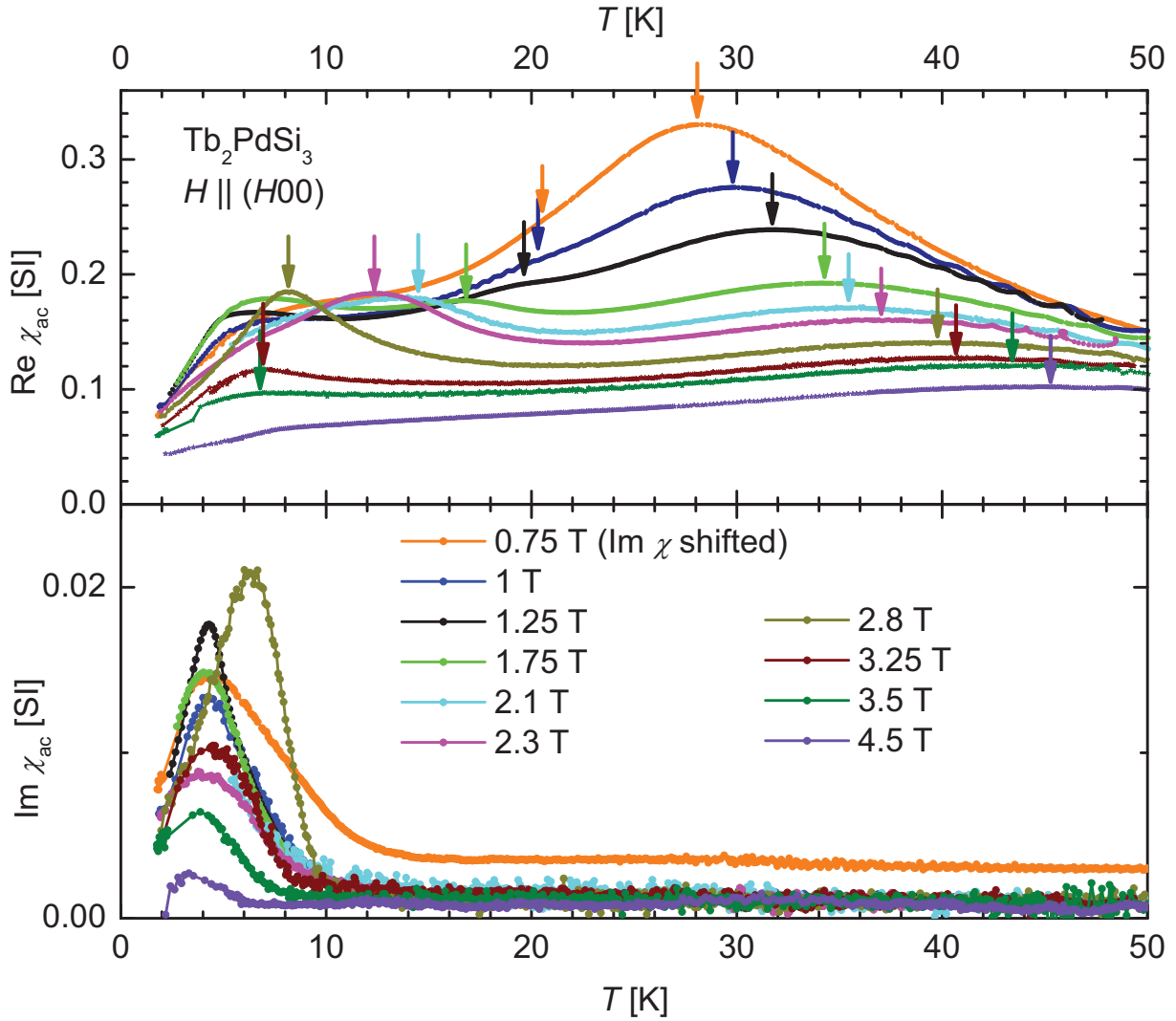


Figure 5.4: Real and imaginary part of the ac-susceptibility of Tb_2PdSi_3 measured at different magnetic fields as quantified in the figure. The orange curve is the same already shown in figure 5.3; the imaginary part of the orange curve has been slightly shifted in y-direction to allow a better comparison to the following curves. Otherwise, no additional shifts are added. Again, arrows indicate points in the measurement discussed in the text.

Two points are marked with arrows: the temperature T_F (28.85 K, 0.75 T) and the temperature $T_{N'}$ (18.5 K, 0.75 T). Both temperatures are continued to be defined as in chapter 5.1.2 as respective maxima of the real part of the susceptibility. Following the trend the increase of the magnetic field is accompanied with an increase of T_F and a decrease of $T_{N'}$. The behavior of T_F with increasing field is easily followed and appears to be nearly linear. The highest determined T_F is approximately 45 K at a magnetic field of 4.5 T. Some curves (especially at external fields 1, 1.25 and 2.3 T) show oscillations of the susceptibility signal at temperatures above 30 K. These originate from an oscillating temperature regulation, but they can be explicitly identified to be non-sample signals, i. e. artifacts.

The $T_{N'}$ transition (around 19 K for 0.75 T), which is also depicted with arrows in figure 5.4 is decreasing with increasing field. While the magnitude of the overall ac-susceptibility

signal decreases with high magnetic fields the signal of the broad maximum assigned to the transition at T_N' seems nearly constant and therefore becomes more and more pronounced up to an external field of 2.8 T. Above 2.8 T (3.25 T) the signal is much smaller. The large reduction of the signal is unexpected for the small increase of magnetic field.

Here, it should be noted that the marked maximum above 2.8 T is possibly not related to the marked maximum in the 2.3 T curve. With the exception of 2.8 T all shown curves can be viewed to be qualitative similar. At low temperatures they show a maximum around 4 K (except 2.8 T). This is related to the maximum attributed to T_2' in chapter 5.1.2 when again the orange curve depicts the connection between figure 5.3 and 5.4. Above 10 K the averaged signal is constant (including 2.8 T), weak and featureless. The magnitude of the signal varies for different fields and only the trend to decrease in magnitude towards the highest measured field (4.5 T) can be noted. However, the curve measured at 2.8 T has the largest signal magnitude (in the maximum) and its temperature position is considerably higher (around 6 K).

5.1.4 Field dependency of the ac-susceptibility measured at selected temperatures

Figure 5.5 shows the real and imaginary part of the ac-susceptibility measured at selected temperatures while varying the external field. The measurements of both real and imaginary part are discussed in direct comparison. The field was swept up to 5 T and back to zero. For temperatures higher than T_2 no hysteresis was observed. Below T_2 the magnetic behavior is hysteretic and moreover time-dependent [Li2003]. The result of a measurement below T_2 can therefore depend on the history of the sample and the time regime of experiment. However, in zero field ac-susceptibility measurements no difference has been found between FC or ZFC sample state.

As seen in the previous chapters the magnitude of the susceptibility decreases rapidly with the application of a magnetic field. Beginning with the measurement at 7.2 K, both real and imaginary part show a small maximum at approximately 0.5 T. The centre of this small maximum is called H_D in the following. This maximum, however, is not detectable at 2.1 K and 4.5 K. Above H_D two maxima are distinguishable up to 14.1 K. The first maximum is centered at 1.46 T at 2.1 K and shifts to higher fields with increasing temperature. The magnetic field connected to this maximum is labeled H_S . The second maximum is hardly seen in the 2.1 K measurement, but clearly for 4.5 K at 2.9 T. This maximum shifts its centre towards lower magnetic fields with increasing temperature and is connected to a critical field H_c . From 14.1 K upwards only one maximum above H_D is seen. This maximum seems to be

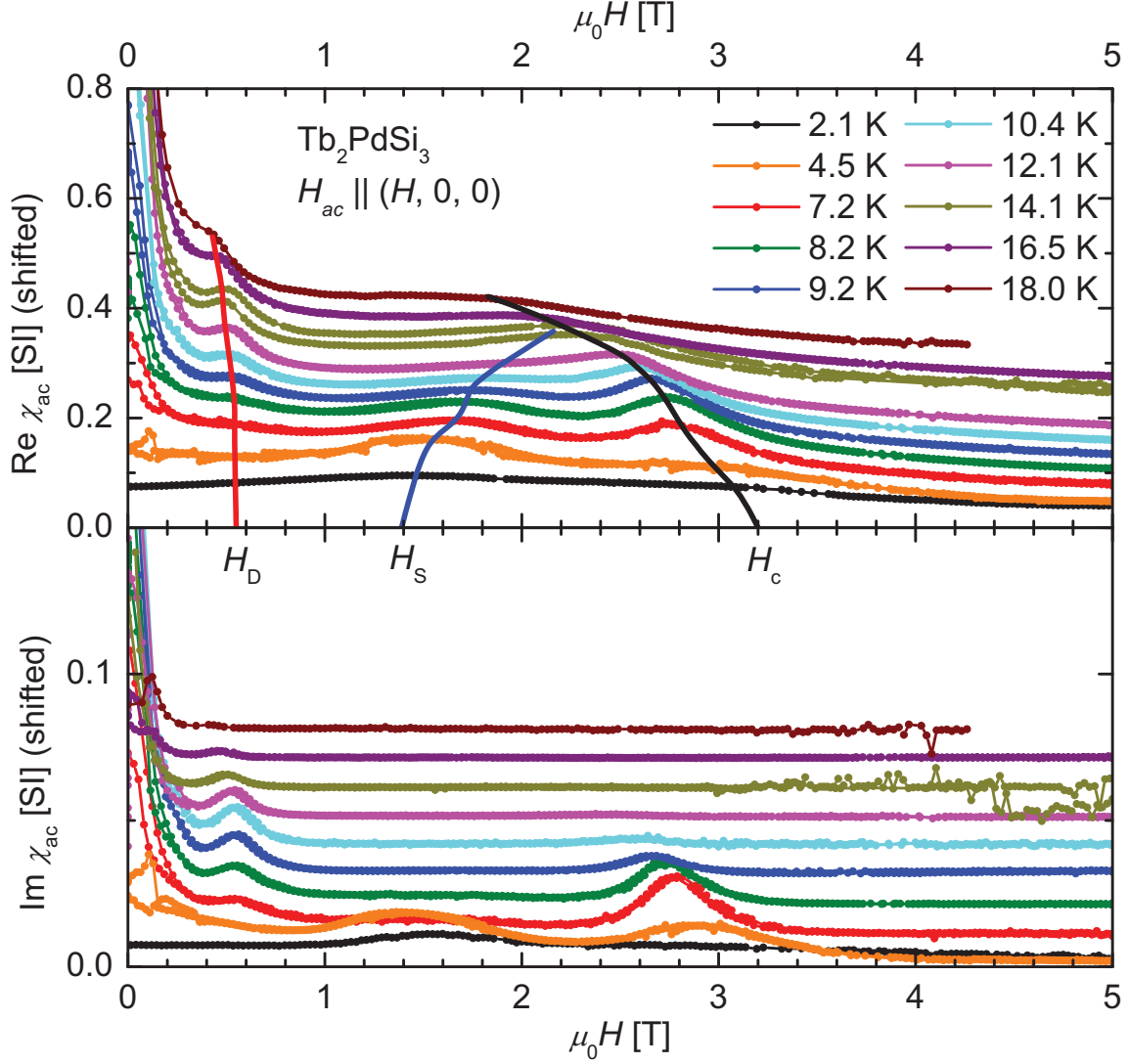


Figure 5.5: Field dependence of real and imaginary part of the ac-susceptibility of Tb_2PdSi_3 measured at different temperatures as indicated in the figure. The curves are slightly shifted with respect to each other (each with $+0.025$ for the real part; $+0.01$ for the imaginary part) for clear arrangement. The lines labelled H_D , H_S and H_C are drawn as guide to the eyes.

connected to H_C rather than H_S . Only the magnitude of the respective maximum in real and imaginary part for the fields H_D , H_S and H_C varies depending on the temperature. Especially, the curves for 2.1 and 4.5 K show a broad maximum at H_S in the imaginary part and a very weak contribution in the real part. The magnitude of the contributions is reversed for the curve measured at 7.1 K where a broad contribution in the real part is opposed to a very weak signal in the imaginary part. The possibility of two distinct effects at H_S and H_C below and above T_2 cannot be fully excluded. But the 4.5 K measurement suggests that the anomaly in both real and imaginary part belongs to the same phenomenon.

5.1.5 Confidence intervals in (T, H) space of the anomalies seen in the ac-susceptibility

The observed maxima in the ac-susceptibility form the base of the phase diagram for Tb_2PdSi_3 . Here, the confidence in the (T, H) position of the observed anomalies is addressed briefly. The errors for the measurements originating from the ac-susceptibility measurement device are small: the error for the magnetic field value is assumed to be negligible; the variance of the temperature is smaller than 0.5 K during the measurements with constant temperature. The temperature dependent measurements have shown a very good reproducibility (less than 0.1 K difference between measurements with identical parameters). The temperature error is therefore estimated to be the same as in the constant temperature scans.

The previous subchapters have emphasized the different anomalies attributed to the temperatures T_N' , T_2 and T_F and the magnetic fields H_D , H_s and H_c . Two of these values, T_F and H_D can easily be identified in the measurements as clear distinguishable maxima on the ac-susceptibility curves. The respective error is limited to the error of the ac-susceptibility measurement. The other characteristic values are identified by broad maxima often positioned as a shoulder on a neighboring maximum. Here, an additional error in position is implied by a shift of the true maximum due to a modulated background. This fact is accounted for with the implementation of an additional value on empirical basis. The error is determined as the 1/4 width of the assumed peak shape (for instance: in figure 5.4 the 1.25 T measurement shows a peak at 19.4 K and the underlying peak shape accounts for an error ± 3.1 K). Additionally, a “frequency shift error” is accounted for in the positions of T_2 and T_2' . The phase diagram has been determined with an ac-frequency of 962 Hz and from extrapolation of T_2 in zero field the “frequency shift error” from 962 Hz to zero is taken as -5 K (only towards lower values). Frequency dependent measurements in a small applied magnetic field (0.2 T) yield the same value. The frequency dependence of T_2' derived from extrapolation on frequency dependent measurements at 0.2 T and 0.75 T are smaller and the underlying “frequency shift error” for T_2' is estimated as -2 K.

5.2 Supporting macroscopic measurements: magnetisation, magnetostriction, resistivity and specific heat

Macroscopic measurements which are regularly used to determine magnetic transitions have been introduced in chapter 1.5. There, in figure 1.1 the magnetization had been compared to the ac-susceptibility. Further magnetization measurements at $T = 2, 4, 16$ and 27 K are shown in Figure 5.6. The grey curve is the measurement started from the virgin

sample state, while the black curve represents the full magnetization loop. At an external field of 10 T the value of the magnetic moment is nearly equal for all temperatures below T_N . The magnetization value for the measurement at $T=27$ K is only slightly smaller.

The shape of the magnetization curves below T_N is similar except for two differences: the

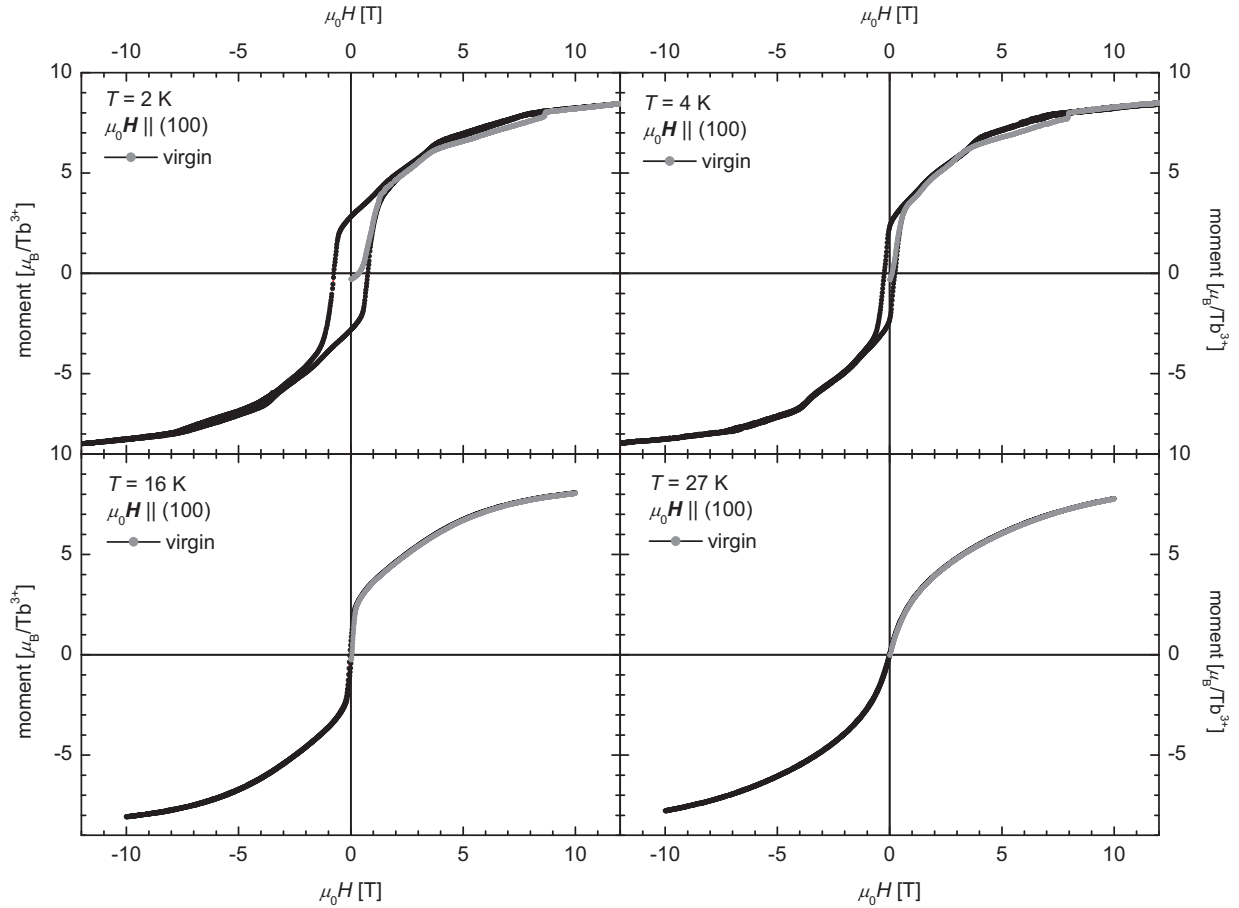


Figure 5.6: Magnetisation curves of Tb_2PdSi_3 with the field applied along the (100) direction. The temperatures are 2 K, 4 K $< T_2 < 16$ K $< T_N < 27$ K. The grey curve is the virgin curve, the black curve is the subsequent 4 segment loop. Both, the hysteresis and the small jump at higher field are vanished above T_2 .

occurrence of a pronounced hysteresis at $T=2$ and 4 K at small fields and a (reproducible) small jump-like anomaly in the virgin-curve at 8.6 and 7.9 T. The jump is probably connected to the critical field of a phase existing below T_2 . Otherwise, the magnetization increases strongly in small fields. The kinks clearly visible at 2 K are smoothed out at higher temperatures.

In chapter 5.1.4, ac-susceptibility data are shown with distinguishable maxima which (taking into account that the susceptibility is the derivative of the magnetization) should also appear as kinks in the magnetization. In contrast to expectations, these kinks are concealed since the sensitivity to magnetic transitions is different between magnetization and ac-

susceptibility. The measured magnetization is dominated by the ferromagnetic component which overlays the small signals of changes in the staggered magnetization of an antiferromagnet. The ac-susceptibility consists of an enveloping function (the derivative of the magnetization), but is still sensitive to the changes of the staggered magnetization of an antiferromagnet. The conclusion of this argument is therefore that the characteristics seen in the ac-susceptibility correspond to transitions from an antiferromagnetic state to another antiferromagnetic state instead of e. g. an antiferromagnetic to ferromagnetic state via a spin-flip process.

Magnetostriction (combining both, magnetostriction via an applied external magnetic field and magnetic contribution to the thermal expansion) had been also measured and is normally viewed as a complementary method to magnetization and ac-susceptibility. However, for the characterization of magnetic transitions a strong magneto-elastic coupling is needed. Also not

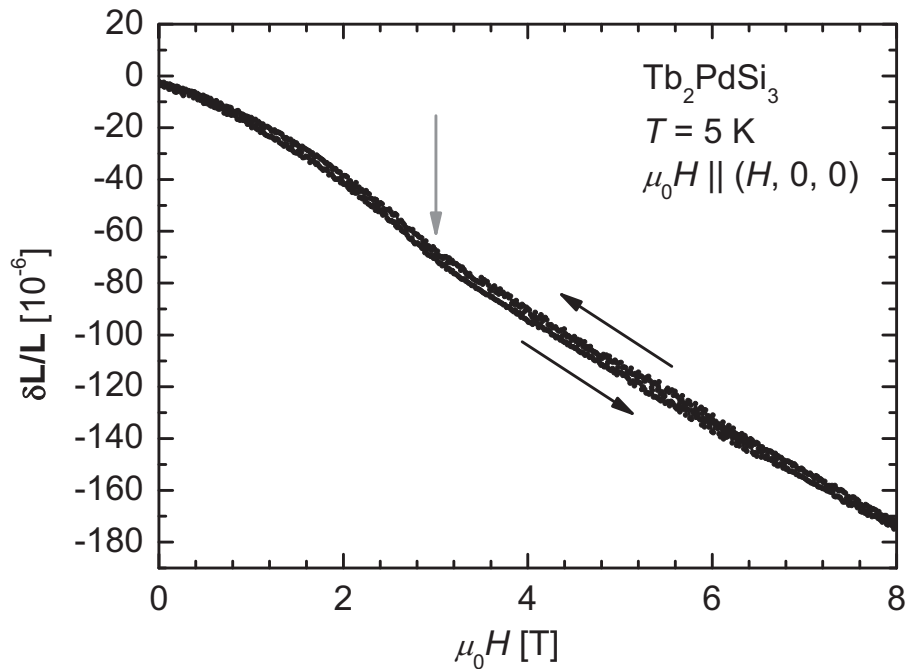


Figure 5.7: Magnetostriction along $(H, 0, 0)$ of single crystalline Tb_2PdSi_3 measured with a magnetic field applied along $(H, 0, 0)$ at $T = 5 \text{ K}$. The direction of the field sweep is indicated. The coefficient of the magnetostriction is negative. The feature observed is marked with a grey arrow and is correlated to H_c .

every transition is accompanied with a strong lattice distortion (e. g. a transition with only the alteration of the propagation vector might not result in a lattice distortion since the averaged forces remain unchanged). A typical magnetostriction measurement for the Tb_2PdSi_3 compound is shown in figure 5.7. Here, the magnetic field is varied at a constant temperature of 5 K. The characteristic points derived from magnetostriction measurements are in good

agreement with the points derived from ac-susceptibility measurements and therefore support the interpretation of the maxima of the susceptibility as points of magnetic phase transitions.

The comparison of magnetization and ac-susceptibility helps to distinguish antiferromagnetic (AFM) to AFM transitions from AFM to ferromagnetic transitions. In the case of Tb_2PdSi_3 all transitions seem to be from an AFM state to a different AFM state with a continuous increase of a ferromagnetic component. The upper critical field H_{c2} had not been observed for Tb_2PdSi_3 and is larger than 14 T.

A measurement of specific heat in zero magnetic field has been made and is shown in figure 5.8. The resulting transition temperatures (from the position of the maxima) are $T_N = 23.12$ K and $T_2 = 4.5$ K. This is noteworthy since the extrapolation of the frequency dependence of T_2 towards zero frequency with the Vogel-Fulcher law yielded a T_2 of 5 K.

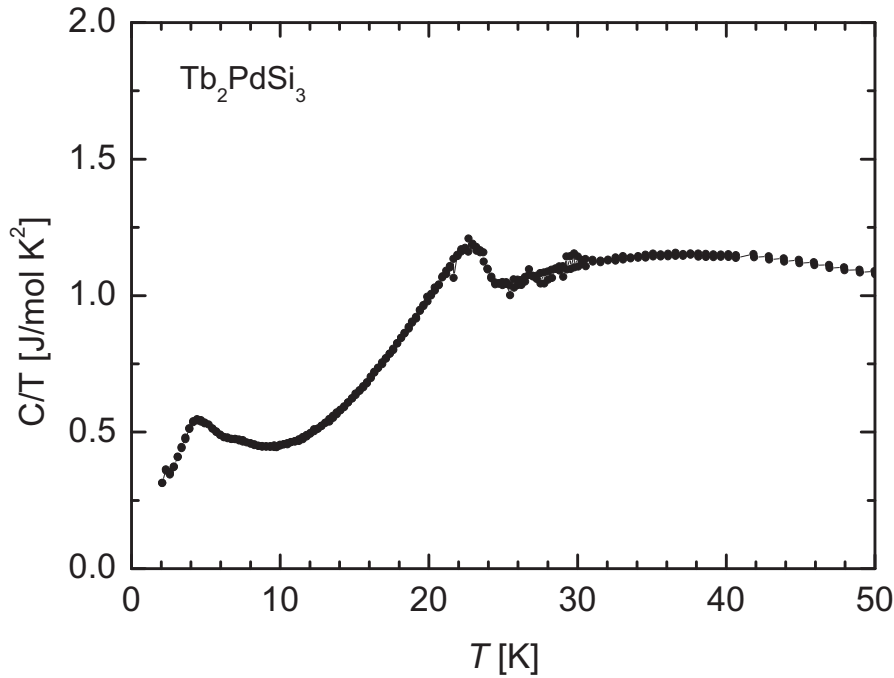


Figure 5.8: Zero field specific heat of single crystalline Tb_2PdSi_3 measured with a PPMS device by courtesy of the Max-Planck-Institute for chemical physics of condensed matter.

5.3 Feature map for Tb_2PdSi_3 derived from the macroscopic measurements

Figure 5.9 shows the feature map compiled from the different macroscopic measurements. The magnetic fields H_D , H_S and H_c as well as T_N and T_2 are marked. The field is limited to 6 T. The measurements of magnetization and magnetostriction in excess of this field range (up to 14 T) did not show signs of an additional phase transition. This means especially that the magnetic field at which Tb_2PdSi_3 is in the ferromagnetic state is higher than 14 T. Linear

extrapolation of the magnetisation crosses the saturation value of $9 \mu_B$ for Tb^{3+} at approximately 20 T for $T = 2$ K.

The feature map consists of all features discussed in the previous chapters. The feature map is extremely rich and several questions arise whether these points are anomalies connected to phase transitions. Are these phase transitions of magnetic nature? And if so, what are the properties of the according magnetic phases? The method to develop the feature map into a magnetic phase diagram is single crystal neutron diffraction in applied magnetic fields. Neutron diffraction will furthermore allow to determine the type of magnetic order, whether it is antiferro- or ferromagnetic and will also yield the magnetic structure. In addition, neutron diffraction yields information about the dimensionality (quasi one-dimensionality was proposed [Paulose2003]) and the correlation lengths of the magnetic structure.

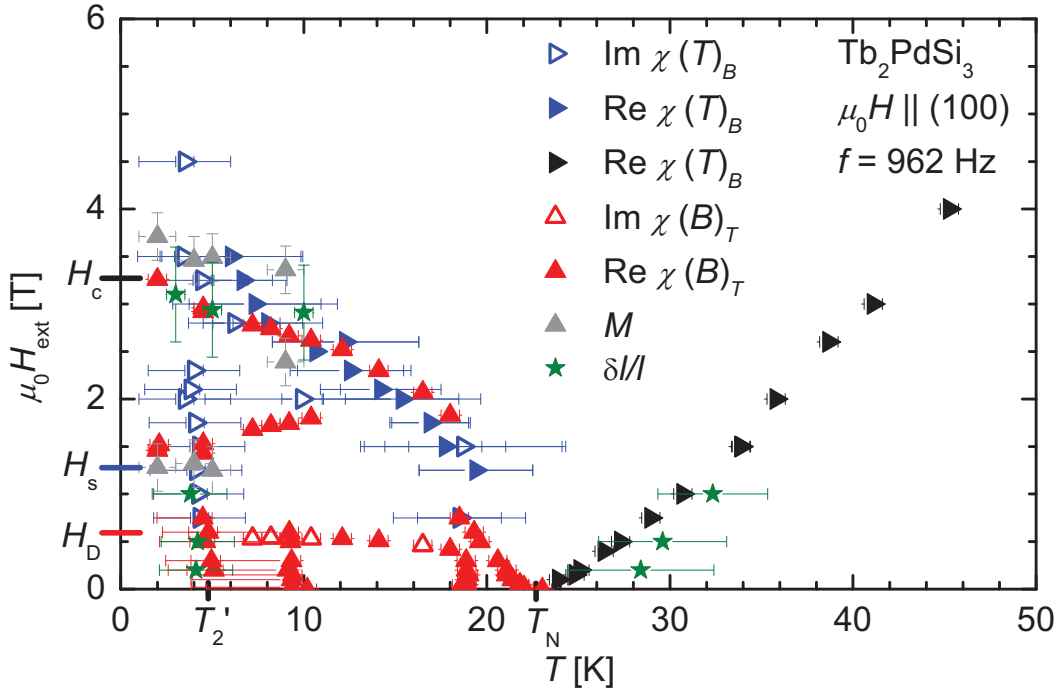


Figure 5.9: Feature map compiled from different macroscopic measurements on Tb_2PdSi_3 for an applied field along the $(H, 0, 0)$ direction. The symbols represent features in the respective measurements (see text). The critical temperatures T_N , T_2 and the critical fields H_D , H_s , H_c are indicated. The black triangular symbols denote anomalies in temperature dependent ac-susceptibility measurements in constant magnetic fields while the red triangular symbols represent field dependent measurements at constant temperature. Open and closed symbols discriminate whether the features are found in the real or the imaginary part of the ac-susceptibility. Additional points taken from magnetostriction measurements depicted as olive coloured stars. Ac-susceptibility data points are from measurements with an ac-frequency of 962 Hz.

5.4 Neutron diffraction in zero magnetic field

5.4.1 Long- and short- range order in Tb_2PdSi_3

A single crystal neutron diffraction measurement always starts with the choice of the scattering plane. In the hexagonal structure three main reciprocal planes exist. These are the $(HK0)$, the (HHL) and the $(H0L)$ planes. Based on the published propagation vector [Szytula1999] and with the hindsight of experiments to follow (e. g. appliance of a magnetic

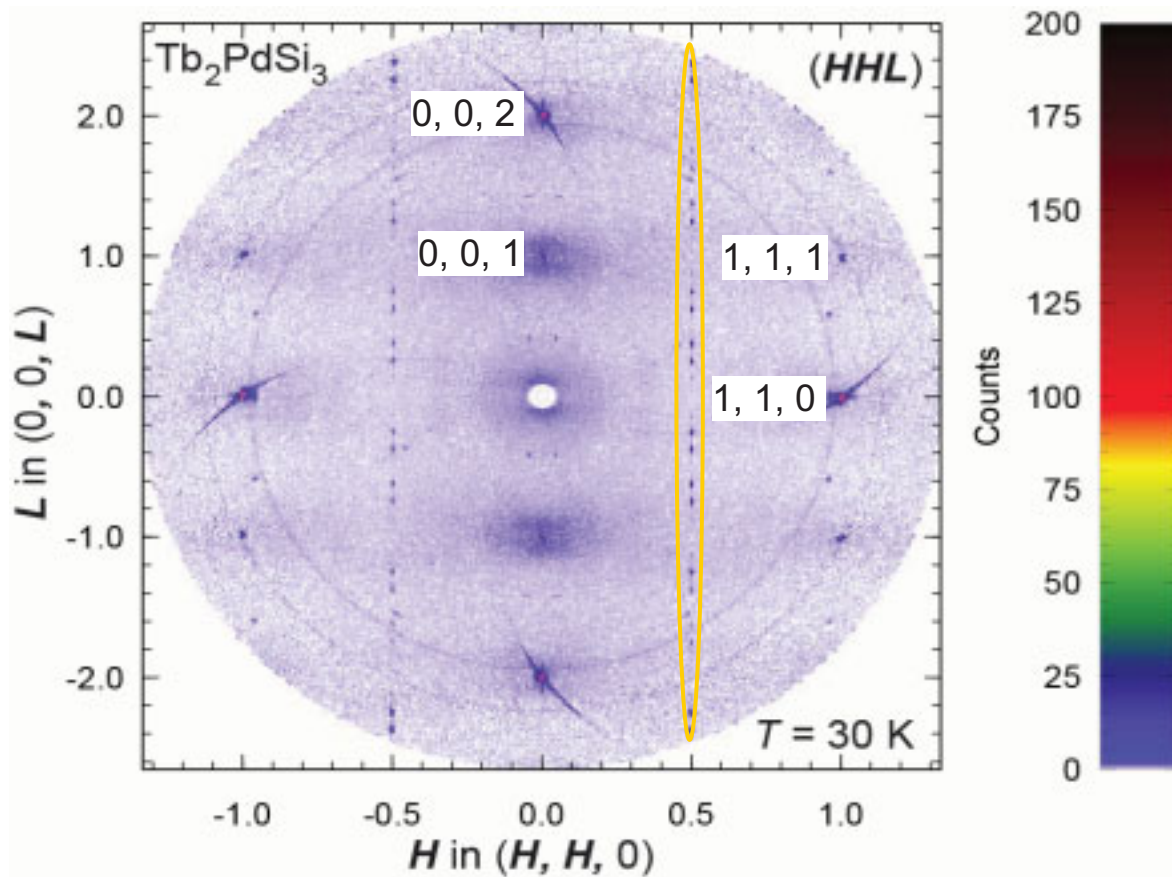


Figure 5.10: Reciprocal (HHL) -plane of Tb_2PdSi_3 above T_N at $T = 30$ K. Reflections due to the AlB_2 -type crystallographic structure are indicated. The reflections due to the crystallographic superstructure are circled exemplarily for $H = 0.5$. The diffuse clouds around the $\{0, 0, 1\}$ indicate ferromagnetic correlations.

field) the reciprocal (HHL) -plane was chosen to begin the investigations on the magnetic structure. Figure 5.10 shows a map of the reciprocal (HHL) -plane measured in zero magnetic field and above T_N (23.6 K) at a temperature of 30 K. 10 nuclear reflections due to the primitive AlB_2 structure $\{0, 0, 1\}$, $\{0, 0, 2\}$, $\{1, 1, 0\}$ and $\{1, 1, 1\}$ are found. The reflections due to the crystallographic superstructure are on $\{0.5, 0.5, n/8\}$ similar to figure 4.1 where the (HHL) -plane of the isostructural Ho_2PdSi_3 is shown. Two rings originate from scattering on polycrystalline aluminum (sample holder, cryostat). Due to the vicinity to T_N magnetic

intensity is found also as broad diffuse intensity around the origin and $\{0, 0, 1\}$. This indicates strong ferromagnetic (FM) correlations above T_N .

Figure 5.11 shows the same reciprocal plane as figure 5.10 but at $T = 50$ mK. The reflections described by the primitive AlB_2 are still visible while the nuclear intensity from the superstructure is masked by intensity from magnetic scattering.

The green circles mark magnetic intensity due to short range antiferromagnetic correlations (SRC). The position of the SRC is $1/6$ and $2/6$ along the $(H, H, 0)$ direction, while it is $1/16$

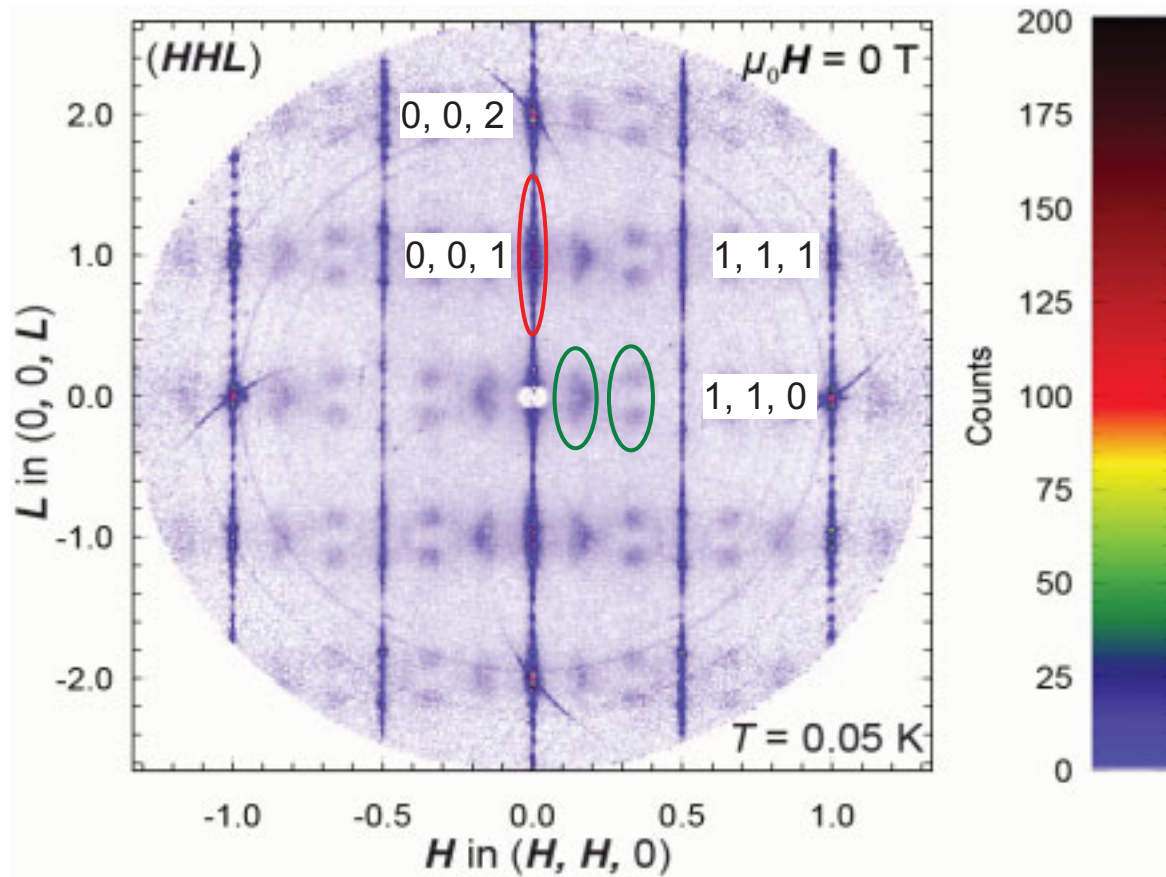


Figure 5.11: full reciprocal (HHL) -plane of Tb_2PdSi_3 at $T = 50$ mK. Reflections due to the AlB_2 -type crystallographic structure are indicated. Further reflections are of magnetic origin. Green circles mark magnetic intensity due to SRC (see text). The red circle marks the section shown in figure 5.12.

and $2/16$ along $(0, 0, L)$ assuming four magnetic reflections in the two marked circles. Figure 5.12 shows the integrated magnetic intensity due to SRC measured at three different temperatures. At the lowest temperature ($T = 3$ K) a broad peak is observed centered at approximately 12° in 2θ . This value complies with the position $(1/6, 1/6, 0)$ in reciprocal space. The intensity on this position decreases with increasing temperature up to 14 K. However, at higher temperatures magnetic intensity due to a fluctuating ferromagnetic moment component is measured near the position of the SRC. As shown in figure 5.10, the

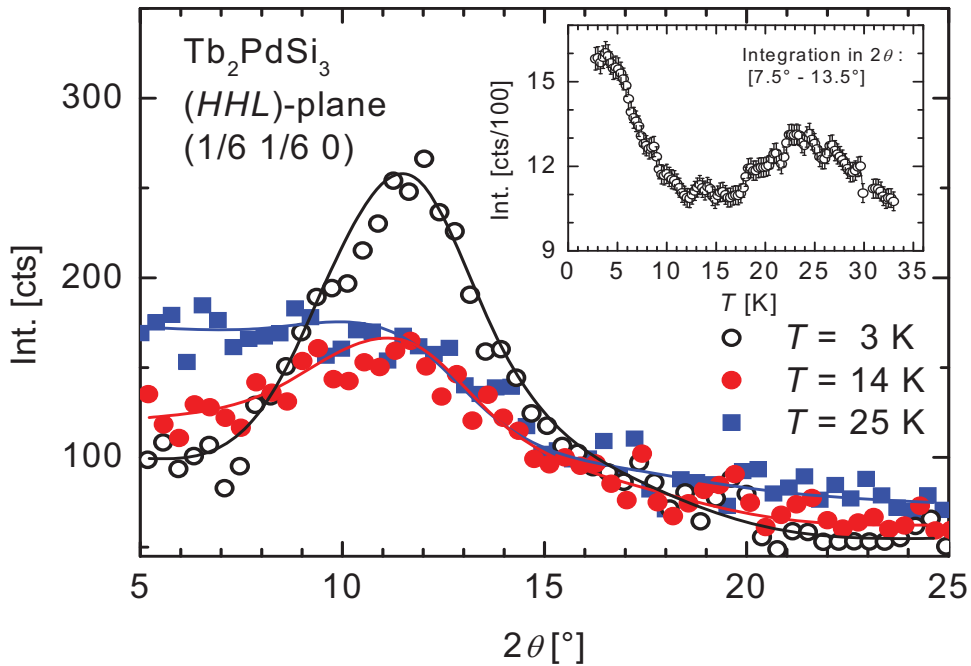


Figure 5.12: Intensity measured on a sample position corresponding to $\mathbf{Q} = (1/6, 1/6, 0)$. Magnetic intensity due to SRC at three different temperatures. The lines are guide to the eyes. The integrated raw data are shown in the inset.

diffuse FM intensity is observed mainly around the origin and the $\{0, 0, 1\}$ reflections. The integrated intensity ($2\theta = 7.5^\circ$ to 13.5°) for the temperature range from 2 K to 33 K is shown in the inset. The FM intensity becomes distinguishable from the background from temperatures larger than 14 K. The FM intensity has a maximum of intensity at T_N .

The temperature dependence of the antiferromagnetic SRC (position $(1/6, 1/6, 0)$) is characterized by the saturation of intensity at a temperature of $T \approx 5$ K. This correlates well with the temperature T_2 . The phase transition exhibiting spin-glass like behaviour at T_2 is therefore connected to the formation of SRC.

Magnetic intensity due to a long range ordered antiferromagnetic (LRO) phase is found at positions $(m/2, 0, n/16)$ and $(m/2, m/2, n/16)$ with $m = 0, 1, 2, \dots$ and n being an odd integer. In figure 5.11 the red circle selects a part of the LRO intensity which is shown in figure 5.13 as section from $(0, 0, 0.5)$ to $(0, 0, 1.5)$. This section shows the antiferromagnetic satellites originating from the nuclear $(0, 0, 1)$ reflection. The position of the reflections is $(0, 0, 1 \pm n/16)$. The magnetic unit cell is therefore four (2×2) times as big in the basal plane and sixteen times as big along the $(0, 0, L)$ -direction compared to the primitive chemical unit cell. The intensity relation between the different harmonics corresponds to a squared-up modulation of the magnetic moments along the $(0, 0, L)$ -direction as shown in the inset of figure 5.13. In agreement with the magnetization measurements, the intensity distribution

indicates an alignment of the magnetic moments mostly within the basal plane. The comparison of intensities corrected by the magnetic form factor [IntTablesCrystC2006] from different reciprocal lattice points gives a ratio which should be proportional to the square sine of the angle formed by the scattering vector and the magnetic moment direction. However, this ratio does not yield a definite magnetic moment direction. This is most probably due to effects of extinction when intensities for small and high Q values are compared. When intensities for relatively high Q values ($0, 0, 0 + \tau$ and $1, 1, 0 + \tau$) are compared the magnetic moment direction seems to have a small $(0, 0, L)$ -component of about 2° . A long-range ordered ferromagnetic component is not observed (if the 30 K spectra is subtracted no intensity is left on the nuclear-positions).

The magnetic unit cell contains 4 magnetic Tb^{3+} -ions in the basal plane (on the $3f$ and the

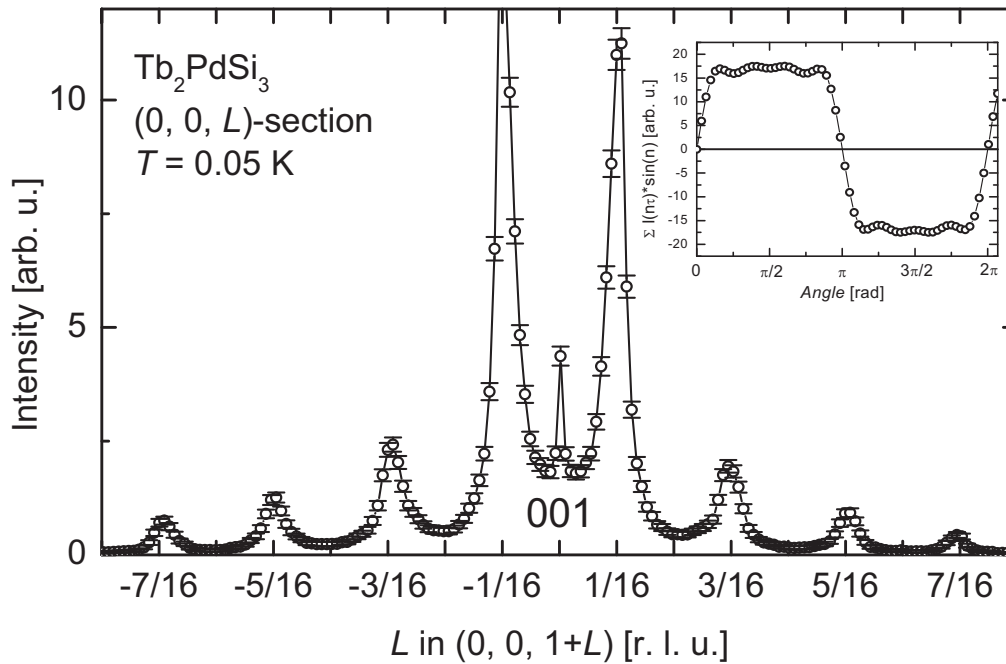


Figure 5.13: Section along $(0, 0, L)$ as indicated by the red circle in figure 5.11. The magnetic reflections are on commensurate $1/16$ positions. The nuclear $0, 0, 1$ is marked. The inset shows the Fourier-transform of the intensity of the magnetic satellites from $-7/16$ to $-1/16$.

$1a$ site in the $P6/mmm$ space group). The doubled unit cell in the basal plane is preset by the crystallographic superstructure. For the description of the magnetic structure it is advantageous to use the doubled unit cell and define the magnetic propagation vector as $\tau = (0, 0, 1/16)$. This allows to be consistent with the definition of the higher harmonics of the propagation vector i. e. the $n*\tau$ are found on $(0, 0, \pm n/16)$ originating from the reciprocal lattice positions of the doubled unit cell. Furthermore, from the opposite viewpoint a

propagation vector of $(m/2, m/2, n/16)$ cannot describe the positions of magnetic intensity along $(0, 0, L)$ without the introduction of reciprocal lattice points at $(0.5, 0.5, 0)$ positions. The definition of the propagation vector $\tau = (0, 0, 1/16)$ is unusual since the indexing of the magnetic reflections uses the doubled basal plane. However, for the discussion of the magnetic structure in zero field and also in applied external magnetic field in a later chapter only the above defined propagation vector needs to be considered. Magnetic intensity is observed also on reciprocal lattice positions $(m/2, 0, n/16)$ describable nearly with the propagation vector given by Szytula et al. [Szytula1999]. These reflections are described also with the definition above. Otherwise a second propagation vector would have to be introduced. The descriptions of the magnetic structure for some of the other $R_2\text{PdSi}_3$ use the primitive chemical unit cell alone (as already shown in chapter 3 for Gd_2PdSi_3). The magnetic structure of the Tb_2PdSi_3 compound, however, cannot be understood without the four times enlarged basal plane unit cell.

The temperature dependence of the normalized magnetic intensity due to the LRO is displayed in figure 5.14. In contrast to the SRC, the characteristic temperature of the LRO is $T_N = 23$ K for all harmonics of the propagation vector. Furthermore, the normalized intensities of all harmonics of the propagation vector show within their respective error the same temperature dependence. This indicates a complete squared-up LRO magnetic structure in the

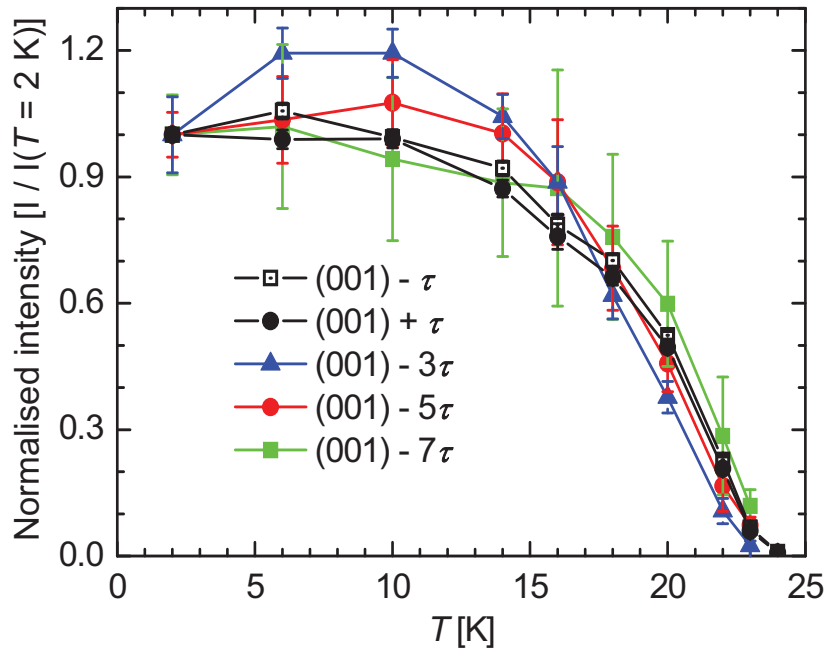


Figure 5.14: Normalized intensity of the different harmonics of the propagation vector of the magnetic LRO in Tb_2PdSi_3 .

whole temperature range below T_N . The squaring-up process is classified to either be progressive or discontinuous [Gignoux1991]. The squaring-up process found in Tb_2PdSi_3 is not progressive but discontinuous. Normally, the discontinuous squaring-up process is observed as a second transition in the magnetic ordered state as for example in DyGa_2 [Gignoux1991]. The coincidence of ordering and discontinuous squaring-up cannot be found for any other example than Tb_2PdSi_3 .

5.4.2 Additional observations leading to a magnetic structure proposal

Comparing the magnetic intensities, the reciprocal ($H0L$) plane looks similar to the (HHL) plane in the ordered state. The magnetic reflections are describable with a propagation vector $\tau = (0, 0, 1/16)$ and the enlarged basal plane as shown for the (HHL) plane. The comparison between the reciprocal (HHL) and ($H0L$) plane assumes their intensity along $(0, 0, L)$ is equal in all measurements. Therefore, intensities of different measurements (i. e. data acquired in 5 years) are normalized so that the intensity along $(0, 0, L)$ is equal. The first experiment in 2002 in a standard orange cryostat is defined as standard.

The LRO magnetic intensity along $(1, 0, L)$ is larger than the LRO magnetic intensity along $(1, 1, L)$. The averaged ratio between 20 corresponding magnetic reflections is 1.4 ± 0.3 . This indicates the in-plane magnetic moment direction to be between $(H, H, 0)$ and $(H, 0, 0)$ rather than along one of these directions. This statement assumes an equal domain distribution. The reflections are only comparable if this is true. With the further constraint that the sum of the angle is 30° , the magnetic moment angle is 13.7° to $(H, H, 0)$.

Sections along $(0.5, 0, L)$ and $(0.5, 0.5, L)$ show a similar ratio of the magnetic intensity for the corresponding magnetic reflections. Compared to the sections along $(1, 0, L)$ and $(1, 1, L)$, a strong difference has to be noted: In the $(0.5, 0, L)$ and $(0.5, 0.5, L)$ sections the 3τ reflection is the strongest. This indicates a modification of the squared-up arrangement. Furthermore, in the $(0.5, 0, L)$ section the 7th harmonic cannot be observed at low values of L but only at higher. Along $(0.5, 0.5, L)$ section this behavior seems to be reversed. Together, this indicates a different spin-sequence for the Tb^{3+} ions on the $3f$ and the $1a$ sites.

A long range ordered ferromagnetic component would add intensity on a nuclear Bragg peak depending on the angle between scattering vector and magnetic moment direction. For example consider a ferromagnetic component along $(0, 0, L)$ which would increase the measured intensity on $\{1, 0, 0\}$, $\{1, 1, 0\}$ and $\{1, 0, 1\}$ reflections but not on the $\{0, 0, 1\}$ reflection. To conveniently identify a ferromagnetic component difference spectra are used. A measurement above 30 K is subtracted from a measurement in the ordered state. This had

been done for the reflections mentioned in the example above. No significant intensity for the difference on the $\{1, 0, 0\}$, $\{1, 1, 0\}$ and $\{1, 0, 1\}$ reflections is observed and this leads to the conclusion that a long range ordered ferromagnetic component is absent.

5.4.3 Comment on the published magnetic structure

So what evolves from these findings: a direct calculation and subsequent comparison of the spectra with a program like FullProf [FullProf2001] is in principle possible and could be used to verify magnetic structure proposals. These refinement procedures are often used to process powder measurements. The attempt of magnetic structure determination with a powder measurement was made already by Szytula et al. [Szytula1999]. In the following it is shortly described how the refinement of the magnetic structure from the powder data could lead to a wrong magnetic structure proposal. Szytula et al. proposed a two phase structure consisting to 75 % of an incommensurate spiral with a propagation vector $\tau = (0.486, 0, 0.174)$ and a magnetic moment along the $(0, 0, L)$ direction (which was not in agreement with magnetization measurements as already stated with the first measurements after the availability of single crystals [Bitterlich2001]). The remaining 25 % were contributed to a spin-glass component assigned to broad reflections in the spectrum. For both phases the critical temperature is T_N . This structure proposal is the result of a magnetic refinement calculation. Although the whole spectrum is refined the model is apparently based on one main observation. This particular observation is the strong increase of the intensity of the $1, 0, 0$ and $1, 0, 1$ reflection below T_N in the powder data. This observation is the best one to distinguish between ordered and disordered state in the powder data. It is best described with an ordered ferromagnetic component with the moment direction along $(0, 0, L)$. The single crystal data (see figure 5.13) however show the gain of intensity to be due to the antiferromagnetic satellites. The magnetic reflections $1, 0, 0 \pm \tau$ and $1, 0, 1 \pm \tau$ are on nearly the same 2θ position as the nuclear $1, 0, 0$ and $1, 0, 1$ reflection. These satellites can therefore not be separated from the nuclear reflection in powder data.

5.4.4 Heuristic magnetic structure model for Tb_2PdSi_3 - ansatz

In order to generate a heuristic magnetic structure model from the scratch it is important to rule out the simple models which are NOT in agreement with the experimental data. In the following a heuristic approach on the magnetic structure modeling of Tb_2PdSi_3 is described. This model is expected to reproduce the main observations of single crystal magnetic neutron

scattering. No LRO ferromagnetic intensity is found below T_N and magnetic reflections due to a LRO are observed on reciprocal lattice positions $(m/2, m/2, n/16)$ with $m = 0, 1, 2, \dots$ and $n = 1, 3, 5, \dots$. For even values of m the relative intensities of the higher harmonics (i. e. values of n) correspond to a squared-up modulation. For the odd values of m the highest intensity is found for $n = 3$ but still all higher harmonics (up to 7th order) are present.

The calculation of magnetic intensities was performed using IC-POWLS [ICPWMan]. This program is capable of calculating magnetic intensities also from very large magnetic unit cells. The calculation includes the Lorentz factor. Further corrections have not been considered. In general, additional corrections would include the Debye-Waller factor, extinction and absorption correction. In the case of Tb_2PdSi_3 the absorption is relatively small [NeutronData2002]. The extinction correction can either be measured (which had not been done) or calculated (which is difficult for an irregular shaped sample). The measurements on the Tb_2PdSi_3 single crystal had shown that the FWHM of the crystallographic reflections is large enough to justify the neglect of an extinction correction. Finally, the Debye-Waller factor had not been considered to be of large impact due to the low temperatures at which the measurement was performed. Technically, IC-POWLS also includes a fitting routine to optimize parameters. These parameters include moment direction, moment magnitude and the (incommensurate) propagation vector. These parameters, however, are of less importance in the case of Tb_2PdSi_3 . The magnetic moment magnitude is assumed to be constant since the observed squared-up structure normally only occurs in a fully ordered moment structure. The most interesting question is the spin sequence of the magnetic atoms. The spin sequence hereby denotes the direction of the magnetic moment in respect to the magnetic starting atom. These spin sequences had to be guessed anyway. The problem is the large magnetic unit cell with two different magnetic atoms (the four times cell) resulting in a spin sequence for 64 magnetic atoms. The magnetic structure model is partly the product of guesswork (spin-sequence) and parts of optimization. Once a successful spin sequence had been found, the parameters for optimization left were magnetic moment magnitude and magnetic moment direction.

A known problem of the proposed magnetic model for the LRO structure is: it will be wrong. The above described SRC is supposed to be composed of the same magnetic atoms as the LRO structure. No evidence for a phase separation is found in the experimental data. Strongest evidence is the same periodicity along the $(0, 0, L)$ direction e. g. $1/16$. Therefore, the SRC are supposed to arise from frustrated magnetic moments within the LRO structure. The occurrence of the second order of the magnetic intensity due to SRC is sign that more

than one magnetic moment within the arrangement in the LRO structure has a degree of freedom and is forming the SRC magnetic intensity. Two possibilities had been considered but both were rejected. First, in a direct approach the magnetic unit cell would be further enlarged with the additional factor nine (three times three) in the basal plane. The subsequent problem to calculate with spin sequences for 576(!) magnetic atoms had been deemed impossible with the used program. Aside the experiment yielded around 40 independent magnetic reflections (including the ones due to SRC) and the model is already under-determined. The second possibility is to limit the influence of the SRC on the LRO to only a reduction of the magnetic moment. Then a decreased value of the magnetic moment over the spin sequence of the LRO for all included magnetic atoms is taken into account. The magnetic moment in the proposed structure is close to the full magnetic moment and the magnetic moment decrease is within the experimental error.

5.4.5 Heuristic magnetic structure model for Tb_2PdSi_3 - result

The model uses the four magnetic Tb^{3+} ions on the $3f$ and $1a$ sites. On both sites the Tb^{3+} has a moment of $9\mu_B$. The spin-sequence for the ions on the $3f$ site is a square function 8 times "+" followed by 8 times "-". The moment direction is along $(H, H, 0)$. The magnetic moment at $1a$ uses the slightly different spin-sequence of ++----+---++++-- which results in the $3/8$ reflection appearing stronger than the $1/8$ reflection along the $(0.5, 0.5, L)$ and $(0.5, 0, L)$ section. The best agreement with the experimental data has this moment pointing along the $(-H, 0, 0)$ direction (120° to the $3f$). The magnetic moment direction of this specific ion provokes only slight changes in the relative intensity.

The described model is compared with the measured data in table 4. It has two strong points. First, it describes successfully the extinction rules applied. Second, the overall trend of the relative intensity is given correctly.

Some discrepancies between calculated and observed intensities remain. These are attributed to the incompatibility of the LRO-model and the SRC as well as unequal domain population and effects of an irregular shaped sample. Furthermore, no correction for absorption or extinction effects had been made.

For a quantitative comparison of the model with the experiment the angular space of (HOL) and (HHL) plane was overlaid and summed up over the angle ω (180°). The "powderized" single crystal data is shown in figure 5.15. The result includes all magnetic reflections up to

H	K	L	$n\tau$	I_{calc}	I_{obs}
0	0	0	3	26526	26969
0	0	0	5	7054	8275
0	0	0	7	3634	2676
0	0	1	-7	2783	2408
1	0	0	-1	6076	4178
1	0	0	-3	7382	15102
1	0	0	-5	3388	2113
0	0	1	-5	3066	4058
0	0	1	-3	5690	8005
1	0	1	-5	3075	1580
0	0	1	-1	39612	27597
1	0	1	-3	6380	8072
1	1	0	-1	3244	242
1	1	0	-3	3860	438
1	1	0	-5	1751	299
0	0	1	1	34038	23686
1	0	1	-1	4972	3052
2	0	0	-1	30605	8099
2	0	0	-3	3747	1682
0	0	1	3	3596	4113
2	0	0	-5	1693	875
1	0	1	1	4535	3094
1	1	1	-5	1765	520
2	0	0	-7	1248	460
2	0	1	-7	1254	442
1	1	1	-3	3865	2736
0	0	1	5	1407	1722
1	0	1	3	4848	6177
2	0	1	-5	1713	1214
1	1	1	-1	3171	1028
2	0	1	-3	3783	2631
1	0	1	5	1965	950
0	0	1	7	906	615
1	1	1	1	3033	1041
2	0	1	-1	30395	8273

Table 4: Comparison of measured and calculated magnetic intensity with the model described in the text. The intensity is scaled to match the nuclear 2, 2, 0 and 0, 0, 2 reflections. The description is in the $(2a, 2a, c)$ unit cell.

$2\theta \approx 53^\circ$ for the propagation vector τ . Above this angle, additional magnetic satellites from reciprocal lattice points, which are neither in the (HOL) nor in the (HHL) plane are observed. The “reflection” around 1.5° is parasitic intensity from the incident beam. Especially at small scattering angles the model is in excellent agreement with the measurement. The main discrepancies are found for $2\theta \approx 20^\circ, 52^\circ$ and 55° . The corresponding magnetic reflections are $\{0.5, 0, 0 -3\tau\}$ for 20° , $\{1, 0, 1 -1\tau\}$ and $\{0.5, 0.5, 1 +1\tau\}$ for 52° and among some minor

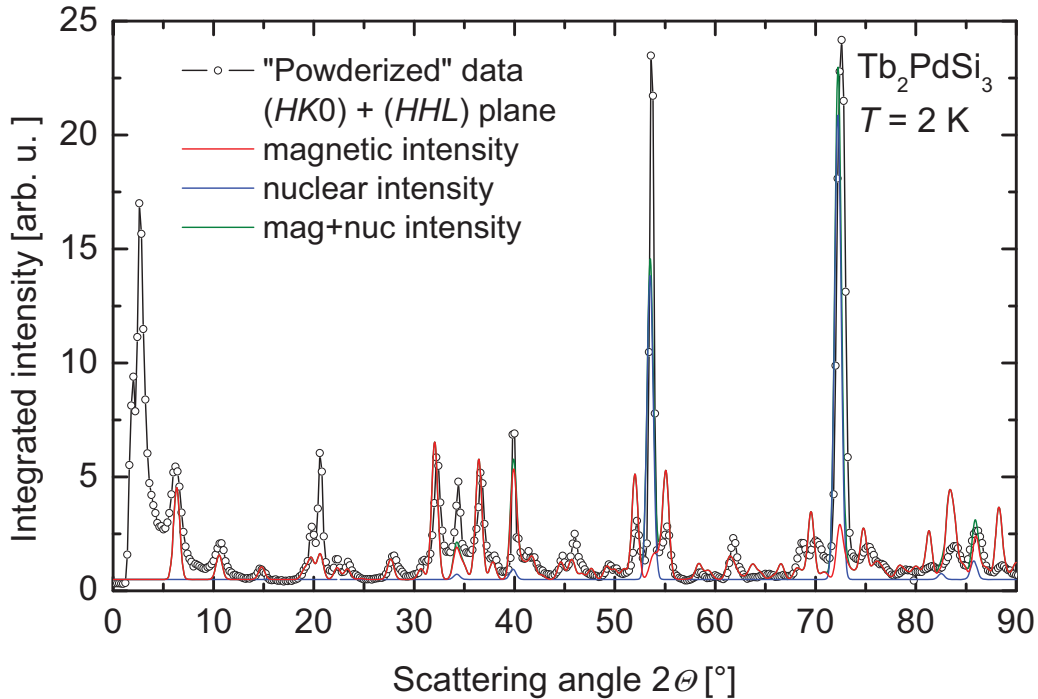


Figure 5.15: “Powderized“ diffraction data of the Tb_2PdSi_3 single crystal measurement (black). Plotted as red, blue and yellow lines are the calculated intensities from the magnetic structure model. Above 53° magnetic intensities from other reciprocal planes is included.

reflections the $\{1, 0, 1 + 1\tau\}$ for 55° . The disagreements cannot be fully explained by the presented magnetic structure model. The main reason for the disagreement and the shortcoming of the magnetic structure model is to be found in the coexistence of the LRO with the SRC. The presented model is in excellent agreement for the low Q values where the magnetic structure is determined by the squared-up modulation of the magnetic atoms on the $3f$ site. The disorder which is brought about by the crystallographic superstructure is packed altogether into the magnetic moment on the $1a$ site (with its spin-sequence). It has been mentioned that the magnetic ions sequence along the c -direction change in the respective site-symmetry. The magnetic structure model does not account for this in an appropriate way, but with the auxiliary spin sequence for the magnetic ion on the $1a$ site. The justification for this approach is the excellent agreement for low Q values, the good prediction of relative intensities and the correct extension rules.

5.5 Neutron diffraction in magnetic fields – multiple magnetic phase transitions

In chapter 5.3 the phase diagram or feature map has been shown (figure 5.9). In chapter 5.4 the zero field magnetic structure below T_N and T_2 has been discussed and a possible spin arrangement to explain the magnetic intensity due to the LRO phase has been presented. The nature of T_2 has been identified as the occurrence of SRC. In this chapter the results of

magnetic neutron diffraction in applied magnetic fields are discussed. Outlining the approach, first the development of the LRO structure with a field applied along the $(H, 0, 0)$ direction at $T = 2$ K based on the full reciprocal (HHL) -planes is traced. Then the behavior of the SRC in magnetic fields is discussed, again making most use of the full reciprocal (HHL) planes. After the discussion of these experiments and the explanation of the peculiarity of each magnetic phase, additional experiments from PANDA at higher temperatures are presented to understand also the high temperature phases in the magnetic phase diagram. In the case of measurements on the development of the SRC in magnetic field the diffractograms from PANDA are best understood with the cross reference to the full reciprocal maps from E2.

5.5.1 LRO coexistence of two phases in applied magnetic fields

Figure 5.16 shows the $(0, 0, L)$ section (with L from 1 to 2) in magnetic fields at $T = 2$ K. This figure elucidates the development of the LRO in dependence of magnetic fields. The black curve is the section in zero field which may be compared to the curve shown in figure 5.11. Here, the section is centered between the nuclear $0, 0, 1$ and $0, 0, 2$ reflection. In zero field, the magnetic reflections are on the $n/16$ positions where n is an odd integer (highlighted

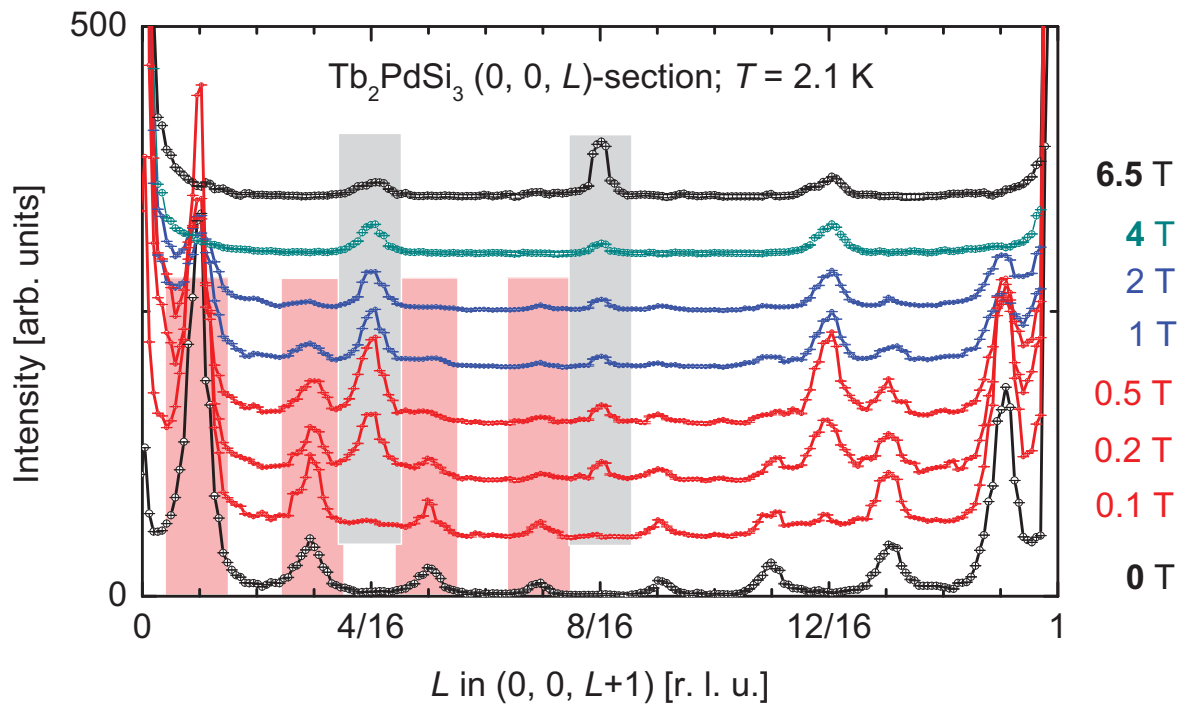


Figure 5.16: Sections along $(0, 0, L)$ from the $0, 0, 1$ to the $0, 0, 2$ reflection. The according magnetic fields are indicated on the right hand side of the figure. The reflections $0, 0, 1 + n\tau$ for $(n = 1, 3, 5, 7)$ belonging to the zero field antiferromagnetic structure are highlighted in salmon while the reflections characteristic for the FiM phase (see text) are highlighted in grey.

with a salmon background in figure 5.16). With the application of a small magnetic field of 0.1 T additional (weak) magnetic reflections on positions $4/16 = 1/4$ (also on $12/16$) and $8/16 = 1/2$ appear (highlighted in grey). The magnetic intensity on these positions is increasing with increasing magnetic field while the zero field intensities are decreasing rapidly. This field range extends up to $H_D = 0.5$ T. Above H_D the relation of the magnetic intensities varies only slightly up to $H_s = 1.5$ T. Above H_s the magnetic intensity due to the zero field magnetic structure decreases continuously and finally vanishes between 3.5 T and 4 T (being the field steps at this experiment). The behavior of the LRO in magnetic fields is summarized in figure 5.17 where the intensity over field is shown for selected magnetic satellites. The final disappearance of the zero field magnetic structure can be brought into correlation with the line in the phase diagram which marks an anomaly in the ac-susceptibility at $H_c = 3.3$ T.

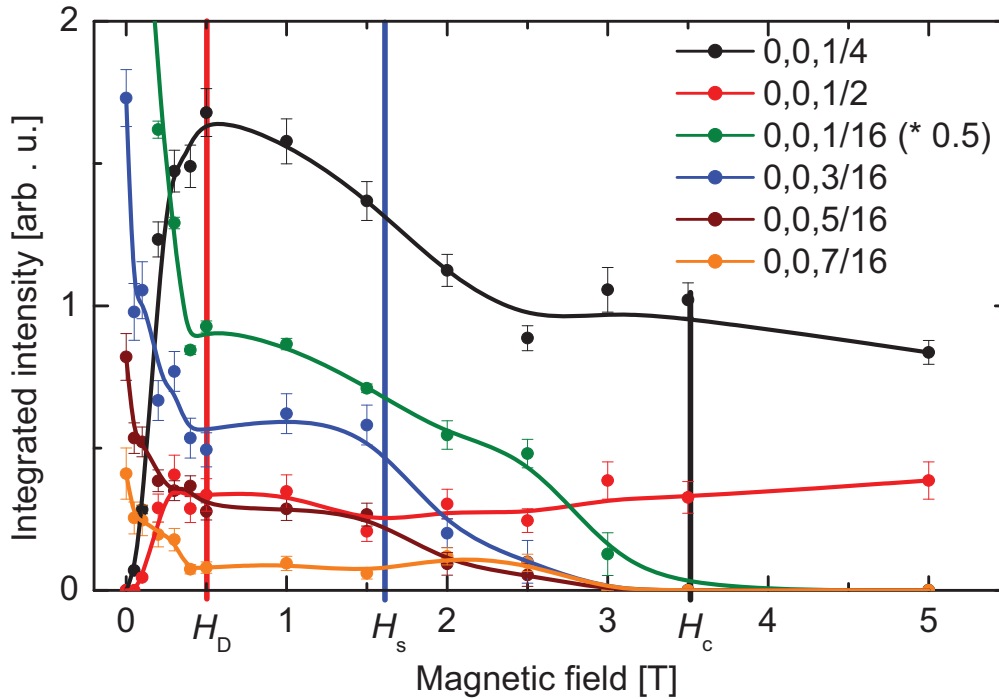


Figure 5.17: Integrated intensities for $0, 0, 1 -n\pi$ magnetic satellite reflections. The $0, 0, 1/16$ reflection has been scaled by a factor of 0.5. The data points are scatter mostly due to selective background subtraction. The error-bars are based on an estimation of the influence of selective background subtraction. The lines serve as guide to the eye.

Above H_c only the second phase (in the following referred to as FiM) defined by magnetic reflections on the position $1/4$ and $1/2$ along the $(0, 0, L)$ direction and strong ferromagnetic contributions on the $0, 0, 1$ reflection remains. The FiM phase coexists with the zero field

phase apparently in the area framed by H_c and T_N in smallest applied magnetic fields. The other characteristics of the FiM phase are further described in chapter 5.6.

5.5.3 Short- to long-range order transition in applied field for $T < T_2$

The SRC found in zero magnetic field also reacts on an applied magnetic field along the easy axis. Referring to figure 5.11 the intensity due to short range order was found on positions $(1/6, 1/6, 1/16)$ and $(2/6, 2/6, 2/16)$. Figures 5.18 and 5.19 show full reciprocal planes with a magnetic field parallel to $(H, 0, 0)$ at 2 T and 4 T, respectively. While the changes in the LRO are not apparently from these reciprocal planes the intensity due to SRC changes are drastic and one can identify three different phases. Applying a magnetic field first seems to have no effect on the SRC up to H_s (the “s” originates from the change of the SRC). Above H_s magnetic intensity is found on incommensurate positions $\{0.13, 0.13, 0.1\}$ and $\{0.37, 0.37, 0.1\}$ as can be seen in figure 5.18 for 2 T (circled in red). The half width of the reflections is anisotropic indicating different correlation lengths or low-dimensional order.

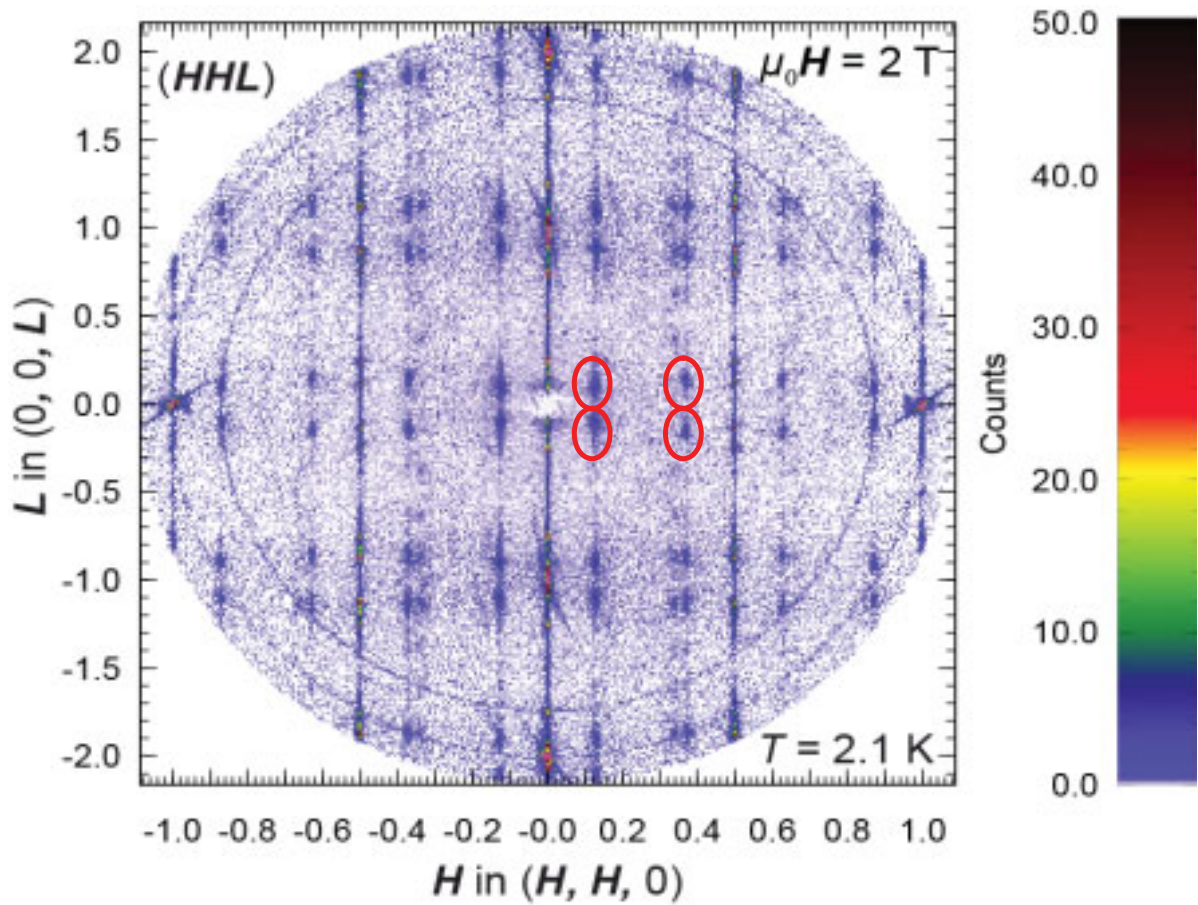


Figure 5.18: Full reciprocal (HHL) -plane of Tb_2PdSi_3 at $T = 2.1 \text{ K}$ and an external field of 2 T. The magnetic intensity due to iS-LRO (see text) is found on $\{0.13, 0.13, 0.1\}$ and $\{0.37, 0.37, 0.1\}$ positions and is marked in the figure with red circles. Weak magnetic reflections in the vicinity of the $\{0.37, 0.37, 0.1\}$ positions are due to the onset of the cS-LRO phase.

The phase will be labelled iS-LRO (incommensurate Short to Long Range Order) in the following. At the field H_s the SRC phase undergoes an apparently discontinuous phase transition to the iS-LRO phase. This phase seems to change in a continuous transition up to H_c . Above H_c magnetic intensity is found on commensurate positions $(1/6, 1/6, 2/8)$ and $(2/6, 2/6, 1/8)$. The reflections appear to be more isotropic indicating the return to a more 3-dimensional order. Still, the reflections are on a modulated background which is streak-like along $(0, 0, L)$. This phase will be labeled as cS-LRO (commensurate Short to Long Range Order). Magnetic intensity due to cS-LRO has been found up to a magnetic field of 6.5 T at $T = 2$ K. The upper critical field at $T = 2$ K of the cS-LRO might be connected to a feature seen in the magnetization measurement at a field of 8.5 T (the jump in the virgin magnetization curve).

The inverse half width of reflections can be used as estimation for the correlation length of the magnetic order. Using equation (16) (see chapter 4) and approximate the instrument

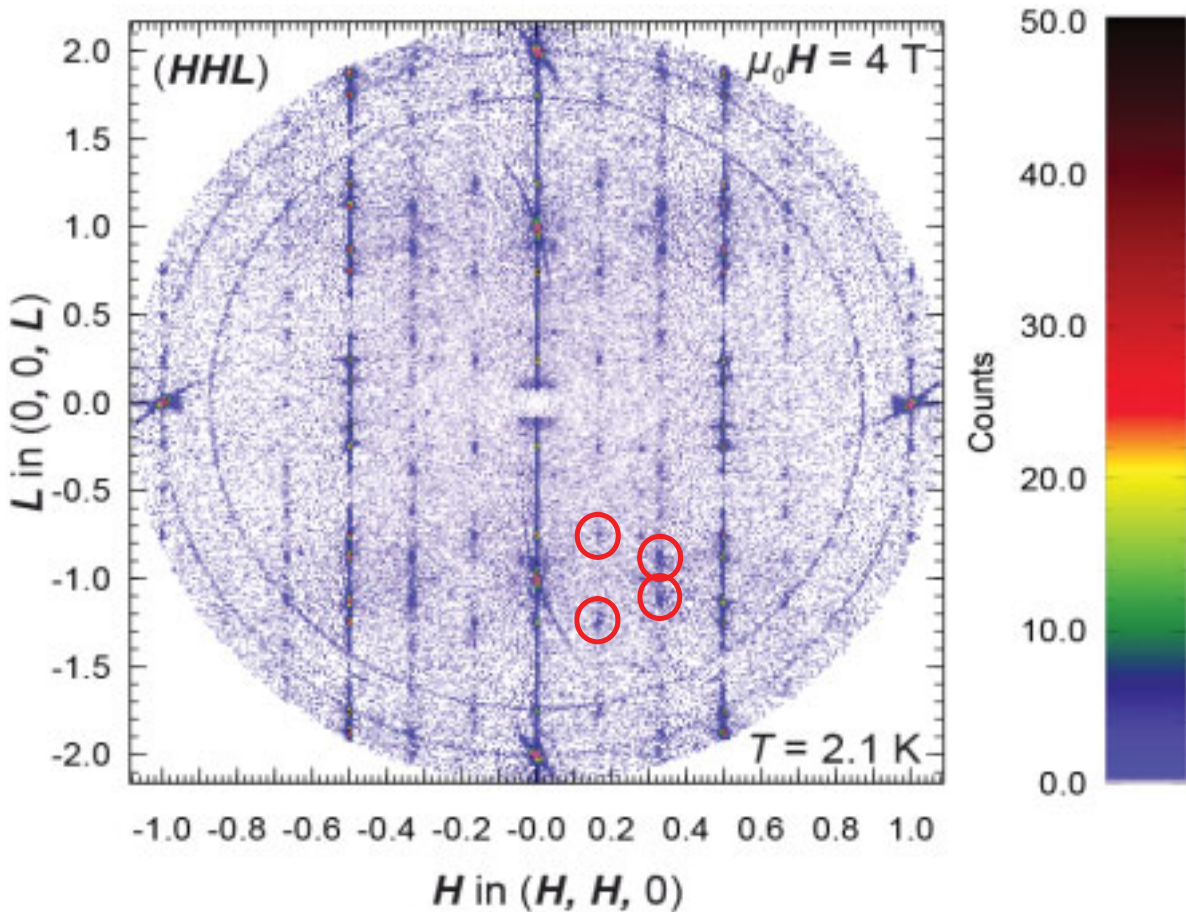


Figure 5.19: Full reciprocal (HHL) -plane of Tb_2PdSi_3 at $T = 2.1$ K and an external field of 4 T. The magnetic intensity due to cS-LRO (see text) is found on $(1/6, 1/6, 2/8)$ and $(2/6, 2/6, 1/8)$ positions. The magnetic intensity due to cS-LRO is weak compared to the magnetic reflections due to the FiM phase but distinguishable from the background up to the highest measured field of 6.5 T. The intensities on the antiferromagnetic reflections on the $(0.5, 0.5, L)$ positions are larger than on $(0, 0, L)$ in the FiM phase.

resolution as the half width of a nuclear peak the correlation length of the SRC phase is about 28 Å. This length is in the order of the length of a magnetic unit cell for the SRC phase. The correlation length of the iS-LRO is 60 Å in c -direction and 510 Å in $(H, H, 0)$ -direction. The cS-LRO has a correlation length of 120 Å in c -direction and 380 Å in $(H, H, 0)$ -direction.

5.5.4 Magnetic phases found for $T_2 < T < T_N$ in applied fields

The magnetic phases of Tb_2PdSi_3 in applied magnetic fields and below T_2 have been describe above. T_2 has already been identified as critical temperature for the SRC in zero magnetic fields. Is T_2 also the critical temperature for the SRC in applied magnetic fields? Is T_2 also connected to the phases iS-LRO and cS-LRO, as indicated by the feature map? Figure 5.20 shows three plots of a $(H, H, 0.89)$ section measured at the PANDA spectrometer at $T = 2$ K in zero field (black), $T = 12$ K in zero field (red) and at 0.75 T (blue). The $T = 2$ K curve is shifted in order to compare the measurements. The dataset (2 K) originates from an earlier measurement. It is unclear whether the background signal has been improved due to changes in the instrument setup or if the change is intrinsic. In the latter case a possibility is an increased background from incoherent magnetic scattering. The magnetic intensity due to

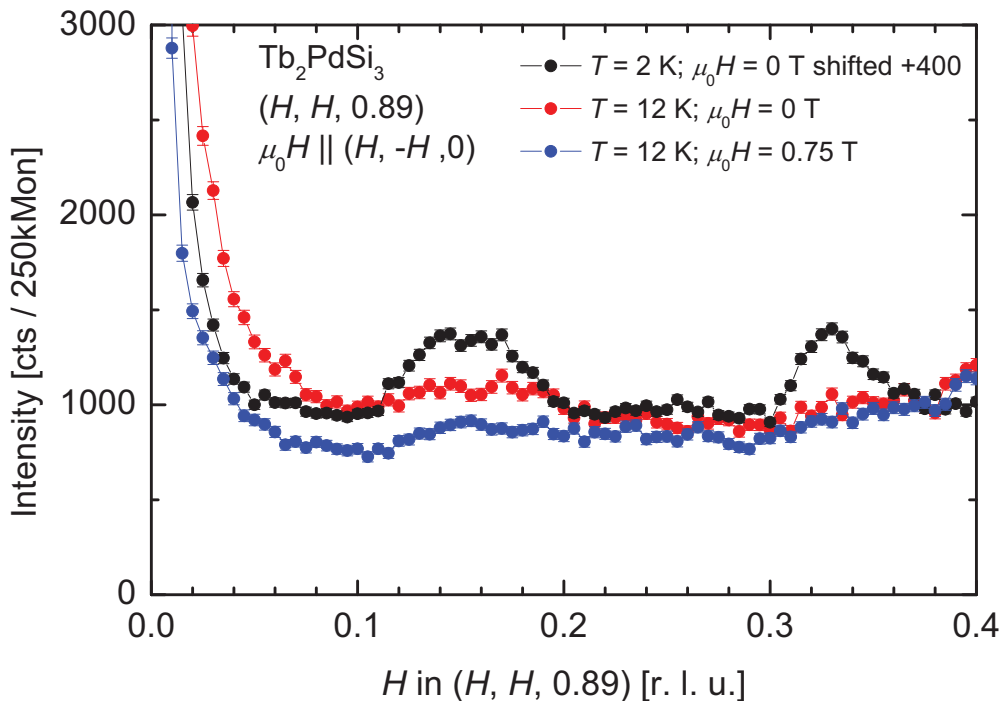


Figure 5.20: Section along $(H, H, 0.89)$ over the positions where magnetic intensity due to SRO is found in zero field (black curve). Above T_2 the intensity is greatly reduced and the background enhanced due to paramagnetic scattering. The application of a small field leads to a small reduction of the paramagnetic background.

SRC is strongly reduced comparing the $T = 12$ K zero field to the $T = 2$ K zero field measurement. Further, a small magnetic field below H_s does not affect the intensity on this position. Crossing the phase line build by H_s a sharp peak is observed even above T_2 as figure 5.21 shows. Above H_c no magnetic intensity on this position is observed. Comparing the

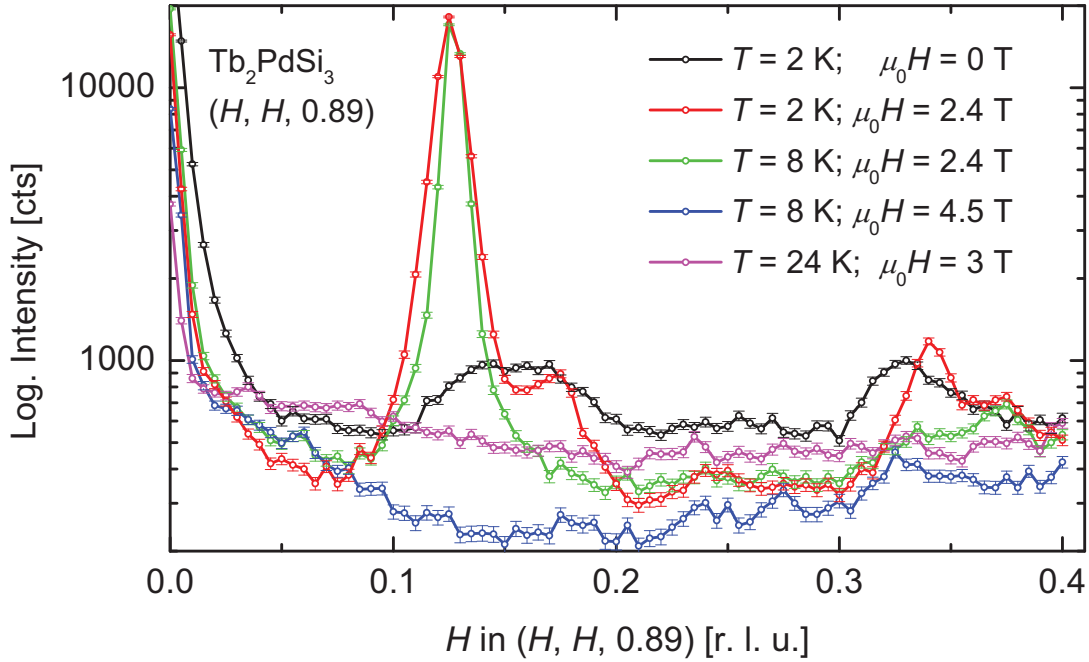


Figure 5.21: Section along $(H, H, 0.89)$ over the positions where magnetic intensity due to SRO is found in zero field (black curve is the same as in figure 5.20). An applied field $H_s < H < H_c$ leads to the peak characteristic for the iS-LRO phase (green and red curve). The 2nd harmonic of the iS-LRO phase seems to be absent above T_2 . Note the logarithmic intensity scale.

section in the iS-LRO phase (red) with the measurement above T_2 (green) some changes can be seen: First, below T_2 (red curve) a small shoulder appears around 0.17. Second, the peak at the 0.33 position seems absent above T_2 (the green curve). Unfortunately, this phase has not been characterized in detail with neutron diffraction in a E2 measurement. From the present data the conclusion can be drawn that the area formed by the phase lines connecting T_2 , H_s and H_c surrounds a magnetic phase bearing some similarity to the iS-LRO phase. This phase is labeled as iS-LRO'. Figure 5.22 shows a $(H, H, 0.75)$ section at a magnetic field of 4 T and different temperatures. The peak observed at $T = 2$ K at $H = 0.166$ is characteristic for the cS-LRO phase. As can be emphasized the intensity is strongly reduced at $T = 8$ K and absent at 14 K. T_2 is therefore also the critical temperature for the cS-LRO phase. Summarizing, T_2 is most likely the critical temperature for the SRC, iS-LRO and cS-LRO magnetic phases. The magnetic phase iS-LRO' is found in a distinctive area bounded by the lines connecting T_2 , H_s and H_c .

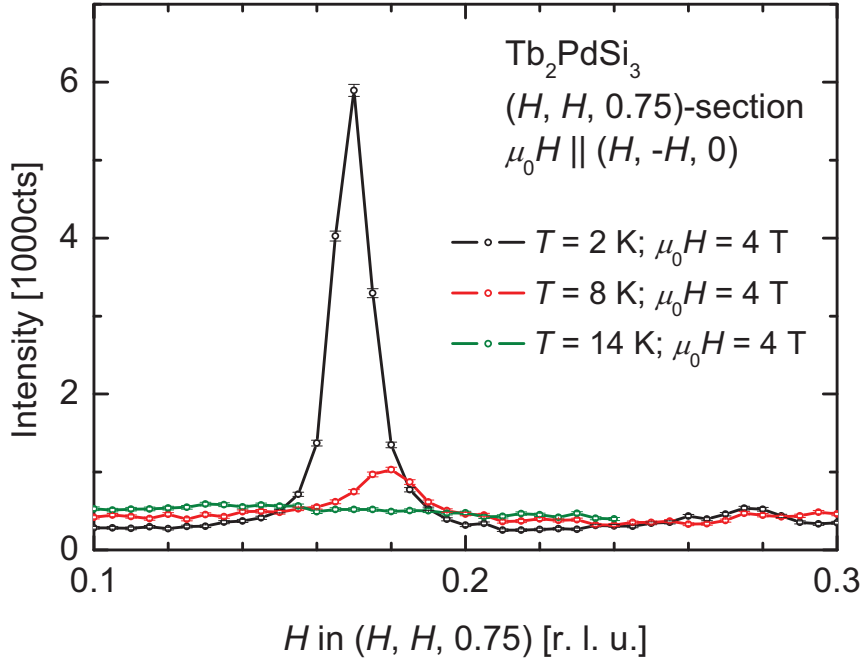


Figure 5.22: Section along $(H, H, 0.75)$ over the positions where magnetic intensity due to cS-LRO is found. The intensity is much weaker above T_2 and absent at $T = 14$ K.

5.6 The high field LRO phase of Tb_2PdSi_3 : FiM

The FiM entitled phase does exist in a large area of the phase diagram in smallest applied magnetic fields with a minimum field around T_N . Above T_N the phase boundary separates the paramagnetic phase from the FiM phase. The existence of the FiM phase in these regions has been proven by measurements on the PANDA spectrometer. Exemplary scans at high fields in a wide temperature range are shown in figure 5.24. The figure shows sections along $(0, 0, L)$ centred around the $0, 0, 1$ reflection. The characteristics of the FiM phase are a strong ferromagnetic contribution on the crystallographic positions, magnetic reflections on $0, 0, 1/4$ and $0, 0, 1/2$ as well as magnetic intensity mimicking the nuclear superstructure on $1/2, 1/2, n/8$ positions. The magnetic intensity on these positions is slightly stronger for the reflection with $L = 1/8$ compared to $L = 2/8$. The magnetic reflection on the $L = 3/8$ positions is very weak. This is depicted in figure 5.25 where sections along $(0.5, 0.5 L)$ are shown for three magnetic fields. The very weak peaks in the zero field measurement (black curve) on the $n/8$ positions are the crystallographic superstructure reflections. Their intensity does not change above T_N and therefore no magnetic contribution on the position of the superstructure reflections exists in zero-field.

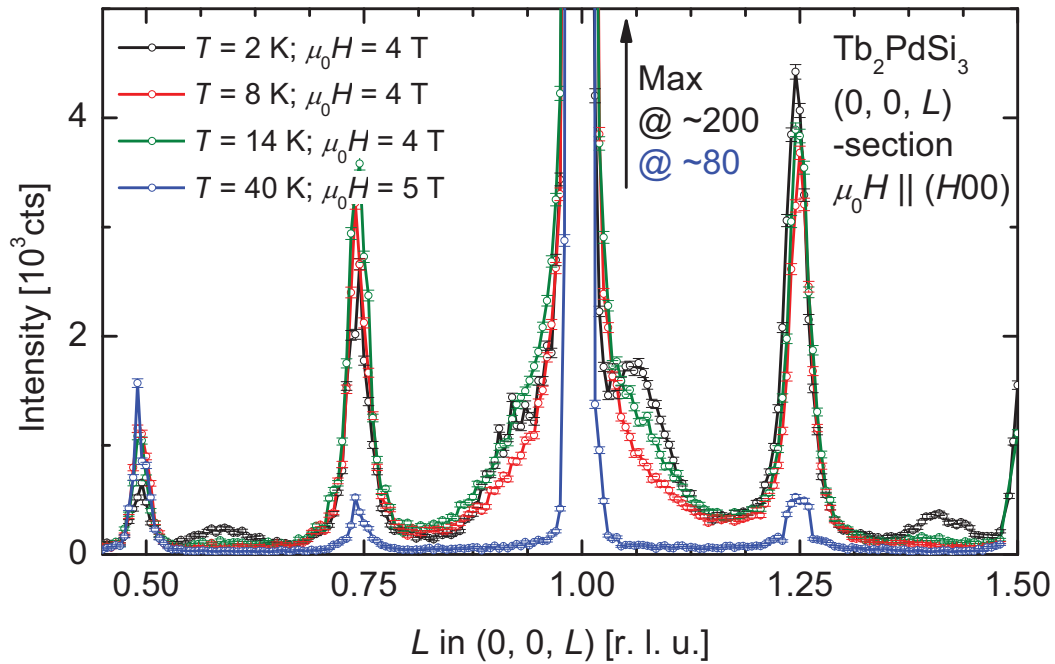


Figure 5.23: Sections along $(0, 0, L)$ as indicated in figure 5.11 at different magnetic fields and temperatures. The reduced intensity of the blue curve is attributed to the higher temperature. The intensity on the $1/2$ position is however increasing with increasing field, comparable to the behaviour at $T = 2$ K (figure 5.16).

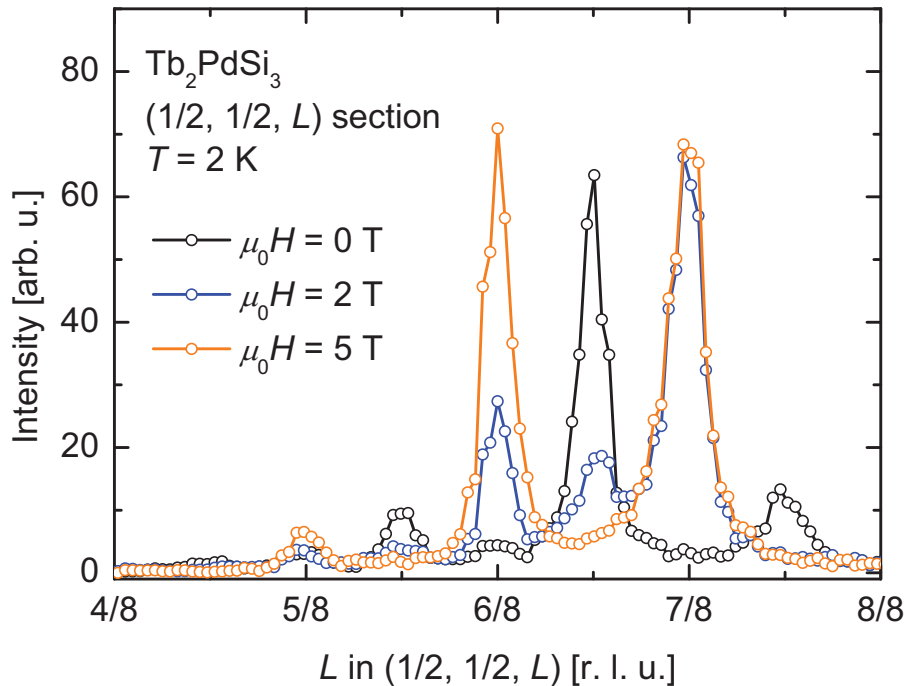


Figure 5.24: Section along $(1/2, 1/2, L)$ at different magnetic fields. The magnetic reflections change completely from the $1/16$ to the $1/8$ regime above 3 T. The intensity seems to be non-sensitive on further increase of the field.

The most interesting side of the FiM phase is the possibility to induce antiferromagnetic modulation from the paramagnetic state by the application of a magnetic field. The three axis graph, figure 5.25 shows summarized intensity on $(0, 0, 1/2)$ in dependence of the applied magnetic field. The intensity scans did not stretch over the whole peak. As consequence the characteristic feature of the transition PM to FiM is restricted to a characteristic point in the change of intensity. A change of the half width of the magnetic peaks cannot be excluded. The intensity on the $0, 0, 1/2$ reflection does grow apparently continuously for applied magnetic fields. The blue line in the (T, H) plane in figure 5.25 is the phase separation line found in the magnetic phase diagram. The position of the phase boundary coincides with an

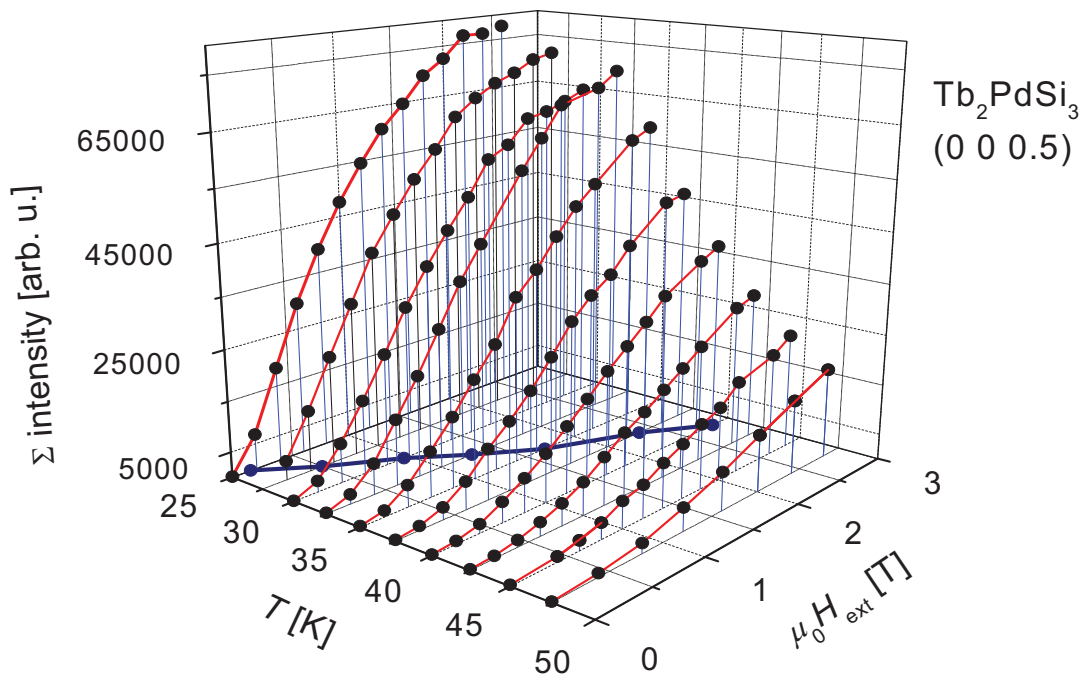


Figure 5.25: Magnetic intensity on $0, 0, 1/2$, characteristic for the FiM phase plotted in intensity vs. temperature and external magnetic field. The blue line in the (T, H) plane is the line from the magnetic phase diagram.

inflection point of the intensity vs. field curves. The measurements shown in figure 5.25 have been performed with the aim to clarify the nature of the transition PM to FiM. Unfortunately, in retrospect the measurements have been too limited both in field and temperature range. Having this stated, neither the ac-susceptibility measurement nor the magnetisation data have been able to identify a critical field for the FiM phase. To clarify this essential point high field magnetisation measurements are needed. A first experiment had shown the need for a rigid sample fixation.

The magnetic structure of the FiM phase is yet unresolved. Likewise the zero field magnetic structure, two different Tb sites from the crystallographic superstructure are

necessary to describe the experimental data. Similar to the zero field phase different spin sequences are expected for both sites. The reason for this assumption is the absence of a $0, 0, 1/8$ reflection. The so far tried ideas are to use the doubled cell with two atom sites and different spin-sequences. However, the interference terms always produce “unwanted” intensity on the $0, 0, L$ positions. Most likely this phase can be described as arrangement of spins with an angle to the $(H, 0, 0)$ direction. The antiferromagnetic intensity arises from the alternating sequence of this angle between the antiferromagnetic moments. The increase on the ferromagnetic position is described likewise. Noteworthy is the robustness of the $1/2, 1/2, 1/8$ and the $1/2, 1/2, 2/8$ magnetic reflections with the increase of the magnetic field. The antiferromagnetic inter-site-exchange seems to be much stronger between the two different Tb sites ($1a$ and $3f$) being responsible for the magnetic intensity on these positions compared to the intra-site-exchange on the $3f$ sites which contribute mostly to the magnetic intensity on the $(0, 0, L)$ section.

5.7 Phase diagram of Tb_2PdSi_3 : interpretations and conclusions

The anomalies derived from ac-susceptibility and magnetization created the feature map (figure 5.9) which in turn is the first hint for the magnetic phase diagram. The method of neutron diffraction allowed to probe the different regions of the feature map. From the complementary methods of ac-susceptibility and neutron diffraction a final phase diagram can be constructed. Six different phases were identified and their respective microscopic properties characterized. Between 20 K and T_N a yet unnamed phase (working name: the “Zwickel”) is found. The magnetic structures at 12 K, 18 K and 20 K did not show any differences except the expected overall decrease in intensity. Figure 5.26 shows the final, color coded magnetic phase diagram for Tb_2PdSi_3 . The triangles are derived from the anomalies in the ac-susceptibility and are drawn with their respective error bars. The different colored areas represent the different magnetic phases. The variety of them and the multiple coexistence of different phases (in some areas threefold) is to be addressed in terms of exchange interaction and frustration. The crystal electric field is the reason for the magnetic anisotropy between basal plane and the c -axis. The magnetic moments are confined within the basal plane and an applied field probably only cants the magnetic moments out-of plane. This effect seems to be continuous. The biggest effect of the crystal electric field regarding the magnetic phase diagram for the $(H, 0, 0)$ direction is the small in-plane anisotropy which is probably only of interest in high fields.

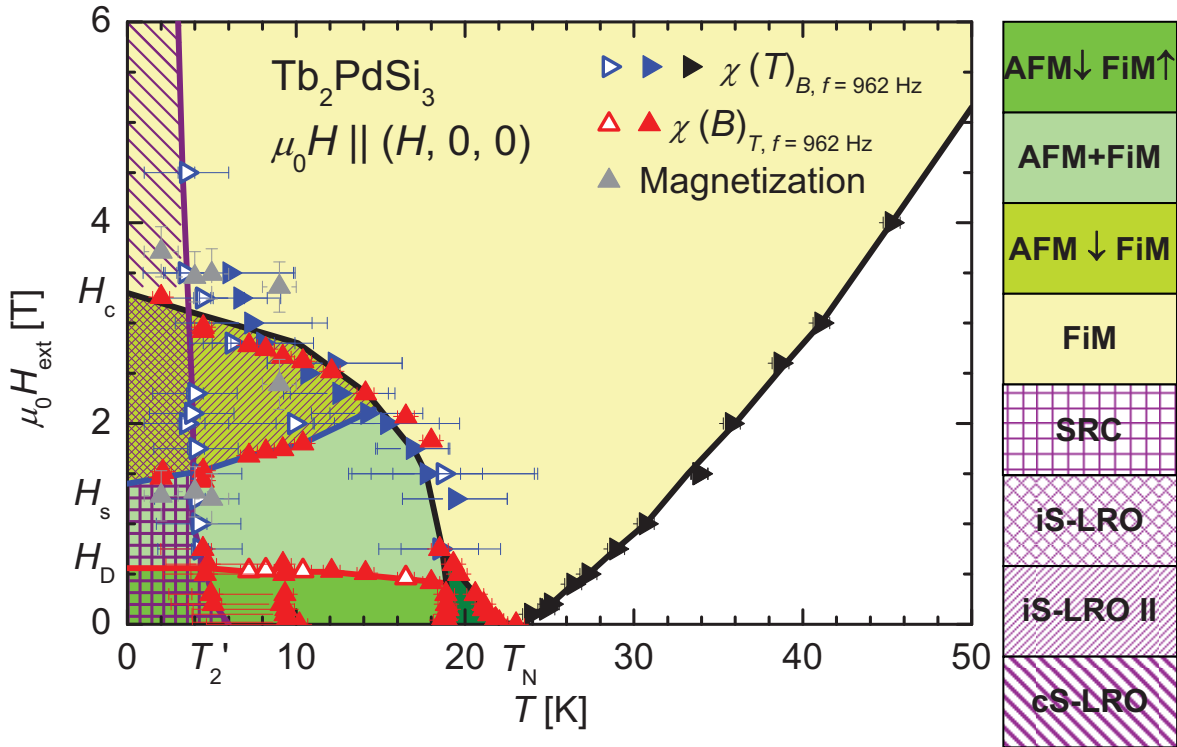


Figure 5.26: Color coded magnetic phase diagram of Tb_2PdSi_3 for an applied field along the $(H, 0, 0)$ direction. The different observed phases are indicated on the right side. The drawn lines of the phase diagram are based on the results of neutron diffraction in magnetic fields (see text).

In neutron diffraction, ferromagnetic fluctuations have been observed above T_N . Antiferromagnetic fluctuations on $L \sim 1/16$ positions seem to be absent. At T_N the compound orders in a full squared-up antiferromagnetic structure with a very large unit cell. Disorder is still present in this magnetic phase. The disordered moments undergo a phase transition at a lower temperature T_2 forming an ordered phase with short correlations (SRC). A recent angular-resolved-photo-emission-spectroscopy (ARPES) measurement [Ivonosov2008] has determined a Fermi-surface nesting vector in the basal plane to be $(1/6, 1/6, L)$. On exactly these positions the SRC below T_2 is observed. At low temperatures and in zero magnetic field the configuration of LRO+SRC is stable but obviously the “quasi hexagonal symmetry” with the rare earth atoms forming equilateral triangles does not allow another arrangement. Once this symmetry is broken by the application of a small magnetic field a second LRO phase, denoted FiM occurs. The FiM phase seems to be favored by magnetic moments due to the exchange interaction. The strong ferromagnetic fluctuations in the paramagnetic phase are not necessarily a sign of an underlying additional ferromagnetic phase since the FiM phase has already a very strong ferromagnetic component. The attribution of the ferromagnetic fluctuations observed above T_N to the FiM phase is therefore a possible interpretation.

The geometric frustration is directly opposing the exchange interaction. This argument is re-emphasized by the possibility to invoke the FiM phase directly from the paramagnetic

state. Disorder is still present in the FiM phase. The cS-LRO phase is found at very low temperatures (below T_2') up to a field of 6.5 T and exists probably also to higher fields (up to ~ 8.5 T). However, the zero field LRO and the FiM phase form a large area of coexistence. This area is confined by the critical field H_c of the LRO. Within this area the two iS-LRO phases are found, too. The SRC found in zero field undergoes a phase transition in an applied field to the iS-LRO phases. The reason for this can either be the broken symmetry condition of the equilateral triangles or the modification of the Fermi-surface and a resulting change of the in-plane RKKY exchange interaction. The incommensurate nature of this phase supports the latter. Since the critical field of the iS-LROs is also H_c the assumption is valid that the iS-LRO phases is nested within the zero field LRO. The change from the iS-LRO to the cS-LRO is not so much a phase transition from one S-LRO to another but the disappearance of the “parent” phase from which they are dependent in the first place.

The Gd_2PdSi_3 compound presented in chapter 3 featured a similarity in the phase diagram as Tb_2PdSi_3 . Also in the Gd-compound a transition line with the characteristics of the FiM phase could be observed. Since Gd^{3+} is an *S*-state ion the observation of a FiM-phase in Gd_2PdSi_3 would exclude CEF effects to play a dominant role in the formation of the FiM phase. As had already been stated Gd-compounds are not suited for neutron diffraction. Ho-compounds are much better suited and the magneto-crystalline anisotropy in Ho-compounds is expected to be small. Thus the Ho_2PdSi_3 compound is suited to investigate the possibility of a FiM-like phase in a compound with a weaker anisotropy as in the case of Tb_2PdSi_3 . The results of this investigation are presented in the next chapter.

6. Ho₂PdSi₃

In chapter 2 it had been emphasized that the dominant crystal electric field in Ho₂PdSi₃ is apparently not dominated by one parameter, setting this compound aside from the other members of the R₂PdSi₃ series. This opens the possibility for the magnetic easy axis determined by the CEF to be neither parallel to the *a*- nor to the *c*-direction, but to a crystallographic non-preferred direction. While the magnetic easy axes represent the free energy minimum of the CEF-Hamiltonian, the (exchange-) interaction may favour a different magnetic moment direction. One possibility is the anisotropic dipole-dipole interaction. The Ho₂PdSi₃ compound bridges therefore the case Gd₂PdSi₃ and the case Tb₂PdSi₃ in terms of the CEF contribution. In addition, the possibility of higher multipole interactions may be considered. As far as this can be interpreted from macroscopic data (figure 2.4), the onset of RKKY interaction at T_N does not seem to modify the magnetic moment direction

6.1 *Ac-susceptibility and a phase diagram for Ho₂PdSi₃*

The magnetic phase diagram is derived from the ac-susceptibility measured along the (0, 0, *L*)-direction. This is in the first instance justified by the magnetization measurement where transitions were observed only for the (0, 0, *L*)-direction (figure 2.17). The influence of a magnetic field along the (*H*, 0, 0)-direction will only be discussed briefly. Figure 6.1 shows the temperature dependent measurements along the *c*-direction of the ac-susceptibility at selected external fields. In the low field region up to 0.5 T, drastic changes in small field values are observed. The maximum in the real and imaginary part at T_N (7.7 K) shifts with small fields to smaller transition temperatures (as to be expected for a PM to AFM transition). Interestingly, the maximum value of the susceptibility first increases with increasing field up to a field value of 0.1 T. There, an additional anomaly occurs where the susceptibility is strongly enhanced over a temperature range of 2 K. The imaginary part is enhanced even further. In comparison to the magnetization, this is the field range where the hysteretic increase is observed. Above 0.1 T the values of the susceptibility decreases with increasing field (or towards saturation in the magnetization). For a field of 0.2 T the susceptibility values are smaller than the zero field values. The broad maximum observed in the real part of the susceptibility around 8 K at 0.2 T shifts to increasing temperature for increasing field and is therefore not connected to T_N . The transition connected to T_N manifests as a small step in the real part, but in the imaginary part still a maximum is observed. The transition at T_2 (2.2 K in zero field) in very small fields either is found at temperatures lower than 2 K or is suppressed. Two additional measurements at 50 mK and 1 K indicate the latter. The right side of figure

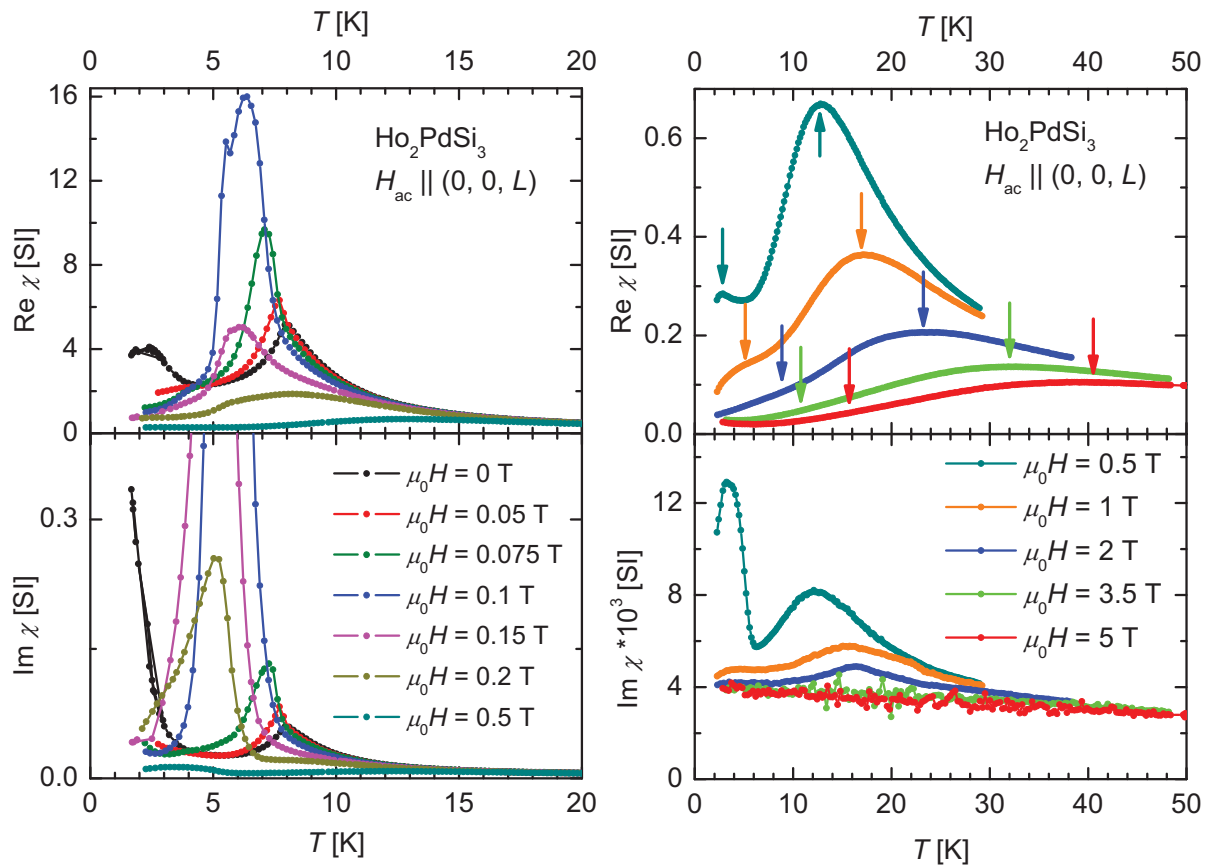


Figure 6.1: Ac-susceptibility (real- and imaginary part) for Ho₂PdSi₃ measured along the (0, 0, L)-direction at constant field. The different applied fields are colour coded. The graphic on the left side shows the region from 0 to 0.5 T; the graphic on the right side shows the continuation up to 5 T with different scales. The measurement at 0.5 T is shown in both graphs (dark cyan).

6.1 shows the measurements for higher fields. The 0.5 T measurements (connecting left and right side of the figure) show two maxima. The maximum at around 3 K cannot be traced to a feature in smaller magnetic fields. It is probable that this transition is superimposed in the 0.2 T curve by the enhancement of the susceptibility. However, it is also difficult to correlate this feature to an anomaly in the susceptibility in higher magnetic fields. In the curve measured at 1 T it is still possible to imagine a small underlying maximum centered at 5.7 K in the real part. The course of the anomaly was tried to follow to higher fields. The uncertainty of the position in (T, H) for this anomaly is attributed for in the error. It seems that this anomaly is observed at higher temperatures for higher fields.

The second anomaly found in the ac-susceptibility for fields equal and above 0.5 T is a broad maximum (~ 11 K for 0.5 T). The maximum seems to broaden with increasing fields. It can be tracked in the measurement curves toward higher temperatures with increasing magnetic field.

Field dependent ac-susceptibility measurements at constant temperature look all similar. In the imaginary part a large maximum is observed around 0.1 T. This explains the strong enhancement observed in the temperature dependent measurement at this field.

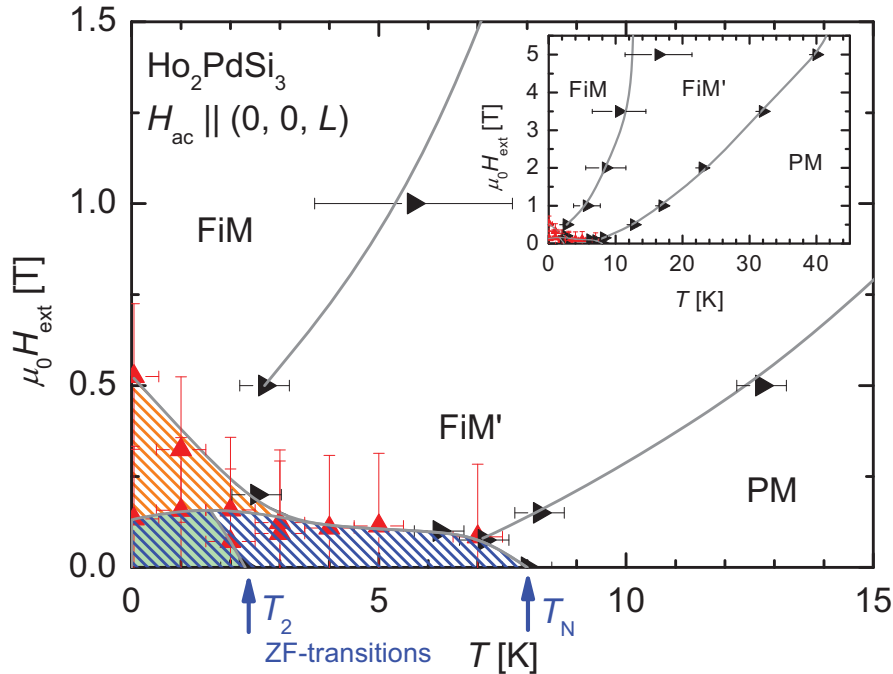


Figure 6.2: Phase diagram for Ho_2PdSi_3 when a magnetic field is applied along the $(0, 0, L)$ direction. The inset shows the course of the phase diagram to high magnetic fields.

The combination of all the features in the ac-susceptibility leads to the magnetic phase diagram shown in figure 6.2. This phase diagram is particular due to its field and temperature range. Everything connected to the zero-field magnetic structure happens in the narrow field range up to 0.5 T and for temperatures $0 < T < T_N$. In this region, three areas can be distinguished. Above 0.5 T and in a large temperature range a somehow familiar phase boundary is observed. In Gd_2PdSi_3 (see chapter 3) a similar line has been observed. In Tb_2PdSi_3 (see chapter 5) this phase line was identified as FiM phase. In contrast to the aforementioned compounds the phase found in Ho_2PdSi_3 seems to have an additional phase transition in this region. The low temperature area is labeled FiM and the area at higher temperatures is marked as FiM'. As seen in chapter 2 the transition to the ferromagnetically saturated phase, e. g. H_{c2} was not observed up to 13 T.

The difficulty to investigate Gd-compounds with neutrons has already been mentioned. Ho-compounds are much better accessible in terms of neutron scattering with the additional benefit that the effect of the magneto-crystalline anisotropy is expected to be small. Ho_2PdSi_3 and Gd_2PdSi_3 are good to be compared. It will be shown in the following that Ho_2PdSi_3 is

indeed in some terms very similar to Gd₂PdSi₃ but on the other hand, similarities to Tb₂PdSi₃ are also found.

6.2 Neutron diffraction on Ho₂PdSi₃

Neutron diffraction on Ho₂PdSi₃ has been performed on all neutron instruments presented in chapter 1.5. All measurements used the same single crystal with a mass of 2.9 g. The shape of this crystal is slightly irregular with 6 oriented faces grinded on the once cylindrical sample of 9 mm length and 5 mm diameter.

6.2.1 Zero and low field ($\mu_0 H < 0.8$ T) magnetic structure

Figure 6.3 shows the full reciprocal plane ($HK0$) of Ho₂PdSi₃ at 1.5 K below T_N and T_2 . In the figure the reciprocal vectors $(1, 0, 0)$ and $(0, 1, 0)$ are marked for better orientation. Above T_N the cohort of observed reflections in this plane are due to the symmetrically equivalent faces $\{1, 0, 0\}$, $\{1, 1, 0\}$ and the $\{2, 0, 0\}$ on the outer rim of the circular plane. Scattering on the polycrystalline aluminium of the sample holder and the cryostat yields two faint Debye-Scherrer rings. Below T_N magnetic Bragg peaks appear on positions $\{\mathbf{G} \pm (1/7, 0, 0)\}$, where \mathbf{G} is a reciprocal lattice vector. Further lowering the temperature leads to the progressive appearance of reflections resulting from higher harmonics (odd integers) of the propagation

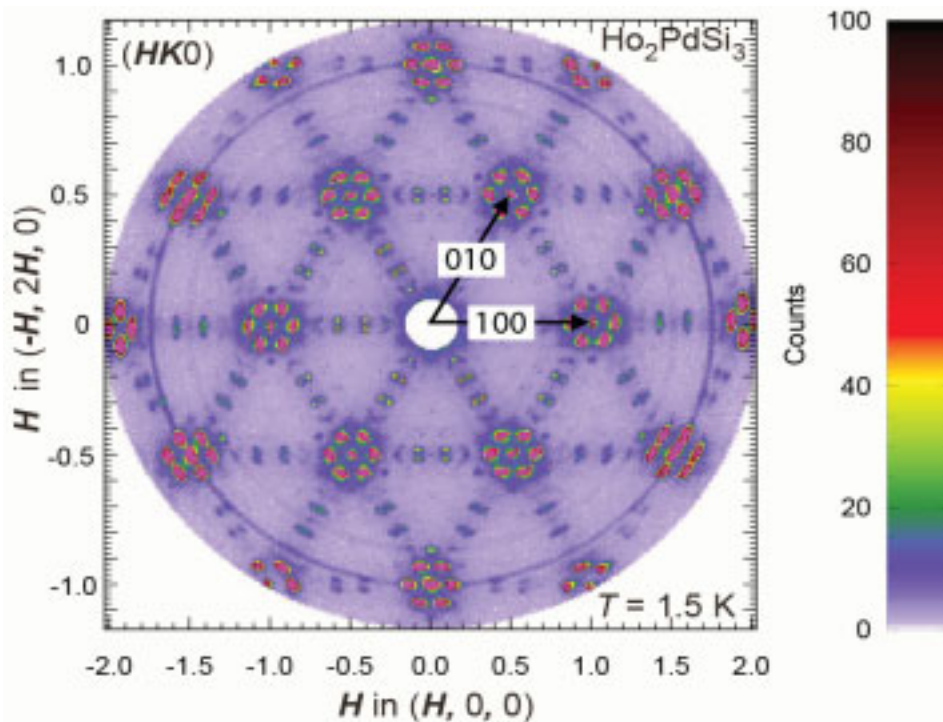


Figure 6.3: Full reciprocal ($HK0$)-plane of Ho₂PdSi₃ at $T = 1.5$ K. The reciprocal lattice directions $(1, 0, 0)$ and $(0, 1, 0)$ are marked with arrows. The two rings originate from the scattering on polycrystalline aluminium from the sample holder and the cryostat.

vector. The assumption that the transition at T_2 (~ 2.2 K) is equivalent to the one observed in the Er₂PdSi₃ compound [Frontzek2007, also in chapter 7] is drawn. As can be seen already in figure 6.3, the magnetic reflections are split in perpendicular direction to the “main” propagation direction $(H, 0, 0)$. The exact propagation vector is therefore $\tau = (1/7-\delta, 2\delta, 0)$ with a small component δ of order 10^{-3} . Only a small magnetic contribution to the intensity is found on the $\{1, 0, 0\}$ indicating a mainly antiferromagnetic phase. This finding was further quantified by the experiment on the PANDA spectrometer where a set of reflections $\{H, 0, L\} \pm \tau$ had been measured. The ferromagnetically ordered moment is estimated to be smaller than $0.2 \mu_B$. The magnetic moment direction can be estimated from the fact that neutrons are only sensitive to the magnetization density perpendicular to the scattering vector Q . The respective figure is shown in the appendix and indicates the moment direction to be mostly along the c -axis.

The low temperature and zero field phase characterized by the propagation vector $(1/7-\delta, 2\delta, 0)$ was confirmed at $T = 0.187$ K and $\mu_0 H = 0$ T. The black curve in figure 6.4 shows the Q dependent intensity along the direction $(H, -2H, 0)$ centred at $2/7, 0, 0$ which is also the -5τ position in zero field. The situation at the magnetic satellite reflection positions is complicated by the fact that for instance the Q position $2/7, 0, 0$ is at the same time both $+2\tau$ with respect to $0, 0, 0$ and -5τ with respect to $1, 0, 0$. As shown with the black curve of figure 6.4, the peak in the middle is actually the $+2\tau$ reflection while the -5τ reflections with lower intensity constitute the shoulders on the two sides. From zero field measurements the determination of the transverse component δ is difficult. A rough figure for δ in the zero magnetic field is 0.004 r. l. u.. However, when a magnetic field is applied parallel to $(0, 0, L)$ the -5τ reflection is strongly enhanced (compare the red curve in figure 6.4). In the field range between 0.2 T and 0.7 T the position of both reflections $+2\tau$ and -5τ can be described with a δ around 0.0024 relative lattice units in $(1/7-\delta, 2\delta, 0)$ which is equivalent to a magnetic unit cell 400 times as big as the primitive AlB₂ unit cell. Apparently, the transverse component of the propagation vector is part of the zero field and low field magnetic structure. It is present up to the critical field where the antiferromagnetic structure is destroyed (around 0.8 T, the green curve in figure 6.4). Above 0.8 T no magnetic intensity is found in the $(HK0)$ plane.

From the diffraction data in a magnetic field applied in the basal plane two conclusions for the low field magnetic structure can be drawn. In the (HHL) scattering geometry, the magnetic field is parallel to $(H, -H, 0)$, when a vertical magnet is used. As shown in figure 6.3 magnetic reflections are found on all symmetric equivalent positions. For increasing magnetic

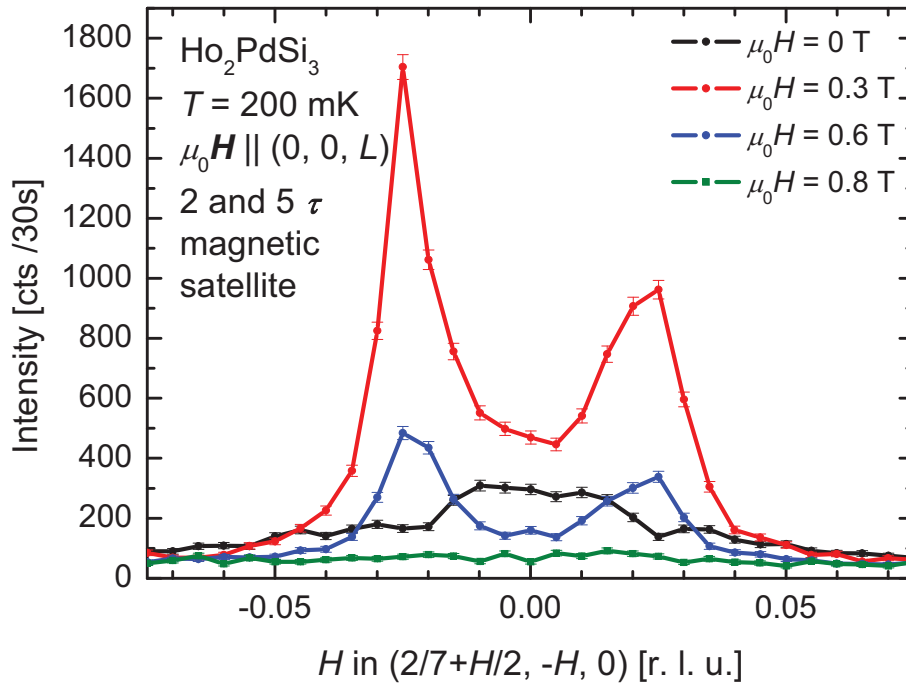


Figure 6.4: Section along the $(H, -H, 0)$ direction-crossing perpendicular the 2 and 5 τ magnetic satellite, respectively. The measurement is at base temperature (200 mK) with different applied magnetic fields parallel to $(0, 0, L)$.

fields the intensity of reflections with τ parallel to the magnetic field direction is increasing while the intensity decreases in the other cases. At an applied magnetic field of 5 T the magnetic intensity on $1/7, -1/7, 1$ is increased by a factor of three while the intensity of the symmetrical equivalent positions $1/7, 0, 1$ and $0, 1/7, 1$ has disappeared.

The first conclusion is therefore, that the zero field magnetic structure in Ho₂PdSi₃ is a single- τ , multi-domain structure. The second conclusion is that the low-field magnetic structure is relatively insensitive to an applied field in the basal plane. This is in agreement with the ac-susceptibility and magnetization measurements for a field applied along $(H, 0, 0)$. In both cases no apparent phase transition could be observed up to 5 T.

6.2.2 High field magnetic structure ($\mu_0 H > 0.8$ T)

In applied magnetic fields, a new antiferromagnetic phase is found. In both investigated cases (field parallel $(H, -H, 0)$ and $(0, 0, L)$) this new phase was observed. The propagation vector $(1/2, 1/2, 1/8)$, coincides with the nuclear superstructure reflections. Accordingly, magnetic intensity was found on the same positions as the crystallographic superstructure reflections. Figure 6.5 shows the field dependence of the reflections at the $1, -0.5, n/8$ positions. The intensity on these positions is not affected by temperature in zero field

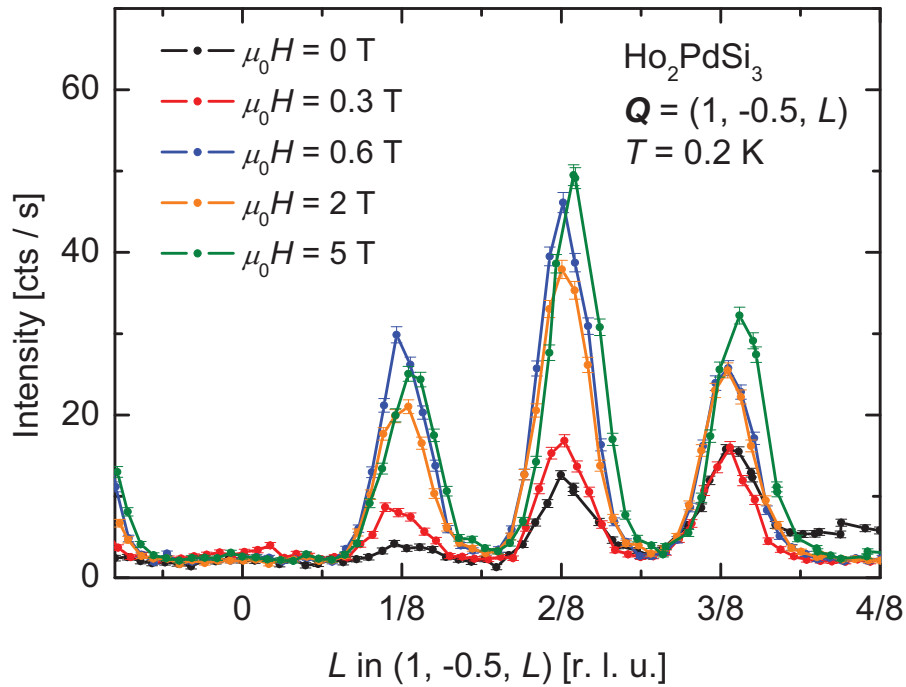


Figure 6.5: Section along the $(1, -0.5, L)$ direction measured at base temperature (200 mK) with increasing magnetic field (parallel $(0, 0, L)$). The $(1, -0.5, L)$ direction is equivalent to $(0.5, 0.5, L)$. The measurement in zero field has been made with a larger incident beam size and has been linearly corrected to the background at $L = 0$ of the field measurements.

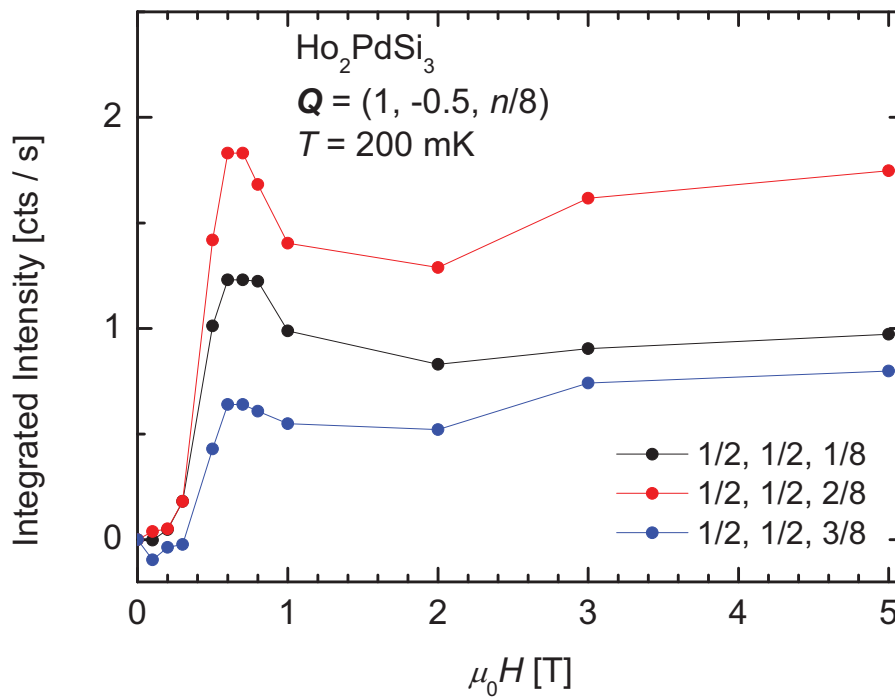


Figure 6.6: Integrated intensities over magnetic field of the reflections shown in figure 6.5. Again the field is along $(0, 0, L)$ and the temperature is 200 mK. The contribution at zero field is subtracted.

indicating the crystallographic structure as solitary reason for intensity on these positions in zero field. In small magnetic fields at base temperature a large increase of intensity on these positions is observed. Figure 6.6 shows the integrated intensity of the three reflections. The magnetic intensity vs. field plot shows maxima for the three reflections around 0.8 T, coinciding with the critical field for the zero field structure. Above 1 T the plot shows an unexpected behaviour with a further increase of the magnetic intensity with increasing field up to the highest measured field of 5 T. The increase of the ferromagnetic intensity on e. g. the 1, 0, 0 reflection is in general agreement with the observed macroscopic magnetization presented in chapter 2. The differences can be accounted due to extinction effects and are corrected as described in chapter 1.5.9.

6.3 Possible scenarios

The observed magnetic structures are non-trivial. Two scenarios are considered possible which will be discussed in the following. (The second scenario is based on an idea of F. Tang [Tang2008] and will be published in a forthcoming cooperate publication).

Both scenarios consider the existence of two different Ho³⁺ sites as important for the observed magnetic structures. The difference between both scenarios is whether the two different Ho³⁺ sites mainly affect either the exchange interaction or the local CEF. The first scenario considers equal magnetic moments that are coupled indirect via an exchange interaction mediated by the conduction electrons (RKKY). The conduction electron density and therefore the exchange interaction at the Ho³⁺ is modulated by the Pd-Si order. The CEF effect here only gives rise to the magneto-crystalline anisotropy. This is referred to as equal moment scenario in the following.

In the second scenario [Tang2008] the local site symmetry yields two different ground states for the Ho³⁺ ion, resulting in different magnetic moments for each site. The exchange interaction is in this scenario only responsible for the zero field magnetic structure. The exchange is weak so that a small external field (< 0.8 T) is sufficient to override it and all observed effects in applied fields result from the two different magnetic moments.

6.3.1 Zero field magnetic structure

In zero field and below T_2 , the simple sine-modulated structure model which has been derived from powder measurements [Szytula1999] does not satisfy the findings of the higher harmonics which imply a squared-up structure. However, a full squared-up modulation with a

propagation of $(1/7, 0, 0)$ cannot be realized without a ferromagnetic component which seems to be absent in powder and single crystal data.

In the case of an equal moment structure, it is possible that the magnetic moments are squaring up with a net magnetic moment per unit cell along $(H, 0, 0)$. This could be in a fan-type structure where the magnetic moments are aligned close to the c -direction (but in more than two directions). If the net moment is very small, the FM reflections would be too small to be resolved. This is very likely because although the magnetic moment direction is mainly along the c -axis, the CEF anisotropy for Ho³⁺ is relatively small as shown by the exchange of the magnetic easy axis with increasing temperature (see chapter 2). The net magnetic moment per unit cell is then balanced by the perpendicular component of the propagation vector. This could mean for instance some large sequence of parallel aligned moments which then is followed by an equal large sequence of moments aligned antiparallel to the first. This sequence is somehow related to a “spin-slip” structure and is possible favored energy-wise by the absence of a ferromagnetic stray field.

In the second scenario [Tang2008] the Ho³⁺ ions have two different ground states with different magnetic net moment. The magnetic moment modulation of $1/7$ is then a consequence of the smallest possible antiferromagnetic arrangement of the given magnetic moments. This arrangement might be in favor in terms of the free energy even if the exchange interaction would not imply a commensurate arrangement. Such an arrangement would not produce a perpendicular component. Therefore, the component δ of the propagation vector indicates a regular reverse of the arrangement i. e., a kind of regularly arranged micro domains.

The observations in an applied magnetic field perpendicular to the c -axis i. e., in the basal plane comply with both scenarios. The effect of the magnetic field is to change the population of the domains. Furthermore, the magnetic moments are forced to align parallel to the magnetic field against the magneto crystalline anisotropy.

The discussed scenarios for the zero-field structure is still more an idea than calculated model. The reason is the very large magnetic unit cell of the zero field structure with the number of free parameters overshadowing the number of observations.

6.3.2 High field magnetic structure

In the case of the high field structure calculations are easier to perform since the number of magnetic moments involved is ‘only’ 4×8 . Still the number of free parameters is much higher than the number of observations making assumptions necessary. The calculation has been

done for the data set measured when the magnetic field was applied parallel $(0, 0, L)$. The modeling for the case with field parallel $(H, -H, 0)$ is also possible in both scenarios. In the following the attempts to fit the data based on the equal moment scenario is presented.

The first model assumes a full ordered moment structure consisting of 8 layers stacked in the c -direction. Each layer has a ferromagnetic component of the magnetic moment parallel to the c -direction. In the case of exchange interaction, an angle between the magnetic moments and to the c -axis is introduced. This angle varies in applied fields from 15° to 9° . The magnetic moment component in the basal plane has to be strict antiferromagnetic to comply with the measured reflections. The direction of the magnetic moment in the plane can be chosen freely under the assumption that at least a three-fold symmetry is conserved. The intensity variations will then be balanced by the contributions from the different domains (equal population assumed). This simple model uses the collinear antiferromagnetic sequence $++---+-$ along the c -axis for the moment fraction in the basal plane while the moment fraction parallel $(0, 0, L)$ is ferromagnetic. Additionally, the moments are antiferromagnetically arranged along the $(H, 0, 0)$ direction. The results of this model are compared to the experimental data and are shown in figure 6.7 for two exemplary magnetic fields.

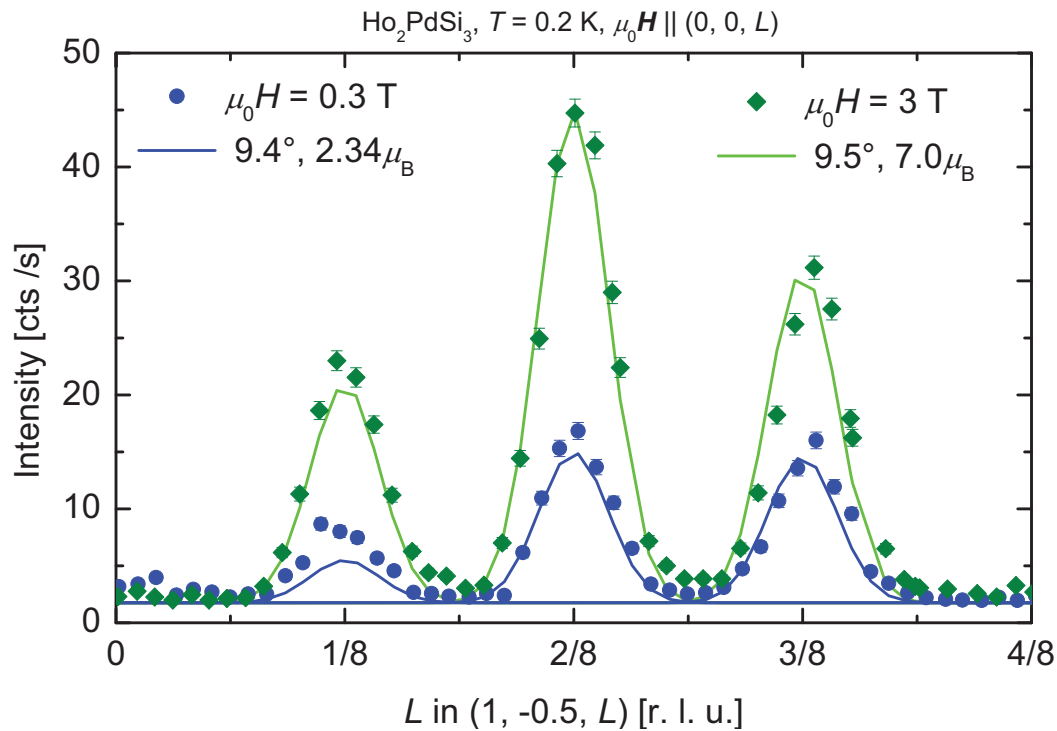


Figure 6.7: Comparison of the model calculation with the experiment (field parallel $(0, 0, L)$). The nuclear contribution and a constant background is added to the model calculation. The $2/8$ reflection has been used for the fitting and the differences can therefore be seen on the $1/8$ and $3/8$ reflection. The biggest discrepancy is found for the $1/8$ reflection at 0.3 T which is underestimated.

The nice feature on this model is that only two parameters are left free: magnitude of the magnetic moment and angle of the magnetic moment towards the c -axis. The ferromagnetic intensity is mostly affected by the magnitude of the magnetic moment while the AFM intensity is mostly affected by the angle of the magnetic moment towards the c -axis. Since the relative intensity between the harmonics of the propagation vector changes only slightly the intensity vs. field relation can be modeled from smallest to highest field. This is visualized in figure 6.8 where the magnitude of the magnetic moment and the angle (inset) is shown. Especially the angle shows an unexpected behavior. In small field the angle rapidly decreases

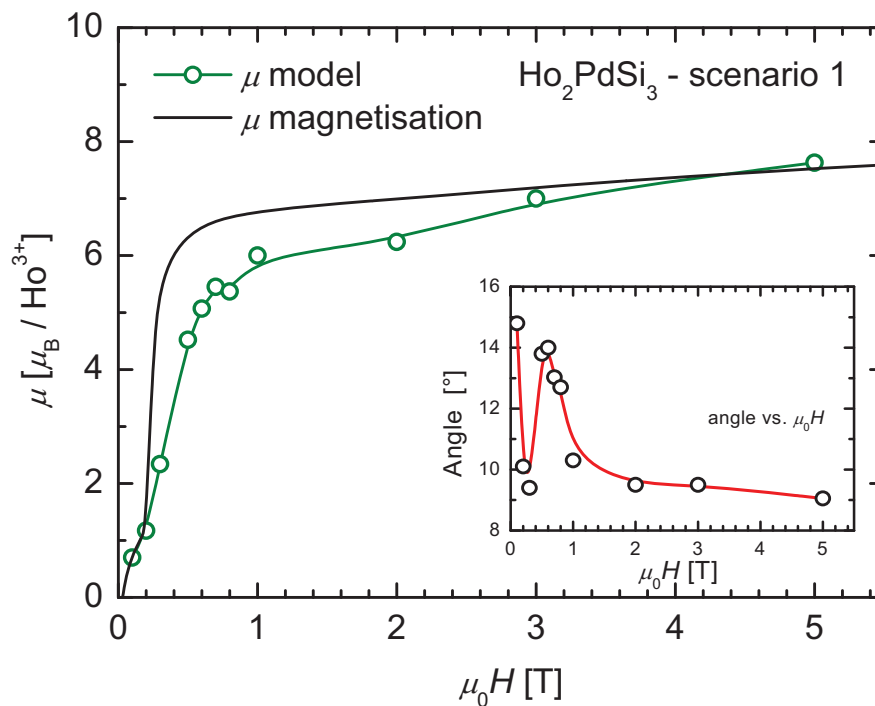


Figure 6.8: Magnetic field dependence (field parallel $(0, 0, L)$) of the two model parameters of scenario one: magnetic moment and angle (inset). The lines are guide to the eye. The black line shows the course of the macroscopic magnetisation from chapter 2.

as the magnetic moments are forced to orient parallel to the c -axis. Above 0.3 T this tendency is suddenly reset and the angle is restored to its initial value. Above 0.5 T the angle again decreases fast, but the rate of decrease in applied magnetic fields is reduced gradually. A possible explanation for the observed behavior is the formation of small areas of the high field phase in the sample. With increasing field the areas grow gradually, but the magnetic moments inside react to the external field. At a field above 0.3 T the small areas begin to overlap thereby increasing the coherence and the strength of the exchange interaction. This

could explain the calculated “reset” of the angle between moment and c -axis. For comparison the macroscopic magnetization from chapter 2 (figure 2.18) is plotted also in figure 6.8.

In the second scenario [Tang2008], it is assumed that the difference between the two Ho³⁺ sites results from different CEF states. Thus their response to the external field is varying. The magnetic unit cell is of the size 1x2x8. The 8 layers are stacked along the c -axis and two moments (μ_1 and μ_2) are in each layer. The stacking sequence of (μ_1 and μ_2) is the same as used in the model presented before (replacing “+” with μ_1 and ”-” with μ_2). Applying a field along c -axis, both moments try to align to the field, however the magnitude of the moments change with different rate. Over the whole field range the magnitude of both moments increases. Initially, the difference between both moments seems to decrease. Above 0.3 T however the difference is increasing strongly corresponding to the increase of intensity in the range 0.3 ~ 0.6 T. After that, one of the moments is reaching its saturation which is not necessarily the saturation moment of the free ion since the saturation in magnetization seems not yet reached until 13 T (see figure 2.18), the difference between the two moments is decreasing corresponding to the decrease in intensity from 0.8 T to 2 T. For further increase of the field, one moment keeps increasing while the other one increases slower, resulting in the further increase of the AFM intensity. The described behavior of the two magnetic moments is shown in figure 6.9. The data from calculation is very close to the measurement.

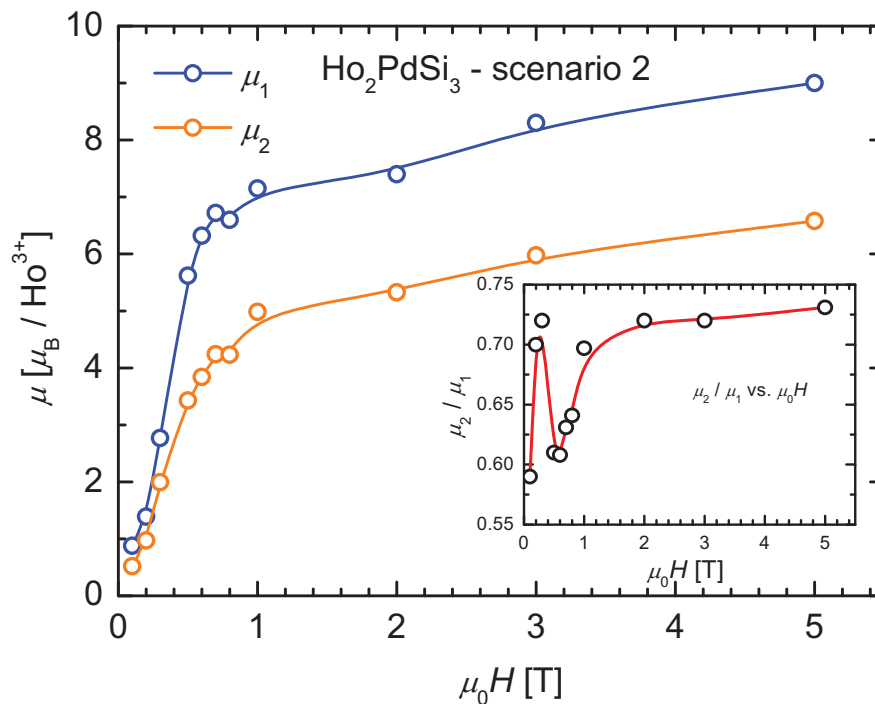


Figure 6.9: Magnetic field dependence (field parallel $(0, 0, L)$) of the two different magnetic moments of scenario two. The inset shows the quotient (μ_2/μ_1). The lines are guide to the eye.

It is worth mentioning that this model does not rule out the possibility of any AFM ordering in the plane. They might be as well present considering the missing moment from the saturation.

6.4 Conclusion

The observed magnetic structures imply a delicate balance between RKKY exchange interaction, crystal electric field, the frustration of nearest neighbour interaction on the triangular lattice and the two different sites of the Ho³⁺ ion.

The zero field magnetic structure was investigated and the propagation vector could be identified to $\tau = (1/7 - \delta, 2\delta, 0)$ where δ is around 0.0024 r. l. u., with the help of a small applied magnetic field. The results clarify the previously reported magnetic structure [Szytula1999]. The magnetic structure is not sinusoidal modulated but rather a squared-up modulated structure. The propagation vector has two components. The 1/7 modulation is commensurate within the experimental error, while the δ component seems to belong to an incommensurate modulation which is superimposed on the first. The zero field magnetic structure of Ho₂PdSi₃ can be compared to the one of Gd₂PdSi₃. Both have the 1/7 modulation in the basal plane. While the magnetic moment of the Gd³⁺ ion is not confined in its direction the magnetic moment of the Ho³⁺ ion is influenced by the surrounding CEF. The compensation of the net magnetic moment of the 1/7 modulation (in a full magnetic moment picture) leads to the observed δ component. In return the magnetic structure of Gd₂PdSi₃, namely the spin-sequence might include all possible directions to compensate the net magnetic moment. The influence of the crystallographic superstructure is apparently weak when the propagation is confined within the rare earth layers.

The existence of an antiferromagnetic structure in applied fields (above 0.8 T) has been proposed and could be identified. The high-field magnetic structure resembles to the case of Tb₂PdSi₃. The differences in the experiment are the absence of reflections along $(0, 0, L)$ in the case of Ho₂PdSi₃. The origin of the difference is to be found in the different magnetic moment direction. When the magnetic field is applied in the basal plane the high field structure is observed coexisting with the zero field structure. The increasing magnetic field only slowly pulls the magnetic moment out of their respective easy direction. The comparison of the magnetic structures of Tb₂PdSi₃ and Ho₂PdSi₃ in field shows the importance of the crystallographic superstructure on the magnetic structure if the propagation is along the $(0, 0, L)$ -direction.

Further experiments like angular dependent magnetisation are needed to distinguish between the two scenarios i. e. to identify an easy magnetic direction at an angle from the main crystallographic directions. Additionally, neutron scattering experiments on Gd₂PdSi₃ can be used to evaluate the role of the CEF for the other R_2 PdSi₃ compounds. The spin sequence which both models use is bijective in respect to the experimental data. No other spin-sequence can be constructed to model the distinctive reflection pattern. Both models can be used to describe the field dependence of the magnetic intensity. Though the presented model for the high field magnetic structure is not definite and the real structure may even be a combination of two different models the spin sequence (+ + - - + + -) is unambiguous.

7. Er_2PdSi_3 , Tm_2PdSi_3 and Dy_2PdSi_3

7.1 Zero field magnetic structure and the meaning of T_2 in Er_2PdSi_3

The ac-susceptibility measurement of Er_2PdSi_3 with one frequency (962 Hz) has been shown in chapter 2. Here, the frequency dependence of the ac-susceptibility measured along the $(0, 0, L)$ direction is shown in figure 7.1. Recalling the frequency dependency of T_2 in

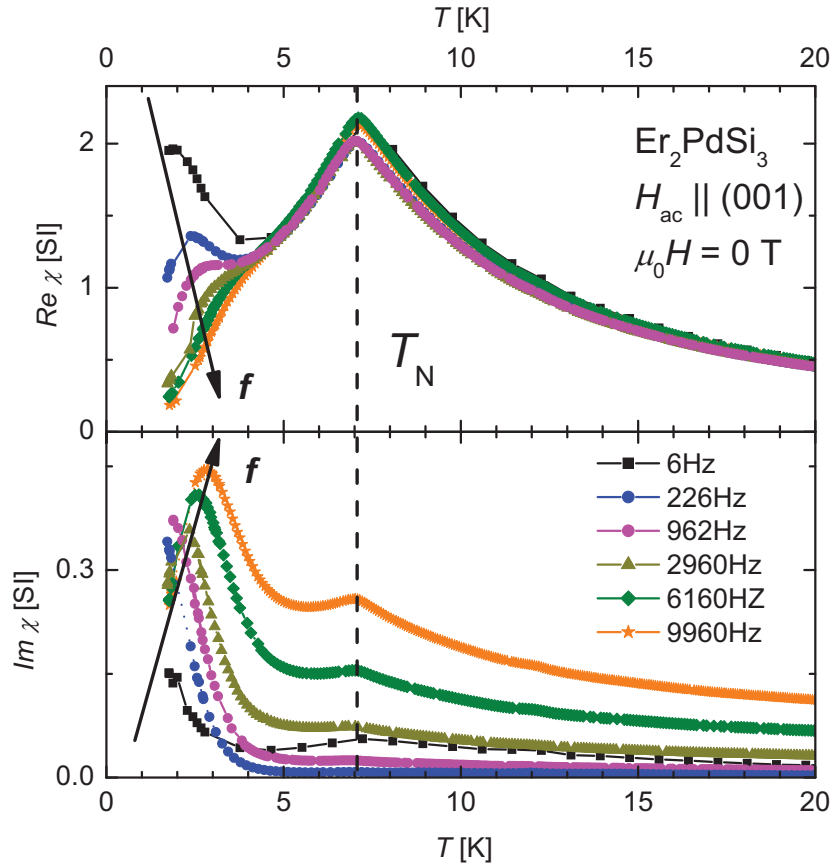


Figure 7.1: Real and imaginary part of the ac-susceptibility for Er_2PdSi_3 measured with an ac-field along the $(0, 0, L)$ -direction. The Néel temperature is marked by a dashed line. The phase transition at T_2 shows a strong dependency on the ac-frequency.

Tb_2PdSi_3 (figure 5.1), figure 7.1 obviously shows a similarity. Er_2PdSi_3 has a strong frequency dependency of T_2 in both real and imaginary part. The imaginary part shows a maximum which is found at higher temperature for increasing frequency as in the case of Tb_2PdSi_3 . The real part of the susceptibility is, however, different. The signal measured at $T = 2$ K decreases in magnitude with increasing frequency.

In chapter 5 it has been emphasized that T_2 is connected to the SRC in Tb_2PdSi_3 . Therefore, neutron scattering on the E2 diffractometer (see 1.5.2) on single crystalline Er_2PdSi_3 had been performed in $(HK0)$ as well as in (HHL) in scattering geometry. As in the Tb_2PdSi_3 compound, LRO magnetic intensity is observed at the lowest temperature. In contrast to

Tb_2PdSi_3 , no magnetic SRO is observed below T_N in the investigated scattering planes. Figure 7.2 shows the reciprocal $(HK0)$ -plane of Er_2PdSi_3 at $T = 4.0$ K. This reciprocal plane contains the nuclear reflections $\{1, 0, 0\}$, $\{2, 0, 0\}$ and $\{1, 1, 0\}$. Two strong rings originate from scattering on polycrystalline copper (sample holder). The positions of the magnetic reflections correspond to the magnetic propagation vector of $\tau = (1/9, 1/9, 0)$ and the antiferromagnetic domains generated from the hexagonal symmetry. The distinction between either a single- τ , multi-domain structure or a multi- τ , single-domain structure is from a zero field diffraction

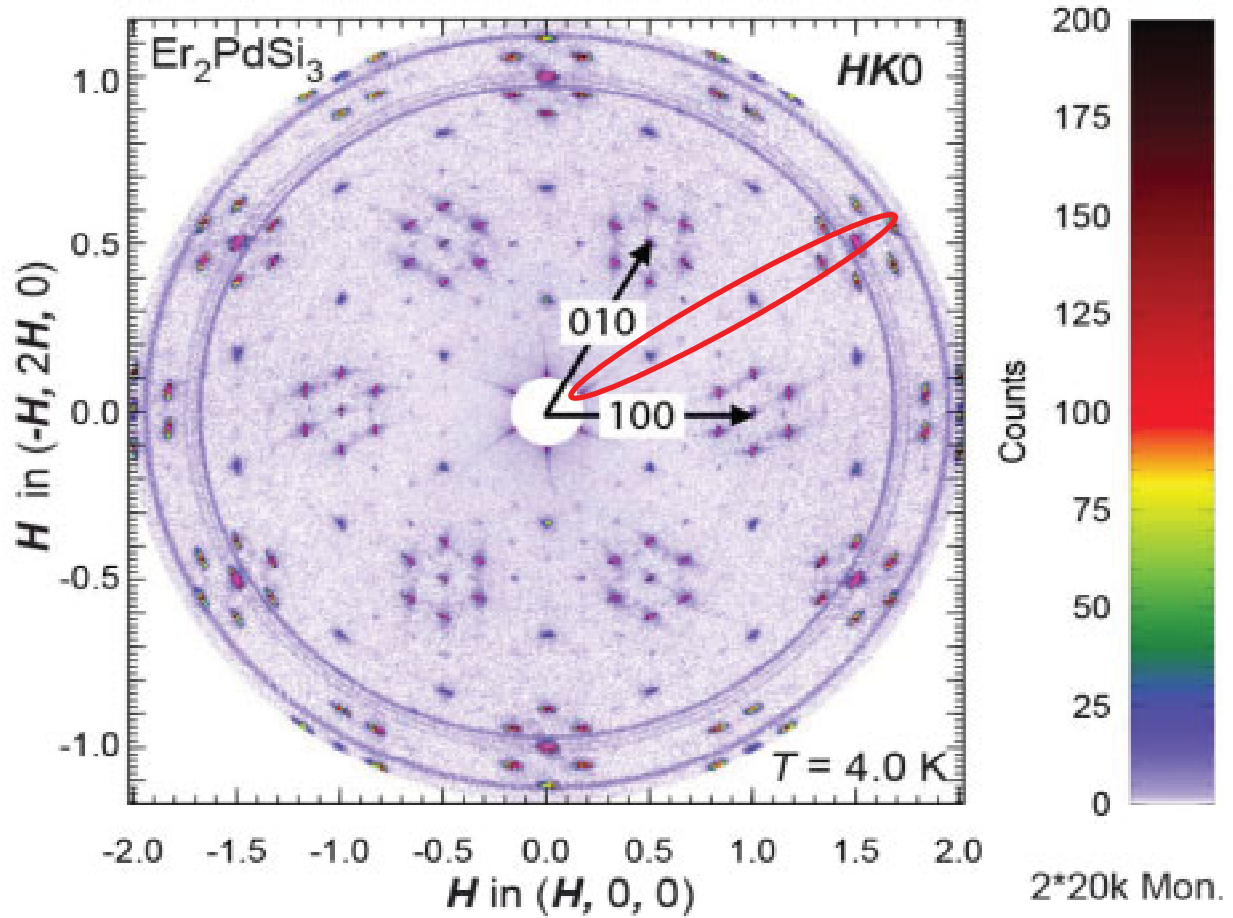


Figure 7.2: Full reciprocal $(HK0)$ -plane of Er_2PdSi_3 at $T = 4$ K. The reciprocal lattice directions $(1, 0, 0)$ and $(0, 1, 0)$ are marked with arrows. The red-circled area marks the section shown in figure 7.3. The two outer rings originate from the scattering on polycrystalline copper from the sample holder.

experiment not possible. The magnetic moments are aligned along the hexagonal c -axis deduced from the intensity distribution measured in (HHL) scattering geometry. This is shown in more detail in the Appendix A. Figure 7.3 shows a section of the reciprocal plane at $T = 0.3$ K along the $(H, H, 0)$ direction. The section is circled in red in figure 7.2. The appearance of different odd harmonics $(1/9, 3/9$ and $7/9)$ at low temperatures indicates a squaring-up of the magnetic moment modulation. Conditional upon the propagation vector the reflections due to odd and even harmonics (if present) coincide on the same positions. In the

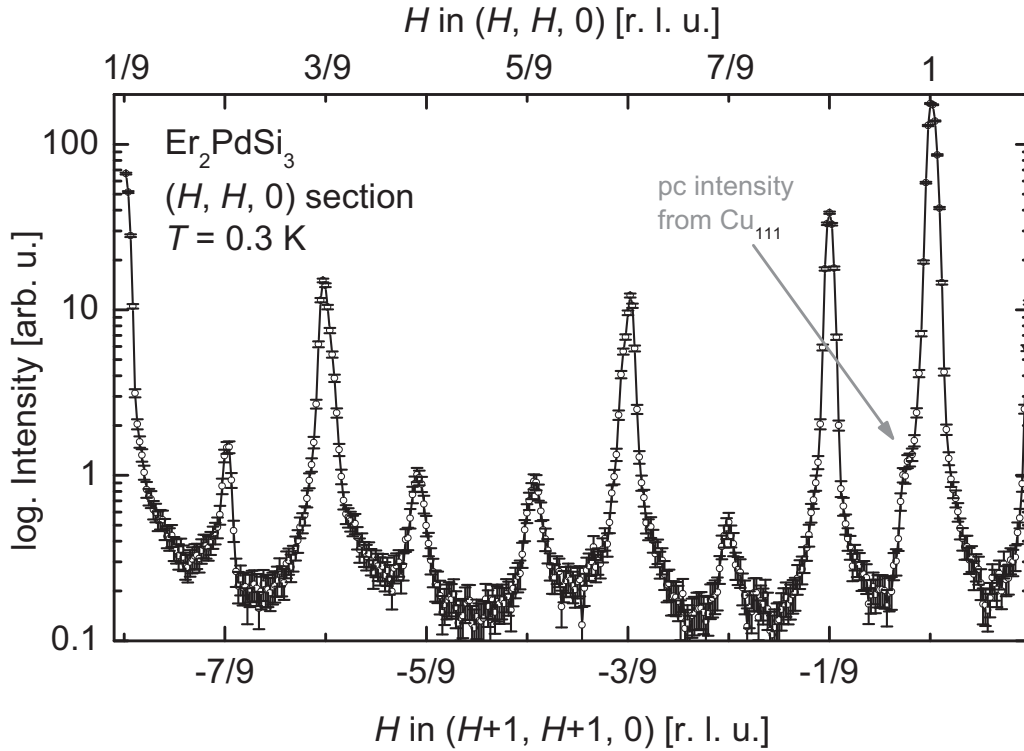


Figure 7.3: Section of the magnetic structure of Er_2PdSi_3 as marked in figure 7.2. The magnetic satellites originating from the 1, 1, 0 reflection are numbered on the bottom axis. Magnetic satellites originating from 0, 0, 0 are numbered on the top axis. Mind the logarithmic intensity scale.

following, only the presence of odd harmonics is assumed. The ratio of the 1/9 to the 3/9 is as to be expected for a squared up modulation 3:1. The ratios of the 1/9 to the 5/9 and 7/9 are however too small (21:1 and 17:1) for a fully squared-up modulation.

Further deviations from a squared up structure are the magnetic satellites near the positions where the 5th harmonics are expected. These magnetic satellites can be indexed with $(0.434\ 0.434\ 0)$ and $(0.562\ 0.562\ 0)$ instead of $(-5/9\ -5/9\ 0)$ and $(5/9\ 5/9\ 0)$, respectively.

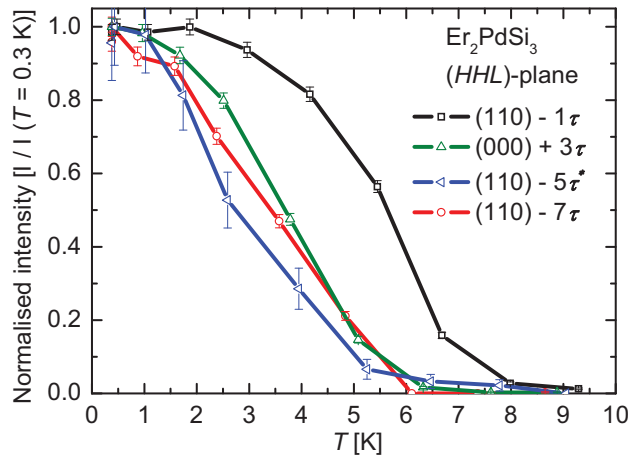


Figure 7.4: Normalised intensity of the different harmonics of the magnetic propagation vector of Er_2PdSi_3 .

Figure 7.4 shows the temperature dependence of the antiferromagnetic satellites. The temperature dependence of the 1st harmonic is drastically different from that of the other satellites. While the 1st harmonic is present in the whole magnetically ordered temperature range below $T_N = 7$ K the other satellites are starting to gain in intensity only from below 5 K. Their intensity increases steadily with decreasing temperature in an upturned curvature until the intensity saturates around 2 K corresponding to the characteristic temperature T_2 found in the ac-susceptibility.

From the before mentioned fact and the absence of SRC it can be concluded that Er₂PdSi₃ first enters a simple sinusoidal amplitude modulated antiferromagnetic phase below T_N while, upon lowering the temperature, the magnetic structure squares-up continuously down to T_2 . In the temperature range between 0.3 K and T_N all magnetic intensity is of LRO-type. Therefore, the transition found in the ac-susceptibility at T_2 is the transition to a squared-up magnetic structure. Possibly, the temperature T_2 in the compound Ho₂PdSi₃ is bound to the same phenomenon as in Er₂PdSi₃. Apparently, the frequency dependence in ac-susceptibility measurements of magnetic phase transitions from sine- to squared-up modulation had never been investigated before. Publications on this issue were searched for but could not be retrieved.

The variations of the magnetic structure with respect to a full squared-up structure are not surprising. The propagation vector with its odd denominator is incompatible with a purely antiferromagnetic, full-ordered moment, squared-up structure. If a collinear, full magnetic moment structure is assumed the odd denominator implies a ferromagnetic net component per magnetic unit cell. This is the similar case in Ho₂PdSi₃ but there a second component of the propagation vector was identified. It had been speculated that this second component equals the net magnetic moment per unit cell generated by the propagation vector. Different to Ho₂PdSi₃ no second component of the propagation vector is found in Er₂PdSi₃. If the magnetic structure is a full ordered moment structure then in consequence a net (ferro-) magnetic moment is expected. This FM component has been observed on the 1, 1, 0 reflection. A calculation of the FM intensity yields a ferromagnetically ordered moment of 2.05 μ_B . In the picture of a collinear, full moment structure, this corresponds to an AFM structure in which 50 magnetic moments are aligned parallel to (0, 0, L) and the remaining 31 are aligned anti-parallel. The simplest approach of 4*(5*(+)) and 4*(-)) and 5*(6*(+) and 3*(-)) in a consecutive arrangement, however, does not reproduce the observed AFM intensity. Again, the problem to deduce the correct spin-sequence is present. The here presented ansatz can be used as a base for a combination calculation with a subsequent sorting routine.

Whether this calculation could result in a unique magnetic structure solution is still doubtful. The real magnetic structure is probably even larger than it is deduced from the propagation vector. Especially the positions of the 5th harmonics do indicate this possibility.

In a recent neutron scattering experiment indications for kinetic inhibition of the magnetic order has been found. After cooling the sample below T_N (but above T_2) no magnetic reflections at $\mathbf{G}+\boldsymbol{\tau}$ could be found. The sample was then warmed up above T_N and cooled down again. After this heat treatment the known magnetic structure was observed.

7.2 Magnetic neutron diffraction of Tm₂PdSi₃

Tm₂PdSi₃ orders at around 1.8 K. Ac-susceptibility has been measured down to 0.4 K without indication of a second phase transition in this temperature range (see figure 4.6). The measurement used a special setup during a neutron diffraction experiment [Faulhaber2008]. The low ordering temperature made the characterization difficult or impossible by the macroscopic methods and measurement systems, successfully used on the other compounds. In fact, the possibility of neutron diffraction at low temperatures became earlier available than the possibility of low-temperature ac-susceptibility. The derivation of the phase diagram and the investigation of the magnetic structure in magnetic fields are planned in the future. A recent experiment indicates the existence of a high field AFM phase also for this compound, which might be correlated to the FiM phase of Tb₂PdSi₃ and Ho₂PdSi₃.

The neutron scattering in zero field experiment used the E2 diffractometer with a ³He-VTI insert. An earlier experiment with the same setup indicated the *c*-component of the propagation vector to be 1/16, but the in-plane component could not be resolved. The positions of the reflections due to the in-plane component of the propagation vector seemed to be a mixture of at least two different planes observed simultaneously due to lack of resolution, specifically in the direction perpendicular to the scattering plane. This is the direct result of the usage of a focused monochromator, which causes the neutron beam to be vertically divergent.

The experiment on E2 used a not-focused monochromator, significantly increasing the resolution in the out of plane direction. The flat-cone technique of the E2 allowed us to map the reciprocal space by measuring $(H, K, n/16)$ and $(H+n/16, H-n/16, L)$ planes with $n = 0, \dots, 7$. The comparison with a measurement above T_N indicates the absence of a ferromagnetic contribution on the nuclear positions. Figure 7.5 shows the reciprocal $(H+1/16, H-1/16, L)$ -plane at $T = 0.4$ K. Weak intensity due to a nuclear contribution is found as tails of $\{0, 0, 2\}$

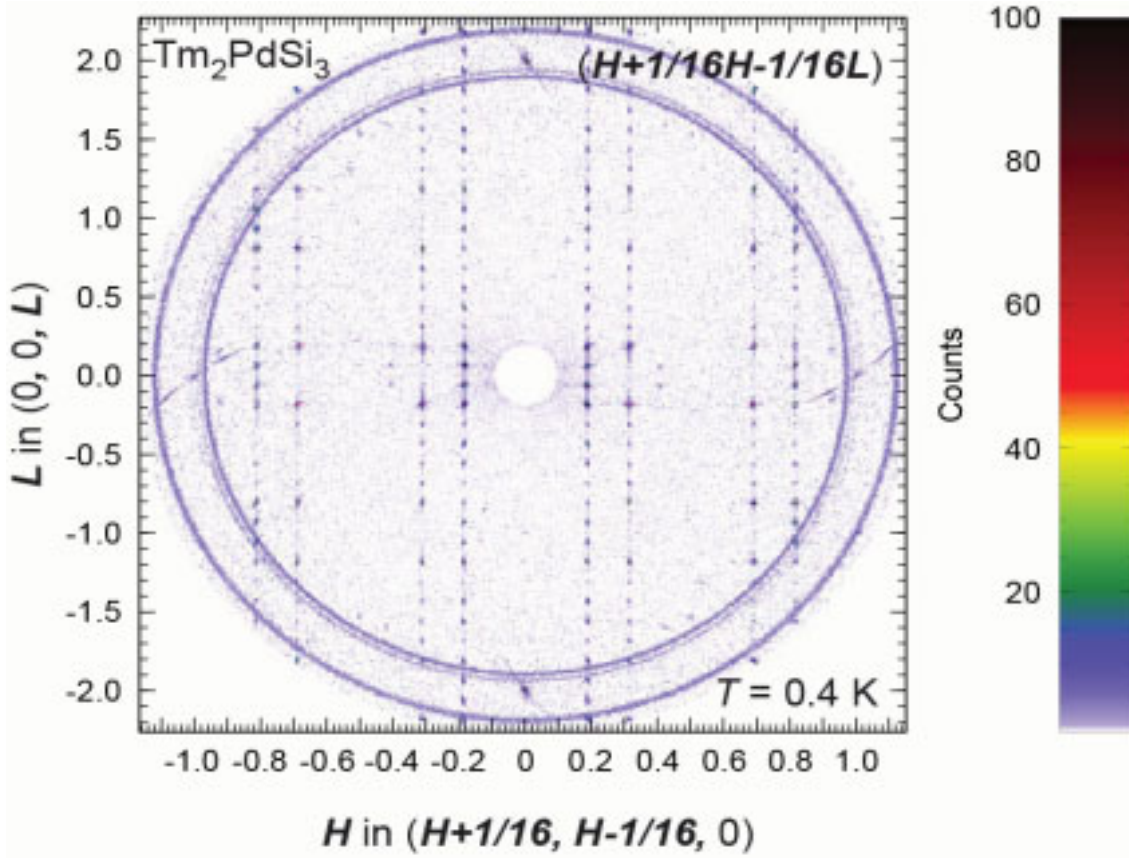


Figure 7.5: Reciprocal $(H+1/16, H-1/16, L)$ -plane of Tm_2PdSi_3 at $T=0.4$ K. The observed scattering on the $\{0, 0, 2\}$ and $\{1, 1, 0\}$ positions is due to the limited resolution and the strong intensity of the reflections. It originates from the neighbouring (HHL) -plane. The weaker $\{0, 0, 1\}$ reflections are not observed. The magnetic intensity observed for $|H| = 3/16, 5/16, 11/16$ and $13/16$ is not observed in the neighbouring planes with a distance of $(1/16, -1/16, 0)$.

and $\{1, 1, 0\}$. In addition, the rings from the scattering on the copper sample holder are present. Magnetic intensity is found on positions for $|H| = 3/16, 5/16, 11/16$ and $13/16$ from a lattice point. The corresponding L values are $m/16$ with m being an odd integer.

The magnetic structure is difficult to describe. The magnetic intensity as a function of the scattering vector indicates a magnetic moment direction in the order of 30° to the c -axis. In a commensurate description two propagation vectors are needed $\tau_1 = (1/8, 1/8, 1/16)$ and $\tau_2 = (1/8+1/16, 1/8-1/16, -1/16)$. These vectors, their higher harmonics and the sum of the two can index all of the observed magnetic intensity. However, on some positions given by these two vectors no magnetic intensity is observed, especially for $L = m/16$ for even values of m . The clarification of the magnetic structure is beyond this thesis due to the large magnetic unit cell and the difficulty to separate the contributions from different domains. It is planned to study the magnetic structure of Tm_2PdSi_3 in applied magnetic fields to achieve a single domain state.

The magnetic structure of Tm_2PdSi_3 is insofar of importance for the understanding of the series $R_2\text{PdSi}_3$ since the moment direction in this compound has an in-plane component as well as one parallel to the c -axis. The resulting magnetic structure can be compared to Er_2PdSi_3 and Ho_2PdSi_3 regarding the in-plane component of the propagation vector and to Tb_2PdSi_3 which has the identical L -component of the propagation vector. In contrast to Tb_2PdSi_3 the magnetic structure cannot be described with a partly enlarged unit cell and one propagation vector $(0, 0, 1/16)$ since no magnetic intensity is observed for $H = 0$.

7.3 Magnetic neutron diffraction of Dy_2PdSi_3

The magnetic structure of Dy_2PdSi_3 has been investigated in a recent E2 measurement [HMIRReport2008] to complete the set of magnetic structures for the heavy rare earths of the $R_2\text{PdSi}_3$ series. Dysprosium has a high absorption cross section for neutrons and the investigation of the magnetic structure with neutron diffraction is still in an early stage. Some statements are therefore only speculative. However, the results shown for the reciprocal

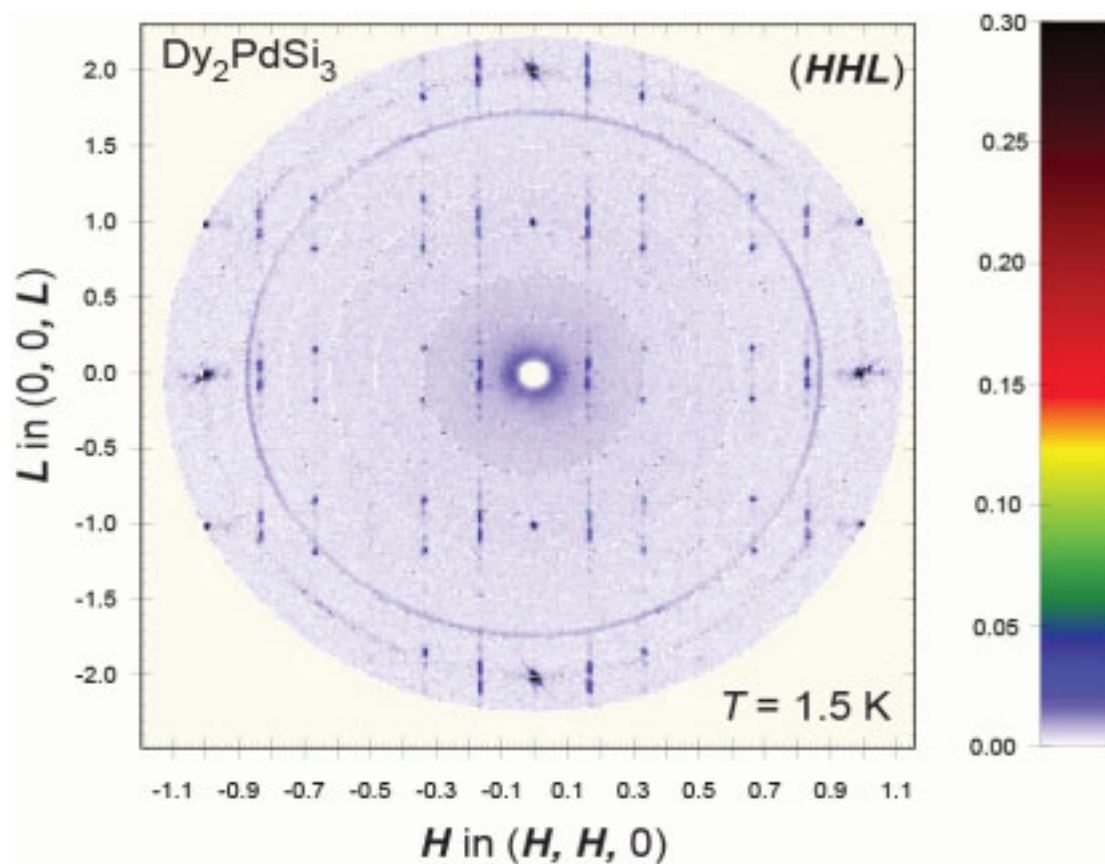


Figure 7.6: Reciprocal (HHL) -Plane of Dy_2PdSi_3 at $T = 1.5$ K measured at the E2 diffractometer after its revision. The ring-texture is due to the computed composition of the new four area detectors. The blue ring-line originates from scattering on the aluminium sample holder. Intensity due to the nuclear superstructure is present at $H = 0.5$ although very faint. The magnetic reflections are always double-peaks.

(*HHL*)-plane in figure 7.6 fit well in the context of the above discussed magnetic structure of Tm₂PdSi₃ and are presented despite the initial status of the investigations. Similar to Tm₂PdSi₃ the magnetic moment direction seems to be neither along the *c*-axis or in-plane. As described in chapter two the magnetic easy axis changes around 25 K from in-plane (the high temperature easy-axis predicted by the Stevens-factor α) to the *c*-axis. Under the influence of a magnetic field the easy axes do exchange again (around 2.5 T at $T = 2$ K, see figure 2.17). In figure 7.6, magnetic intensity due to the zero-field magnetic structure is found at positions describable with the propagation vectors $\tau = (1/6, 1/6, 1/24)$. Additional magnetic intensity is found on positions with $L = n/24$ values. This fact indicates a non-sine modulated structure in *L*-direction. Further magnetic intensity is also found for values two times τ .

The magnetic structure and the magnetic phase diagram of Dy₂PdSi₃ are beyond the scope of this thesis and the zero field structure is presented mainly for two reasons. First, the initial idea of the magnetic propagation vector is the basis for the following investigations. Second, the case of Dy₂PdSi₃ does compare to Tm₂PdSi₃. In both compounds the direction of the magnetic moment is neither in-plane nor parallel to the *c*-axis. The resulting magnetic structure has in both cases a large magnetic unit cell in-plane and an even larger unit cell in *L*-direction. The factor 24 indicates again the closeness to the crystallographic superstructure. The in-plane propagation of $(1/6, 1/6, L)$ is in good agreement with predictions for the Fermi-nesting in this series. These predictions are supported by angle-resolved-photo-emission measurements [Ivonosov2008].

8. Discussion and Conclusions

The systematic comparison of susceptibility and magnetization for the series of $R_2\text{PdSi}_3$ has been made in chapter 2. The quantification of this comparison, namely the calculation of the dominant CEF parameter and the value of the exchange interaction is presented in the first part of this chapter. Detailed investigations of the macroscopic and microscopic magnetic properties have been presented in the chapters 3, 5 and 6 for Gd_2PdSi_3 , Tb_2PdSi_3 and Ho_2PdSi_3 . In the second part of this chapter concepts are tested to understand the magnetic behavior in general. Combined with the initial result of neutron scattering on Dy_2PdSi_3 , Er_2PdSi_3 and Tm_2PdSi_3 the possible underlying mechanisms for the observed magnetic properties with the hindsight of the special crystallographic structure are discussed.

8.1 The role of the CEF effect in $R_2\text{PdSi}_3$

The paramagnetic behavior of the $R_2\text{PdSi}_3$ compounds in the temperature range 150 K to 300 K is dominated by the CEF effect. In order to quantify the magneto-crystalline anisotropy of the $R_2\text{PdSi}_3$ the results of the ac-susceptibility measurements were analyzed in the framework of CEF Hamiltonian and isotropic two-ion exchange. The CEF Hamiltonian in hexagonal symmetry can be expressed as [Hutchings1964]

$$H_{\text{CEF}} = B_2^0 \hat{O}_2^0 + B_4^0 \hat{O}_4^0 + B_6^0 \hat{O}_6^0 + B_6^6 \hat{O}_6^6 \quad (18)$$

with the CEF parameters B_l^m and the Stevens operators \hat{O}_l^m . In lowest order the paramagnetic behavior due to the CEF can be described by the B_2^0 parameter. Assuming an isotropic two-ion exchange interaction

$$H_{\text{ex}} = \sum_{ij} (-1/2) J(ij) \hat{\mathbf{J}}(i) \hat{\mathbf{J}}(j) \quad (19)$$

it is possible to evaluate the crystal field parameter B_2^0 and the value of the exchange integral $J(\mathbf{Q}=0) = \sum_j J(ij)$. For this purpose, we use the equations [Jensen1991]

$$B_2^0 = -\frac{k_B(\theta_c - \theta_a)}{\frac{6}{5}(\mathbf{J} - \frac{1}{2})(\mathbf{J} + \frac{3}{2})} \quad (20)$$

and

$$J(\mathbf{Q}=0) = \frac{k_B(\theta_c + 2\theta_a)}{\mathbf{J}(\mathbf{J}+1)} \quad (21)$$

where J is the quantum number of the total orbital momentum for the trivalent state of the rare earth ion according to Hund's rule [Hund1925]. Table 5 displays the asymptotic paramagnetic Curie temperatures obtained from the Curie-Weiss fit together with the values for B_2^0 and $J(\mathbf{Q} = 0)$. The error for the asymptotic Curie temperature and therefore the error for B_2^0 and $J(\mathbf{Q} = 0)$ originate from the standard deviation of the Curie-Weiss fit, a systematic error for the temperature measurement (± 0.25 K) and for the calibration of the susceptibility. The susceptibility of the Ho_2PdSi_3 compound does not show a Curie-Weiss behavior up to

R	$\alpha \cdot 10^2$	$\langle r^2 \rangle [\text{\AA}^2]$	$B_2^0 [\mu\text{eV}]$	$B_2^0/\alpha [\text{meV}]$	$B_2^0/(\alpha \cdot \langle r^2 \rangle) [\text{meV}/\text{\AA}^2]$	$J(\mathbf{Q}=0) [\mu\text{eV}]$	$\alpha \cdot 10^2$
Gd	-	0.2428	-	-	-	500 \pm 17	-
Tb	-1.0101	0.2302	98 \pm 5	-9.74 \pm 0.48	-42 \pm 2	32 \pm 8	-1.0101
Dy	-0.6349	0.2188	14 \pm 3.3	-2.30 \pm 0.52	-10 \pm 2	29 \pm 5.5	-0.6349
Er	0.2540	0.1991	-25 \pm 2.5	-10.18 \pm 0.98	-51 \pm 5	0.4 \pm 4.5	0.2540
Tm	0.10101	0.1905	-60 \pm 2	-6.0 \pm 0.2	-31 \pm 1	-25 \pm 4	0.10101

Table 5: Compilation of results of the Curie-Weiss analysis for $R_2\text{PdSi}_3$ and theoretical values for R^{3+} ions:

- α Stevens parameter from reference [Hutchings1964];
- $\langle r^2 \rangle$ averaged $4f$ wave function from reference [Fulde1986];
- θ_c and θ_a asymptotic paramagnetic Curie temperatures from the Curie-Weiss analysis for the measurements parallel c and a , respectively;
- B_2^0 and $J(\mathbf{Q}=0)$ parameters from equations (4) and (5); θ_c and θ_a are listed in table 1;

300 K and therefore the determination of the B_2^0 CEF parameter is not possible from our measurement. The second calculated parameter from the ac-susceptibility measurements in the paramagnetic state is the magnitude of the exchange interaction $J(\mathbf{Q} = 0)$ which is positive (ferromagnetic) for $R = \text{Gd}$, Tb and Dy , negative (antiferromagnetic) for $R = \text{Tm}$ and close to zero for $R = \text{Er}$. The value for Gd_2PdSi_3 is an order of magnitude larger compared to the others. According to [Jensen1991] the exchange interaction $J(\mathbf{Q} = \boldsymbol{\tau})$ can be calculated with the critical field H_{c2} (at which the sample is ferromagnetic) and the ferromagnetic exchange $J(\mathbf{Q} = 0)$.

$$H_{c2} = \frac{J(J(\mathbf{Q}) - J(\mathbf{Q} = 0))}{g\mu_B} \quad (22)$$

The only $R_2\text{PdSi}_3$ compound for which H_{c2} could be determined is Gd_2PdSi_3 (9.4 T). For Gd^{3+} ($J = 7/2$ and $g = 2$) the resulting value of $J(\mathbf{Q} = (1/7, 0, 0))$ is 0.81 meV. $J(\mathbf{Q} = 0)$ is taken from table 5. The knowledge of the critical fields for the other compounds would allow

to calculate $J(\mathbf{Q})$ also for the other compounds. In addition, if the compounds would have the same propagation vector the critical field could be calculated.

Considering the Tb_2PdSi_3 and Er_2PdSi_3 compounds the model with B_2^0 as the main crystal-electric field parameter is able to describe the paramagnetic properties satisfactorily in the high temperature limit. The CEF parameter divided by the Stevens factor B_2^0/α (table 5) is nearly equal for these two compounds. The determination of the easy and hard magnetic axis from the sign of the Stevens factor α is also correct for Ce_2PdSi_3 [Saha2000] and Tm_2PdSi_3 . Saha et al. determined the B_2^0 value to be 870 μeV for Ce_2PdSi_3 using a CEF model [Saha2000]. The values of B_2^0/α are approximately: -15 meV for Ce_2PdSi_3 , -6 meV for Tm_2PdSi_3 and -10 meV for Tb_2PdSi_3 and Er_2PdSi_3 . These values still contain the average $\langle r^2 \rangle$ over the $4f$ wave functions. Therefore, dividing B_2^0 by the Stevens factor α and the average $\langle r^2 \rangle$ values (see e.g. [Fulde1986]) one obtains a main crystal electric field parameter of $-40 \text{ meV}/\text{\AA}^2$ for the $R_2\text{PdSi}_3$ series (see table 5). These values are equal within a margin of 25 % for the investigated $R_2\text{PdSi}_3$ compounds except for Dy_2PdSi_3 . The value of the CEF parameter compares to the CEF parameter of the pure rare-earth metals. Using the known asymptotic paramagnetic Curie temperatures [Jensen1991] and utilizing the identical calculation the main crystal electric field parameter is in a comparable range ($-33 \text{ meV}/\text{\AA}^2$ for Tb; $-39 \text{ meV}/\text{\AA}^2$ for Dy; $-65 \text{ meV}/\text{\AA}^2$ for Er; $-52 \text{ meV}/\text{\AA}^2$ for Tm). The intersecting Pd / Si layers slightly increase the anisotropy when the magnetic moment is in the basal plane (Tb), while they slightly decrease the anisotropy when the magnetic moment is along the c -axis. In the case of Dy another role of the Pd / Si might be indicated. As stated higher order parameters of the CEF-Hamiltonian might be reconsidered. The crossing of easy and hard magnetic axis is also observed in compounds where the CEF leads to a ground state of mixed wave functions [Morin1988].

The magnetization measurements in the ordered state indicate a delicate balance between antiferromagnetic and ferromagnetic exchange interactions. All investigated compounds show hysteretic behavior in applied magnetic fields. In the case of Gd_2PdSi_3 , Er_2PdSi_3 and Ho_2PdSi_3 transitions to a magnetic phase with an induced ferromagnetic component at low external fields are observed. Tb_2PdSi_3 and Dy_2PdSi_3 seem to have a ferromagnetic component even in zero-field indicated by the strong increase of the magnetization in small fields. The proximity to ferromagnetism also becomes manifest in the positive values of $J(\mathbf{Q} = 0)$. However, neutron diffraction in zero field did not observe a ferromagnetic component neither in polycrystalline Dy_2PdSi_3 [Szytula1999] nor in Tb_2PdSi_3 (see chapter 5.3).

The CEF is dominated by the B_2^0 term for Tb_2PdSi_3 and Er_2PdSi_3 and determines the magnetic easy direction within the ordered state, too. In contrast, the magnetic easy and magnetic hard directions in the ordered state are determined by higher order terms for Dy_2PdSi_3 and Ho_2PdSi_3 . This corresponds to the crossing of magnetic easy and hard direction in the paramagnetic state far above the Néel temperature in both compounds.

8.2 Zero field magnetic structures

Accompanied by the necessary experiments for the thesis additional measurements on Ce_2PdSi_3 (neutron diffraction) and Pr_2PdSi_3 (ac-susceptibility on polycrystalline material) have been performed and are presented in table 6. These results are shown only for completeness and will not be discussed further. All previous published magnetic structures by Szytula et al. [Szytula1999], which were derived by means of neutron diffraction on powder, have been corrected by the presented single crystal diffraction measurements. Especially, the tendency to a full ordered moment structure as ground state of the $R_2\text{PdSi}_3$ had been overlooked in the powder measurements due to the small intensity of the higher harmonics.

The zero field magnetic structures can apparently be classified into two cases. Either, the magnetic propagation vector is confined to the basal plane as in Gd_2PdSi_3 , Ho_2PdSi_3 and

Compound	$T_N; T_2$ [K]	τ [r. l. u.]	Comments	Reference
Ce_2PdSi_3	3; ~ 2	(0.22, 0, 0.2), (-0.35, 1, 0.1)	AFM; multi- τ ?; μ ?	preliminary results*
Pr_2PdSi_3	1.67; 0.63	-	magnetic structure unknown	preliminary results*
Nd_2PdSi_3	17	FM	$\mu \parallel c$	[Szytula1999]
Eu_2PdSi_3	40; 10	-	Eu^{2+} from lattice constants; magnetic structure unknown	[Mallik1998]
Gd_2PdSi_3	21.5; -	(1/7, 0, 0)	$\mu \perp c$?	this work*
Tb_2PdSi_3	23.6; 5	(0, 0, 1/16)	2* a , squared up; $\mu \perp c$ onset of SRC at T_2	this work
Dy_2PdSi_3	8.2; 2.6	(1/6, 1/6, 1/24)	non-sine mod. at 1.5K; “squaring-up” at T_2 ? μ ?	this work*
Ho_2PdSi_3	8.0; 2.3	(1/7+ δ , -2 δ , 0)	squared up at 1.5K; squaring up at T_2 ?; $\mu \parallel c$	this work*
Er_2PdSi_3	7.0; 2	(1/9, 1/9, 0)	squaring up at T_2 ; $\mu \parallel c$	this work
Tm_2PdSi_3	1.8; -	(1/8, 1/8, 1/16) (3/16, 1/16, 1/16)	squared up; $\mu \sim 30^\circ$ to c	this work*

Table 6: Overview of the magnetic structures as far as they could be clarified with the here presented work. Results with a question mark are insufficiently experimentally backed. (* so far unpublished results). Investigations on $R_2\text{PdSi}_3$ with the light rare earths Ce and Pr are commencing.

Er_2PdSi_3 or the propagation vector is along the c -axis as in Tb_2PdSi_3 , Dy_2PdSi_3 and Tm_2PdSi_3 . In the first case the magnetic structure is determined by the antiferromagnetic exchange in the rare earth layers and will be referred to as intra-plane compounds. In Ho_2PdSi_3 and Er_2PdSi_3 it seems experimentally assured that also the direction of the magnetic moments is along the c -axis. In the case of Gd_2PdSi_3 the magnetic moment direction is not restricted by CEF effects and might be a special case. Apparently, the crystallographic superstructure does not play a role in these cases.

In the second case the antiferromagnetic exchange is via the Pd/Si layers. This case will be referred to as inter-plane compounds. In the inter-plane compounds the crystallographic superstructure does influence the resulting magnetic structure heavily. The magnetic unit cell of Tb_2PdSi_3 , Dy_2PdSi_3 and Tm_2PdSi_3 in zero field is an integer multiple of the crystallographic superstructure cell. In applied magnetic field (for the case of Tb_2PdSi_3) the magnetic structure mimics the crystallographic structure even stronger.

The application of a magnetic field modifies not only the magnetic structure but probably even the type of exchange. Ho_2PdSi_3 exhibits antiferromagnetic intensity on exactly the same positions where the nuclear superstructure peaks are found when a field is applied. Here, the magnetic field seems to change the exchange from intra-plane to inter-plane. The connection to the FiM phase will be drawn in the next chapter.

Still, questions on particularities of the observed zero-field magnetic structure remain. The investigation of the magnetic structures in an applied magnetic field might give the possibility to distinguish clearly the contribution from different magnetic domains.

8.3 Generic phase diagram

The comparison of the magnetic properties of the closely investigated Tb_2PdSi_3 with other members of the $R_2\text{PdSi}_3$ series can be done for either a specific feature like T_2 or with hindsight of generalized magnetic properties of the $R_2\text{PdSi}_3$ with R being a trivalent heavy rare earth ion. The issue of the T_2 seems to be different when Tb_2PdSi_3 is compared with Er_2PdSi_3 as had been presented in chapter 7. Most of the $R_2\text{PdSi}_3$ compounds ($R = \text{Tb}, \text{Dy}, \text{Ho}, \text{Er}, \text{Tm}$) have a zero-field-long-range antiferromagnetic full ordered moment structure. This fact is indicated by the squared-up modulation found at low temperatures. The full ordered moment structure is in general the ground state. The transition to the ground state can be either by the progressive squaring up or by a first-order spontaneous squaring up of the magnetic structure [Gignoux1991]. The transition is normally found below the respective Néel temperature. The progressive squaring-up process is observed in Er_2PdSi_3 (and indicated

in Ho_2PdSi_3) with a transition at T_2 . The spontaneous squaring-up process seems realized in Tb_2PdSi_3 and Tm_2PdSi_3 (and indicated in Dy_2PdSi_3). This transition, however, takes place at the Néel temperature. The direct transition from paramagnetic state to squared-up ground state seems to be a special feature of the $R_2\text{PdSi}_3$ compounds as it is not reported in the sighted literature. The difference between spontaneous and progressive squaring-up seems connected to the case of either intra-plane or inter-plane exchange. The former gives apparently rise to the progressive squaring-up while the latter favours the spontaneous transition.

In the sighted literature a progressive squaring-up is normally not connected to an anomaly in a quantity accessible with a macroscopic measurement. Much less a frequency dependency of the ac-susceptibility has been connected to progressive squaring-up. The finding of the frequency dependency of T_2 in Er_2PdSi_3 and (also indicated in Ho_2PdSi_3) strongly suggest this connection. It is worthwhile to investigate other compounds where a progressive squaring up occurs with frequency dependent ac-susceptibility measurements.

The example of Tb_2PdSi_3 connects the frequency dependency of the ac-susceptibility to the full development of the SRC. Among the $R_2\text{PdSi}_3$, Tb_2PdSi_3 is the only compound for which SRC have been observed. In this case, the frequency dependence and the increase in the imaginary part are acknowledged behavior in spin-glasses [Binder1986]. The development of the SRC can be seen as a spin liquid phase. The exciting story is the formation of such a phase within a long-range ordered antiferromagnetic state. The phase diagram indicates the strong influence of the geometric frustration and the incompatibility to the ordered magnetic structure types.

Tb_2PdSi_3 shows the rich magnetic phase diagram for the field applied along the magnetic easy direction which had been discussed at length in chapter 5. The phase diagrams of Gd_2PdSi_3 and Ho_2PdSi_3 exhibit analogue courses and phase boundaries. Figure 8.1 shows the idea of a generic phase diagram for the $R_2\text{PdSi}_3$ compounds. This diagram is inspired after the Tb_2PdSi_3 phase diagram and is much simplified leaving the various transitions in the AFM region aside. Is there enough evidence to generalize the behavior of the $R_2\text{PdSi}_3$ in such a simplified diagram?

The phase line separating the paramagnetic phase (PM) and the FiM phase seems to exist for $R = \text{Gd}, \text{Tb}, \text{Ho}, \text{Dy}, \text{Er}$ which accounts to all systematically investigated $R_2\text{PdSi}_3$ with the exception of the Tm_2PdSi_3 compound. This phase line does not necessarily begin at T_N as it seems to be the case in Tb_2PdSi_3 . While the identification of the course of this phase transition around T_N is ambiguous it seems that in Tb_2PdSi_3 the transition temperature marks a tri-

critical point where the phases PM, AFM and FiM meet. In the other compounds the FiM-like phase seems to begin its existence in a small but finite magnetic field.

The existence of the FiM phase has been unambiguously confirmed in the cases of Tb_2PdSi_3 and Ho_2PdSi_3 . In these compounds the magnetic field has been applied in the $(H, 0, 0)$ -direction in the first case and the $(0, 0, L)$ -direction in the second case. The result is a magnetic structure with antiferromagnetic modulation mimicking the crystallographic superstructure. Independent from the magnetic moment direction relative to the

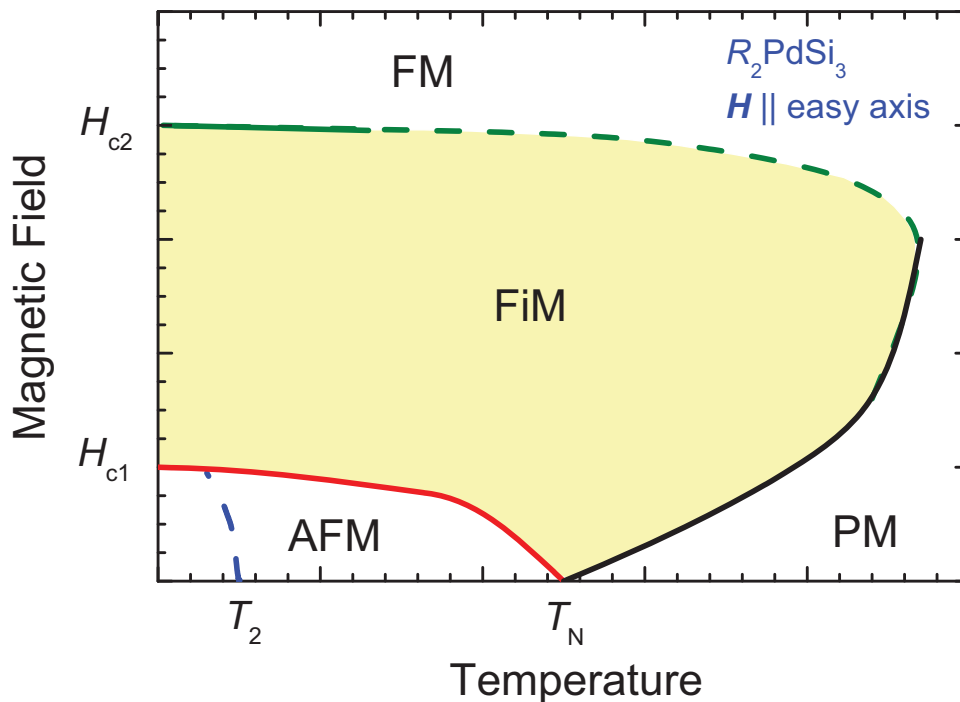


Figure 8.1: Hypothetical generic phase diagram for $R_2\text{PdSi}_3$ compounds freely after the phase diagram for Tb_2PdSi_3 . The AFM and FiM phase boundary lines are found also in the other compounds. The nature of the T_2 transition (if present) may be different throughout the series. The connection from H_{c2} to the phase boundary between FiM and PM state is not assured experimentally.

crystallographic structure (whether in-plane or along the hexagonal axis or some arbitrary direction) the compounds have a phase with antiferromagnetic order above their respective Néel temperature in magnetic fields. The application of a magnetic field normally opposes an antiferromagnetic structure, eventually destroying it at a critical field. The exchange interaction yields different zero field structures but in a magnetic field similar structures are found at least for two compounds.

Especially, the octuplication of the magnetic unit cell in comparison with the primitive chemical unit cell is indicating the influence of the crystallographic superstructure. The magnetic moment direction seems to have a lesser role since in Tb_2PdSi_3 the moments are in

the basal plane while the main part of the magnetic moment points along the $(0, 0, L)$ -direction for the Ho_2PdSi_3 compound. Still, the underlying mechanism of the magnetic structure formation is ambiguous. The magnetic structures of three compounds, Dy_2PdSi_3 , Tb_2PdSi_3 and Tm_2PdSi_3 , are connected to the crystallographic superstructure.

In chapter 6 a possible explanation for the case of Ho_2PdSi_3 has been presented where the antiferromagnetic modulation is given by the modulation of a small in-plane component of the magnetic moment. This possible explanation is to be favored over the cases of CEF-reduced magnetic moments and orbital ordering if a similar structure can be identified in Gd_2PdSi_3 .

The Gd_2PdSi_3 compound shows for both directions a nearly identical phase diagram. Also, a FiM-like phase is found in the phase diagram. However, its magnetic structure is yet to be determined. The possible FiM phase finally is terminated at high magnetic fields when the magnetic moments align parallel to the magnetic field. A saturation field of 9.4 T is found for instance in Gd_2PdSi_3 . In Tb_2PdSi_3 and Ho_2PdSi_3 the saturation field is higher than the experimentally accessible range (> 13 T). The existence of a critical field which terminates any phase with antiferromagnetic modulation is obvious. The FiM-phase seems to be independent from the magneto-crystalline anisotropy. This result is of great importance since it reduces the discussion of the probable underlying mechanism to RKKY exchange interaction and its frustration.

A special case is Er_2PdSi_3 . The conclusion in this short paragraph will be the need for more experimental data. In chapter 2 the magnetization of Er_2PdSi_3 (the field applied along the easy direction) at low temperatures shows the coincidence of the critical field inducing the ferromagnetism and the critical field of the zero field magnetic structure. However, the magnetic phase diagram suggests a FiM like transition and also magnetic correlations influencing the susceptibility from around 25 K downwards.

Indications exist for magnetic correlations above T_N for most of the $R_2\text{PdSi}_3$ compounds. The zero field magnetic structure found for the $R_2\text{PdSi}_3$ features a large magnetic unit cell. Both findings indicate the frustration of the nearest neighbor exchange interaction. The generic phase diagram and the observation of the FiM phase in Tb_2PdSi_3 and Ho_2PdSi_3 indicates the existence of a magnetically ordered phase with antiferromagnetic modulation which can be induced with a magnetic field above the actual ordering temperature.

Three models for the underlying mechanism leading to the observed FiM phases had been thought of. All of them will be discussed as a possible explanation for the behavior of the $R_2\text{PdSi}_3$ in magnetic fields. They share that none of them is really satisfying (otherwise it would not be three) but all of them take into account the special crystallographic

superstructure of the $R_2\text{PdSi}_3$. The pro and contra and the proposals themselves are briefly discussed in the following:

1. The first model to explain the FiM phase and its characteristic is the induced ferromagnetic state with a displacement of the rare earth ions. The $R_2\text{PdSi}_3$ compounds are close to the FM state as indicated by the positive values of $J(\mathbf{Q}=0)$. FM and AFM exchange interaction are competing and a magnetic field let the ferromagnetism prevail. The rare earth ions would be displaced depending on their surrounding Pd/Si layer. For instance, a rare earth ion might have more space in z -direction if its neighbor is a Si ion compared to the case if its neighbor is a Pd ion. The magnetic field then leads to a displacement with a magnitude depending on the neighbor thus reproducing the crystallographic structure. The difference in the displacement might yield the necessary contrast to explain the magnetic intensities (not calculated).
2. The second model proposes quadrupolar ordering as cause of the FiM phase. The quadrupols formed by the $4f$ electron distribution order through exchange with their neighbors. Quadrupolar interactions are observed often in high symmetric (e. g. cubic) systems and when the bilinear exchange interaction is small (e. g. for compounds with a small DeGennes factor as Tm or Ce). The quadrupolar moments [Fulde1986] are ordered in the hexagonal case due to the B_2^0 parameter. A possible ordering in magnetic fields would lead to a B_2^2 term. This model would therefore impose the crystallographic superstructure to be of non-hexagonal site symmetry or alternatively impose a distortion of the lattice by the application of an external field. This would lead to an antiferromagnetic quadrupolar ordering. However, such a transition is normally of first order [Aléonard1990]. The transition to the FiM phase has been shown to be continuous for Tb_2PdSi_3 also to high temperatures and high fields. Also, the connection to the Néel temperature (the tri-critical point in Tb_2PdSi_3) would be accidentally. Finally, Gd_2PdSi_3 does not have a quadrupolar moment.
3. The third model proposes a very strong difference of the CEF on the different rare earth sites due to the crystallographic superstructure. Furthermore, the influence of the CEF on the wave functions is strong enough to alter the ground state. Then, the surrounding crystal electric field defines the ground state wave function of the rare earth ion. Since the rare earth ions have different surroundings (either they are neighbored by Pd and Si or by Si alone) different ground states are imaginable. The crystallographic superstructure can further modify the exchange interactions. The exact nature of the exchange interaction (RKKY, dipole-dipole and possible a DM-like contribution (see chapter 1)) is left open.

The FiM phase is a ferromagnetic phase but with different magnitude of the magnetic moments in this picture. That the magnetic intensity depends on the magnetic field can be explained by the change of the mixing ratio of the wave functions. However, this model cannot explain the experimental indication of a FiM phase in Gd_2PdSi_3 . In addition, the evidence for different magnetic moments due to different ground states is missing in zero field.

8.4 Estimation of magnetic exchange coupling

The magnetic properties of the $R_2\text{PdSi}_3$ are hard to quantify. Especially, the field at which the sample becomes ferromagnetic could not be determined except for the cases of Er_2PdSi_3 and Gd_2PdSi_3 (see chapter 2). In the following some very simple approaches are made to retrieve more information from the properties of the rare earth ions and the measured quantities in the (T, H) space. The potential of a magnetic moment in an external field is given by $V = \mu_B * B$. The ordering temperature T_N and the critical magnetic field H_c can be scaled according to the relation

$$\mu_s \mu_0 H_c = k_B T_N \quad (23)$$

where μ_s is the saturation moment and k_B the Boltzmann constant. As an example, Er_2PdSi_3 saturates in the easy direction at a magnetic field of 1.2 T (which equals the critical field $H_{c1,2}$ in this compound). The magnetic moment saturation value of the Er^{3+} ion equals $\mu_s = 9 \mu_B$; the left term of relation (23) divided by k_B yields $T_{N\text{-calc.}} = 7.2$ K which is close to the observed ordering temperature of $T_N = 7$ K. Starting with the observed ordering temperature the calculated critical field $H_{c1,2}$ is 1.1 T. While this seems a trivial for the case of Er_2PdSi_3 it brings some interesting questions for the other compounds and the associated FiM phase. Especially, since most of the compounds do not achieve the saturated state at considerable high fields. Also, the other compounds seem to feature two critical fields H_{c1} and H_{c2} where the first notes the critical field for the (zero-field-)antiferromagnetic state and the second the field needed to align the magnetic moments parallel, i. e. the ferromagnetic state.

In the case of Gd_2PdSi_3 the field value at which the sample becomes ferromagnetic (9.4 T) yields an ordering temperature of 44 K. This temperature coincides with the first signs of magnetic correlations in the susceptibility (see chapter 3). Calculated from the value of T_N (= 22.3 K) the expected critical field is around 4.7 T. Reconsidering the phase diagram of Gd_2PdSi_3 (see chapter 3) the critical field H_{c1} is in the order of 4 T and is therefore in the order of the expected critical field from the ordering temperature. The values are listed again in table 7 among the calculation for the other compounds if this is possible. The values of H_{c1}

R	T_N [K]	$\mu_0 H_{c1}$ cal./exp. [T]	$\mu_0 H_{c2}$ [T]	T_N cal. [K]	$T_{\text{corr.}}$ [K]	$\mu_0 H_{c2}$ cal. [T]
Gd	22.3	4.7 / 4 ± 0.5	9.4	44	45	9.6
Tb	23.6	3.9 / 3.6 ± 0.1	-	--	93	15.4
Dy	8.2	1.2 / -	-	--	86	12.8
Ho	7.7	1.1 / 0.5 ± 0.3	-	--	-	--
Er	7.0	1.15 / 1.2 ± 0.1	1.2	7.2	25	4.1
Tm	1.8	0.4 / -	-	--	40	8.5

Table 7: Comparison between critical temperature and critical magnetic field (applied in the easy-direction) for the different rare earths in the $R_2\text{PdSi}_3$. The calculated (cal.) value is derived in each case from the quantity in the previous column. The values of $T_{\text{corr.}}$ are characteristic temperatures above T_N for each of the rare-earths. In Gd_2PdSi_3 it is the temperature when the susceptibility becomes anisotropic. For $R = \text{Tb}, \text{Er}$ the maximum in the susceptibility along the hard magnetic axis is chosen. In $R = \text{Dy}, \text{Ho}$ and Tm $T_{\text{corr.}}$ is determined from the temperature from which on the paramagnetic behaviour can be described with a Curie-Weiss law as emphasized in chapter 2.

calculated from the respective Néel temperature are near the experimentally determined ones. In order to achieve another estimate of the critical field H_{c2} has been calculated from $T_{\text{corr.}}$, the temperature where magnetic correlations are likely to effect the system.

The problem with this concept is the selection of $T_{\text{corr.}}$. The nature of the magnetic correlations indicated in the ac-susceptibility remains a mystery. Neutron diffraction above T_N yielded FM correlations in Tb_2PdSi_3 (see chapter 5) but they seem to be connected to T_N rather than $T_{\text{corr.}}$. No magnetic correlations were found in neutron diffraction on the E2 above T_N in Er_2PdSi_3 in $(HK0)$ and (HHL) geometry. The influence of the magneto-crystalline anisotropy due to higher order CEF parameters is also neglected in this concept.

8.5 Conclusion

“These results clearly reveal that this compound [Tb_2PdSi_3] is an exotic magnetic material” [Paulose2003]. The $R_2\text{PdSi}_3$ are not exotic magnetic materials. Although complicated, especially with its special crystallographic superstructure, the presented results can be understood in the light of four main factors: exchange interaction, geometric frustration of the exchange, strong coupling of the exchange to the structure and crystal electric field effect. Especially the exchange interaction and the frustration lead to the relative large number of different magnetic phases.

The crystallographic structure of $R_2\text{PdSi}_3$ is not the simple AlB_2 structure with a statistically distribution of Pd and Si ions. Instead, the crystallographic structure is determined by the ordering of Pd and Si in the layers separating the rare earth layers. A definite crystallographic structure model is still missing. The heuristic model suggests the possibility of the coexistence of multiple variants. These variants are connected via stacking faults. This picture qualitatively explains the observed intensities of the crystallographic superstructure.

The mechanism behind the spin-glass like features in Er_2PdSi_3 and Tb_2PdSi_3 at the transition temperature T_2 is discussed. Interestingly, the mechanism is different for both compounds. In Er_2PdSi_3 T_2 is identified with the full squaring up of the magnetic structure. An interesting idea is the re-examination of the frequency dependency of examples of compounds with a known squaring-up transition since this topic seems yet to be untouched. In Tb_2PdSi_3 T_2 is connected to the development of SRC.

The explanation for most of the reported complex magnetic behavior observed in macroscopic measurements is the large number of different magnetic phases in applied fields. Especially in the region below H_{c1} multiple magnetic structures are realized. In the example of Tb_2PdSi_3 these magnetic structures seem to be coexistent in a large part of the phase diagram. Comparing two macroscopic measurements with different magnetic fields will easily lead to the comparison of the investigated property of one magnetic structure with another, different one. This may lead to wrong conclusions for effects like the nature of magnetoresistance [Majumdar2000] in Tb_2PdSi_3 . Other interpretations from the macroscopic measurements on $R_2\text{PdSi}_3$ might also need modification.

The concept of the generic phase diagram elucidates the strong coupling of magnetic and crystallographic structure. The Pd / Si layers give rise to a division between an intra-plane and inter-plane exchange. The Pd / Si superstructure might even counteract the magnetic ordering and be the reason aside from geometric frustration for the observed correlations above T_N .

Compared to other rare earth compounds with the AlB_2 structure the Néel temperatures are comparable suggesting a similar exchange interaction. For instance with terbium as rare earth ion the Néel temperatures are 20 K, 32 K, and 11 K for TbGa_2 , $\text{TbSi}_{1.67}$ and Tb_2RhSi_3 , respectively [Ball1995, Schobinger1989 and Chevalier1984]. Compared to the hcp-structured rare earth metal the exchange interaction is one order of magnitude smaller (T_N for Tb is 230 K [Jensen1991]). The alloying of the rare earths with silicon and transition metal plus silicon disturbs the exchange interaction. As seen in $R_2\text{PdSi}_3$ the impact on the dominant CEF parameter can be small, but a stronger influence on the higher order parameters is suggested.

The magnetic properties and magnetic structure of the series $R_2\text{PdSi}_3$ are distinct from other rare earth intermetallic compounds with an AlB_2 derived structure by the strong correlation to the crystallographic superstructure.

Appendix A – Magnetic moment direction of Er_2PdSi_3 and Ho_2PdSi_3

Magnetic intensity is calculated for Er_2PdSi_3 to determine the magnetic moment direction. In the (HHL) scattering plane three equivalent reflections can be observed the $0, 0, 0 + 3\tau$, the $0, 0, 1 + 3\tau$ and the $0, 0, 2 + 3\tau$. The scattering vector \mathbf{Q} is separated to a part parallel to the c -axis Q_{\parallel} and a perpendicular part Q_{\perp} . The latter is 0.1642 \AA^{-1} for $+3\tau$. The quotient Q_{\perp}/Q_{\parallel} defines an angle α . If the magnetic moment is parallel to the c -axis the magnetic intensity should scale with the sine of α squared. The data for this comparison is extracted from figure 7.2 with the integration routine of TvTueb. The integrated intensity and the measured intensity scale in good agreement with sine of α squared (see table 8). Therefore, the magnetic moment direction in the zero-field magnetic structure is along $(0, 0, L)$.

Reflection	α [°]	$\sin^2\alpha$	Int. Intensity	$I(0, 0, 0 + 3\tau)^*$ $\sin^2\alpha$
$0, 0, 0 + 3\tau$	90	1	3230	3230
$0, 0, 1 + 3\tau$	33.2	0.2998	938	968
$0, 0, 2 + 3\tau$	18.12	0.0967	308	312

Table 8: Comparison of measured magnetic intensity depending on $(0, 0, L)$ for Er_2PdSi_3 .

Similar to the case of Er_2PdSi_3 is the argumentation for Ho_2PdSi_3 . However, in this case the direct calculation for several peaks leads to ambiguous results and the results are therefore presented in a figure instead in a comparison of calculated values. The lower part of figure A.1 shows the integrated intensities for the first harmonic on several positions. The data has been measured on the PANDA spectrometer at $T = 3.5 \text{ K}$. The calculation with the square sine α and an additional the magnetic form factor correction is shown in the upper part of the figure. Two features have to be noted:

The first feature is an asymmetry from $(-H, 0, L)$ to $(+H, 0, L)$. This asymmetry is most likely a product of the irregular shape of the single crystal. Especially, in the corrected curve for $L = 0$ the change in intensity is almost linear.

The second feature are the large values of the corrected curve for $L = 2$. The most likely explanation for the deviation is the larger influence of the uncorrected background for the relative small values of the intensity.

When only the curves for $L = 0$ and $L = 1$ are compared the conclusion that the magnetic moment is parallel to the c -direction can be drawn. The data points are on nearly the same

position. The detailed re-examination with an additional background correction for the $L = 2$ measurement is planned.

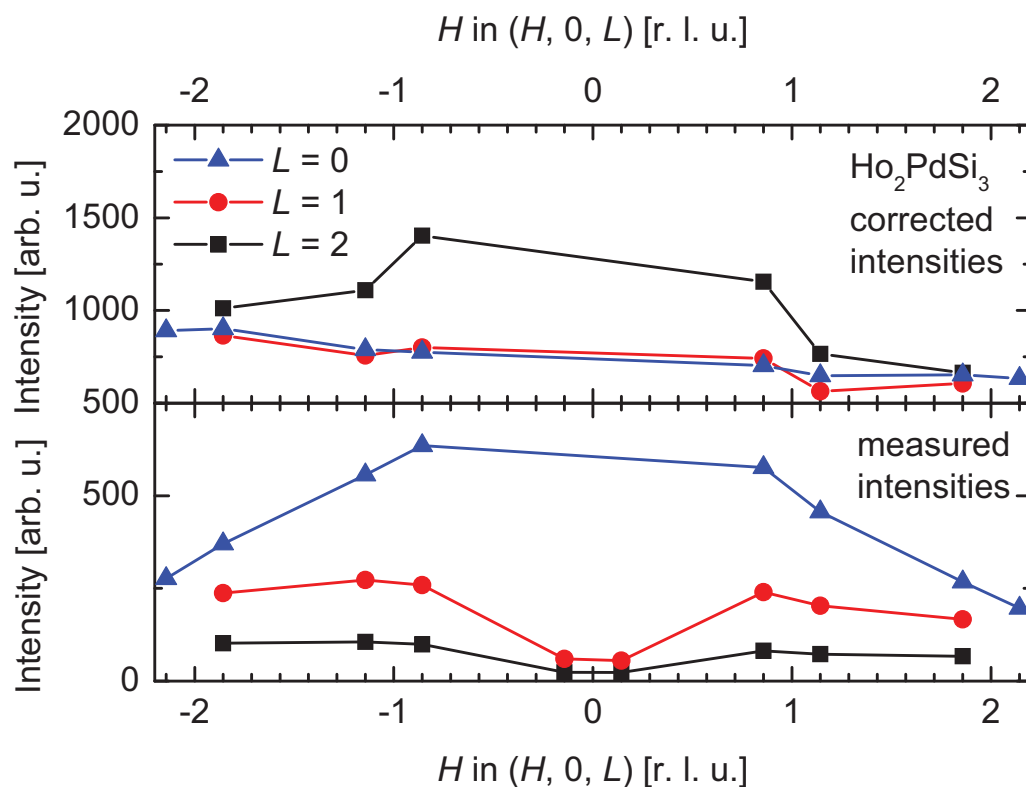


Figure A.1: Determination of the magnetic moment direction in Ho_2PdSi_3 . The magnetic intensity of the first harmonic measured for different values of L (black, red and blue) curve is shown in the lower part. The correction with the $\sin^2\alpha$ (see text) and the magnetic form factor is shown in the upper part.

Appendix B – CEF transitions

In the course of the thesis inelastic neutron spectroscopy was performed on SV-29 a time-of flight spectrometer in the Forschungszentrum Jülich. The investigated samples were powder samples of Y_2PdSi_3 , Tb_2PdSi_3 , Er_2PdSi_3 and Tm_2PdSi_3 . The aim was to use the data to establish a crystal electric field level scheme. The observed CEF transitions have been checked with a Tb_2PdSi_3 single crystal on the PANDA cold triple axis spectrometer in Munich. Additionally the TOFTOF, a time of flight spectrometer in Munich was used to measure Ho_2PdSi_3 . The presented data is an integration of the small- Q region. The results are presented without further comment.

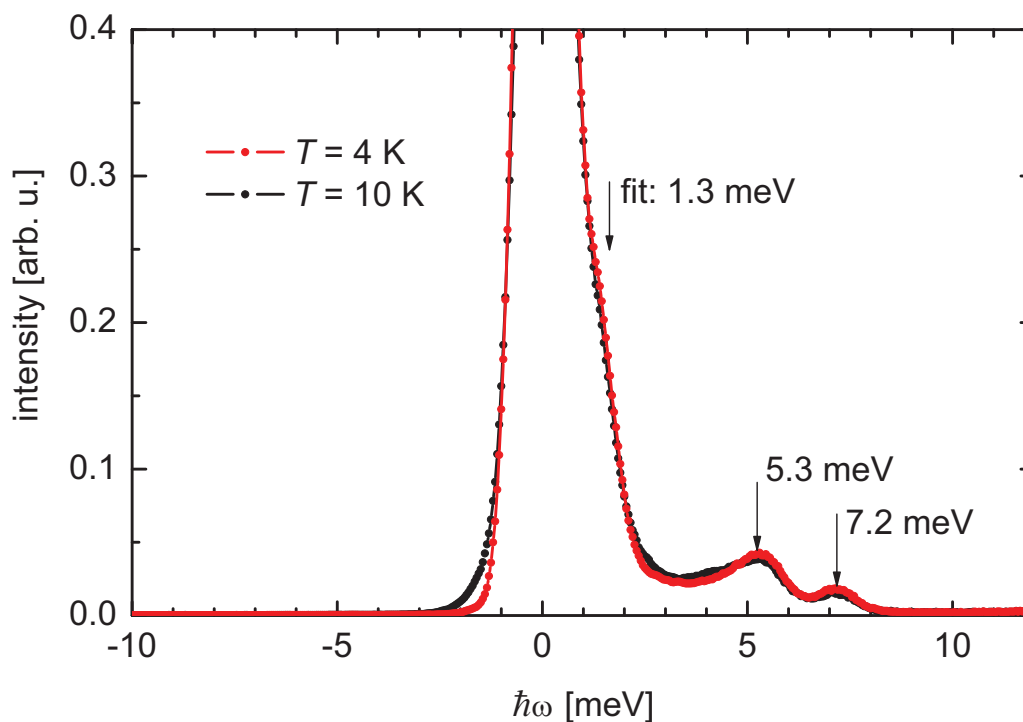


Figure A.2: Time-of-flight data for Ho_2PdSi_3 at different temperatures.

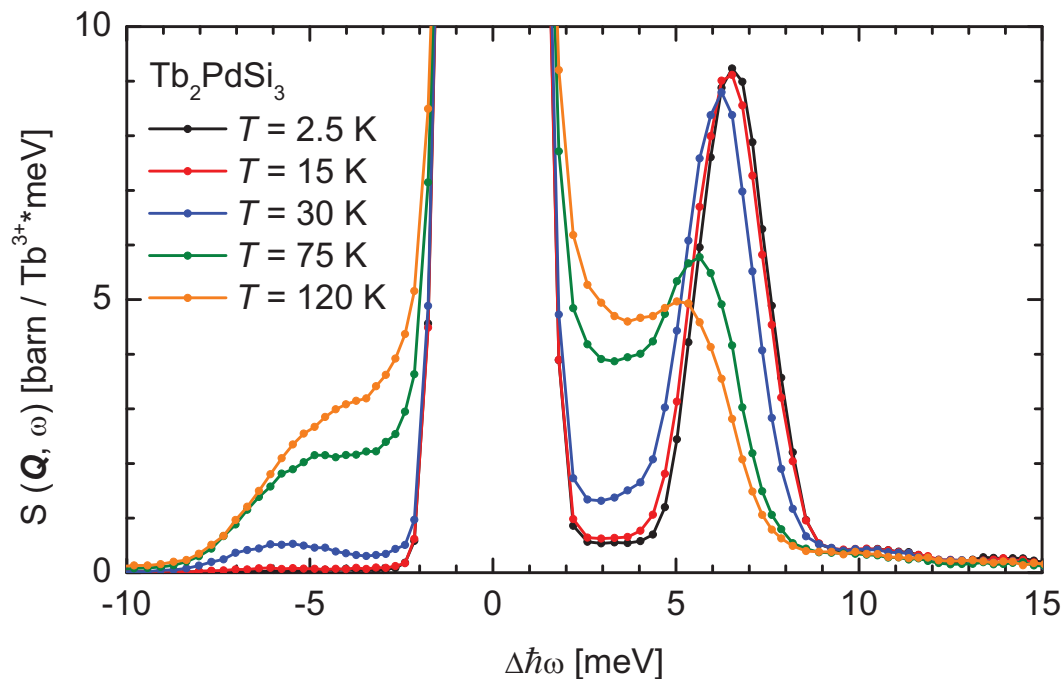


Figure A.3: Time-of-flight data for Tb_2PdSi_3 at different temperatures.

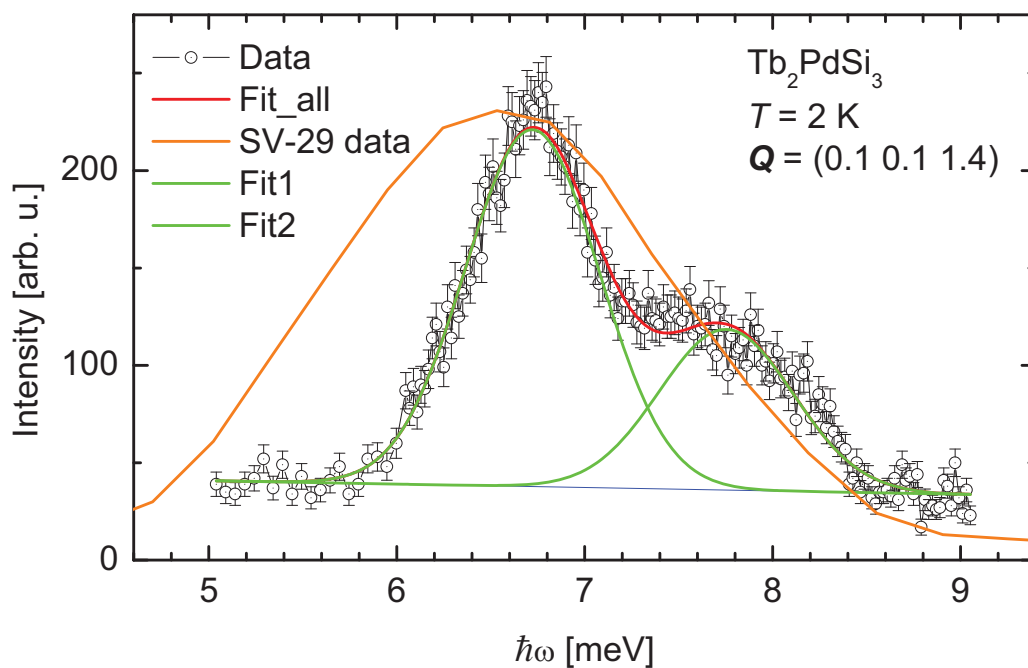


Figure A.4: Single crystal measurement of Tb_2PdSi_3 on the PANDA spectrometer in comparison to the TOF data.

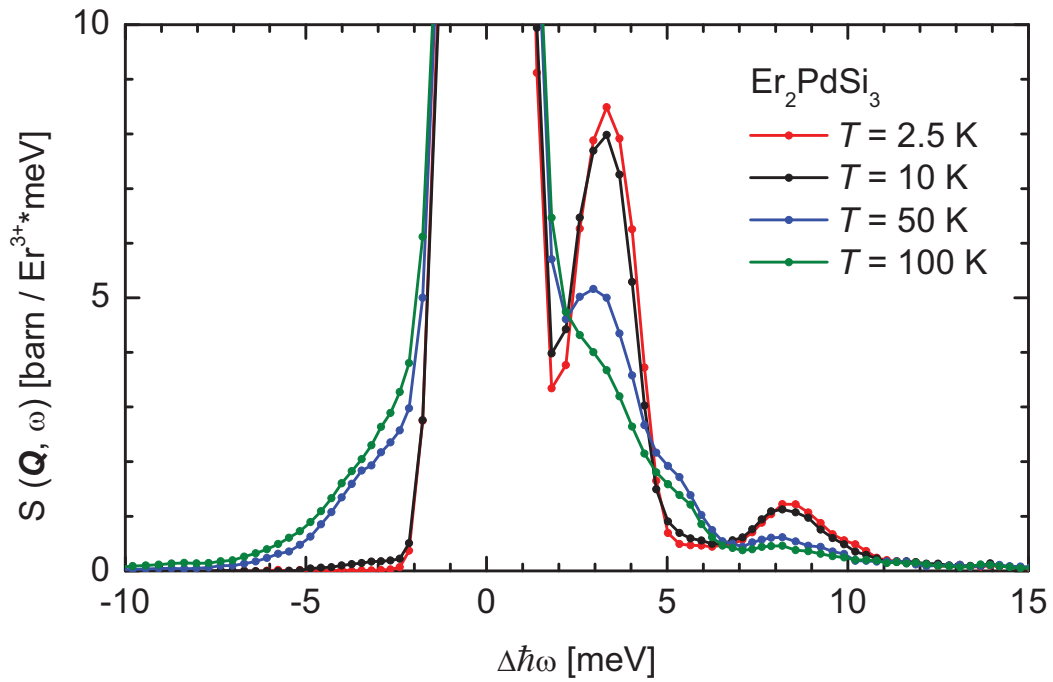


Figure A.5: Time-of-flight data for Er₂PdSi₃ at different temperatures.

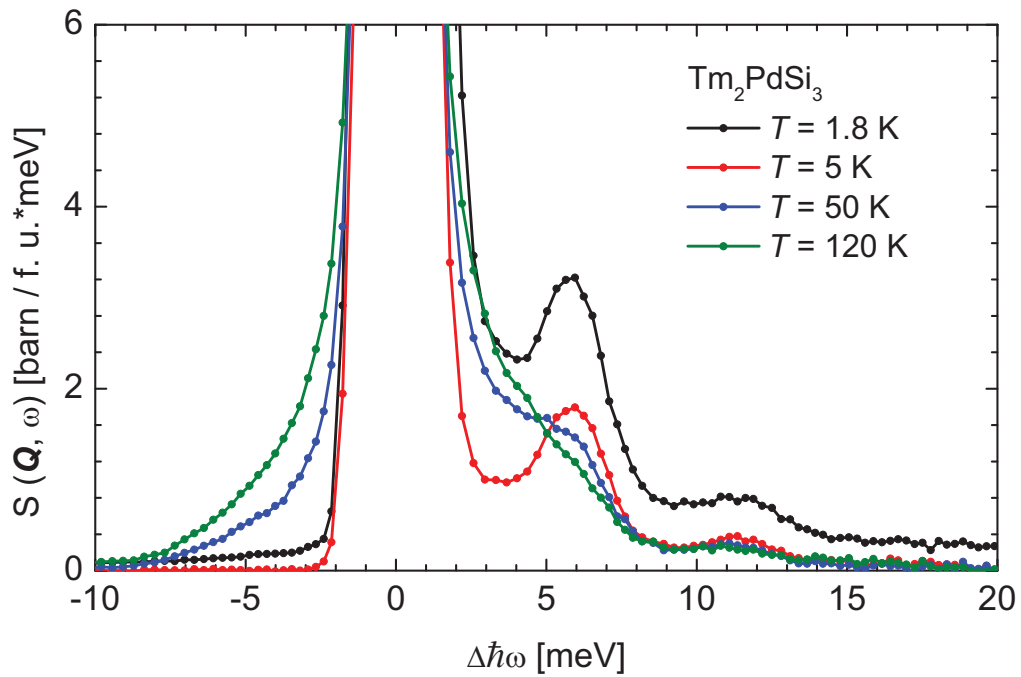


Figure A.6: Time-of-flight data for Tm₂PdSi₃ at different temperatures.

Appendix C – Lattice constants of R_2PdSi_3

The lattice constants determined from the diffraction experiments are given in table 9. Additionally, figure A.7 shows the reciprocal and real directions of a hexagonal grid.

R	a [Å] @ 300 K	c [Å] @ 300 K	a [Å] @ 2 K	c [Å] @ 2 K	ρ [kg/m ³]	M [g/mol]
Ce	-	-	4.141	4.302	6119	470.9
Gd	4.079	4.098	4.066	4.091	7160	505.2
Tb	4.048	4.037	4.043	4.024	7411	508.5
Dy	-	-	4.06	4.03	7442	515.7
Ho	4.076	4.021	4.073	3.959	7597	520.5
Er	4.064	3.991	4.059	3.986	7666	525.2
Tm	4.057	3.970	4.051	3.966	7785	528.6

Table 9: Overview of the lattice constants for the R_2PdSi_3 determined in the course of the thesis. The lattice constants agree with previous measured values [Szytula1999]. The density is calculated using the unit cell volume at 2 K with the given molar mass M .

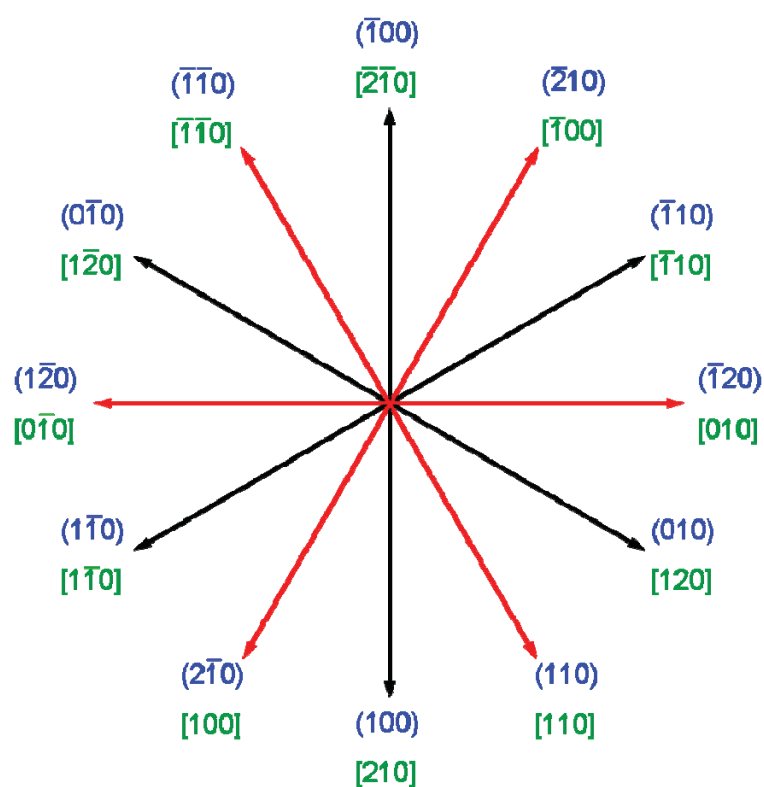


Figure A.7: Reciprocal (in round brackets) and real directions (in square brackets) of the basal plane.

List of figures

Figure	Title	Page
1.1	Comparison of magnetisation and ac-susceptibility of Tb_2PdSi_3	15
1.2	Schematic sketch of a neutron diffractometer	22
2.1	Real part of the zero field ac-susceptibility of Gd_2PdSi_3	27
2.2	Real part of the zero field ac-susceptibility of Tb_2PdSi_3	27
2.3	Real part of the zero field ac-susceptibility of Dy_2PdSi_3	28
2.4	Real part of the zero field ac-susceptibility of Ho_2PdSi_3	28
2.5	Real part of the zero field ac-susceptibility of Er_2PdSi_3	29
2.6	Real part of the zero field ac-susceptibility of Tm_2PdSi_3	29
2.7	DeGennes scaling plot for R_2PdSi_3	31
2.8	Inverse Gd_2PdSi_3 ac-susceptibility	32
2.9	Inverse Er_2PdSi_3 ac-susceptibility	33
2.10	Inverse Tb_2PdSi_3 ac-susceptibility	33
2.11	Inverse Dy_2PdSi_3 ac-susceptibility	34
2.12	Inverse Ho_2PdSi_3 ac-susceptibility	35
2.13	Inverse Tm_2PdSi_3 ac-susceptibility	36
2.14	Gd_2PdSi_3 magnetization at $T = 2$ K	37
2.15	Er_2PdSi_3 magnetization at $T = 1.8$ K	38
2.16	Tb_2PdSi_3 magnetization at $T = 2$ K	38
2.17	Dy_2PdSi_3 magnetization at $T = 2$ K	39
2.18	Ho_2PdSi_3 magnetization at $T = 1.8$ K	40
2.19	Tm_2PdSi_3 magnetization at $T = 2$ K	41
3.1	Real part of the ac-susceptibility of Gd_2PdSi_3 (constant magnetic field)	43
3.2	Real part of the ac-susceptibility of Gd_2PdSi_3 (constant temperature)	44
3.3	Magnetic phase diagram of Gd_2PdSi_3 with an ac-field along $(0, 0, L)$	45
3.4	Magnetic phase diagram of Gd_2PdSi_3 with an ac-field along $(H, 0, 0)$	46
3.5	$(H, -H, 0)$ section of resonant magnetic X-ray scattering of Gd_2PdSi_3	47
3.6	Differential neutron spectra of polycrystalline Gd_2PdSi_3	48
3.7	$(1/2, 1/2, L)$ -section of resonant magnetic X-ray scattering of Gd_2PdSi_3	50
4.1	Reciprocal (HHL) -plane of Ho_2PdSi_3	52
4.2	Section along $(0.5, 0.5, L)$ for Ho_2PdSi_3	53
4.3	Basal plane projection of the four possible layers of the triclinic model	55
4.4	The superstructure reflection $0.5, 0, 3+2/8$ for Tb_2PdSi_3	57
4.5	Picture of the structure model for Ho_2PdSi_3 [Dshemuchadse2008]	59
5.1	Real and imaginary part of the ac-susceptibility of Tb_2PdSi_3	62
5.2	Vogel-Fulcher plot for the frequency shift of T_2 found in Tb_2PdSi_3	64
5.3	Real and imaginary part of the ac-susceptibility of Tb_2PdSi_3 part 1	65
5.4	Real and imaginary part of the ac-susceptibility of Tb_2PdSi_3 part 2	67
5.5	Field dependence of the ac-susceptibility of Tb_2PdSi_3	69
5.6	Magnetisation curves of Tb_2PdSi_3	71
5.7	Magnetostriction along $(H, 0, 0)$ of Tb_2PdSi_3	72
5.8	Specific heat of Tb_2PdSi_3	73
5.9	Feature map of Tb_2PdSi_3	74
5.10	Reciprocal (HHL) -plane of Tb_2PdSi_3 at $T = 30$ K	75
5.11	Reciprocal (HHL) -plane of Tb_2PdSi_3 at $T = 50$ mK	76

5.12	Intensity measured on $\mathbf{Q} = (1/6, 1/6, 0)$ for Tb_2PdSi_3	77
5.13	Section along $(0, 0, L)$ as indicated in figure 5.11	78
5.14	Temperature dependence of LRO in Tb_2PdSi_3	79
5.15	“Powderized” single crystal data of Tb_2PdSi_3	85
5.16	Sections along $(0, 0, L)$ from the for Tb_2PdSi_3 in applied magnetic fields	86
5.17	Integrated intensities for $0, 0, 1 - n\tau$ magnetic satellite reflections	87
5.18	Reciprocal (HHL) -plane of Tb_2PdSi_3 at $T = 2.1$ K and $H = 2$ T	88
5.19	Reciprocal (HHL) -plane of Tb_2PdSi_3 at $T = 2.1$ K and $H = 4$ T	89
5.20	Section along $(H, H, 0.89)$ part 1	90
5.21	Section along $(H, H, 0.89)$ part 2	91
5.22	Section along $(H, H, 0.75)$	92
5.23	Comparative sections along $(0, 0, L)$	93
5.24	Section along $(1/2, 1/2, L)$ at different magnetic field	93
5.25	Magnetic intensity on $0, 0, 1/2$	94
5.26	Color-coded magnetic phase diagram of Tb_2PdSi_3 for $(H, H, 0)$	96
6.1	Ac-susceptibility for Ho_2PdSi_3 along $(0, 0, L)$	99
6.2	Phase diagram for Ho_2PdSi_3 with an ac-field along $(0, 0, L)$	100
6.3	Reciprocal $(HK0)$ -plane of Ho_2PdSi_3 at $T = 1.5$ K	101
6.4	Section along the $(H, -2H, 0)$ direction of Ho_2PdSi_3	103
6.5	Section along the $(1, -0.5, L)$ direction of Ho_2PdSi_3 for $T = 200$ mK	104
6.6	Integrated intensities vs. magnetic field	104
6.7	Comparison of the model calculation with the experiment	107
6.8	Magnetic field dependence scenario one	108
6.9	Magnetic field dependence scenario two	109
7.1	Real and imaginary part of the ac-susceptibility for Er_2PdSi_3	112
7.2	Reciprocal $(HK0)$ -plane of Er_2PdSi_3 at $T = 4$ K	113
7.3	Section of the magnetic structure of Er_2PdSi_3 as marked in figure 7.2	114
7.4	Normalised intensity of the different harmonics	114
7.5	Reciprocal $(H+1/16 H-1/16 L)$ -plane of Tm_2PdSi_3 at $T = 0.4$ K	117
7.6	Reciprocal (HHL) -Plane of Dy_2PdSi_3 at $T = 1.5$ K	118
8.1	Hypothetical generic phase diagram for $R_2\text{PdSi}_3$	126
A.1	Determination of the magnetic moment direction in Ho_2PdSi_3	134
A.2	Time-of-flight data for Ho_2PdSi_3 at different temperatures	135
A.3	Time-of-flight data for Tb_2PdSi_3 at different temperatures	136
A.4	Single crystal measurement of Tb_2PdSi_3 on PANDA	136
A.5	Time-of-flight data for Er_2PdSi_3 at different temperatures	137
A.6	Time-of-flight data for Tm_2PdSi_3 at different temperatures	137
A.7	Reciprocal and real directions of the basal plane	138

List of tables

Table	Title	Page
1	Compilation of results of the Curie-Weiss analysis for $R_2\text{PdSi}_3$ and theoretical values for R^{3+} ions	30
2	Comparison of measured and calculated nuclear intensity with the model described in the text (layer sequence ACBBDACD)	56
3	Observed FWHM for the different reflections measured both along $(0, 0, L)$ and $(H, 0, 0)$	58
4	Comparison of measured and calculated magnetic intensity with the model described in the text	84
5	Crystal electric field parameter from the Curie-Weiss analysis	121
6	Overview of the magnetic structures	123
7	Comparison between critical temperature and critical magnetic field	130
8	Comparison of magnetic intensity depending on $(0, 0, L)$ for Er_2PdSi_3	133
9	Lattice constants for the $R_2\text{PdSi}_3$	138

Bibliography

- [Aléonard1990] *Quadrupolar interactions in rare earth intermetallics*, R. Aléonard, P. Morin, J. Magn. Magn. Mat. **84** (1990) 255
- [Attard2002] *Thermodynamics and statistical mechanics*, Phil Attard, Elsevier Academic Press (2002)
- [Bachmann1972] *Heat Capacity Measurements on Small Samples at Low Temperatures*, R. Bachmann, F. J. DiSalvo, Jr., T. H. Geballe, R. L. Greene, R. E. Howard, C. N. King, H. C. Kirsch, K. N. Lee, R. E. Schwall, H.-U. Thomas, R. B. Zubeck, Rev. Sci. Instrum. **43** (1972) 205
- [Ball1992] *Complex magnetic phase diagrams in hexagonal rare-earth compounds*, A. R. Ball, D. Gignoux, D. Schmitt, F. Y. Zhang, J. Magn. Magn. Mat. **104-107** (1992) 170
- [Ball1993] *Long period magnetic commensurability in PrGa*, A. R. Ball, D. Gignoux, D. Schmitt, J. Magn. Magn. Mat. **119** (1993) 96
- [Ball1994] *Magnetic properties and complex phase diagram of hexagonal NdGa₂*, A. R. Ball, D. Gignoux, J. R. Fernandez, D. Schmitt, J. Magn. Magn. Mat. **137** (1994) 281
- [Ball1995] *Exchange interactions in RGa₂ compounds*, A. R. Ball, D. Gignoux, D. Schmitt, F. Y. Zhang, J. Magn. Magn. Mat. **140-144** (1995) 1121
- [Ballou1998] *Geometric frustration in Rare Earth antiferromagnetic compounds*, R. Ballou, J. Alloys Compd. **275-277** (1998) 510
- [Binder1986] *Spin glasses: Experimental facts, theoretical concepts, and open questions*, K. Binder, A. P. Young, Rev. Mod. Phys. **58** (1986) 801
- [Bitterlich2000] *Züchtung und physikalische Eigenschaften von Seltenerd-Übergangsmetall-Einkristallen*, H. Bitterlich, Dissertation TU Dresden (2000)
- [Blundell2001] *Magnetism in Condensed Matter*, Stephen Blundell, Oxford University Press, New York, (2001)
- [Brenig1992] *Statistische Theorie der Wärme – Gleichgewichtsphänomene*, Springer Verlag (1992)
- [Buschow1979] *Intermetallic compounds of rare earths and non-magnetic metals*, K. H. J. Buschow, Rep. Prog. Phys. **42** (1979) 1373
- [Cardoso2003] *Spin glass behavior in RuSr₂Gd_{1.5}Ce_{0.5}Cu₂O_{10-δ}*, C. A. Cardoso, F. M. Araujo-Moreira, V. P. S. Awana, E. Takayama-Muromachi, O. F. de Lima, H. Yamauchi, M. Karppinen Phys. Rev. B **67**, (2003) 020407
- [Chaika2001] *Electronic structure of R₂PdSi₃ (R=La, Ce, Gd, and Tb) compounds*, A. N. Chaika, A. M. Ionov, M. Busse, S. L. Molodtsov, Subham Majumdar, G. Behr, E. V. Sampathkumaran, W. Schneider, und C. Laubschat Phys. Rev. B **64**, (2001) 125121

- [Chan2007] *Trends in Crash Detection and Occupant Restraint Technology*, C.-Y. Chan, Proc. IEEE **95** (2007) 388
- [Chevalier1984] *A New Family of rare earth compounds, the ternary silicides RE_2RhSi_3 ($RE = Y, La, Ce, Nd, Sm, Gd, Tb, Dy, Ho, Er$) - Crystal Structure Electrical and Magnetic Properties*, B. Chevalier, P. Lejay, J. Etourneau, P. Hagenmuller, Solid State Comm. **49** (1984) 753
- [Colarieti2004] *Theory of the magnetic anisotropy of Gd metal*, M. Colarieti-Tosti, S. I. Simak, R. Ahuja, L. Nordström, O. Eriksson, M. S. S. Brooks, J. Magn. Magn. Mat. **272-276** (2004) e201
- [Cole1941] *Dispersion and Absorption in Dielectrics – I. Alternating Current Characteristics*, K. S. Cole, R. H. Cole, J. Chem. Phys. **9** (1941) 341
- [Coey2001] *Magnetic Materials*, J. M. D. Coey, J. Alloys Compd. **326** (2001) 2
- [DeGennes1962] *Polarisation de charge (ou de spin) au voisinage d'une impureté dans un alliage*, P.G. De Gennes, J. Phys. Radium **23**, (1962) 630
- [Deisenhofer2003] *ESR investigation of the spin dynamics in $(Gd_{12x}Y_x)_2PdSi_3$* , J. Deisenhofer, H.-A. Krug von Nidda, A. Loidl, E. V. Sampathkumaran, Solid State Comm. **125** (2003) 327
- [Devishvili2008] A. Devishvili, *personal communication*
- [Doniach1977] *The Kondo lattice and weak antiferromagnetism*, S. Doniach, Physica B **91** (1977) 231
- [Dshemuchadse2008] *Strukturuntersuchung an modulierten Seltenerd-Palladium-Siliziden*, J. Dshemuchadse, Diplomarbeit TU Dresden (2008)
- [Dshemuchadse2008_2] J. Dshemuchadse, *personal communication*
- [Ehrenfest1933] *Phasenumwandlungen im ueblichen und erweiterten Sinn, classifiziert nach den entsprechenden Singularitaeten des thermodynamischen Potentials*, P. Ehrenfest, Koninklijke Akademie van Wetenschappen te Amsterdam, Proceedings **36** (1933)
- [Elhajal2002] *Dzyaloshinski–Moriya interactions in the kagomé lattice*, M. Elhajal, B. Canals, C. Lacroix, Physica B **312-313** (2002) 716
- [Elliot1961] *Phenomenological Discussion of Magnetic Ordering in the Heavy Rare-Earth Metals*, R. J. Elliot, Phys. Rev. **124** (1961) 346
- [ElMassalami2007] *Magnetoelasticity and H-T phase diagram of $TbNi_2B_2C$* , M. ElMassalami, M. Amara, R.-M. Galéra, D. Schmitt, H. Takeya, Phys. Rev. B **76** (2007) 104410
- [Fretwell1999] *Fermi Surface as the Driving Mechanism for Helical Antiferromagnetic Ordering in Gd-Y Alloys*, H. M. Fretwell, S. B. Dugdale, M. A. Alam, D. C. R. Hedley, A. Rodriguez-Gonzalez, S. B. Palmer, Phys. Rev. Lett. **82** (1999) 3867

- [Faulhaber2008] *Magnetische Eigenschaften von $CeCu_2(Si_{1-x}Ge_x)_2$* , E. Faulhaber, Dissertation TU Dresden (2008)
- [Frontzek2004] *Magnetic properties of Tb_2PdSi_3* , **M. Frontzek**, A. Kreyssig, M. Doerr, J.-U. Hoffman, D. Hohlwein, H. Bitterlich, G. Behr, M. Loewenhaupt, *Physica B* **350** (2004) e187
- [Frontzek2006] *Magneto-crystalline anisotropy in R_2PdSi_3 ($R = Tb, Dy, Ho, Er, Tm$) single crystals*, **M. Frontzek**, A. Kreyssig, M. Doerr, M. Rotter, G. Behr, W. Löser, I. Mazilu, M. Loewenhaupt, *J. Magn. Magn. Mat.* **301** (2006) 398
- [Frontzek2007] *Frustration in R_2PdSi_3 ($R = Tb, Er$) compounds: Spin-glass or magnetic short range order? Neutron diffraction studies*, **M. Frontzek**, A. Kreyssig, M. Doerr, A. Schneidewind, J.-U. Hoffman, M. Loewenhaupt, *J. Phys.: Condens. Matter* **19** (2007) 145276
- [Fulde1986] *Magnetic excitations in crystal-field split 4f systems*, P. Fulde, M. Loewenhaupt, *Adv. Phys.* **34** (1986) 589
- [FullProf2001] *AN INTRODUCTION TO THE PROGRAM FULLPROF 2000*, J. Rodriguez-Carvajal, FullProf Manual, (2001)
- [Gerthsen1986] *Physik*, C. Gerthsen, H. O. Kneser, H. Vogel, Springer Verlag (1986)
- [Gignoux1991] *Rare earth intermetallics*, D. Gignoux and D. Schmitt, *J. Magn. Magn. Mat.* **100** (1991) 99
- [Gignoux1993] *Competition between commensurate and incommensurate phases in rare-earth systems: Effects on H-T magnetic phase diagrams*, D. Gignoux and D. Schmitt, *Phys. Rev. B* **48** (1993) 12682
- [Gignoux1997] *Magnetism of Compounds of rare earths with non-magnetic metals*, D. Gignoux and D. Schmitt, *Handbook of magnetic materials* 10, Elsevier Science B. V.
- [Gondek2007] *Magnetic ordering in ZrNiAl-type crystal system*, Lukasz Gondek, Andrzej Szytula, *J. Alloys Compd.* **442** (2007) 111
- [Gordon1997] *Substitution in Ce_2TMSi_3 intermetallic compositions with $T = (Cr, Mn, Fe, Co, or Ni)_x(Pd or Au)_{1-x}$* , R. A. Gordon, C. J. Warren, M.G. Alexander, F.J. DiSalvo, R. Pöttgen, *J. Alloys Compd.* **248** (1997) 24
- [Graf2008] Christian Graf, *personal communication*
- [Graw2000] *Constitution and crystal growth of RE_2TMSi_3 intermetallic compounds*, G. Graw, H. Bitterlich, W. Löser, G. Behr, J. Fink, L. Schultz, *J. Alloys Compounds* **308** (2000) 193
- [Harris2002] *Design of an Integrated Motor/Controller Drive for an Automotive Water Pump Application*, N. C. Harris, T. M. Jahns, S. Huang, *Proc. IEEE Ind. Appl. Soc. Annu. Meeting* **3** (2002) 2028

- [Heber1976] *Spingläser – einige typische physikalische Eigenschaften und Modelle*, G. Heber, JMMM **2** (1976) 4
- [HERCULES1993] *Neutron and Synchrotron Radiation for Condensed Matter Studies*, J. Baruchel, J. L. Hodeau, M. S. Lehmann, J. R. Regnard, C. Schlenker, Volume I, Springer Verlag (1993)
- [Hund1925] *Atomtheoretische Deutung des Magnetismus der seltenen Erden*, F. Hund, Z. Phys. A **33** (1925) 855
- [Hurd1982] *Varieties of Magnetic Order in Solids*, C. M. Hurd, Contemp. Phys. **23** (1982) 469
- [Hutchings1964] *Point-charge calculations of energy levels of magnetic ions in crystalline electric fields*, M. T. Hutchings, Solid State Phys. **16** (1964) 227
- [ICPWMan] *IC-Powls: A Program for Calculation and Refinement of Commensurate and Incommensurate Structures using Powder Diffraction Data*, W. Kockelmann, E. Jansen, W. Schäfer, G. Will, Mitteilung aus dem Mineralogischen Institut der Universität Bonn Außenstelle für Neutronenbeugung Jülich
- [IntTablesCrystA1989] *International Tables for Crystallography, Volume A*, Edited by Theo Hahn, Kluwer academic publishers Dordrecht / Boston / London (1989)
- [IntTablesCrystC2006] *International Tables for Crystallography, Volume C*, First online edition, <http://it.iucr.org/>, International union of crystallography (2006)
- [Ivonosov2008] *Electronic Structure and Nesting-Driven Enhancement of the RKKY Interaction at the Magnetic Ordering Propagation Vector in Gd_2PdSi_3 and Tb_2PdSi_3* , D. S. Inosov, D. V. Evtushinsky, A. Koitzsch, V. B. Zabolotnyy, S. V. Borisenko, A. A. Kordyuk, **M. Frontzek**, M. Loewenhaupt, W. Löser, I. Mazilu, H. Bitterlich, G. Behr, J.-U. Hoffmann, R. Follath, B. Büchner, Phys. Rev. Lett. **102** (2009) 046401
- [Iyer2005] *Novel magnetic behavior of single-crystalline Er_2PdSi_3* , K. Iyer, P. L. Paulose, E. V. Sampathkumaran, **M. Frontzek**, A. Kreyssig, M. Doerr, M. Loewenhaupt, I. Mazilu, W. Löser, G. Behr, Physica B **355** (2005) 158
- [Jahn2001] *Einführung in Magnetismus und Magnetlabor*, L. Jahn, Vorlesungsskriptum, 4. Entwurf, Institut für Angewandte Physik, Technische Universität Dresden (2001)
- [Jensen1991] *Rare Earth Magnetism*, J. Jensen, A. R. Mackintosh, Clarendon Press, Oxford (1991)
- [JülichLectures2005] *Neutron Scattering – Lectures of the Laboratory Course held at the Forschungszentrum Jülich*, T. Brückel, G. Heger, D. Richter, R. Zorn, Schriften des Forschungszentrum Jülich Reihe Materie und Material, **28** (2005)
- [Köbler2006] *Effective spin description of crystal field effects in $NdAl_2$* , U. Köbler, A. Hoser, JMMM **299** (2006) 145

- [Kotsanidis1990] *Magnetic Properties of the ternary rare earth silicides R_2PdSi_3 ($R = Pr, Nd, Gd, Tb, Dy, Er, Tm$ and Y)*, P. A. Kotsanidis, J. K. Yakinthos, E. Gamari-Seale, J. Magn. Magn. Mat. **87** (1990) 199
- [Kryder1993] *Magneto-optical storage materials*, M.H. Kryder, Annu. Rev. Mater. Sci. **23** (1993) 411
- [Lacroix1991] *Magnetic properties of the Kondo lattice*, C. Lacroix, J. Magn. Magn. Mat. **100** (1991) 90
- [Landau1980] *Statistical Physics*, L. D. Landau and E. M. Lifshitz, 3rd edition, Pergammon Press, London, 1980
- [Lecomte1983] *Frequency Dependent Magnetic Susceptibility and Spin Glass Freezing in $PtMn$ Alloys*, G.V. Lecomte, H. v. Löhneysen, E. F. Wassermann, Z. Phys. B Condensed Matter **50** (1983) 239
- [Li2003] *ac susceptibility and magnetic relaxation of R_2PdSi_3 , $R=Nd, Tb$, and Dy* , D. X. Li, S. Nimori, Y. Shiokawa, Y. Haga, E. Yamamoto, Y. Onuki, Phys. Rev. B **68** (2003) 012413
- [Loewenhaupt2003] *Evidence for the coexistence of low-dimensional magnetism and long-range order in Ca_3CoRhO_6* , M. Loewenhaupt, W. Schäfer, A. Niazi, E. V. Sampathkumaran, Europhys. Lett. **63** (2003) 374
- [Lovesey1984] *Theory of neutron scattering from condensed matter*, S. W. Lovesey, Oxford University Press (1984)
- [Lüthi1980] *Crystal field effects in Rare Earth systems*, B. Lüthi, J. Magn. Magn. Mat. **15-18** (1980) 1
- [Maeda1999] *Variation of the work function of Gd caused by the polarization of conduction electrons*, Takao Maeda, Shigeru Saito, JMMM 196-197 (1999) 694
- [Majumdar1999] *Unexpected modification of magnetic properties by Y substitution in Eu_2PdSi_3* , Subham Majumdar, R. Mallik, E. V. Sampathkumaran, P. L. Paulose, and K. V. Gopalakrishnan, PRB **59** (1999) 4244
- [Majumdar1999_2] *Magnetic relaxation behaviour in $Gd_{2-x}Y_xPdSi_3$ alloys*, Subham Majumdar, E. V. Sampathkumaran, D. Eckert, A. Handstein, K.-H. Müller, S. R. Saha, H. Sugawara, H. Sato, J. Phys.: Condens. Matter **11** (1999) L329
- [Majumdar2000] *Anisotropic giant magnetoresistance, magnetocaloric effect, and magnetic anomalies in single crystalline Tb_2PdSi_3* , S. Majumdar, E. V. Sampathkumaran, P. L. Paulose, H. Bitterlich, W. Löser und G. Behr, Phys. Rev. B **62**, (2000) 14207
- [Majumdar2001] *Magnetic and transport behavior of single-crystalline Dy_2PdSi_3* , S. Majumdar, H. Bitterlich, G. Behr, W. Löser, P. L. Paulose, E. V. Sampathkumaran, Phys. Rev. B **64** (2001) 12418
- [Majumdar2001_2] *Magnetic ordering and the Kondo effect in the alloys, $Ce_2Co_{1-x}Pd_xSi_3$* Subham Majumdar, E.V. Sampathkumaran, J. Magn. Magn. Mat. **223** (2001) 247

- [Mallik1998] *Complex magnetism in a new alloy, Eu_2PdSi_3 , with two crystallographically inequivalent sites*, R. Mallik, E. V. Sampathkumaran, M. Strecker, G. Wortmann, P. L. Paulose, Y. Ueda, JMMM 185 (1998) 135
- [Mallik1998_2] *Observation of a minimum in the temperature-dependent electrical resistance above the magnetic-ordering temperature in Gd_2PdSi_3* , R. Mallik, E. V. Sampathkumaran, M. Strecker, G. Wortmann, Europhys. Lett. **41** (1998) 315
- [Mallik1999] *Magnetic anomalies in Gd_2PdSi_3* , R. Mallik, E. V. Sampathkumaran, P. L. Paulose, H. Sugarawa, H. Sato, Physica B **259-261** (1999) 892
- [Mansuripur1997] *Principles and Techniques of Optical Data Storage*, M. Mansuripur, G. Sincerbox, Proc. IEEE **85** (1997) 1780
- [Mazilu2005] *Single crystal growth of the Er_2PdSi_3 intermetallic compound*, I. Mazilu, **M. Frontzek**, W. Löser, G. Behr, A. Teresiak, L. Schultz, J. Crystal Growth 275 (2005) e103
- [Mazilu2006] *Einkristallzüchtung und Konstitutionsuntersuchungen von magnetisch geordneten Seltenerd-Übergangsmetallverbindungen*, Dissertation, Technische Universität Darmstadt, 2006
- [Mazilu2007] *Phase diagram studies on Er_2PdSi_3 and ErPd_2Si_2 intermetallic compounds*, I. Mazilu, A. Teresiak, J. Werner, G. Behr, C.D. Caob, W. Loser, J. Eckert, L. Schultz, J. Alloys Compd **454** (2008) 221
- [Moriya1960] *Anisotropic Superexchange Interaction and Weak Ferromagnetism*, T. Moriya, Phys. Rev. **120** (1960) 91
- [Morin1988] *Susceptibility formalism for magnetic and quadrupolar interactions in hexagonal and tetragonal rare-earth compounds*, P. Morin, J. Rouchy, D. Schmitt, PRB **37** (1988) 5401
- [Motohashi2005] *Competition between ferromagnetism and spin glass: The key for large magnetoresistance in oxygen-deficient perovskites $\text{SrCo}_{1-x}\text{M}_x\text{O}_{3-\delta}$ ($M=\text{Nb, Ru}$)*, T. Motohashi, V. Caignaert, V. Pralong, M. Hervieu, A. Maignan, and B. Raveau, Phys. Rev. B **71**, (2005) 214424
- [NeutronData2002] *Neutron Data Booklet*, A. J. Dianoux, G. Lander, Institut Laue-Langevin (2002)
- [Nolting1997] *Quantentheorie des Magnetismus, Band I + II*, W. Nolting, Teubner Verlag (1997)
- [diNovi1968] *Application of the pulse method to a specific heat and density independent measurement of thermal conductivity: extension of the method to very small specimens*, R. A. di Novi, J. Phys. E **1** (1968) 379
- [Paulose2003] *Anisotropic spin-glass-like and quasi-one-dimensional magnetic behavior in the intermetallic compound Tb_2PdSi_3* P. L. Paulose, E. V. Sampathkumaran, H. Bitterlich, W. Löser und G. Behr, Phys. Rev. B **67**, (2003) 212401

- [Pierre1990] *Magnetic properties of rare earth silicide single crystals RSi_{2-x} ($R = Pr, Nd, Gd$)* J. Pierre, S. Auffret, E. Siaud, R. Madar, E. Houssay, A. Rouault, J. P. Senateur, JMMM **89** (1990) 85
- [Pierre1992] *Magnetic and transport properties of rare earth silicides RSi_{2-x}* J. Pierre, S. Auffret, B. Lambert-Andron, R. Madar, A. P. Murani, J. L. Soubevrux, J. Magn. Magn. Mat. **104-107** (1992) 1207
- [Rahman1985] *Promising Applications of Neodymium Boron Iron Magnets in electrical machines*, M. A. Rahman, G. R. Slemon, IEEE Trans. Magn. **21** (1985) 1712
- [Rotter1998] *A miniature capacitance dilatometer for thermal expansion and magnetostriction*, M. Rotter, H. Müller, E. Gratz, M. Doerr, M. Loewenhaupt, Rev. Sci. Instrum. **69** (1998) 2742
- [Rotter2000] *Anisotropic magnetic exchange in orthorhombic RCu_2 compounds ($R = rare earth$)*, M. Rotter, M. Loewenhaupt, S. Kramp, T. Reif, N. M. Pyka, W. Schmidt, R. van de Kamp, Eur. Phys. J. B **14** (2000) 29
- [Rotter2001] *Noncollinear amplitude-modulated magnetic order in Gd compounds*, M. Rotter, M. Loewenhaupt, M. Doerr, A. Lindbaum, H. Michor, Phys. Rev. B **64** (2001) 014402
- [Rotter2003] *Dipole interaction and magnetic anisotropy in gadolinium compounds*, M. Rotter, M. Loewenhaupt, M. Doerr, A. Lindbaum, H. Sassik, K. Ziebeck, B. Beuneu, Phys. Rev. B **68** (2003) 144418
- [Saha1999] *Magnetic anisotropy, first-order-like metamagnetic transitions, and large negative magnetoresistance in single-crystal Gd_2PdSi_3* , S. R. Saha, H. Sugawara, T. D. Matsuda, H. Sato, R. Mallik, E. V. Sampathkumaran, Phys. Rev. B **60** (1999) 12162
- [Saha2000] *Magnetic, thermal, and transport properties of single crystals of antiferromagnetic Kondo-lattice Ce_2PdSi_3* S. R. Saha, H. Sugawara, T. D. Matsuda, Y. Aoki, H. Sato, E. V. Sampathkumaran, Phys. Rev. B **62** (2000) 425
- [Saha2000_2] *Resistivity minimum and anisotropy in R_2PdSi_3 ($R=Ce, Gd$)* S. R. Saha, H. Sugarawa, T. D. Matsuda, Y. Aoki, H. Sato, E. V. Sampathkumaran, Physica B **281-282** (2000) 116
- [Sampathkumaran2002] *Magnetic behavior of single-crystal Ho_2PdSi_3* , E. V. Sampathkumaran, H. Bitterlich, K. K. Iyer, W. Löser, G. Behr, Phys. Rev. B **66** (2002) 052409
- [Sampathkumaran2002_2] *Superparamagnetic-like ac susceptibility behavior in the partially disordered antiferromagnetic compound Ca_3CoRhO_6* , E. V. Sampathkumaran, A. Niazi, Phys. Rev. B **65** (2002) 180401
- [Sato1990] *Induced anisotropy in reentrant $Ni_{77}Mn_{23}$ studied by transverse ac susceptibility*, T. Sato, Phys. Rev. B **41** (1990) 2550

- [Saslow1988] *Scenario for the Vogel-Fulcher “law”*, W. M. Saslow, Phys. Rev. B **37** (1988) 676
- [Schobinger1989] *Crystallographic and magnetic structure of TbSi_{1.67} and TbSi_{1.67-8}*, P. Schobinger-Papamantellos, D. B. de Mooij, K. H. J. Buschow, J. Magn. Magn. Mat. **79** (1989) 231
- [Shull1949] *Detection of Antiferromagnetism by Neutron Diffraction*, C.G. Shull, J. S. Smart, Phys. Rev. **76** (1949) 1256
- [Slater1964] *Atomic Radii in Crystals* J.C.Slater, Journal of Chemical Physics **41** (1964)
- [Smith1976] *New mechanisms for magnetic anisotropy in localised s-state moment materials*, D. A. Smith, J. Magn. Magn. Mat. **1** (1976) 214
- [Soong2001] *Investigation of Interior Permanent Magnet Offset-Coupled Automotive Integrated Starter/Alternator*, W. L. Soong, N. Ertugrul, E. C. Lovelace, T. M. Jahns, IEEE Ind. Appl. Soc. Annu. Meeting **1** (2001) 429
- [SR830Man2006] *MODEL SR830 DSP Lock-In Amplifier*, Stanford Research Systems, (2006)
- [Stevens1952] *Matrix Elements and Operator Equivalents connected with the Magnetic Properties of Rare Earth Ions*, K. W. H. Stevens, Proc. Phys. Soc. A **65** (1952) 209
- [Stevens1997] *Magnetic ions in Crystals*, K. W. H. Stevens, Princeton University Press, New Jersey, (1997)
- [Stoner1953] *The Analysis of Magnetization Curves*, E. C. Stoner, Rev. Mod. Phys. **25** (1953) 2
- [Strnat1990] *Modern permanent magnets for applications in Electro-Technology*, K. J. Strnat, Proc. IEEE **78** (1990) 923
- [Szytula1993] *Neutron diffraction study of Ce₂RhSi₃, Nd₂RhSi₃ and Tb₂RhSi₃*, A. Szytula, J. Leciejewicz, K. Maletka, J. Magn. Magn. Mat. **118** (1993) 302
- [Szytula1999] *Magnetic behaviour of R₂PdSi₃ compounds with R=Ce, Nd, Tb-Er*, A. Szytula, M. Hofmann, B. Penc, M. Ślaski, Subham Majumdar, E. V. Sampathkumaran, A. Zygmunt, J. Magn. Magn. Mat. **202** (1999) 365
- [Szytula2000] *Magnetic behaviour and electronic structure of the R₂PdSi₃ (R=Ce, Nd, Tb-Er) compounds*, A. Szytula, M. Hofmann, B. Penc, M. Slaski, S. Majumgar, E. V. Sampathkumaran und A. Zygmunt, Acta Phys. Pol. A **97**, (2000) 823
- [Szytula2003] *Electronic structure and magnetism of rare-earth intermetallic compounds* A. Szytula, A. Jezierski, B. Penc, Physica B **327** (2003) 171-176
- [Tang2008] F. Tang, *personal communication*

- [Thompson2000] *The future of magnetic data storage technology*, D. A. Thompson, J. S. Best, IBM J. Res. Develop. **44** (2000) 311
- [Tsutsui1979] *Studies on the Sm-Co Magnet as a Dental Material*, H. Tsutsui, Y. Kinouchit, H. Sasaki, M. Shiota, T. Ushitat, J. Dent. Res. **58** (1979) 1597
- [Walter1984] *Treating crystal field parameters in lower than cubic symmetries*, U. Walter, J. Phys. Chem. Solids **45** (1984) 401
- [Watanuki2006] *Physical properties and phase diagram of geometrically quadrupolar frustrated system DyB_4* R. Watanuki, H. Mitamura, T. Sakakibara, G. Sato, K. Suzuki, Physica B **378-380** (2006) 594
- [Yosida1965] *Long-range magnetic coupling in Metals*, K. Yosida, A. Okiji, Phy. Rev. Lett. **14** (1965) 301
- [Zachariasen1967] *A General Theory of X-Ray Diffraction in Crystals*, W. H. Zachariasen, Acta Cryst. **23** (1967) 558

Additional publications:

- [Mazumdar2008] *Crystalline Electric Field Effects in $PrNi_2B_2C$* , C. Mazumdar, M. Rotter, **M. Frontzek**, H. Michor, M. Doerr, A. Kreyssig, M. Koza, A. Hiess, J. Voigt, G. Behr, L.C. Gupta, M. Prager, M. Loewenhaupt, Phys. Rev. B **78** (2008) 144422
- [Weissbach2008] *Intergrowth of several solid phases from the Y-Ni-B-C system in a large YNi_2B_2C crystal*, T. Weissbach, T. Leisegang, A. Kreyssig, **M. Frontzek**, J.-U. Hoffmann, D. Souptel, A. Köhler, G. Behr, P. Paufler, D. C. Meyer, J. Appl. Cryst. **41**, (2008) 738

Reports:

- [HMI-Report2002] *Crystallographic and magnetic structure of Tb_2PdSi_3* , M. Frontzek, A. Kreyssig, J.-U. Hoffmann and D. Hohlwein, BENSCH Experimental Reports 2002
- [HMI-Report2002_2] *Crystallographic and magnetic structure of Tb_2PdSi_3* , M. Frontzek, A. Kreyssig, J.-U. Hoffmann and D. Hohlwein, BENSCH Experimental Reports 2002
- [HMI-Report2004] *Crystallographic superstructure of R_2PdSi_3 , ($R = Tb, Ho, Er, Tm$) compounds* M. Frontzek, S. Raasch and T. Lonkai, BENSCH Experimental Reports 2004
- [HMI-Report2005] *Magnetic structure of Er_2PdSi_3 and Tm_2PdSi_3* , M. Frontzek, A. Kreyssig, E. Faulhaber, J.-U. Hoffmann and Uwe Amann, BENSCH Experimental Reports 2005
- [Jülich-Report2005] *Crystal electric field scheme of R_2PdSi_3 ($R = Tb, Er, Tm$)*, M. Frontzek, Forschungszentrum Jülich Experimental Reports 2005/6
- [HMI-Report2006] *Magnetic structure of Tm_2PdSi_3* , M. Frontzek, A. Kreyssig, S. Raasch, J.-U. Hoffmann and Uwe Amann, BENSCH Experimental Reports 2006

- [ILL-Report2006] *Magnetic structure of GdPt₃Si, Gd₂PdSi₃ and GdCuSn*, M. Rotter, A. Devishvili, P. Rogl, E. Royanian, N. Melnychenko, H. Michor, M. Frontzek, T. Tsutaoka, ILL Experimental Reports 2006
- [HMI-Report2008] *Magnetic structure of Ce₂PdSi₃ and Dy₂PdSi₃*, W. D. Stein, M. Frontzek, J.-U. Hoffmann, A. Hoser, BENSC Experimental Reports 2008

Danksagung

Mit ein paar kleinen Zeilen Text möchte ich versuchen allen zu danken, die bei der Entstehung dieser Arbeit einen Anteil hatten. So sehr man aber auch bemüht ist seine Empfindungen in Worte zu kleiden ist dieses Unterfangen meist nie zufriedenstellend, da die Beziehung die man zu seinen Mitmenschen im Laufe der Zeit aufgebaut hat durch Sprache meist nur unzureichend erfasst wird. Da wir nun mal schon am abstrahieren sind, möchte ich ganz abstrakt meiner „Alma Mater“, der Technischen Universität Dresden, für insgesamt 12 schöne Jahre (da sind die 3/8 wieder) danken.

Diese Arbeit wurde am Institut für Festkörperphysik unter der Leitung meines Doktorvaters Professor Michael Loewenhaupt angefertigt. Ohne Ihn wäre diese Arbeit nie zustande gekommen. Er hat mir die ganze Zeit über jegliche wissenschaftliche Freiheit gewährt. Diese Freiheit ermöglichte auch mir die Aneignung eines breiten Spektrums an physikalischen Messmethoden, das ich als meinen großen Lohn aus Dresden mitnehmen werde. Die fortwährende Finanzierung meiner Stelle durch die Deutsche Forschungsgemeinschaft und mit dem Auslaufen des SFB 463 durch das HZB ist durch sein Betreiben zustande gekommen. Ich freue mich, dass ich Professor Loewenhaupt für „meine“ R_2PdSi_3 Systeme begeistern konnte und er Ergebnisse dieser Arbeit einem internationalem Auditorium vorgestellt hat. In den wissenschaftlichen Diskussionen mit mir gab es bestimmt den einen oder anderen Augenblick wo er über meine wackligen Interpretationen innerlich mit den Augen gerollt hat. Diese Arbeit hat wissenschaftlich an Qualität durch ihn gewonnen.

Meinem Zweitgutachter Professor Markus Braden möchte ich für die schnelle und unkomplizierte Zusage danken diese Aufgabe zu übernehmen.

Das Institut für Festkörperphysik ist mir in dieser gesamten Zeit ein Zuhause gewesen, mit vielen lustigen, netten, freundlichen Personen und Persönlichkeiten. Arbeit hat auch einfach oft Spaß gemacht und ich hoffe, dass dieser Geist im IFP weiter bestehen wird. Die neue Gruppe unter Professor Hans-Henning Klauss (ich führ Euch jetzt nicht alle einzeln auf) gibt mir diesbezüglich aber Hoffnung. Vom IFP danken möchte ich: Mathias Dörr dessen Ordnung im Labor ich das ein oder andere Mal mit meinem Chaos angereichert habe, Elke Wachsmuth zu der ich immer mit jedem kleinen oder größeren Problem kommen durfte und letztendlich Astrid Schneidewind, unserer Außenstelle am PANDA, für die freundliche Nachfrage nach dem Fortschritt dieser Arbeit.

Dank gilt auch den Personen die mich an den verschiedenen Großforschungseinrichtungen bei meinen Experimenten unterstützt haben, ob an der APS, ESRF, ILL, LLB, NIST, HZB, FRM-II, oder FZ-Jülich. Ich habe mich immer willkommen gefühlt und dieses

Gemeinschaftsgefühl der Neutronenstreugemeinde finde ich bewundernswert und stellt einen Hauptgrund für mich dar, weiterhin ein „Neutronenstreuer“ bleiben zu wollen.

Julia Dshemuchadse möchte ich danken für die Diskussionen und Korrekturarbeit in dem 4. Kapitel. Irina Mazilu, Günther Behr und Wolfgang Löser haben durch die Züchtung der von mir untersuchten Einkristalle die detaillierte Untersuchung der R_2PdSi_3 ermöglicht.

Ohne Andreas Kreyszig wäre diese Arbeit vermutlich auch nicht entstanden. Er hatte mich damals zu meiner Diplomarbeit unter seine Fittiche genommen, und damit großen Einfluss auf meine Entwicklung als Wissenschaftler genommen. Dem Umstand, dass ich ihn auch nach seinem Weggang jederzeit mit Fragen belästigen konnte und er immer Anteil an meiner Arbeit genommen hat liegt eine Freundschaft zugrunde die irgendwo zwischen dem zweiten oder dritten Reaktorkoller begann.

Fei Tang möchte ich dafür danken, dass diese Arbeit eine würdige Fortsetzung findet. Ich sehe dem nächsten halben Jahr in dem wir noch gemeinsam an den R_2PdSi_3 forschen mit Freude entgegen.

Danke an Enrico Faulhaber, der mich die sechs Jahre als Zimmergenossen ertragen durfte. Fachlich eine Hausnummer, hochbegabt und talentiert immer mit offenen Ohren für andere Probleme und einfach auch ein guter Freund. Nicht umsonst war meine Antwort auf „Ich weiß nicht“ oft einfach „Ich frag mal Enno“.

Meinen Freunden und meiner Familie muss ich danken für Rückhalt und Beistand. Ohne Euch hätte ich es wohl auch nicht geschafft – Danke Euch allen (Ihr seid gemeint).

Denise, Dir danke ich für zwei Jahre großer Gefühle, für das in den Arm nehmen, wenn mal wieder nichts zusammenlief, für Dein Mitleiden bei meiner Arbeit. Pass auf Dich auf, mein Mädchen.

Diese Arbeit und mich selbst gäbe es nicht ohne meinen Vater Dietrich und meine Mutter Ulrike. Heute glaube ich das meine Zuwendung zur Physik teilweise auch eine Antwort auf seinen frühen Tod, ein Versuch ihm irgendwie im Geiste nahezusein, war. Meiner Mutter kann ich gar nicht adäquat danken: Sie hat den größten Einfluss daran das ich jetzt diese Zeilen tippe, mich immer ermutigt meinen Weg zu gehen, bei allen Rückschlägen an meiner Seite gestanden und immer an mich geglaubt – Danke.

Versicherung

Hiermit versichere ich, dass ich die vorliegende Arbeit ohne unzulässige Hilfe Dritter und ohne Benutzung anderer als der angegebenen Hilfsmittel angefertigt habe; die aus fremden Quellen direkt oder indirekt übernommenen Gedanken sind als solche kenntlich gemacht. Die Arbeit wurde bisher weder im Inland noch im Ausland in gleicher oder ähnlicher Form einer anderen Prüfungsbehörde vorgelegt.

Die vorliegende Dissertation wurde am Institut für Festkörperphysik der Technischen Universität Dresden unter der wissenschaftlichen Betreuung von Herrn Professor Loewenhaupt angefertigt.

Ich erkenne hiermit die Promotionsordnung der Technischen Universität Dresden an.

Matthias Dietrich Frontzek

